Seismic Performance of Hollow Rectangular Reinforced Concrete Piers with Highly-Confined Corner Elements

Phase III – Web Crushing Tests

Eric M. Hines
Graduate Research Assistant
UCSD

Alessandro Dazio
Postdoctoral Researcher
UCSD

Frieder Seible
Professor
UCSD

December 19, 2001

Abstract

Three fully reversed cyclic structural tests were conducted at roughly 1/5 scale in order to investigate the in-plane web crushing capacity of reinforced concrete structural walls with confined boundary elements. These tests constitute the third phase in a three phase investigation of the seismic performance of hollow rectangular reinforced concrete bridge piers with highly-confined corner elements. Phases I and II investigated in general the flexural and shear behavior of similar structural wall subassemblies and were reported under separate cover [1]. The three test units were designed to have high flexural strengths and minimal wall thicknesses with average shear stress demands ranging from $12.4\sqrt{f'_c}$ to $20.3\sqrt{f'_c}$. All three test units had identical boundary elements but differed geometrically in the depth of the structural wall between the boundary elements. Thus the effect of wall depth and boundary element depth on web crushing was explored.

This report explains the motivation for and the design of the Phase III tests. Test predictions are given with a brief explanation of relevant analytical and material models. Test observations are reported and selected test results are discussed. The experimental web crushing capacities of the test units are compared to the predicted capacities. The contributions of the transverse reinforcement and spirals to the shear resistance of the tension boundary element are discussed. The required development length of the transverse bars in the tension boundary elements are discussed.

Contents

List of Tables

List of Figures

Chapter 1

Introduction

The motivation for the design of hollow rectangular reinforced concrete bridge piers with highly-confined corner elements in introduced. The problem of web crushing as a possible brittle failure mode for hollow rectangular reinforced concrete piers is introduced. Existing web crushing models are discussed and the need for a flexure-shear model of web crushing is emphasized. A potential flexure-shear model for web crushing is introduced based on work originally presented in the report on Phases I and II of this task [1]. Key issues to be resolved experimentally and proposed test setup and instrumentation schemes for addressing these issues are presented.

1.1 Seismic Performance of Hollow Rectangular Reinforced Concrete Piers with Highly-Confined Corner Elements

The current construction of three new toll bridges in the San Francisco Bay Area has made the seismic design of long span bridges a research priority for Caltrans. While designers are confident that the principles applied to the seismic design of shorter spans remain valid for all bridges, important structural details must be developed to accommodate the increase in scale. As with shorter spans, the piers which support these new structures are required to withstand large deformations with no loss of strength during an earthquake event.

Designers have proposed hollow rectangular reinforced concrete piers with highly-confined corner elements for the Second Benicia Martinez Bridge, the Third Carquinez Strait Bridge and the East Bay Spans of the San Francisco-Oakland Bay Bridge* that rely on highly confined boundary elements at the corners for inelastic deformation capacity, and on connecting

*In this report, these bridges will be referred to as the Benicia Martinez Bridge, the Carquinez Bridge and the East Bay Bridge.

structural walls for stiffness and strength. The concrete in the center of such a pier that does not contribute to the flexural compression zone and that is not needed to resist shear or axial load is left out of the pier, creating a hollow core.

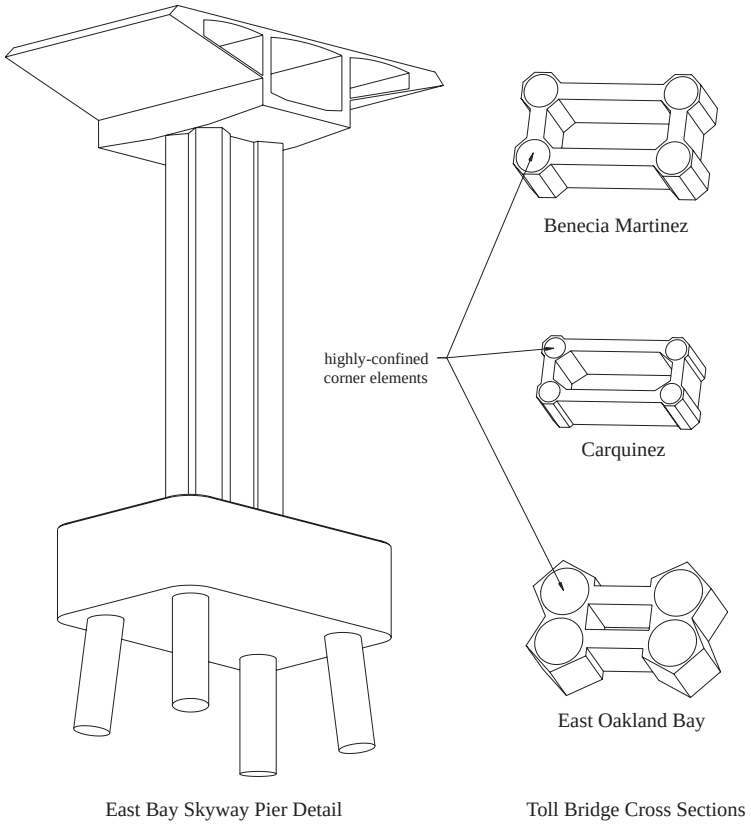

Figure 1.1: Schematic representation of proposed Bay Area bridge piers.

Reducing the mass of these piers by making them hollow decreases their contribution to seismic loads on the bridge. The hollow core ensures greater quality control during construction by reducing the heat of hydration on the interior of the section. This minimizes cracks caused by temperature differences inside the curing pier. Furthermore, reducing the total amount of material required to construct the piers allows for potential savings in construction cost. While cicular hollow piers also address these three issues, designers have, for aesthetic reasons, preferred hollow rectangular piers for all three new toll bridges (see Figure 1.1). First, if the boundary elements are designed to protrude beyond the connecting walls, damage in the pier compression zone is restricted only to the most highly confined regions of the pier, resulting in minimal concentrated spalling of the cover concrete. Second, the hollow rectangular cross sections can assume a number of different shapes and therefore

have allowed designers to create, through the shape of the piers, a strong visual impression that is integrated with the overall bridge form. For instance, in the East Bay Bridge, the skyway piers imitate the suspension bridge tower in form, and thus maintain a consistent visual rhythm throughout the entire bridge.

On the other hand, these piers carry the disadvantage of being difficult to construct. The many angles of the outside formwork require more careful planning and construction than is required by formwork for simple rectangular and circular piers. In addition, the interior form can be extremely difficult to remove, even if it is tapered slightly toward the bottom. Furthermore, the reinforcement cage fits together very tightly and allows little tolerance for threading the transverse bars through the highly-confined corner elements. One disadvantage from both the aesthetic and the psychological points of view is that the cover concrete is prone to spall at the corners under even moderate earthquakes because of its excessive depth.

The scale and complexity of these bridge piers raise questions pertaining to their seismic performance in shear. Since the boundary element spirals do not interlock, but rather are separated by structural walls and tied together with transverse reinforcement, the ability of the walls to form stable compression struts and of the transverse reinforcement and spirals to form adequate tension ties for resisting shear demand needs exploration. These two mechanisms, compression struts and tension ties, work together to transfer shear and must be able to resist the principal compression stresses and the principal tensile stresses inside the wall. If the compression struts lack adequate strength, they will crush, resulting in a rapid loss of strength. If the transverse reinforcement lacks adequate strength it will deform excessively, resulting in large shear cracks in the wall. Under cyclic loading, such large shear cracks will allow the wall concrete to crumble, resulting in a gradual loss of strength. In both cases the strength will drop until the wall begins to behave more as a two column bent than as an integral section. The failure in principal compression is also known as "web crushing" and is the focus of this report.

1.2 Test Program

This report presents the final three tests of a three phase, eight unit, large scale test program. This program had five major objectives.

1. Identify possible failure mechanisms in structural walls with confined boundary ele-

ments.

2. Test the effects of extremely high and extremely low levels of transverse reinforcement on in-plane lateral force-deflection behavior, shear resistance and spread of plasticity.

3. Test the effects of aspect ratio (M/VD) on in-plane lateral force-deflection behavior, shear resistance and spread of plasticity.

4. Characterize the web-crushing capacity of test units with varying wall thicknesses, longitudinal reinforcement ratios and relative depth ratios.

5. Assess the need for anchorage details at each end of the transverse reinforcement.

This report addresses primarily objectives 1, 4 and 5. Discussion of objectives 2 and 3 can be found in the report on Phases I and II [1].

1.3 Development of a Flexure-Shear Model for Web Crushing

A flexure-shear model for web crushing was proposed in the report for Phases I and II [1] which took into account the relationship between structural wall depth and boundary element depth, called the relative depth ratio = D_w/D_b. This model assumes that web crushing occurs in a highly concentrated region at the interface of the structural wall and the compression boundary element. The flexure-shear model therefore opposes the primary assumption of previous pure shear models that compressive stresses resulting from shear are distributed evenly along the section depth. The following section reintroduces the flexure-shear web crushing model proposed in [1].

1.3.1 Pure Shear Models for Web Crushing

Pure shear web crushing models [2, 3, 4] limit the allowable shear stress on the effective concrete cross section, implying that this maximum shear stress is distributed uniformly across the section. The pure shear model is based on the free body diagram in Figure 1.2 The struts are assumed to be uniformly inclined at an angle θ from the vertical, implying that the total area available for axial compression in the struts is $Dt_w cos\theta$. The stresses resisting this axial compression have a horizontal component equivalent to $f_2 sin\theta$, where f_2 is the principal compression stress acting along the axis of the struts. The shear force

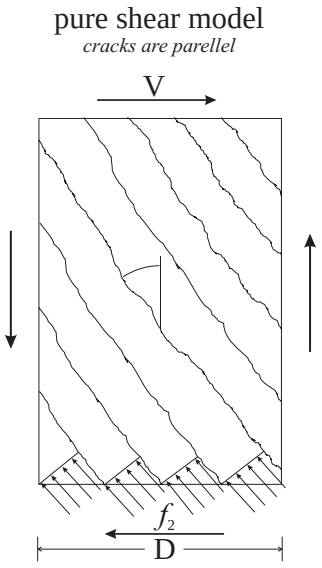

Figure 1.2: Free body diagram for pure shear web crushing equations.

applied to the section is therefore counteracted by the horizontal components of the normal stresses summed over the available area.

$$V = f_2 D t_w cos\theta sin\theta \tag{1.1}$$

Defining f_2 as the maximum concrete compressive stress after compression softening due to expanding shear cracks in the wall and expressing the equation in terms of shear stress, the web crushing stress becomes

$$v_{wc} = k f_c' cos\theta sin\theta \tag{1.2}$$

where k is a concrete strength reduction factor which reduces with increasing shear deformations.

1.3.2 Concerns Raised from Test Observations

Contrary to the assumption of pure shear behavior, upon which pure shear web crushing models are based, the actual phenomenon of web crushing in structural walls with highly-confined boundary elements under seismic loading occurs in a concentrated region of the wall where the struts converge at the compression toe of the column [5, 6] as shown in Figure 1.3. This suggests that the web crushing behavior in a plastic hinge zone does not follow the pure shear model in Figure **??** but rather follows a flexure-shear model (see Figure 1.4).

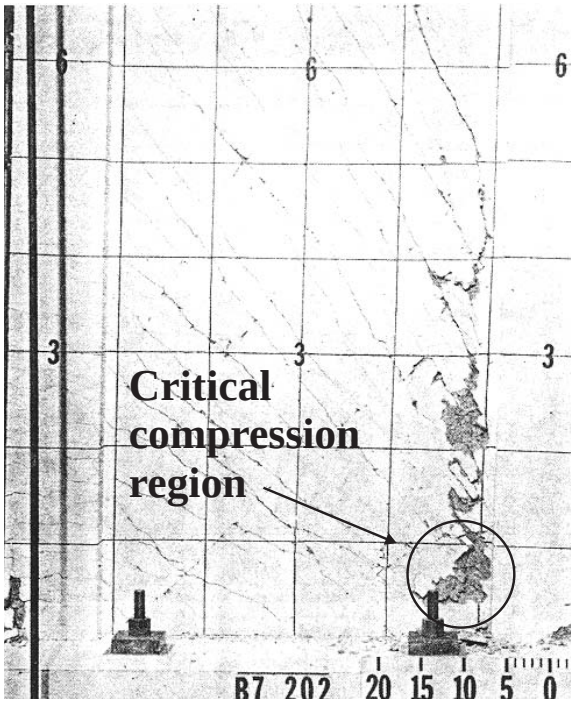

Figure 1.3: Detail of web crushing in a structural wall with confined boundary elements [4].

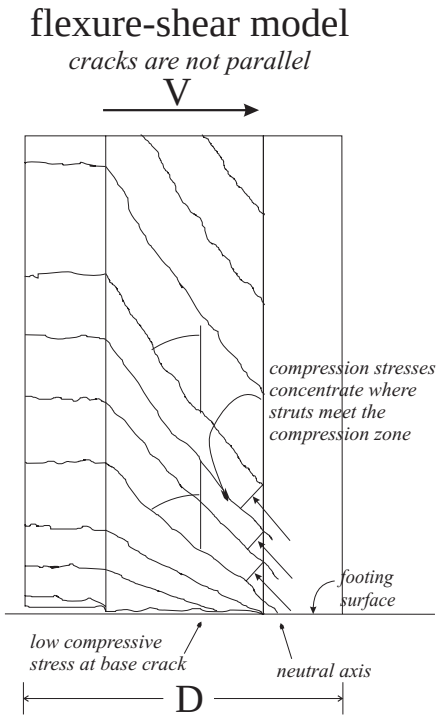

Figure 1.4: Critical compression struts take shear directly into the compression toe.

Typically the critical region crushes just outside of the compression toe and then neighboring struts crush successively either above or to the side of the initial failed struts. Crack patterns for such walls confirm that the diagonal compression stresses are concentrated in this region where the individual struts become thinner and converge in the compression toe (see Figure 1.5).

1.3.3 Flexure-Shear Approach to Web Crushing Demand and Capacity

An alternative expression for web crushing strength can be derived based on the free body diagram pictured in Figure 1.6. Cracks are assumed to be horizontal in the tension boundary element and the longitudinal steel is assumed to behave elastically above a height of h_2.

Based on this free body diagram, the web crushing strength is primarily a function of the parameters in Table 1.1. Although the axial load ratio is not directly included in this list,

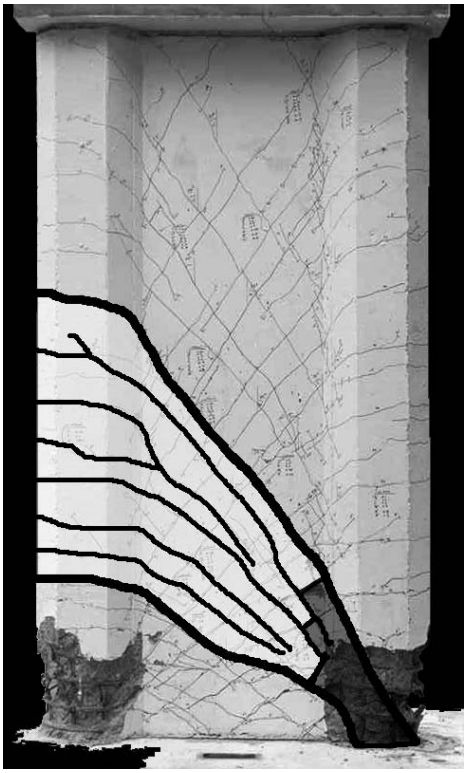

Figure 1.5: Crack pattern and compression struts in the plastic hinge region of UCSD Test Unit 2C.

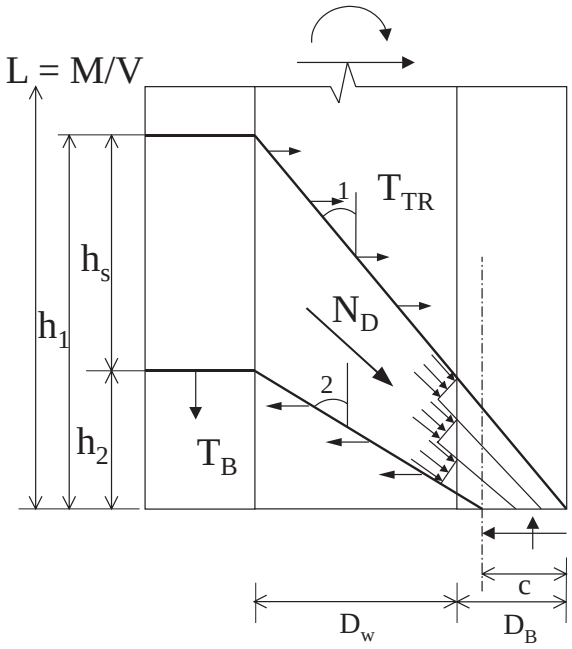

Figure 1.6: Free body diagram for critical compression strut region.

it is implicitly included via the neutral axis depth, c, which increases with increasing axial load. A deeper neutral axis implies an increase in the area of the critical compression struts, and thus an increase in the web crushing capacity, a phenomenon central to Oesterle et al.'s derivation of web crushing strength in 1984 [4].

The demand on the critical compression struts is calculated by summing contributions from the longitudinal and transverse steel. Assuming the longitudinal steel to reach yield at the lower edge of the free body diagram pictured in Figure 1.6, and assuming the stress in the steel to vary linearly from f_{ly} at this lower edge to zero at the point of contraflexure, a net vertical force pulling downward on the bottom of the critical region is produced. This force can be characterized as

$$\Delta T_l = A_{sl} f_{yl} \frac{h_s}{L - h_2} \tag{1.3}$$

where A_{sl} is the total area of longitudinal steel contributing to compression in the strut.

A_{sl} should include at least the steel in a single boundary element and may also include all of the steel in the in-plane structural wall as well as half of the steel in the out-of-plane structural wall which is in tension. Figure 1.7 shows highlighted the entire region over which the longitudinal steel is expected to contribute to the demand on the critical compression struts. f_{yl} is the yield stress for the longitudinal steel, h_s is the height of the region in the

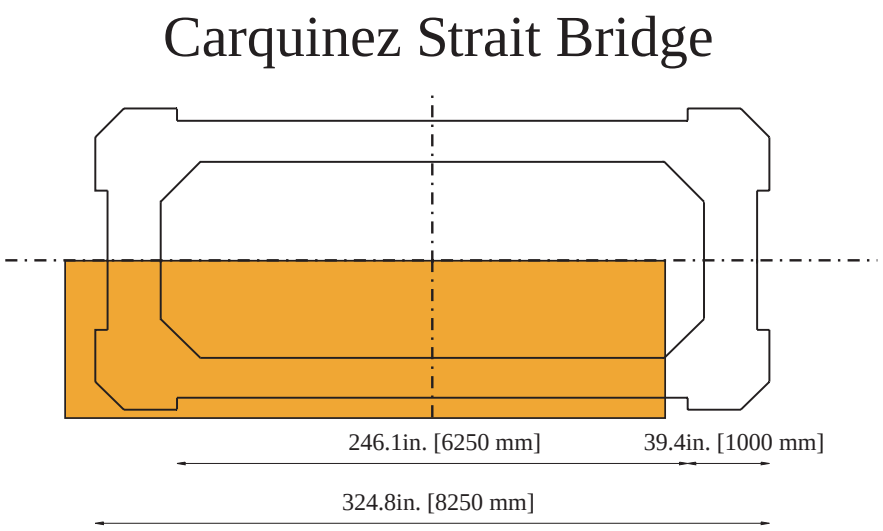

Figure 1.7: Effective region in which longitudinal steel acts on the critical compression strut.

tension boundary element over which the difference in longitudinal stress is evaluated,

$$h_s = (D_w + D_b)cot\theta_1 - (D_w + D_b - c)cot\theta_2 \tag{1.4}$$

and $L - h_2$ is the length over which the longitudinal steel stress varies linearly from zero to yield. Hence, without evaluating the actual shear demand on the column, this expression accounts directly for the effects of aspect ratio and longitudinal steel ratio on compression strut demand.

The horizontal component of the demand on the strut is provided by the net action of transverse steel on the critical compression struts inside the wall, expressed as

$$T_{tr} = A_{str} f_{ytr} \frac{D_w(\cot\theta_1 - \cot\theta_2)}{s_{tr}} \leq \quad T_l tan\theta_{av} \tag{1.5}$$

The transverse steel is assumed to have yielded, and therefore may produce a greater demand than the longitudinal steel. When this is the case, the transverse steel is limited to providing the same demand as the longitudinal steel. Hence, for low amounts of transverse reinforcement the demand on the compression strut lessens, whereas for high amounts of

Demand on the critical compression struts	L	column length M/V
	D	column depth
	ρ_l	longitudinal reinforcement ratio
	ρ_h	transverse reinforcement ratio
	f_y	steel yield stres
Capacity of the critical compression struts	t_w	wall thickness
	D_b	boundary element depth
	c	neutral axis depth
	γ	shear deformation in the plastic hinge region
	f'_c	concrete strength

Table 1.1: Parameters affecting the web crushing strength of bridge piers.

transverse reinforcement the demand plateaus according the the level of longitudinal steel. Clearly this assumption is an approximation that does not correspond to a rigorous calculation of moment equilibrium on the compression strut, and may be refined in future versions of the model.

The total demand on the strut is then calculated as

$$N_D =\Delta\ T_l cos\theta_{av} + T_{tr} sin\theta_{av} \tag{1.6}$$

The strut capacity is calculated based on the wall thickness t_w, minimum strut depth d_s, concrete strength f'_c, and a concrete compressive strength reduction factor k, to account for weakening of compression struts under large tensile strains. This results in the expression

$$N_C = k f'_c t_w d_s \tag{1.7}$$

where d_s is a function of both the neutral axis depth and the depth of the boundary elements.

$$d_s = c' cos\theta_{av} \tag{1.8}$$

$$c' = D_b cot\theta_1 - (D_b - c) cot\theta_2 \tag{1.9}$$

For design is is recommended to use $f_{yle} = 1.3 f_{yl}$ in order to account for strength in the steel beyond the specified design value. While this value is higher than the $1.1 f_{yl}$ recommended for flexural design [7], it accounts for the entire range of grade 60 steel which may have strengths ranging from 60 ksi to 78 ksi. This level of conservatism is thought appropriate for the design evaluation of shear capacity. Furthermore, it is recommended that

$$\phi N_C \geq N_D \tag{1.10}$$

where $\phi = 0.85$, as is typical for the design of transverse reinforcement to resist shear.

1.3.4 Calibration of Concrete Strength

The concrete strength reduction factor, k, decreases as a function of shear strain in the plastic hinge region [8]. Oesterle et al. calculated experimental values for k based on the assumption of pure shear shown in Figure 1.2 with the equation

$$k = \frac{V_{wc}}{0.8Dt_w 0.5f'_c} \tag{1.11}$$

in which they assumed the value of 0.5 to approximate $\sin\theta\cos\theta$. These values matched reasonably well the corresponding theoretical values from the equation proposed by Collins in 1978 [8]

$$k = \frac{3.6}{1 + \frac{2\gamma_m}{\varepsilon_0}} \tag{1.12}$$

where

γ_m	=	the maximum average shear strain in the plastic hinge region prior to web crushing.
ε_0	=	concrete strain at maximum compressive stress

Although the model presented by Collins in 1978 was updated in 1986 [9] to become a function of the principal tensile strain rather than the shear strain, the model proposed here uses Collins's 1978 model in order to compare results directly with Oesterle's tests and conclusions. In addition to the useful comparison with Oesterle's tests, relating the concrete compressive strength to the shear strain is useful in bridge design, since the the relationship implies a direct connection between the expected shear displacements (and hence the expected shear crack widths) of a pier and its web crushing capacity. For the flexure-shear web crushing model proposed here, k must be scaled up by a factor of 2 in order to accomodate changes in geometry and compression strut demand from the pure shear model to the flexure-shear model. N_D replaces the actual ultimate load V_{wc} on the column and $d_s t_w$ replaces $0.8Dt_w$ as the area available to resist the critical compression stresses.

Table 1.2 presents properties for Oesterle et al.'s test units and the corresponding N_C/N_D ratios calculated based on the flexure-shear web crushing model. An N_C/N_D ratio of 1.00 would indicate a perfect prediction of web crushing. The flexure-shear model gave low values of N_D for Test Units B6, B7, B8 and B9 whose shear strength and hence compression strut demand was increased by the presence of axial load. While the flexure-shear model accounts

Test Unit	P/f'_cA_g %	f'_c ksi [MPa]	γ	k	f_y ksi [MPa]	c in. [mm]	t_w in. [mm]	N_C/N_D
B2	0.0	7.78 [53.6]	0.028	0.367	59.5 [410]	7 [178]	4.0 [102]	1.18
B5	0.0	6.57 [45.3]	0.022	0.402	64.4 [444]	5 [127]	4.0 [102]	0.98
B5R	0.0	6.21 [42.8]	0.025	0.356	64.4 [444]	5 [127]	4.0 [102]	0.84
B6	13.4	3.17 [21.9]	0.007	0.85	63.9 [441]	10 [254]	4.0 [102]	1.16
B7	7.6	7.16 [49.4]	0.019	0.478	66.4 [458]	7 [178]	4.0 [102]	1.19
B8	9.0	6.09 [42.0]	0.015	0.595	64.9 [447]	8 [203]	4.0 [102]	1.21
B9	8.5	6.40 [44.1]	0.013	0.655	62.3 [430]	8 [203]	4.0 [102]	1.40
F1	0.0	6.58 [45.4]	0.016	0.560	62.4 [430]	7 [178]	4.0 [102]	0.71
F2	7.3	6.61 [45.6]	0.015	0.595	62.3 [430]	9 [229]	4.0 [102]	1.09

Table 1.2: Capacity/Demand ratios and minimum wall thicknesses for PCA tests on isolated structural walls.

for an increase in capacity due to the presence of axial load by accounting for the neutral axis depth, the effect of axial load on compression strut demand is neglected in the initial model presented here.

Table 1.3 compares the capacity/demand ratios calculated by the four web crushing equations presented in this report both for the tests of Oesterle et al. and for the Phase II tests [1]. While the flexure-shear model does not show better correlation for Oesterle et al.'s tests, it also does not show significantly worse correlation. The flexure-shear model's strength lies in its sensitivity to geometry. Therefore the performance of the model on one geometric type is of little consequence.

For instance, the flexure-shear model predicts more than adequate web crushing strength for the Phase II test units, whereas the other three models predict web crushing in Test Unit 2C. The flexure-shear model is sensitive to the fact that the boundary elements are closer together in the Phase II test units than they are in those tested by Oesterle et al. The height d_s over which the compression strut capacity is calculated is therefore larger in proportion to the distance h_s over which the the primary demand on the compression struts is calculated.

To the authors' knowledge, there exists no substantial experimental evidence to confirm that the flexure-shear web crushing strength is highly dependent on the relative depth ratio D_w/D_b. Section 2.2.2 outlines the design for three test units investigating variations in the relative depth ratio parameter.

Test Unit	N_C/N_D flexure-shear	Oesterle et al. pure shear	Paulay et al. pure shear	ACI pure shear
Oesterle et al. 1976-1979				
B2	1.18	1.24	0.90	1.38
B5	0.98	0.94	0.72	1.14
B5R	0.84	0.76	1.08	1.13
B6	1.16	0.92	0.52	0.73
B7	1.19	1.04	0.71	0.92
B8	1.21	0.80	0.50	0.85
B9	1.40	0.92	0.60	0.87
F1	0.71	0.89	0.60	0.94
F2	1.09	1.05	0.63	0.98
Avg.	1.08	0.98	0.77	1.03
Std. Dev.	0.21	0.17	0.29	0.23
Hines et al. 1999				
2A	3.92	1.23	0.52	1.24
2B	3.76	1.40	0.59	1.32
2C	1.60	0.70	0.29	0.76

Table 1.3: Capacity/Demand ratios and minimum wall thicknesses for PCA tests on isolated structural walls.

1.4 Issues to be Addressed by Testing

Issues addressed by the Phase III Web Crushing Tests are listed below. An explanation of the test setup and instrumentation designed to address the issue follows each listing.

1. What is the web crushing capacity of these walls and how does the UCSD flexure-shear model for web crushing compare with the ACI pure shear provisions?

   - Two of the test units were designed according to the UCSD flexure-shear model for web crushing to fail in web crushing. The third was designed unconservatively according to the ACI provisions for web crushing, but according to the UCSD model it would fail in web crushing only at a very high level of displacement ductility.
   - Shear deformations were measured in the plastic hinge region to check the applicability of Collins' 1978 model for compression softening.

2. To what degree do the boundary element spirals contribute to the total shear capacity of the bridge pier?

   - Boundary element spirals were gaged in the same direction as the transverse bars. Transverse bars were gaged at the center of the boundary element. Comparing the strains in the boundary element spirals and the transverse bars in this location

should indicate the level of force resisted by each.

3. Are anchorage details necessary in the transverse reinforcement, or can the ends of the transverse bars be left straight?

   - Transverse bars were gaged at five locations, including at the center of each boundary element, 5 in. [127 mm] from the end of each bar to determine how much strain was developed in the straight bar at this level. Displacement transducers were mounted onto extensions of selected bars at either end to measure bar end slippage.

4. Can spalling of the architectural concrete be inhibited by providing foam blockouts for the architectural concrete at the column base?

   - 1 in. [25 mm] foam blockouts were provided for the boundary element architectural concrete at the column base.

1.5 Report Outline

The following report details the design, construction, test setup, test observations and measurements from the Phase III Web Crushing Tests introduced earlier. A description of each chapter follows.

Chapter 1: Introduction

The motivation for the design of hollow rectangular reinforced concrete bridge piers with highly-confined corner elements in introduced. The problem of web crushing as a possible brittle failure mode for hollow rectangular reinforced concrete piers is introduced. Existing web crushing models are discussed and the need for a flexure-shear model of web crushing is emphasized. A potential flexure-shear model for web crushing is introduced based on work originally presented in the report on Phases I and II of this task [1]. Key issues to be resolved experimentally and proposed test setup and instrumentation schemes for addressing these issues are presented.

Chapter 2: Test Unit Design and Details

The prototype pier is introduced and the creation of the generalized test unit dimensions are explained. A web crushing parameter study conducted according to the UCSD model

presented in Chapter 1 is presented. Three test units from this study are designed and detailed to be tested at roughly 1/5 scale in the lab.

Chapter 3: Construction

This chapter briefly describes the construction process for the test units, referring to photos in Appendix A. Material properties for all of the concrete and reinforcing steel are tabulated. Measured stress strain curves are shown with theoretical curves for all reinforcing bars.

Chapter 4: Test Protocol and Instrumentation

The test setup, instrumentation, and loading protocol for the Phase III Web Crushing Tests are presented. The test setup was designed to load each test unit cyclically in single bending. The west face of the test unit was instrumented for shear deformations, leaving the east face open for observations, photos and crack width measurements.

Chapter 5: Test Predictions

Existing methods for predicting test unit response are described. The procedure for calculating force-deflection relationships from moment-curvature analysis results is described. Existing models for shear capacity are discussed. Moment-curvature and force-deflection predictions for each test unit are presented with web crushing capacity envelopes according to ACI pure shear provisions and according to the UCSD flexure-shear model.

Chapter 6: Test Observations

Test observations are presented for each level of displacement ductility. These observations refer to the photos in Appendix B. These observations refer to unmarked cracks on the east face of each test unit. Note that while all of the observations in this chapter were made on the test unit east faces, all of the data in Chapter 7 is reported as if looking at the west face of the test units. For scale, each test unit was marked with cross hairs at 12 in. [305] vertical intervals, 12 in. [305] horizontal intervals on the structural wall, and at the center of each boundary element, 6 in. [152] from the extreme end of the test unit. Specific cracks are singled out, and their widths at various locations along the section depth are given for the first positive excursion to each displacement ductility level and at zero load immediately following the excursion.

Chapter 7: Discussion of Test Results

Results are presented as if looking at the test unit west faces, occasionally referring to figures in Appendix C. The west face perspective of the test results contrasts with the east face perspective of the test observations presented in Chapter 6, however it is consistent with the instrumentation drawings in Chapter 4 and with the notion that positive displacement values are plotted on the right hand side of a graph. Test unit hysteretic behavior is evaluated in terms of overall load-deflection response and independent flexural and shear displacements. Shear performance is explored based on transverse bar strains, spiral strains and the slippage of the transverse bars.

Chapter 8: Conclusions

Design and analysis issues are discussed on the basis of the test results. Design recommendations are given where possible and key issues for future research are highlighted.

Appendices A, B, C

Photos of the test unit construction and testing are presented. Additional test data are presented. The data transverse bar strains, spiral strains and transverse bar slippage measurements.

Chapter 2

Test Unit Design and Details

2.1 Overview

The prototype pier is introduced and the creation of the generalized test unit dimensions are explained. A web crushing parameter study conducted according to the UCSD model presented in Chapter 1 is presented. Three test units from this study are designed and detailed to be tested at roughly 1/5 scale in the lab.

2.2 Prototype

This report describes the third phase of a structural testing program which focused on the in-plane behavior of structural walls with boundary elements (barbell shaped sections). Such walls are the basic subassemblies for the entire bridge pier sections introduced earlier.

In order to study the in plane behavior of structural walls with boundary elements in web crushing, it was sufficient to test individual walls, extracted from the prototype rectangular section. Figure 2.1 shows in position (a) a proposed cross section for the Benicia Martinez Bridge and in position (c) a subassembly (barbell shape) extracted from a short side of the pier. The drawing in position (b) shows the entire area of reinforcement expected to contribute to the shear demand on the structural wall subassembly. For the three tests reported here, however, only the reinforcement in the subassembly itself was considered. The test unit section geometry can be seen in Figure 2.2 (c) as a hybrid of the transverse (a), and longitudinal (b) walls of the proposed Benicia Martinez bridge pier. The Phase I and II test units themselves were designed to 17% scale of this hybrid geometry.

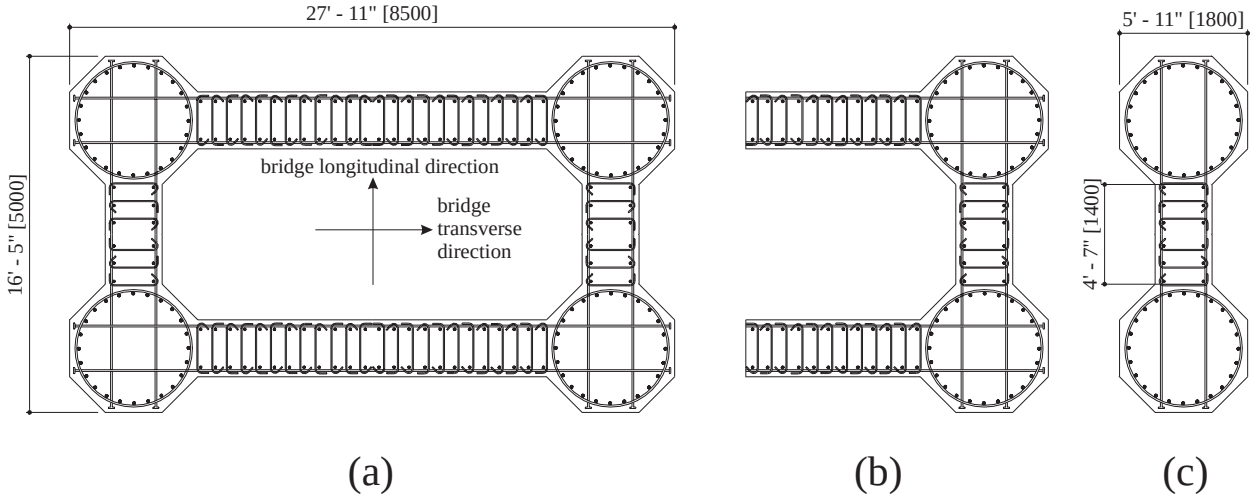

Figure 2.1: (a) Early proposal for a typical cross section of the Benicia Martinez Bridge Piers. (b) True half section with tributary longitudinal reinforcement in the wall. (c) Test subassembly consisting of a single structural wall with boundary elements.

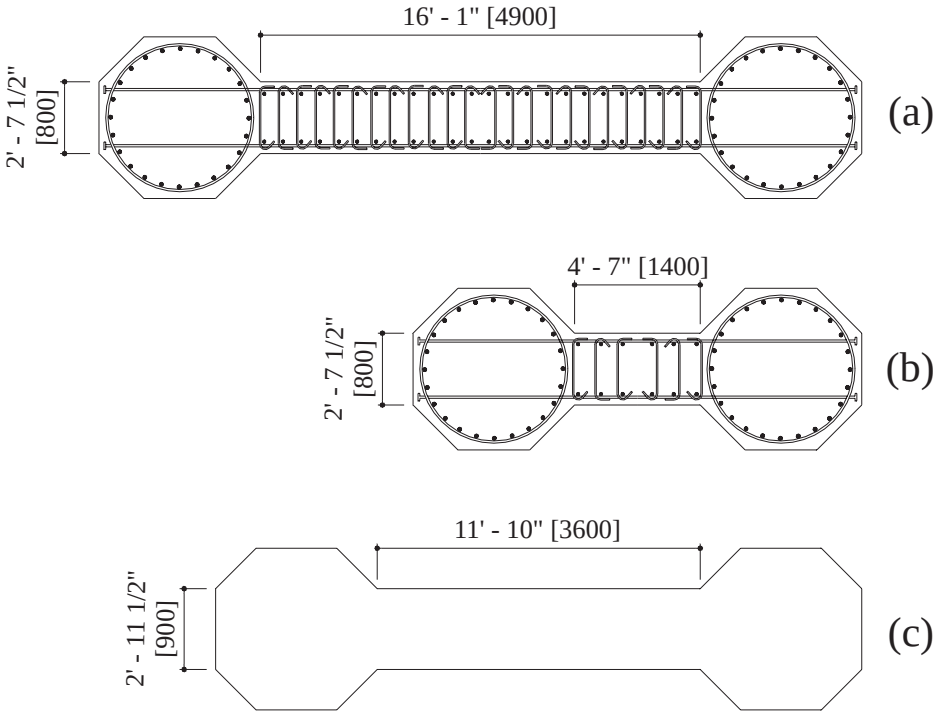

Figure 2.2: (a) Long structural wall in bridge transverse direction. (b) Short structural wall in bridge longitudinal direction. (c) Test unit section geometry generalized from Benicia Martinez prototype.

2.2.1 UCSD Test Phase III – Web Crushing Test Units

The Phase III test units were designed to provide three specific data points for understanding web crushing behavior of structural walls with boundary elements.

- Test Unit 3A was designed with geometry similar to Test Unit 2C [1] ($D_w/D_b = 2.0$), which had a 67% thinner wall than the other Phase I and II test units. Test Unit 3A was designed, however, with almost three times the level of longitudinal reinforcement in the boundary elements in order to ensure its failure in web crushing.

- Test Unit 3B was designed with the same reinforcement ratios and boundary element geometry as Test Unit 3A, but with a shallower wall ($D_w/D_b = 0.5$). This test unit was designed to experience shear stresses up to twice as high as the ACI provisions but still reach a displacement ductility level of at least $\mu_\Delta = 6$ according to the UCSD flexure-shear web crushing model.

- Test Unit 3C was designed with the same reinforcement ratios and boundary element geometry as Test Unit 3A, but with a deeper wall ($D_w/D_b = 4.0$). The geometry and reinforcement ratios for Test Unit 3C a geometry were similar to Oesterle et al.'s Test Unit B7 [6, 4] which failed in web crushing.

2.2.2 Web Crushing Parameter Study

The flexure-shear model for web crushing introduced in Chapter 1 increases in the ratio of web crushing capacity to column ultimate flexural capacity V_{wc}/V_u, as the relative depth ratio between the wall and the boundary elements D_w/D_b is decreased below 2. This contradicts the philosophy implicit in existing web crushing models that the web crushing capacity is always proportional to the total depth D, of the structural wall. Results of a numerical parametric study conducted on seven columns with identical boundary element longitudinal reinforcement, boundary element confinement, boundary element depth, and material properties, but varying wall depth are presented herein in order to point out this difference between the UCSD model and pure shear web crushing models.

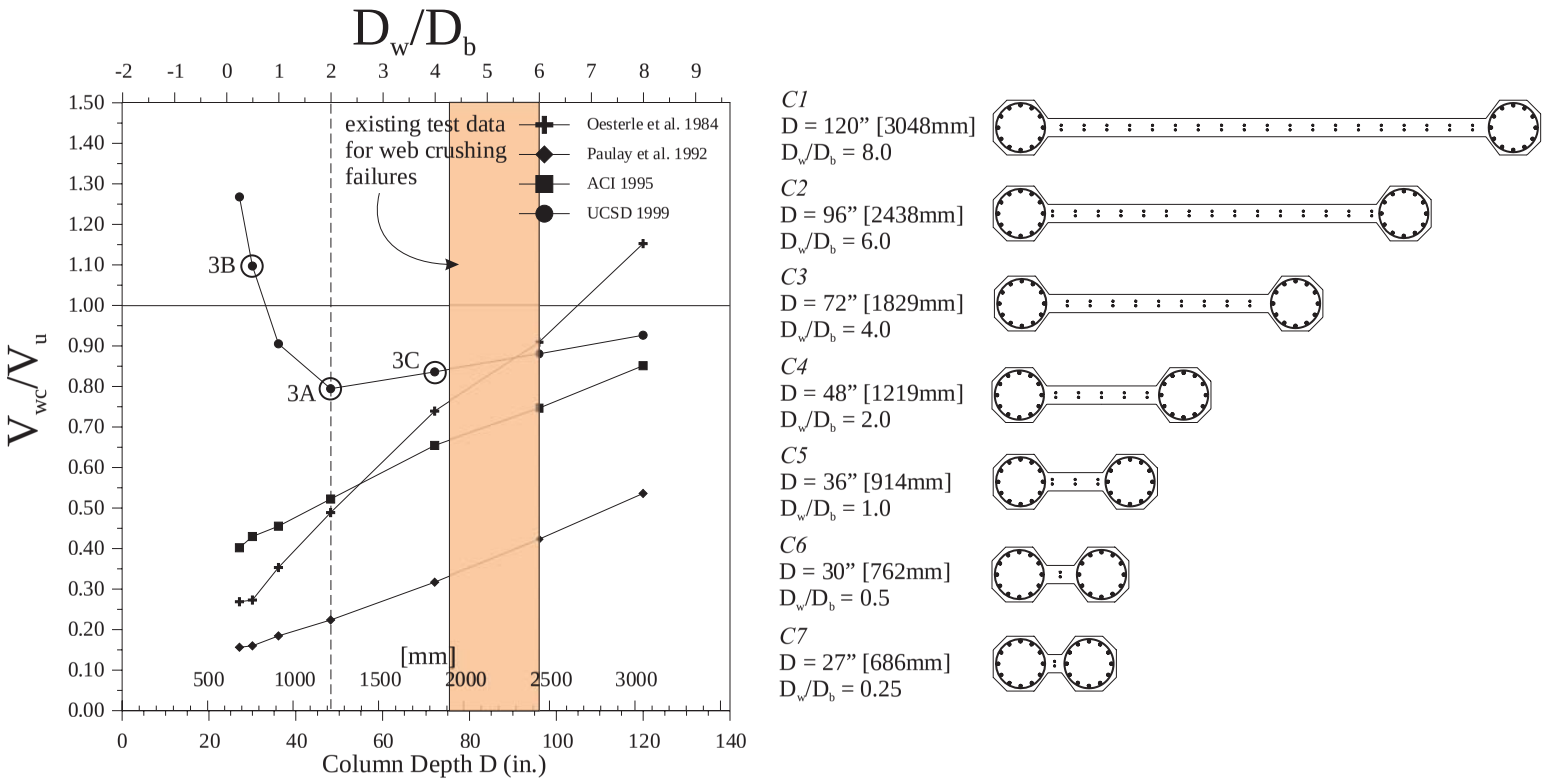

Figure 2.3: Variation in the ratio of web crushing strength to ultimate flexural strength V_{wc}/V_u, as a function of the relative depth ratio D_w/D_b.

Column	M/VD	L		D		D_w		D_b		D_w/D_b	t_w	
		in.	[mm]	in.	[mm]	in.	[mm]	in.	[mm]		in.	[mm]
C1	2.5	300	[7620]	120	[3048]	96	[2438]	12	[305]	8.00	4	[102]
C2	2.5	240	[6096]	96	[2438]	72	[1829]	12	[305]	6.00	4	[102]
C3 (3C)	2.5	180	[4572]	72	[1829]	48	[1219]	12	[305]	4.00	4	[102]
C4 (3A)	2.5	120	[3048]	48	[1219]	24	[610]	12	[305]	2.00	4	[102]
C5	2.5	90	[2286]	36	[914]	12	[305]	12	[305]	1.00	4	[102]
C6 (3B)	2.5	75	[1905]	30	[762]	6	[152]	12	[305]	0.50	4	[102]
C7	2.5	67.5	[1715]	27	[686]	3	[76]	12	[305]	0.25	4	[102]

Table 2.1: Relative Depth Ratio parametric study: geometric properties for columns C1-C7.

Figure 2.3 shows this increase in web crushing capacity predicted by the UCSD model as compared to predictions made based on the pure shear web crushing models. Table 2.1 details the geometric properties of columns C1-C7. Table 2.2 gives numerical values for the V_{wc}/V_u ratios. Note that the assessment equations given by the UCSD model do not directly depend on the value of V_u. Instead, the demand on the critical compression struts is calculated directly from the free body diagram of these struts (see Figure 1.6) as a function of the column dimensions and longitudinal reinforcement. Hence the ratio calculated via the UCSD model is N_C/N_D and not V_{wc}/V_u.

Figure 2.4 shows the theoretical force-displacement curves produced via moment-curvature analyses and assumed equivalent plastic hinge lengths. The values of F'_y and $\ _y'$ were taken from these curves at first yield of the extreme longitudinal reinforcing bar. F_u and $\ _u$ were taken from these curves at either the point where $\varepsilon_s = 0.06$ in the extreme tensile longitudinal bar, or at the point where $\varepsilon_c = 0.02$ for the extreme concrete fiber in compression. $\ _y$ was calculated from the theoretical curves as

$$_y = \Delta\ _y' \frac{F_y}{F'_y} \tag{2.1}$$

where F_y is the theoretical force on the column at which the extreme concrete compression fiber reaches as strain of $\varepsilon_c = 0.004$. Shear deformation in the plastic hinge region at ultimate displacement was assumed to be $\gamma = 0.02$ for all seven columns. Table 2.3 gives the numerical force-deflection properties for the seven columns.

The longitudinal steel in all seven columns consisted of 12 #6 [#19] bars in each boundary element and pairs of #4 [#13] bars spaced at 5 in. [127 mm] intervals inside the wall. The spiral confinement was deformed #3 [#10] bars spaced at 2 in. [52 mm] inside the lower plastic hinge region. The steel yield stress was assumed to be $f_y = 66$ ksi [455 MPa], and

Column	Oesterle et al. V_{wc}/V_u	Paulay et al. V_{wc}/V_u	ACI V_{wc}/V_u	Hines et al. N_C/N_D
C1	1.15	0.54	0.85	0.93
C2	0.91	0.42	0.75	0.88
C3 (3C)	0.74	0.32	0.65	0.84
C4 (3A)	0.49	0.22	0.52	0.79
C5	0.35	0.18	0.46	0.91
C6 (3B)	0.27	0.16	0.43	1.10
C7	0.27	0.16	0.40	1.27

Table 2.2: Column web crushing properties at ultimate displacementΔ_u.

Column	F'_y		Δ'_y		F_y		Δ_y		F_u		Δ_u		$\mu_{\Delta u}$
	kips	[kN]	in.	[mm]	kips	[kN]	in.	[mm]	kips	[kN]	in.	[mm]	
C1	207	[921]	1.09	[27.7]	305	[1357]	1.61	[40.9]	319	[1420]	6.0	[152]	3.7
C2	185	[823]	0.85	[21.6]	268	[1193]	1.23	[31.2]	291	[1295]	5.4	[137]	4.4
C3 (3C)	151	[672]	0.52	[13.2]	223	[992]	0.77	[19.6]	249	[1108]	4.4	[112]	5.7
C4 (3A)	124	[552]	0.37	[9.4]	169	[752]	0.50	[12.7]	208	[926]	3.6	[91]	7.1
C5	116	[516]	0.34	[8.6]	141	[627]	0.41	[10.4]	179	[797]	3.3	[84]	8.0
C6 (3B)	99	[441]	0.28	[7.1]	124	[552]	0.35	[8.9]	158	[703]	3.4	[86]	9.7
C7	97	[432]	0.26	[1.2]	123	[547]	0.33	[8.4]	152	[676]	2.9	[74]	8.8

Table 2.3: Column force-deflection properties.

ultimate stress was assume to be $f_u = 99$ ksi [683 MPa]. Unconfined concrete strength was assumed to be $f'_c = 5$ ksi [35 MPa]. The axial load ratio $P/f'_c A_g$ on each column was assumed to be 0.10, implying slightly larger axial loads for the deeper columns.

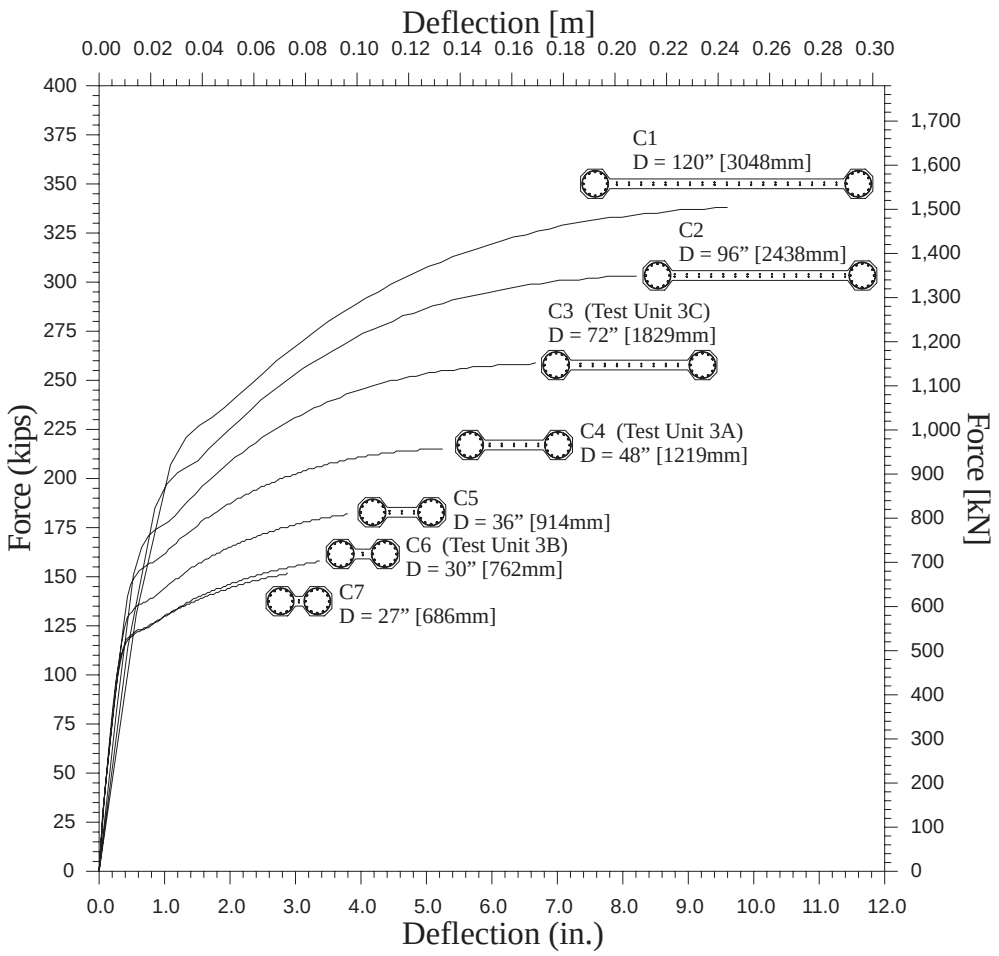

Figure 2.4: Theoretical force-deflection curves for columns C1-C7 of decreasing relative depth ratio D_w/D_b.

2.3 Test Unit Design Details

Test Unit 3A was designed based on the geometry of the subassembly introduced in Figures 2.1 and 2.2, with a wall thickness corresponding to the reduced wall thickness of Test Unit 2C [1]. Longitudinal reinforcement was designed to ensure web crushing according to the flexure-shear web crushing model introduced in Chapter 1 and then kept constant for Test Units 3B and 3C. The 12 #6 [#19] bars in each boundary element had the added advantage of corresponding to the boundary element longitudinal reinforcement provided by Oesterle et al. [5, 6] in several of their walls, including wall B7. The basic geometry and reinforcement configurations for Test Units 3A, 3B and 3C are shown in Figures 2.6, 2.7 and 2.8. Reinforcement ratio values are given in Table 2.4. Footing reinforcement details are given in Figures 2.9 - 2.11.

Transverse reinforcement was designed to satisfy the UCSD three component shear capacity equations [7, 10], which assume resistance to the shear demand consisting of a concrete component V_c, an axial load component V_p and a steel component V_s. For the Phase III test units, an effective crack angle of 35° from the vertical and an effective horizontal run of w_T, the distance between the centroid of tension and the neutral axis, were assumed. All of the steel, both transverse reinforcement and spirals, that intersected this crack was assumed to contribute to a column's shear capacity up to the yield strength of the bars. This crack and the contributing steel are pictured in Figure **??**.

The equations for the V_s component can be written to reflect these assumptions as

$$V_s = A_{str} f_{ytr} \frac{w_T}{s_{tr}} cot(35^\circ) + \frac{\pi}{2} A_{sp} f_{ysp} \frac{w_T - D_w - 2c_o}{s_{sp}} \tag{2.2}$$

where A_{str} is the total area of transverse steel for one horizontal layer, f_{ytr} is the yield stress of the transverse steel, w_T is the distance between the neutral axis and centroid of tension, assumed to act at the center of the tension boundary element, s_{tr} is the vertical spacing of the transverse steel, A_{sp} is the area of spiral steel, f_{ysp} is the yield stress of spiral steel, s_{sp} is the spiral pitch, D_w is the wall depth, and c_o is the depth of the cover concrete. Assuming a simplified version of the V_c component at high ductility as

$$V_c = 0.6 \frac{\sqrt{f'_c}}{0} .8 D t_w \qquad (psi) \tag{2.3}$$

where D is the total section depth, and t_w is the web thickness, and a V_p component of

$$V_p = \frac{P(D-c)}{2L'} \tag{2.4}$$

where P is the axial load, D is the total section depth, c is the neutral axis depth and L' is the column shear span plus half the height of the load stub (9 in. [229 mm]), the shear capacity of each test unit was calculated. Table 2.5 gives the values of each component. Table 2.6 gives the maximum conceivable flexural demand on each test unit V_u, based on a moment curvature analysis of the section, and compares the shear capacity V to the flexural capacity V_u in a ratio. Table 2.6 also gives the ratio of the transverse reinforcement capacity to the code limit given by Equation 2.6. This ratio was calculated as

$$\frac{V_{str}}{(cot35^\circ)8\sqrt{f'_c}0.8Dt_w} \tag{2.5}$$

where the denominator consists of Equation 2.6 and the term $cot35^\circ = 1.43$ to account for the fact that the V_s component used for the test unit design was based on a 35° angle and Equation 2.6 assumes a 45° angle.

The transverse reinforcement and spacing was designed for Test Unit 3A such that $0.85V = V_u$. The same reinforcement and spacing was kept for Test Units 3B and 3C in order to maintain a constant transverse reinforcement ratio $\rho_h = A_{str}/t_w s_{tr}$. Keeping the transverse reinforcement ratio constant resulted in an unconservative transverse reinforcement scheme for 3B and an overconservative transverse reinforcement scheme for 3C. This was acceptable, since the boundary element were expected to play a greater role in resisting shear in Test Unit 3B than in the other test units because of its shallow wall depth. Furthermore, the overconservative level of transverse reinforcement provided insight into the relevance of the code [2] limit on the V_s component

$$V_s \leq 8\sqrt{f'_c}0.8Dt_w \tag{2.6}$$

Test Unit	Aspect Ratio M/VD	Axial Load Ratio P/f'_cA_g	f'_c psi	f'_c MPa	Wall Thickness in.	Wall Thickness [mm]	Reinforcement (%)* ρ_l	ρ_n	ρ_s	ρ_h
3A	2.5	0.093	5380	37.1	4	102	4.29	1.15	2.07	1.38
3B	2.5	0.075	6660	45.9	4	102	4.29	0.92	2.07	1.38
3C	2.5	0.087	5740	39.6	4	102	4.29	1.15	2.07	1.38

* ρ_l longitudinal reinforcement ratio in boundary columns
ρ_n longitudinal reinforcement ratio in structural wall
ρ_s volumetric reinforcement ratio for confinement in boundary elements
ρ_h transverse reinforcement ratio in structural wall

Table 2.4: Test Unit geometry and reinforcement.

Test Unit	V_c kips	V_c [kN]	V_p kips	V_p [kN]	V_{str} kips	V_{str} [kN]	V_{ssp} kips	V_{ssp} [kN]	V_u kips	V_u [kN]	Eq. 2.6 kips	Eq. 2.6 [kN]	V/V_u
3A	7	[31]	26	[116]	164	[730]	42	[187]	202	[899]	90	[401]	1.18
3B	4	[18]	17	[76]	74	[329]	42	[187]	154	[685]	63	[280]	0.89
3C	10	[45]	36	[160]	282	[1255]	42	[187]	254	[1130]	139	[619]	1.46

Table 2.5: Test unit shear capacities.

Test Unit	V kips	V [kN]	V_u kips	V_u [kN]	Eq. 2.6 kips	Eq. 2.6 [kN]	V/V_u	$V_{str}/1.43$Eq. 2.6
3A	239	[1064]	202	[899]	90	[401]	1.18	1.27
3B	137	[610]	154	[685]	63	[280]	0.89	0.82
3C	370	[1647]	254	[1130]	139	[619]	1.46	1.42

Table 2.6: Test unit shear capacity/demand ratios.

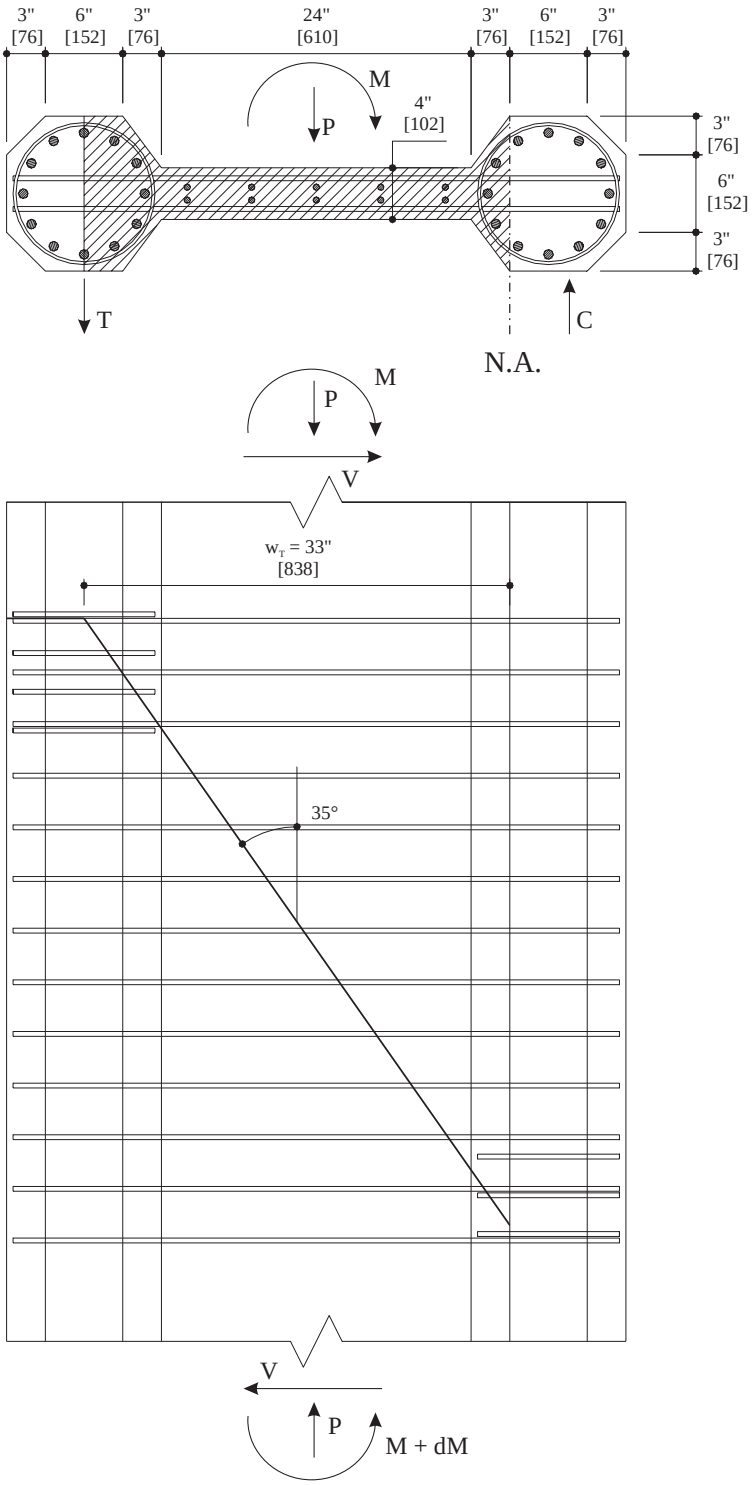

Figure 2.5: Cross section and partial elevation for Test Unit 3A, with the assumed shear crack relevant to the V_s component of shear resistance.

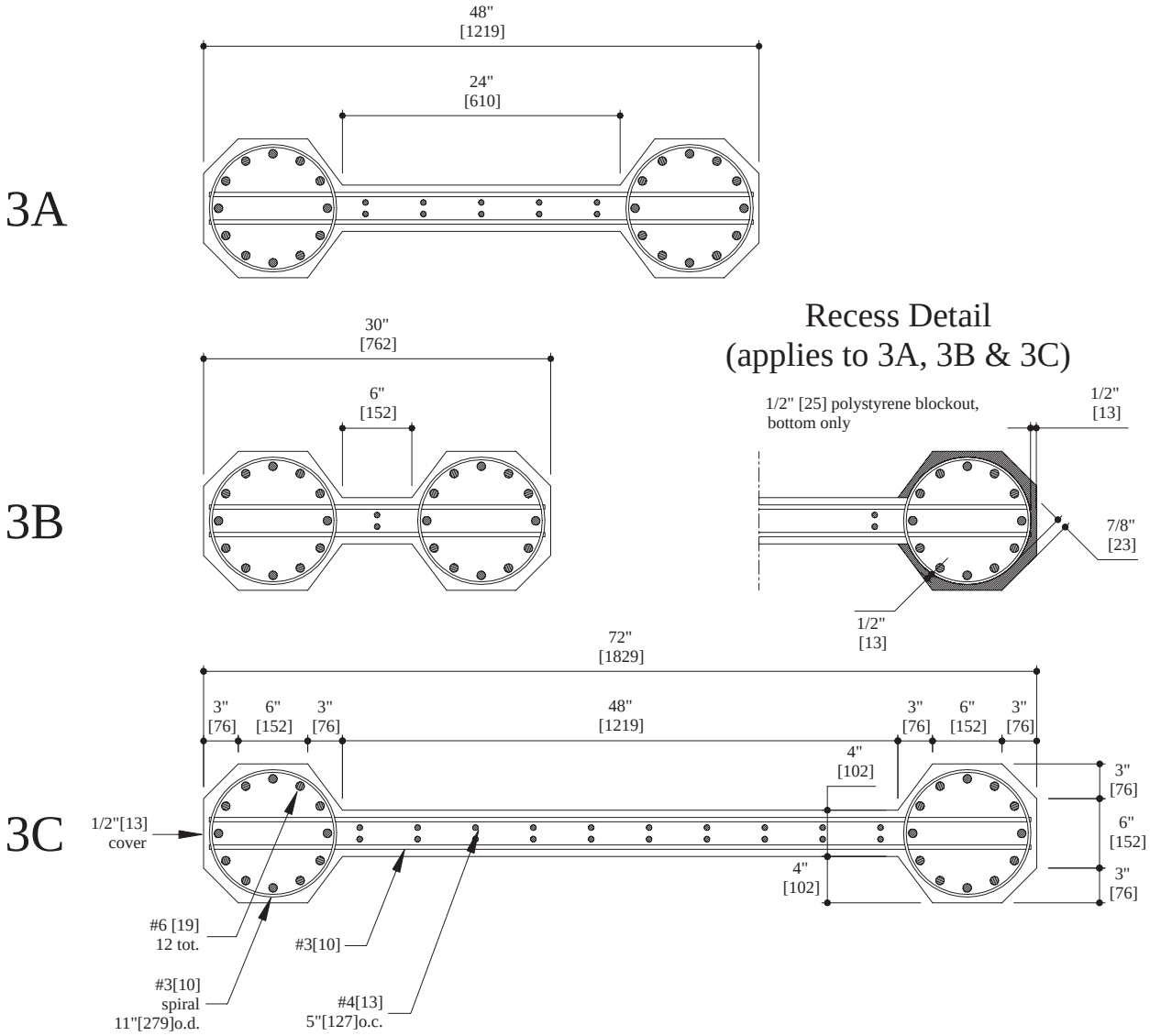

Figure 2.6: Cross section of Test Units 3A, 3B and 3C with reinforcement.

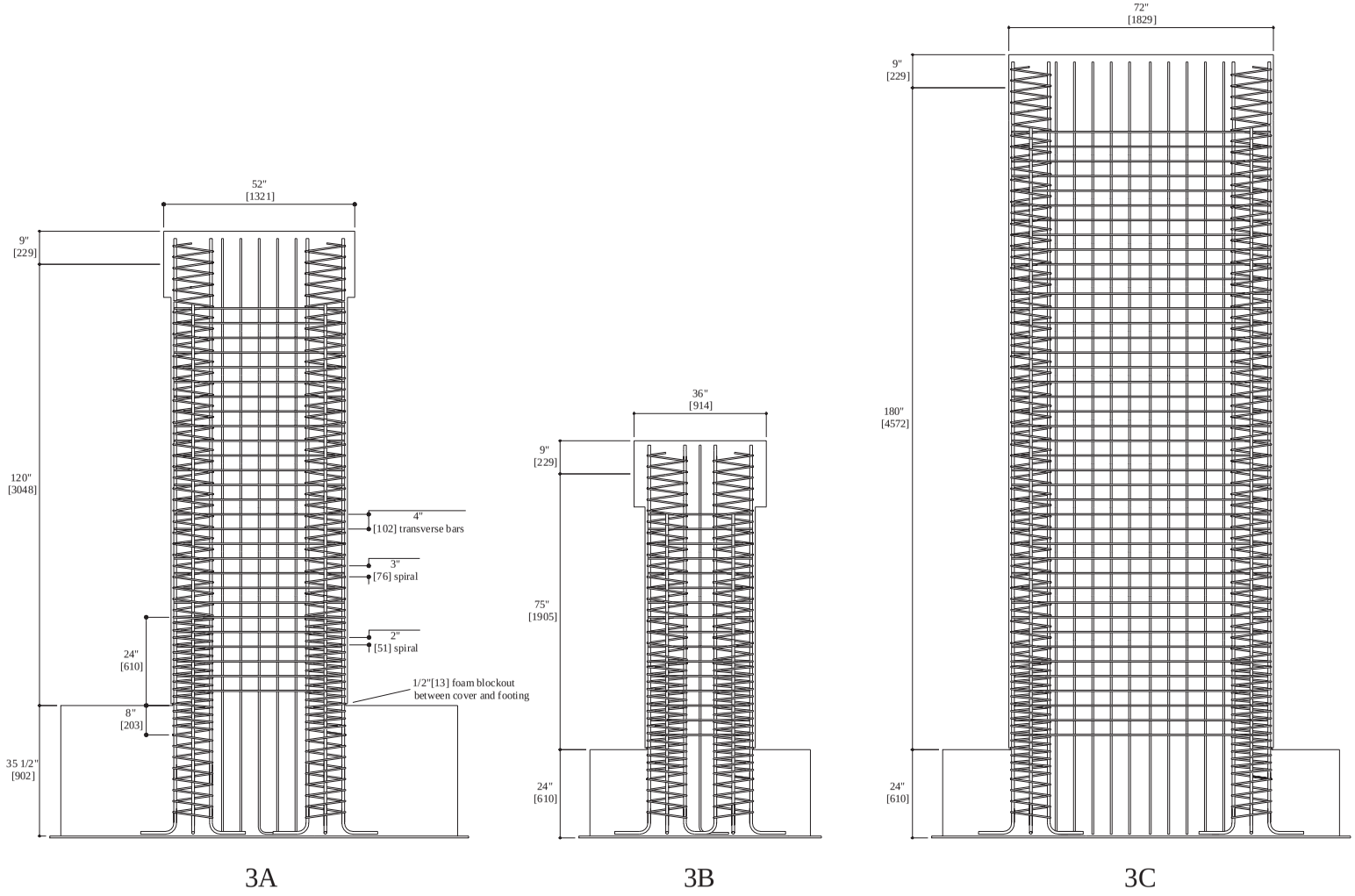

Figure 2.7: West elevations of Test Units 3A, 3B and 3C (Footing reinforcement and some boundary element longitudinal bars not shown).

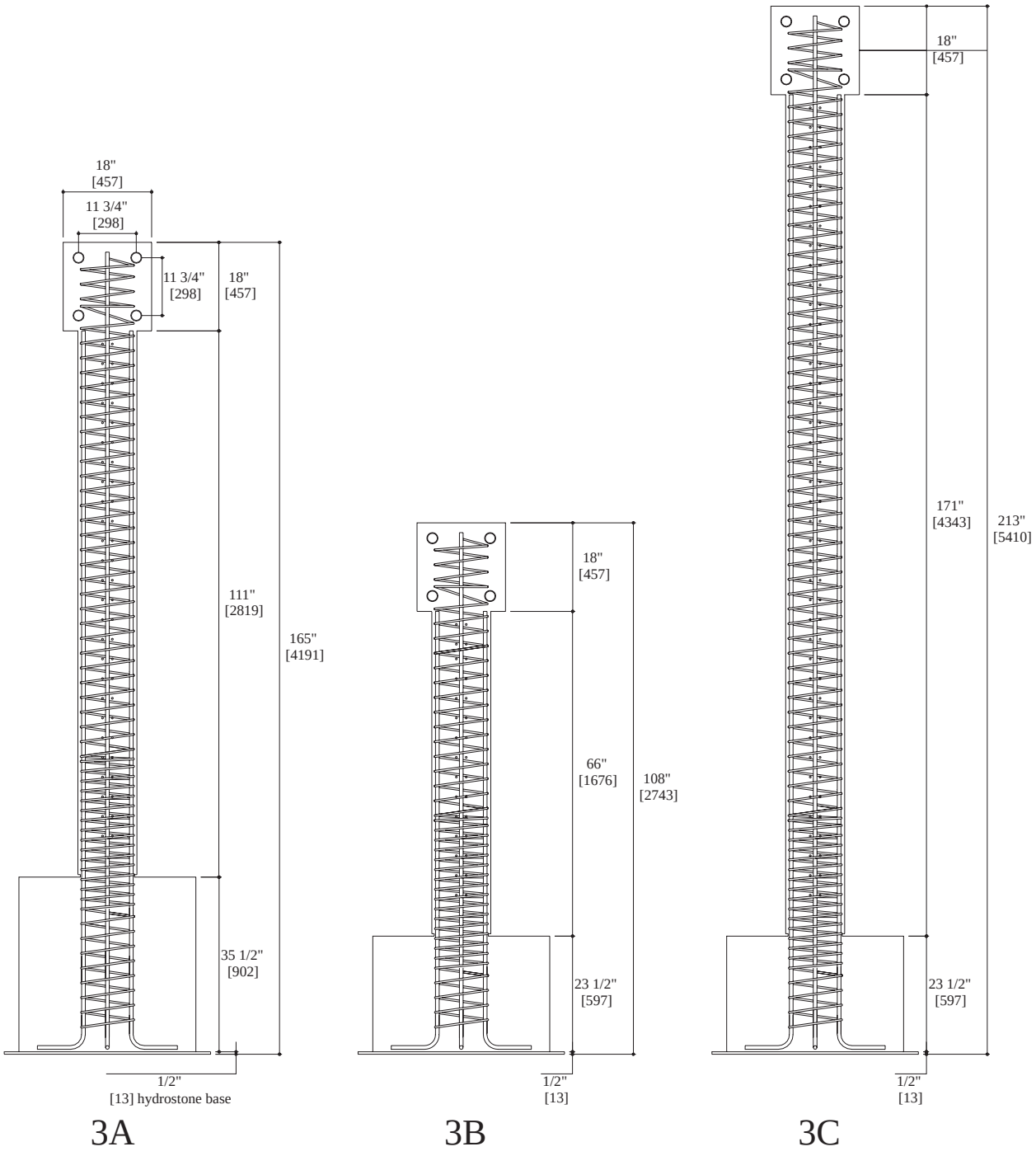

Figure 2.8: South elevations of Test Units 3A, 3B and 3C with reinforcement (Footing reinforcement and some boundary element longitudinal bars not shown).

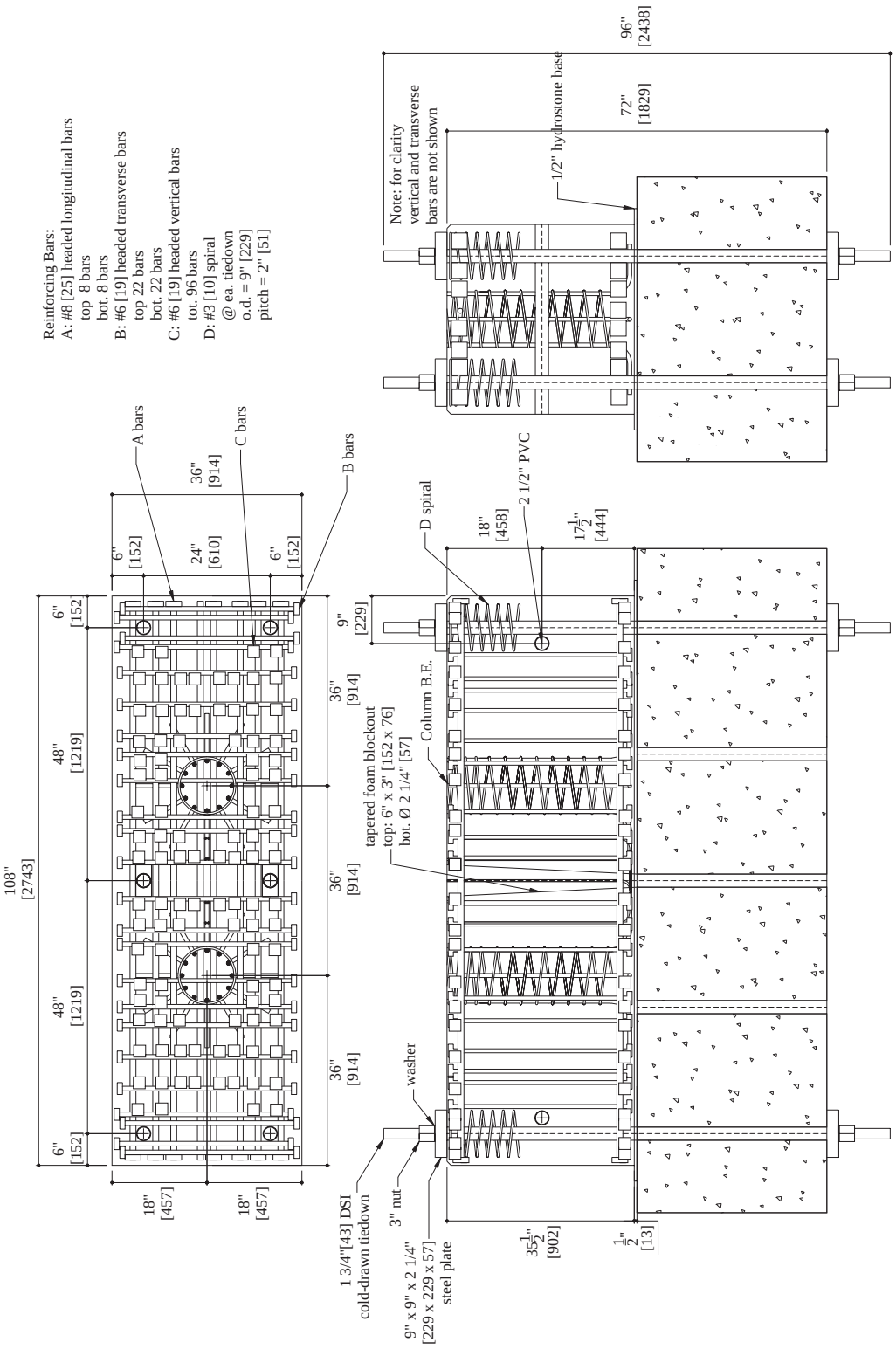

Figure 2.9: Test Unit 3A footing reinforcement plan.

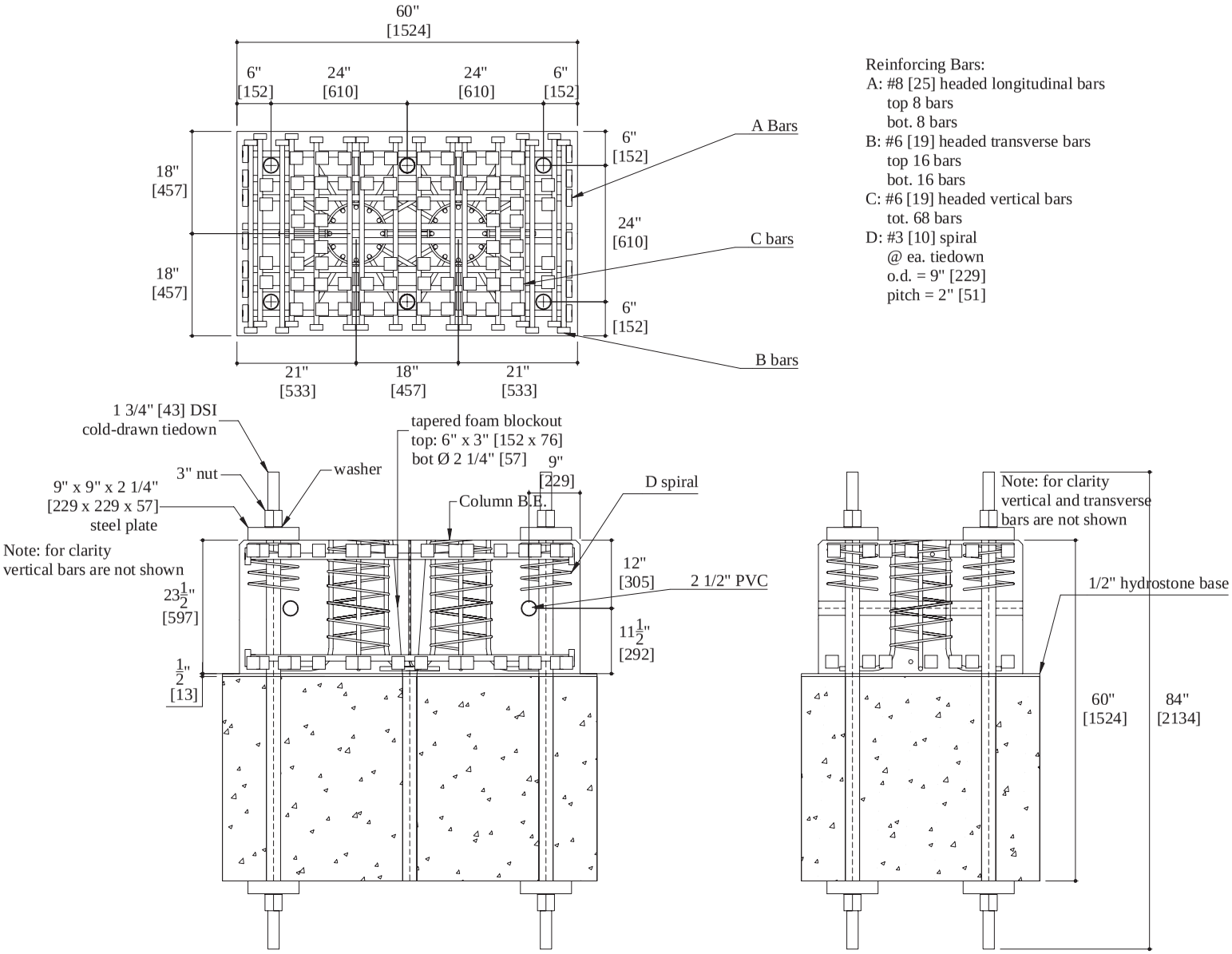

Figure 2.10: Test Unit 3B footing reinforcement plan.

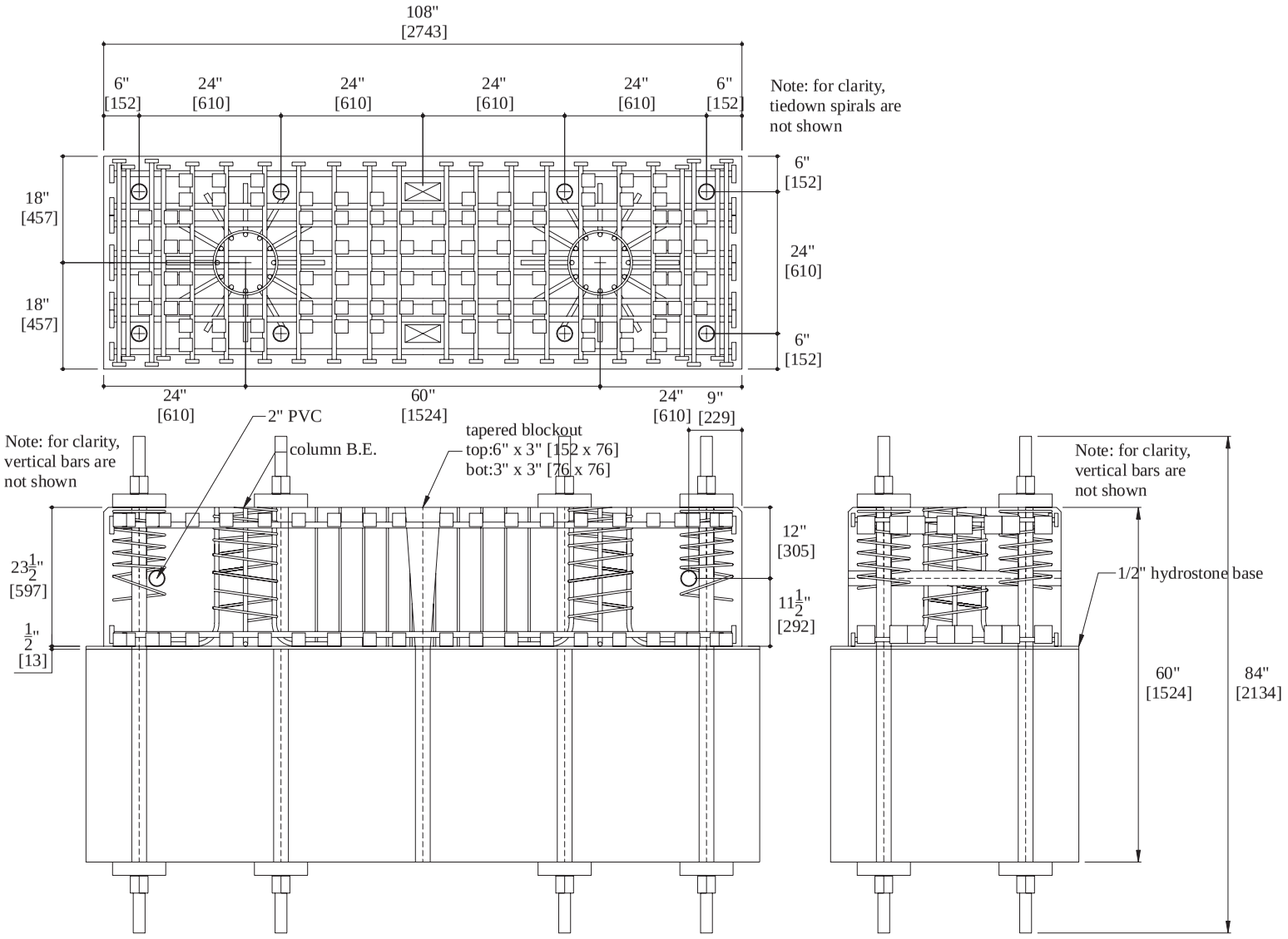

Figure 2.11: Test Unit 3C footing reinforcement plan.

Chapter 3

Construction and Material Properties

3.1 Overview

This chapter briefly describes the construction process for the test units, referring to photos in Appendix A. Material properties for all of the concrete and reinforcing steel are tabulated. Measured stress strain curves are shown with theoretical curves for all reinforcing bars.

3.2 Construction of the Web Crushing Test Units

The three Phase III Web Crushing Test Units test units were constructed similarly to the Phase I and II Flexure and Shear Test Units reported in [1]. After all of the appropriate reinforcing bars had been strain gaged, the boundary elements were tied (see Figure A.1) and set vertically on an out door casting bed (See Figures A.2 and A.7). In order to facilitate the proper horizontal positioning and vertical alignment of the relatively slender boundary elements, they were set directly on the casting bed. The 9 in. [229 mm] tails were nailed into the casting bed, once the boundary elements had been centered. The boundary elements were then held vertically against out of plane movement by steel rods anchored to independent guide posts (see Figure A.7). Another steel rod was tied independently between the boundary elements to maintain their proper in-plane position. With the boundary elements aligned vertically and anchored in place, the footing reinforcement cages were then constructed around them out of headed reinforcement (see Figures A.2, A.3 and A.5). Figure A.5 shows the high amount of confinement provided by spirals and headed reinforcement around the vertical tiedown holes centered 6 in. [152 mm] from each edge. Additional #2 [#6] reinforcing steel was later added to protect the very corner of the footing from spalling off when the test units were tensioned to the lab floor. Once the footings were poured, the columns were

brought into the laboratory, where the transverse bars were added, and the column and load stub formwork were secured in place. Figures A.3 and A.4 show Test Unit 3A both before the footing pour and just before the column pour. Figures A.5 and A.6 show Test Unit 3B both before the footing pour and just before the column pour. Figures A.7 and A.8 show Test Unit 3C during alignment and anchorage of the boundary elements and just before the column pour. Figure A.9 shows the three test units lined up in the lab before assembly of any column and load stub form work. Figure A.10 shows the typical architectural concrete blockout detail provided on both boundary elements at the base of each column. Figure A.11 shows an arial view of the three test units, fully formed, just prior to testing. Figure A.12 shows an elevation view of Test Unit 3C with column and load stub formwork and scaffolding. All three columns and load stubs were cast from the same batch of concrete in a single lift. The columns were then allowed to form cure for at least one week, after which the formwork was removed and their construction was complete.

3.3 Material Properties

The following section presents the material properties for concrete and steel used for the Web Crushing Test Units. Design concrete strength was $f'_c = 34$ MPa (5 ksi) for both the footing and the column of each test unit.

All of the steel specified was grade A-706, however grade A-706 was available only for bars of size #6 [#19] and larger, meaning that only the boundary element longitudinal bars were of this grade, while the #3 [#11] transverse bars and spirals were grade A-615.

Note that all values for ε_{su} are displayed in Figures 3.1 - 3.3 as 0.10. This is a result of the fact that the extensometer used to measure strain in the bars was always removed at $\varepsilon_s = 0.10$ in order not to harm the instrument when the bar fractured. The value $\varepsilon_s = 0.10$ was considered a fair approximation of reinforcing bar strain at ultimate stress.

3.3.1 Concrete Mix Designs and Properties

Each test unit was poured in two lifts, the first being the footing and the second being the column. All three footings were poured on the same day from the same batch of concrete. Likewise, all three columns were also poured on the same day, each in a single lift, from the same batch of concrete.

A single 5 ksi [34 MPa], 3/8 in. [10] aggregate mix design was used for test units. Table 3.1 gives the properties of this mix design.

Tables 3.2 and 3.3 give concrete compressive strengths according to test unit and pour type. The compressive strengths were determined as the average of three tests conducted according to ASTM on 12 in. [305] tall, 6 in. [152] diameter cylinders. Day of test strengths varied within a range of 1280 psi, where the Column 3A day of test strengths were actually lower than the Column 3C day of test strengths even though they were older by 7 days. Column 3B had a compressive cylinder strengths averaging 1280 psi greater than those of Column 3A. This spread of values remained unexplained throughout the testing. Since the concrete in each of the three columns was at least 90 days old on the day of testing, no significant difference in cylinder strength was expected during the two week test period. Therefore all, post test analyses were conducted assuming an average concrete compressive cylinder strength of 5930 psi [40.9 MPa].

Tables 3.5 and 3.4 give column concrete tensile strengths taken from cylinder splitting tests.

Item	Weight per yd^3 $[m^3]$ (lb (materials)) (oz (additives))	[kg] [g]	Yield (ft^3)	[m^3]
Cement	672	400	3.42	0.127
Fly Ash	118	70.2	0.920	0.0341
Sloan Canyon Washed Concrete Sand – 49.9%	1363	811	8.18	0.303
Mission Valley 3/8 in. [10] – 50.1%	1330	791	8.20	0.304
Water	358	213	5.74	0.213
WRDA-64 (water-reducer)	23.2	865	–	–
DARAVAIR 1000 (air entrainer)	1.50	56.0	–	–
DARACEM 19 (super-P)	77.0	2870	–	–
Air %	2.0		0.0200	
W/(C + F) Ratio	0.45			
Concrete unit weight (lb/ft^3) [kg/m^3]	142		2285	

Table 3.1: Concrete mix design for columns 5 ksi [34 MPa], 3/8 in. [10] aggregate, 3 in. / 8 in. [76 / 203] design slump.

Pour, Truck	Design Strength (psi)	7 Day (psi)	28 Day (psi)	D.O.T. (psi)	Age days
3A Footing	5000	4660	5900	–	146
3B Footing	5000	4560	6060	–	153
3C Footing	5000	4560	6060	–	139
3A Column	5000	4010	5270	5380	100
3B Column	5000	4010	5270	6660	107
3C Column	5000	4010	5270	5740	93

Table 3.2: Test unit concrete compressive cylinder strengths (psi).

Pour, Truck	Design Strength [MPa]	7 Day [MPa]	28 Day [MPa]	D.O.T. [MPa]	Age days
3A Footing	34.5	32.1	40.7	–	146
3B Footing	34.5	31.4	41.8	–	153
3C Footing	34.5	31.4	41.8	–	139
3A Column	34.5	27.6	36.3	36.8	100
3B Column	34.5	27.6	36.3	45.9	107
3C Column	34.5	27.6	36.3	39.6	93

Table 3.3: Test unit concrete compressive cylinder strengths [MPa].

Pour, Truck	Design Strength (psi)	7 Day (psi)	28 Day (psi)	D.O.T. (psi)	Age days
3A Footing	424	–	390	–	146
3B Footing	424	–	410	–	153
3C Footing	424	–	410	–	139
3A Column	424	–	–	480	100
3B Column	424	–	–	470	107
3C Column	424	–	–	460	93

Table 3.4: Test unit concrete tensile strengths from splitting tests (psi).

Pour, Truck	Design Strength [MPa]	7 Day [MPa]	28 Day [MPa]	D.O.T. [MPa]	Age days
3A Footing	2.92	–	2.69	–	146
3B Footing	2.92	–	2.83	–	153
3C Footing	2.92	–	2.83	–	139
3A Column	2.92	–	–	3.31	100
3B Column	2.92	–	–	3.24	107
3C Column	2.92	–	–	3.17	93

Table 3.5: Test unit concrete tensile strengths from splitting tests [MPa].

Bar Name	Size	f_y	f_u	ε_y	ε_{sh}	ε_{su}	E_s	E_{sh}
Longitudinal	#6	62.0	90.5	0.0021	0.0080	0.10	29000	850
Longitudinal	#3	63.0	99.5	0.0022	0.0080	0.10	29000	1200
Transverse	#3	63.0	99.5	0.0022	0.0080	0.10	29000	1200
Spiral	#3	63.0	99.0	0.0022	0.0030	0.10	29000	1300

Table 3.6: Test unit steel reinforcement properties (ksi).

Bar Name	Size	f_y	f_u	ε_y	ε_{sh}	ε_{su}	E_s [GPa]	E_{sh} [GPa]
Longitudinal	#19	427	624	0.0021	0.0080	0.10	200	5.86
Longitudinal	#10	434	686	0.0022	0.0080	0.10	200	8.27
Transverse	#10	434	686	0.0022	0.0080	0.10	200	8.27
Spiral	#10	434	683	0.0022	0.0030	0.10	200	8.96

Table 3.7: Test unit steel reinforcement properties [MPa].

3.3.2 Reinforcing Steel Properties

Tables 3.6 and 3.7 give the properties for the column reinforcing steel. The footing and load stub steel properties are not listed. The values given are taken from a single bar, representative of three monotonic pull tests performed on each bar type. Since results from the individual tests corresponded closely, it was sufficient to take the properties from a representative bar. Note that the ultimate steel strain, ε_{su} and the modulus of Elasticity, E_s are both listed as constant artificial values. The strain hardening modulus, E_{sh} was determined for each bar by adjusting it in round numbers until the power curve for strain hardening (Equation 5.1) appeared to match the experimental strain hardening curve. Figures 3.1 - 3.3 give for each bar the representative experimental curve along with the theoretical curve based on the values presented in Tables 3.6 and 3.7.

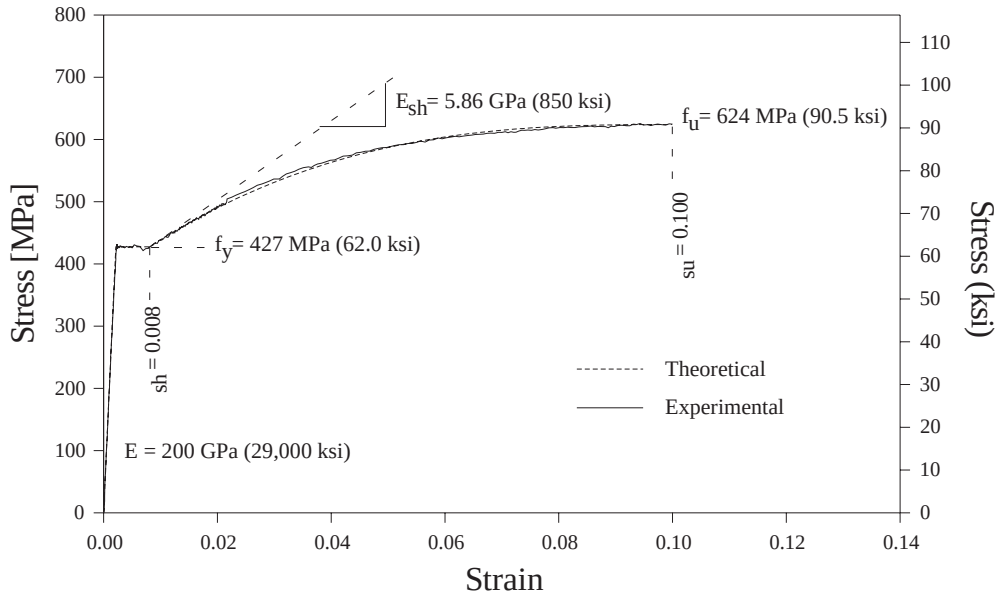

Figure 3.1: Stress strain curves for the #6 [#19] boundary element longitudinal reinforcing bars.

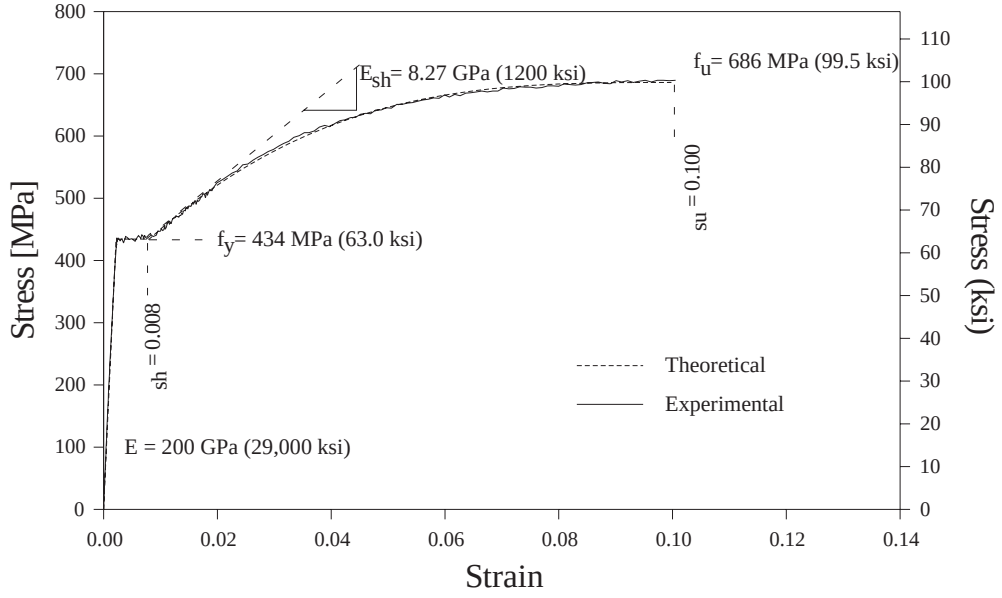

Figure 3.2: Stress strain curves for the #3 [#10] longitudinal and transverse reinforcing bars.

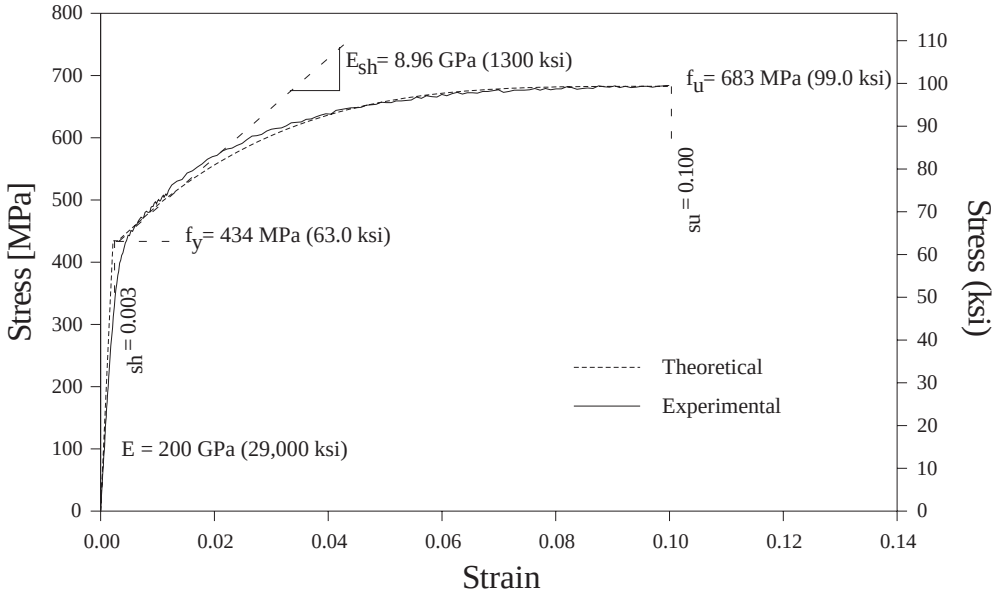

Figure 3.3: Stress strain curves for the #3 [#10] boundary element spirals.

Chapter 4

Test Setup, Instrumentation and Protocol

4.1 Overview

The test setup, instrumentation, and loading protocol for the Phase III Web Crushing Tests are presented. The test setup was designed to load each test unit cyclically in single bending. The west face of the test unit was instrumented for shear deformations, leaving the east face open for observations, photos and crack width measurements.

4.2 Test Setup

The test units were loaded quasi-statically according to a standard, incrementally increasing, fully-reversed cyclic loading pattern, with constant axial load. East elevations of the test setup and loading aparatus are shown in relation to the reaction floor and reaction wall for Test Unit 3A in Figures 4.1 and 4.2. Figures 4.3 and 4.4 show east elevations of the test setups for Test Units 3B and 3C. Lateral load was applied via a single +445 / -250 kip at 4000 psi [+1980 / -1113 kN, at 27.6 MPa], ± 18 in. [457] stroke TJ Vickers, servo-controlled hydraulic actuator. Axial load was provided by two 200 kip [890 kN] hollow core jacks attached to 1 3/8" [35] diameter DSI bars which were anchored to the floor and equipped with independent load cells. The total axial load corresponded to an axial load ratio of $P/f'_cA_g = 0.10$ in each of the test units, assuming $f'_c = 5$ ksi [35 MPa] as the test unit design concrete strength.

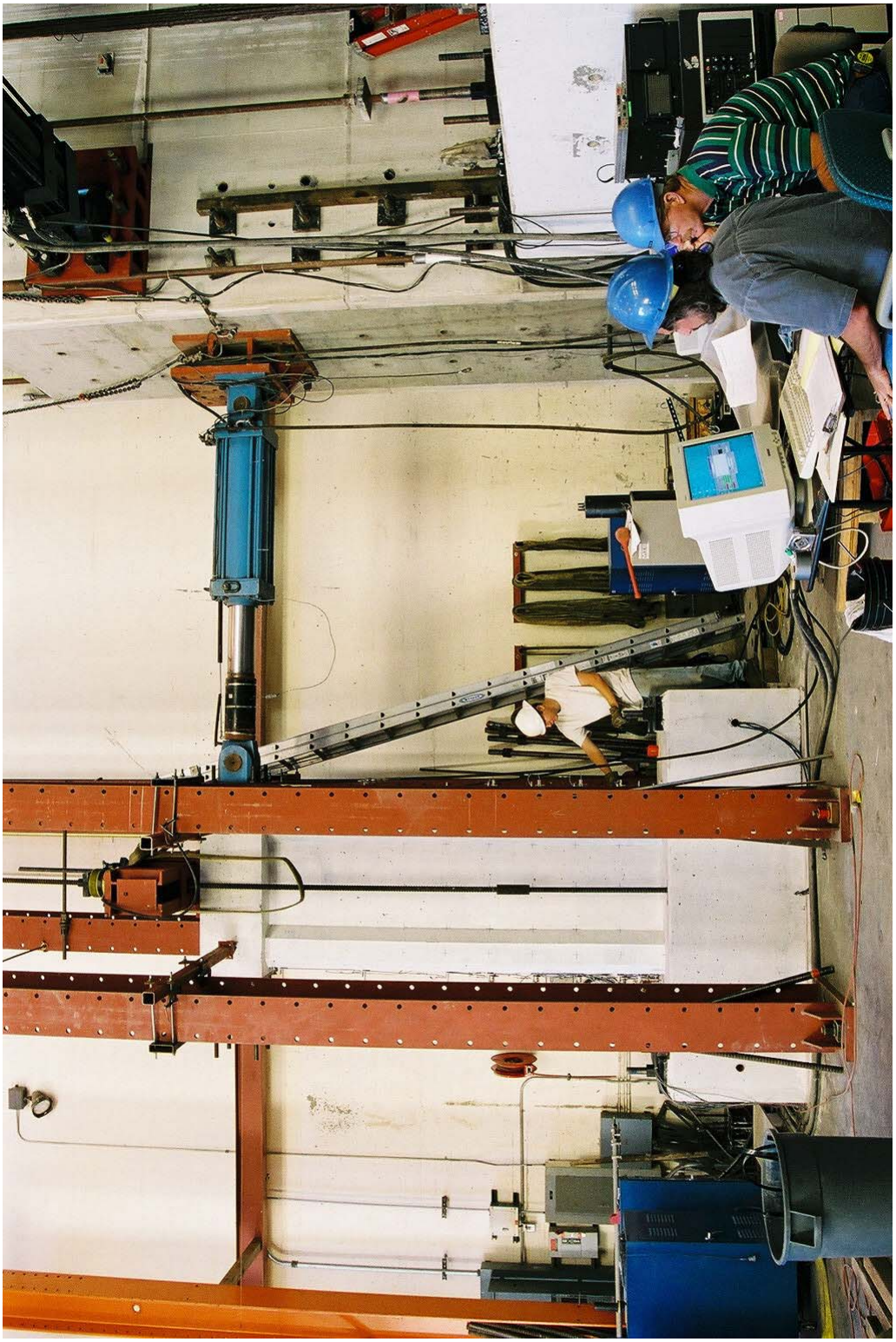

Figure 4.1: Completed test setup for Test Unit 3A with instrumentation, a few hours before testing. East elevation.

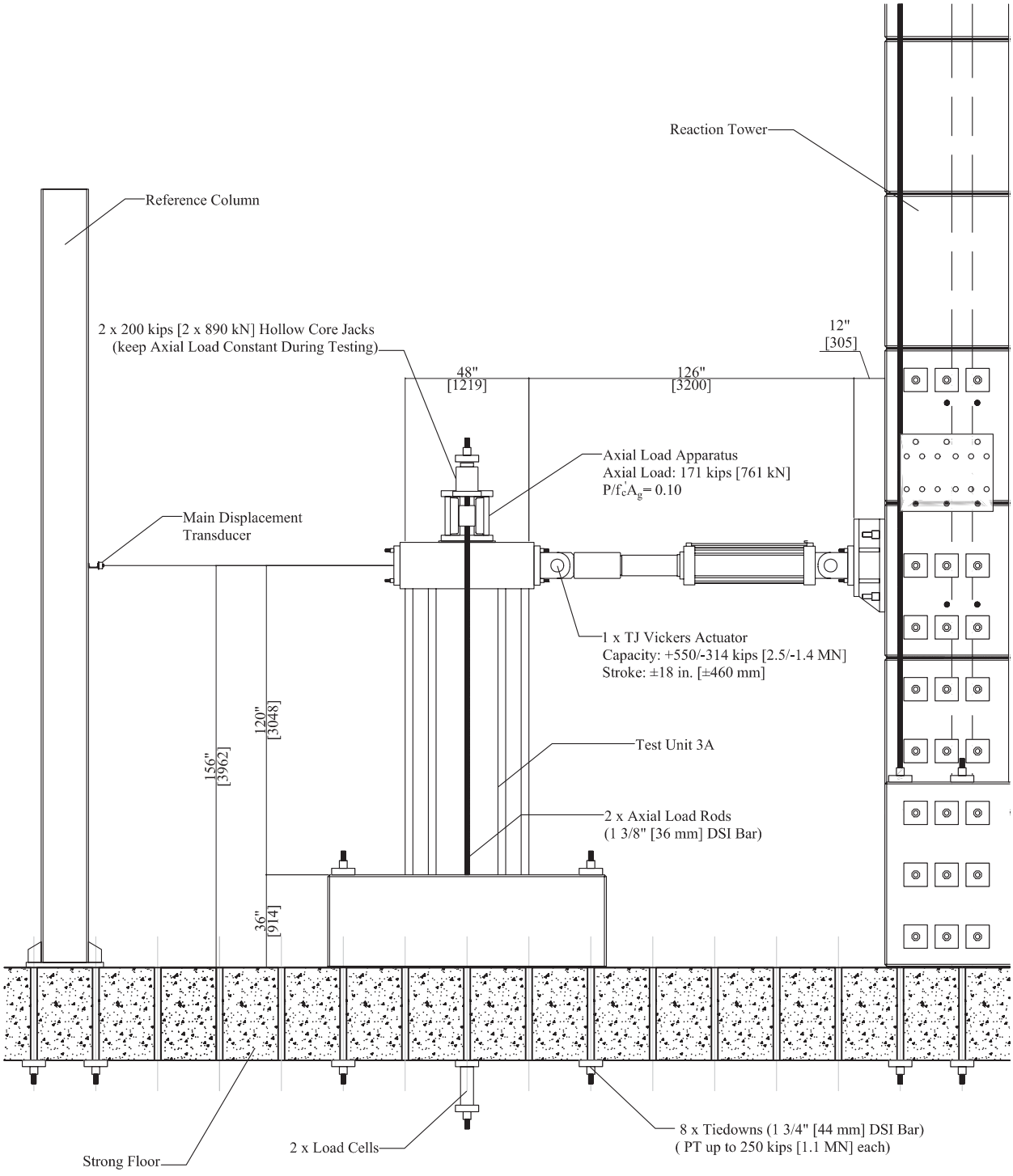

Figure 4.2: Test Unit 3A setup, east elevation.

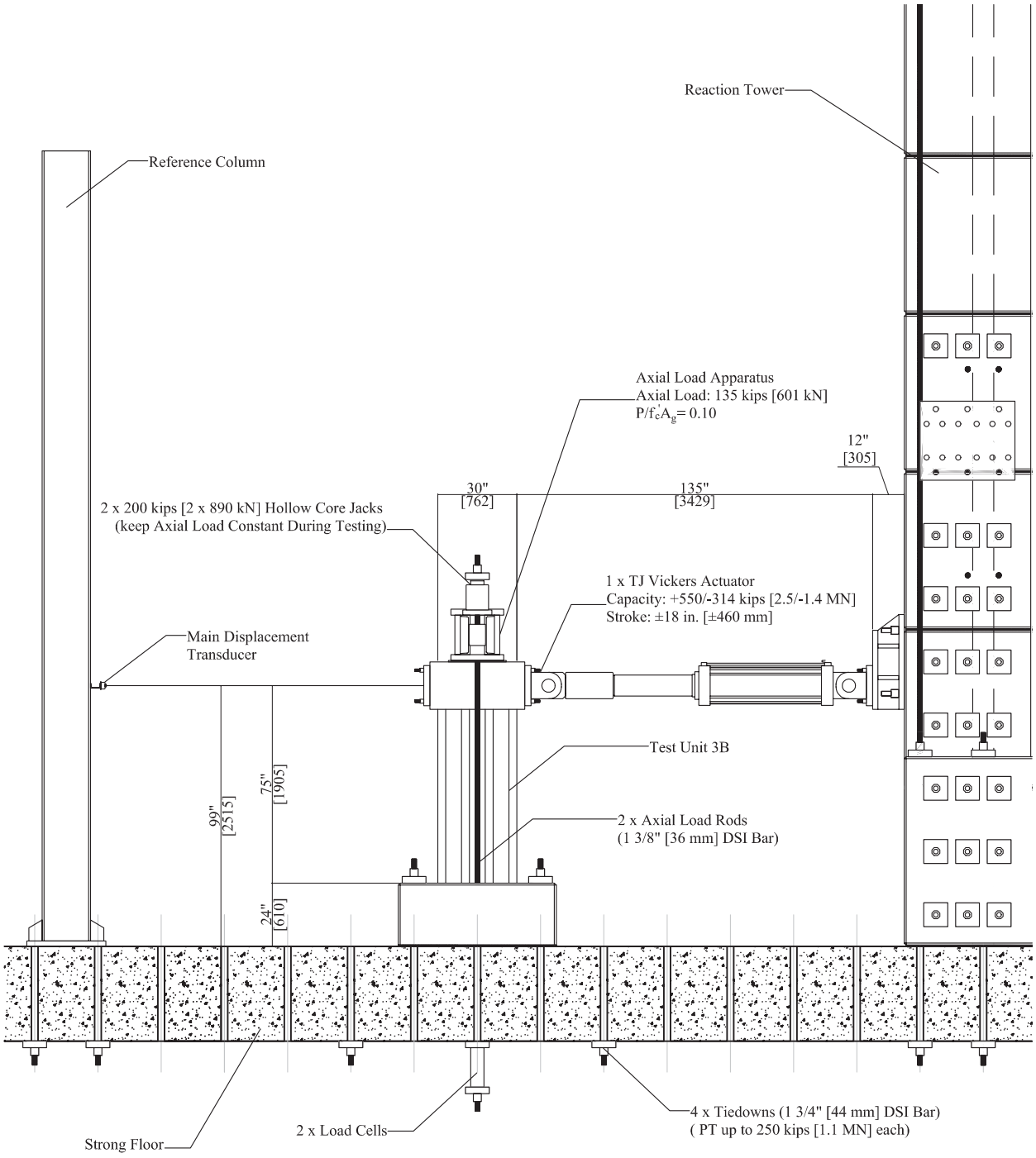

Figure 4.3: Test Unit 3B setup, east elevation.

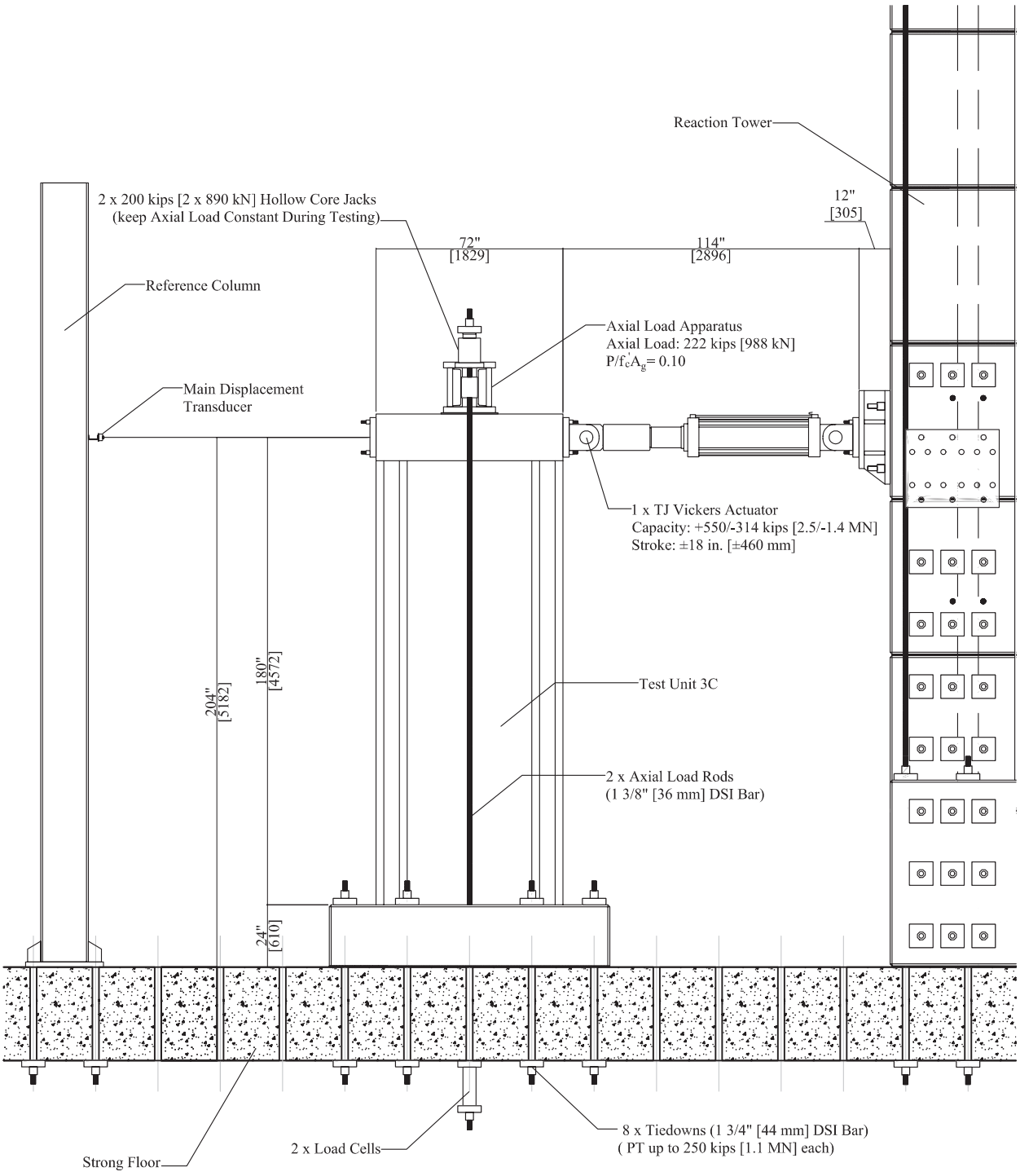

Figure 4.4: Test Unit 3C setup, east elevation.

4.3 Instrumentation

4.3.1 Strain Gages

Reinforcing bar strains were measured with electrical resistance strain gages. The gages used had a 120Ω resistance and a 5 mm (0.2 in.) gage length. The reinforcing bar surface was prepared by sanding smooth a section of bar, roughing the sanded surface with plummer's mesh, and cleaning it with methyl ethyl-keytone. The gages were applied to the prepared surface with a super-adhesive (alpha cyanoacrylate monomer), coated with an acrylic based water-proofing agent and then protected with a vinyl mastic membrane.

Figure 4.5 shows a cross section of the strain gage layout for each of the three test units.

Figure 4.6 shows the longitudinal bar gages distributed along all three column heights.

Figure 4.7 shows the transverse bar and spiral gages distributed along all three column heights. Transverse bar gages were placed at five locations on transverse bars in Test Units 3A and 3C and placed at three locations on transverse bars in Test Units 3B. The center gages were expected to give an adequate distribution of strain along the bar while the two extreme gages were expected to give insight into the development length of the transverse bars anchored into the tension boundary element.

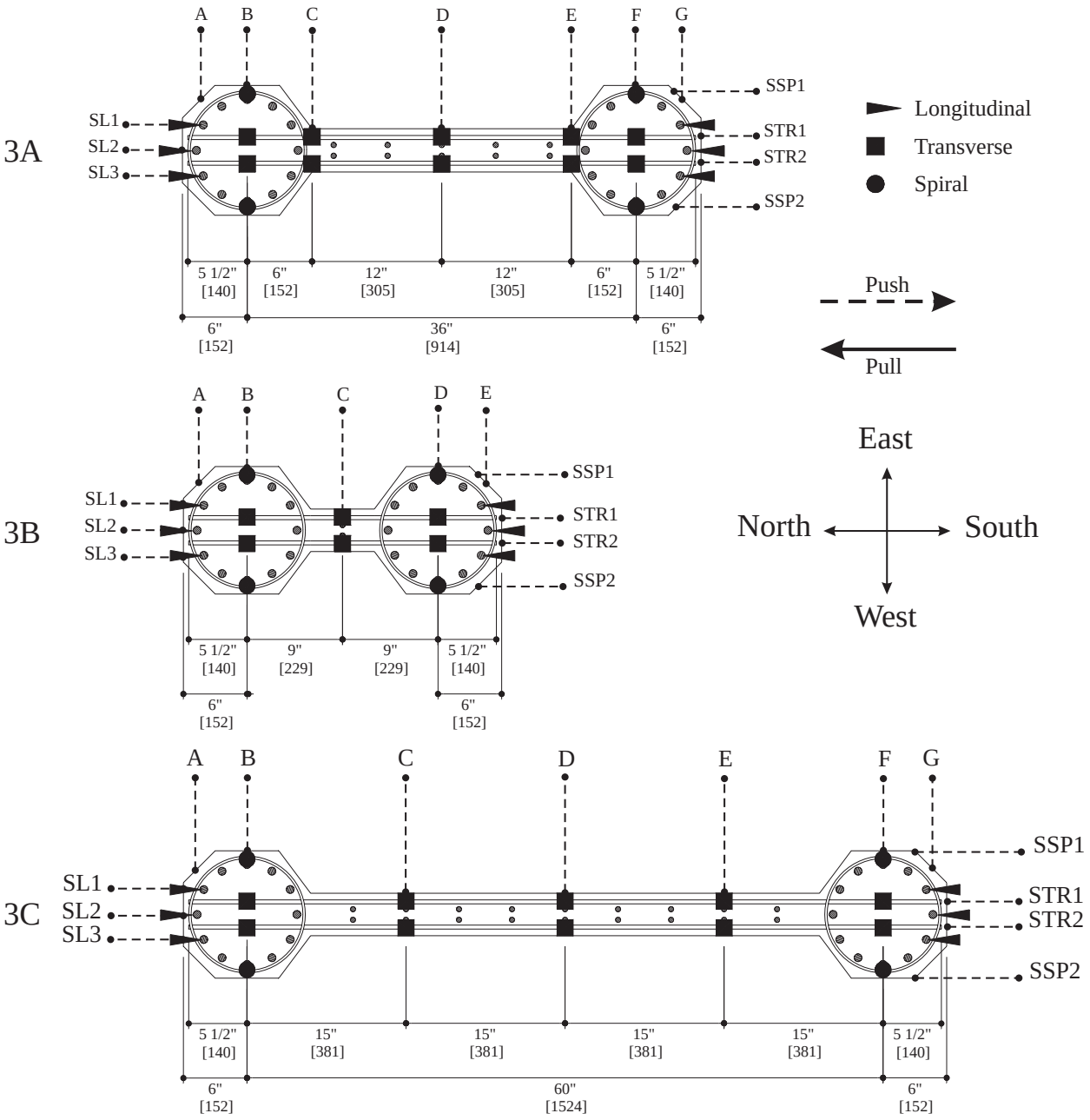

Figure 4.5: Test Units 3A, 3B and 3C, strain gage layout, sections.

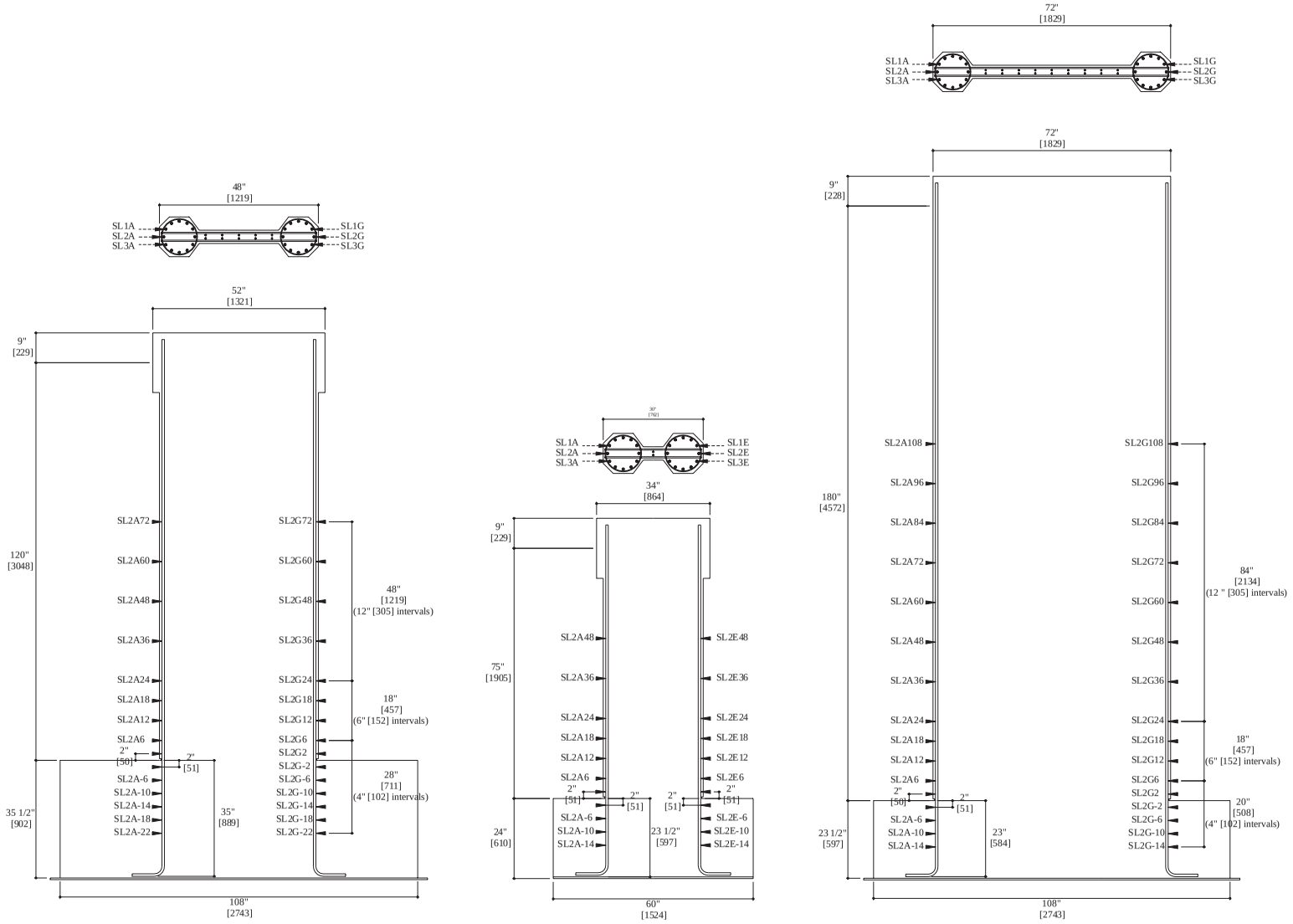

Figure 4.6: Test Units 3A, 3B and 3C, longitudinal bar strain gage layout, west elevations.

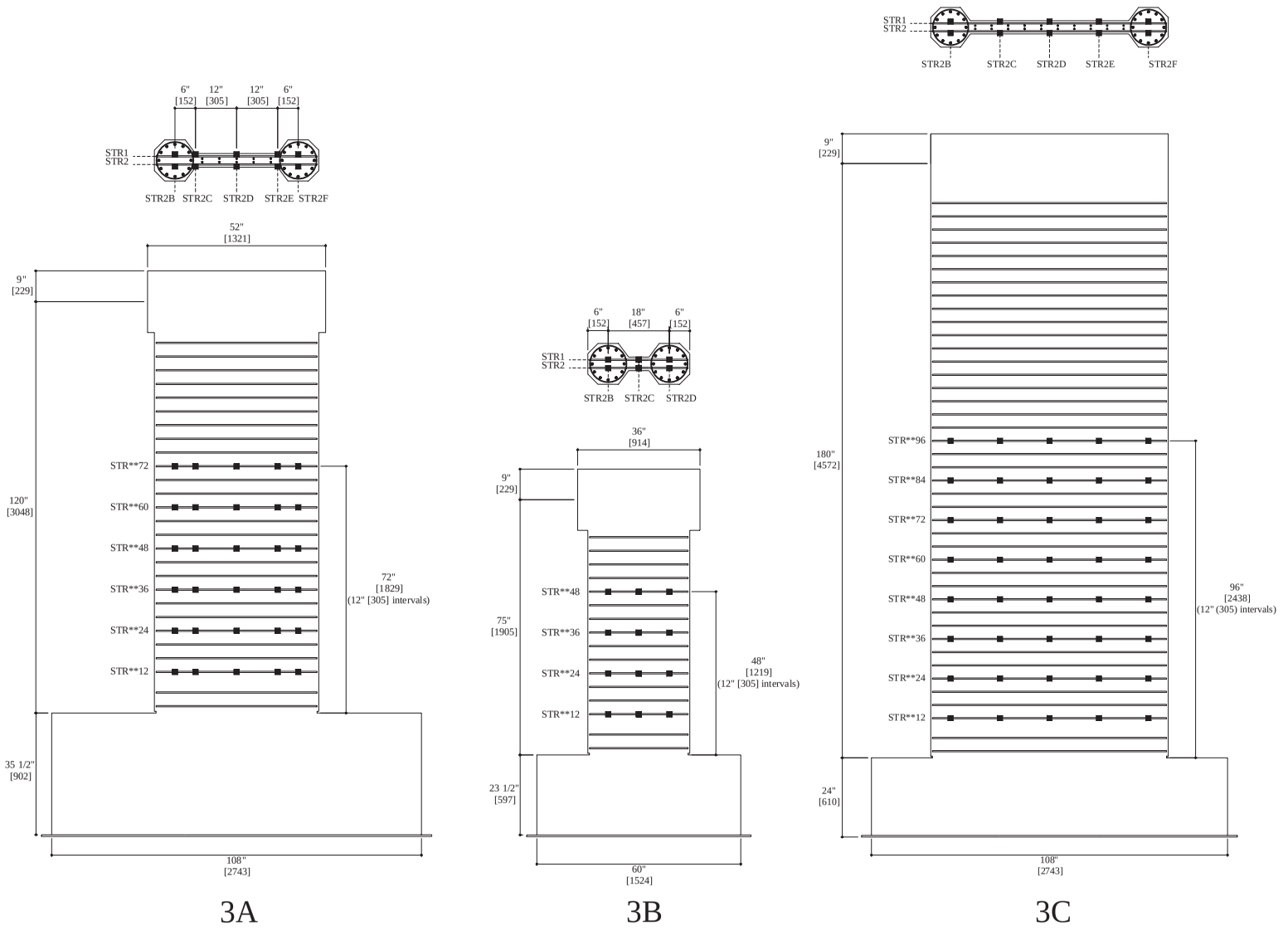

Figure 4.7: Test Units 3A, 3B and 3C, transverse bar strain gage layout, west elevations.

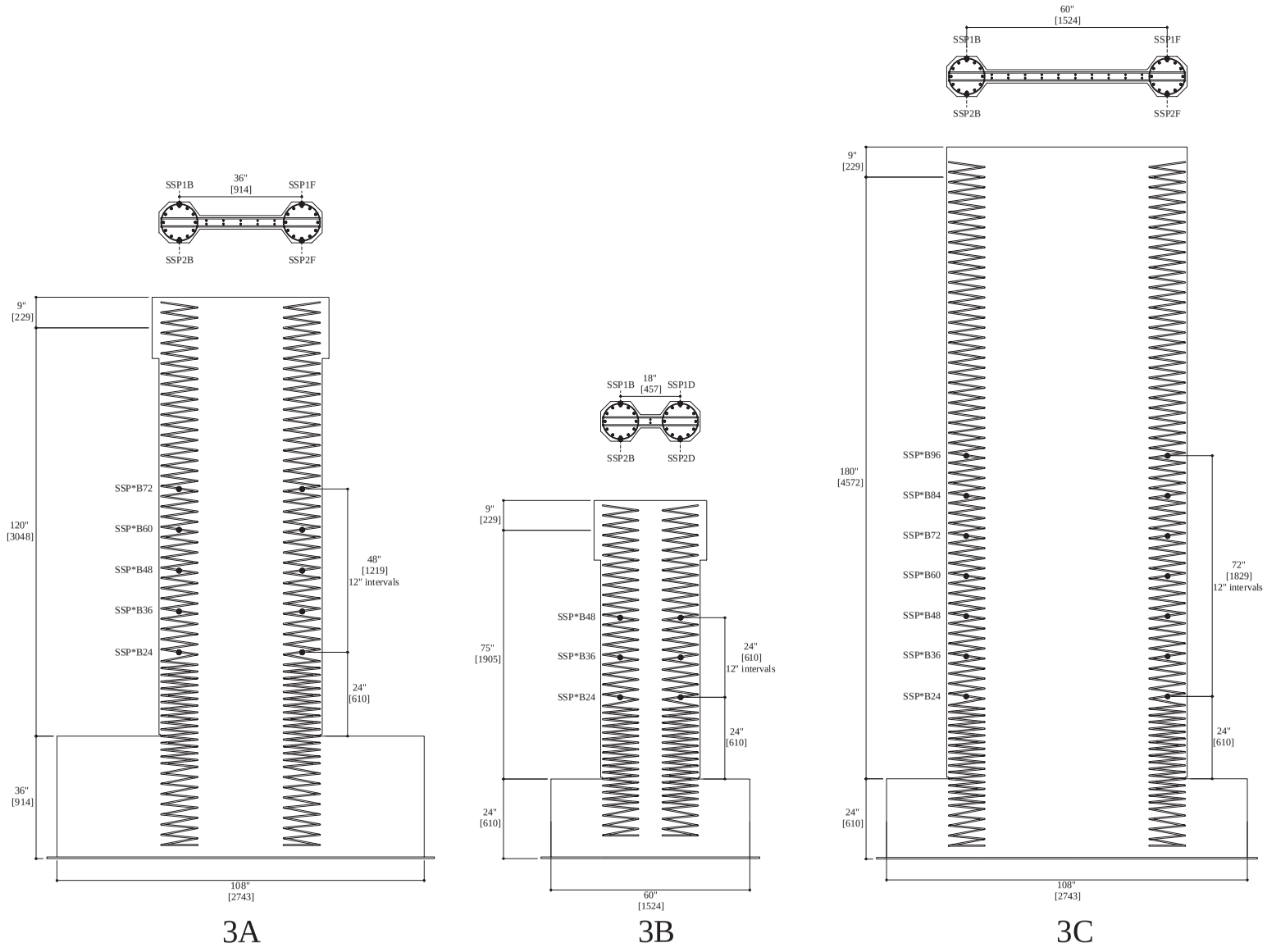

Figure 4.8: Test Units 3A, 3B and 3C, spiral strain gage layout, west elevations.

4.3.2 Curvature Instrumentation

Curvatures were calculated from displacement potentiometer readings as

$$\phi_i = \frac{{}_n - {}_s}{D_\phi L_g} \tag{4.1}$$

where ϕ_i is the curvature at the i^{th} bracket location, ${}_n$ and ${}_s$ are the north and south potentiometer readings at this location, D_ϕ is the distance between the north and south potentiometers (assumed to be $D + 4$ in. [102] for these tests), and L_g is the gage length. Curvatures calculated in this manner were positive in the push direction and negative in the pull direction. Figures 4.15 and 4.16 show photographic details of this curvature instrumentation (see Label A). Label B in each of these figures shows the targets designed to receive the 6 in. [152] and 2 in. [51] potentiometers at the column base. Since the footing concrete immediately surrounding the boundary elements was expected to crack and uplift due to strain penetration, the targets were mounted as cantilevers, based sufficiently far away from the boundary element to avoid disturbances due to strain penetration.

Rotation over a given gage length was calculated simply as

$$\theta_i = \frac{{}_n - {}_s}{D_\phi} \tag{4.2}$$

Displacement due to this rotation was calculated as

$${}_i = \theta_i \left[L - \left(\sum_{j=1}^{i-1} L_{gj} + L_{gi}/2 \right) \right] \tag{4.3}$$

Where L is the column shear span.

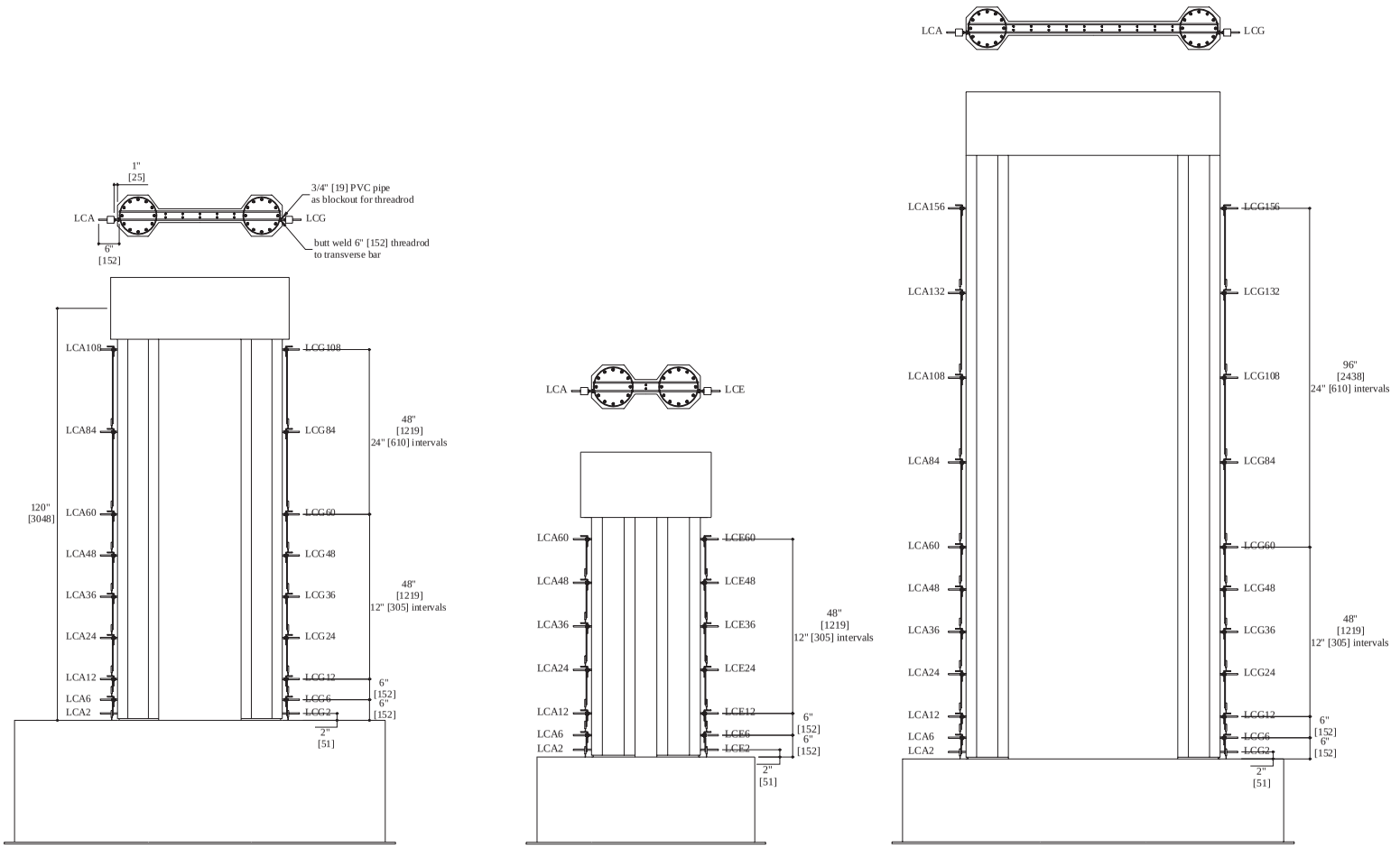

3A 3B 3C

Figure 4.9: Test Units 3A, 3B and 3C, curvature instrumentation layout, west elevations.

4.3.3 Shear Instrumentation

Shear deformation was measured by panels featuring two independent linear potentiometers arranged diagonally on the west column face. Figures 4.10 and 4.11 show that the deformed

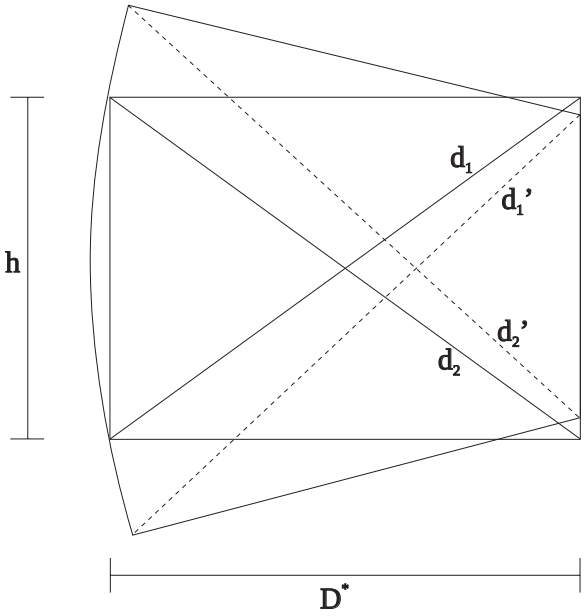

Figure 4.10: Diagonal deformations are equivalent in flexure.

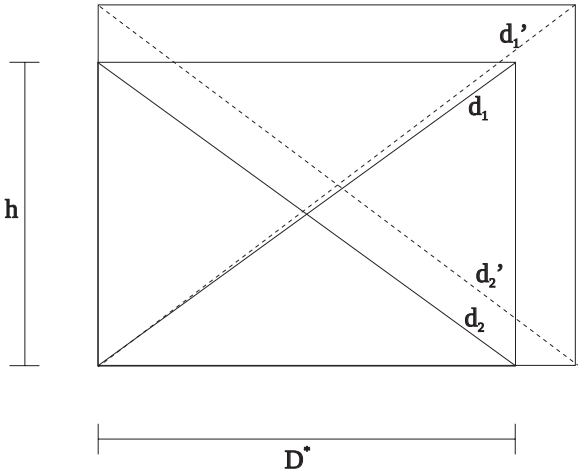

Figure 4.11: Diagonal deformations are equivalent in horizontal and vertical expansion.

diagonal lengths δ_1 and δ_2 remain equal to one another under flexure and under expansion of the region with height h and depth D^*. Only in shear do the deformed diagonals have different lengths. Assuming small angles, the average shear deformation in the region γ, was estimated as the average of the shear deformations calculated on either side of the region.

$$\gamma = \frac{\gamma_1 + \gamma_2}{h} = \frac{_1 + \Delta_{\ 2}}{2h} \tag{4.4}$$

Where the lateral deformations $_1$ and $_2$ due to shear deformation are calculated from the diagonal deformations according to the ratio

$$\frac{}{\delta} = \frac{d}{D^*} \tag{4.5}$$

where

$$\delta = d' - d \tag{4.6}$$

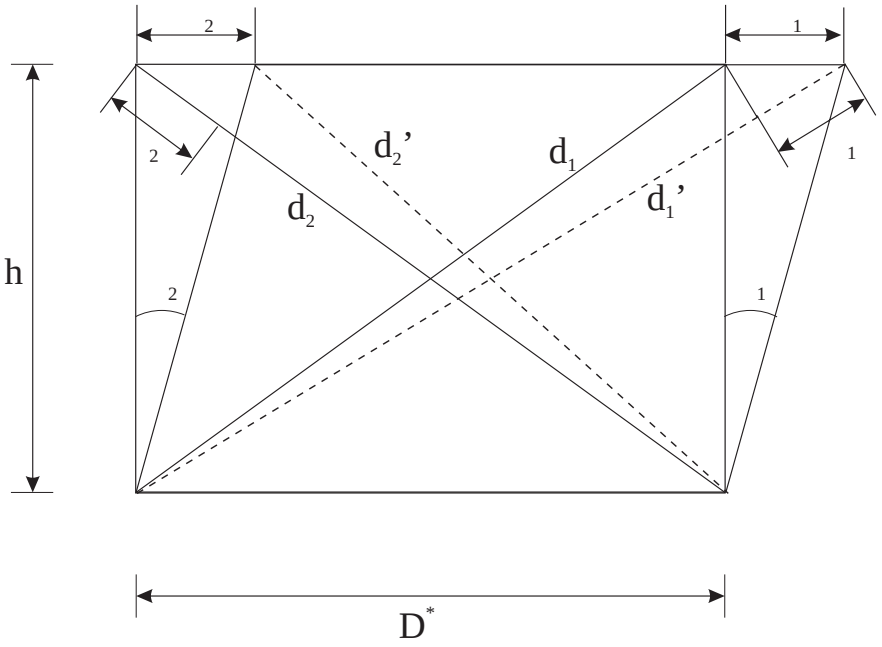

Figure 4.12: Diagonal deformations are used to estimate shear deformation.

as shown in Figure 4.12. Combining Equations 4.4 and 4.5 yields the equation

$$\gamma = \frac{\delta_1 d_1 - \delta_2 d_2}{2hD^*} \tag{4.7}$$

which characterizes the average shear deformation over a given region with height h, and depth D^*. Figure 4.13 shows the panel deformation instrumentation in elevation and section. Figure 4.15 D shows a typical mounting bracket for the shear panel instrumentation. These brackets consisted of 3/8 in. [10] high-precision cold-rolled steel rod, welded to a steel plate that was in turn bolted with 3/8 in. [10] anchors into a given boundary element.

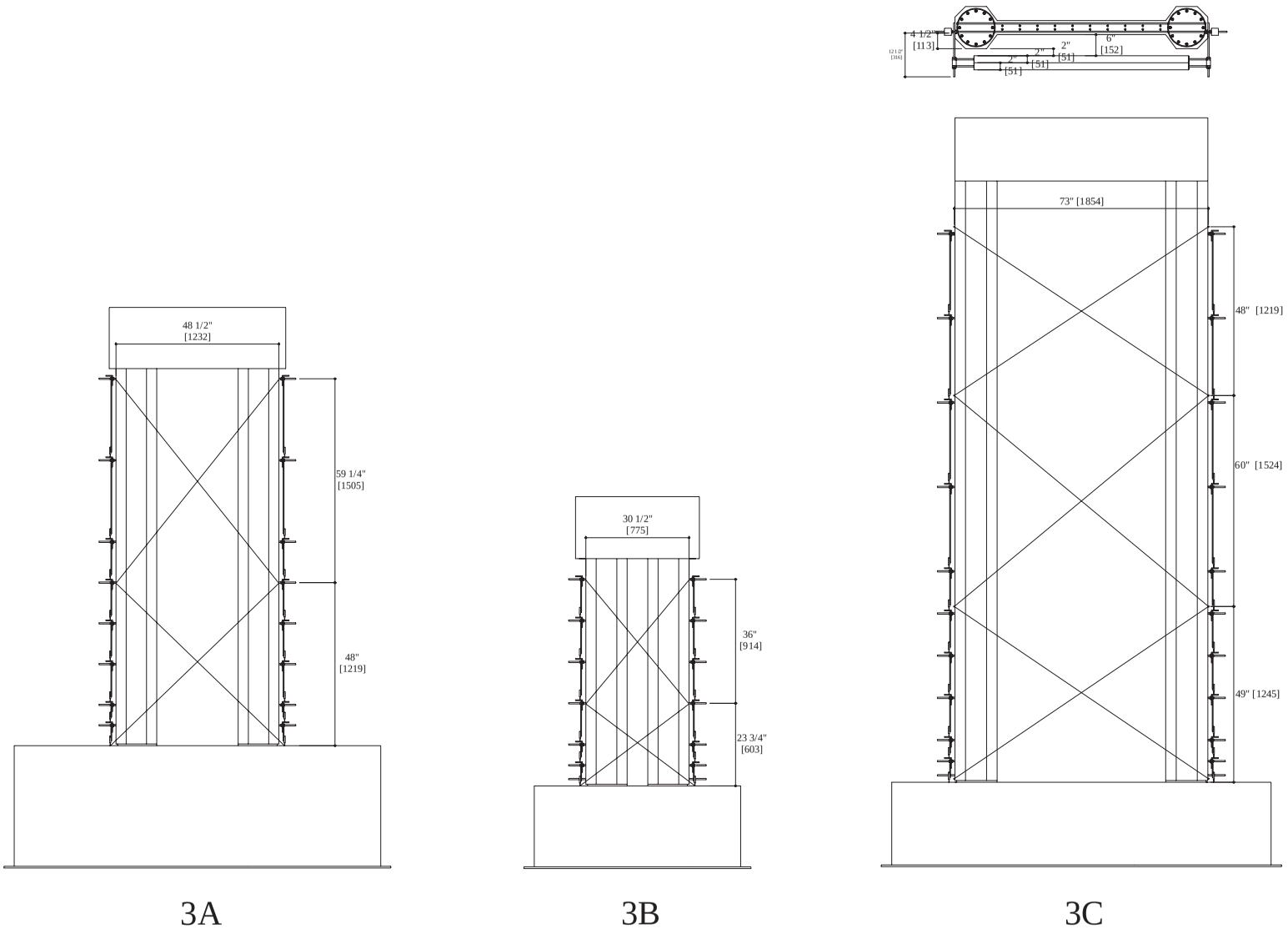

Figure 4.13: Test Units 3A, 3B and 3C, shear instrumentation layout, west elevations.

4.3.4 Slip of Transverse Bars

The Phase III Test Units were instrumented to measure the slippage of the transverse bars on 12 in [305] vertical intervals up to a height of 48 in. [1219] above the footing. The ends of the bars were expected to slip when the bars themselves were engaged to hold the column together in shear. At higher displacement levels, this slippage was expected to become significant because of the increasing flexural crack width. Figure 4.14 shows the slippage instrumentation in detail as it was mounted to the curvature bracketry. If slippage occurred, the bars were expected to slip into the column and compress the displacement potentiometer mounted on an aluminum angle bracket, giving a negative reading. The slippage potentiometers were targeted on plates that extended directly out of the confined core concrete, so that no slippage readings would result from expansion of the cover concrete as had been the result on earlier tests [1, 11]. Figures 4.15 and 4.16 show photographic details of the transverse bars slippage instrumentation.

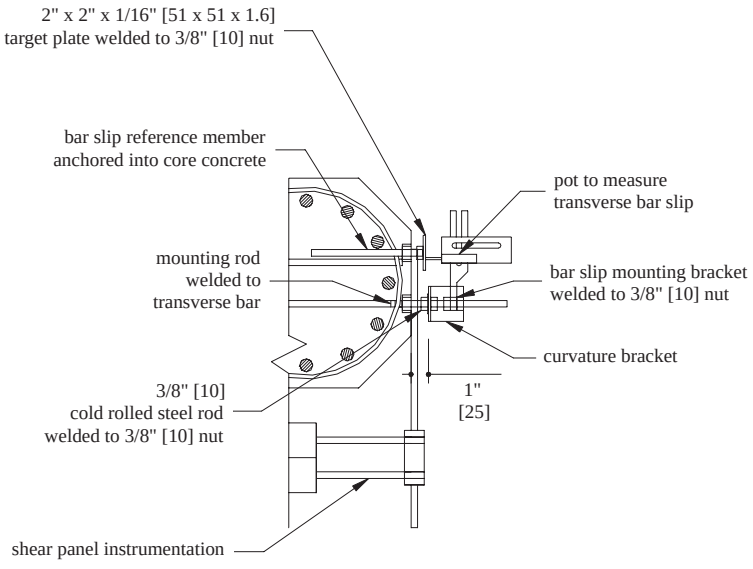

Figure 4.14: Bar slippage, shear and curvature instrumentation detail.

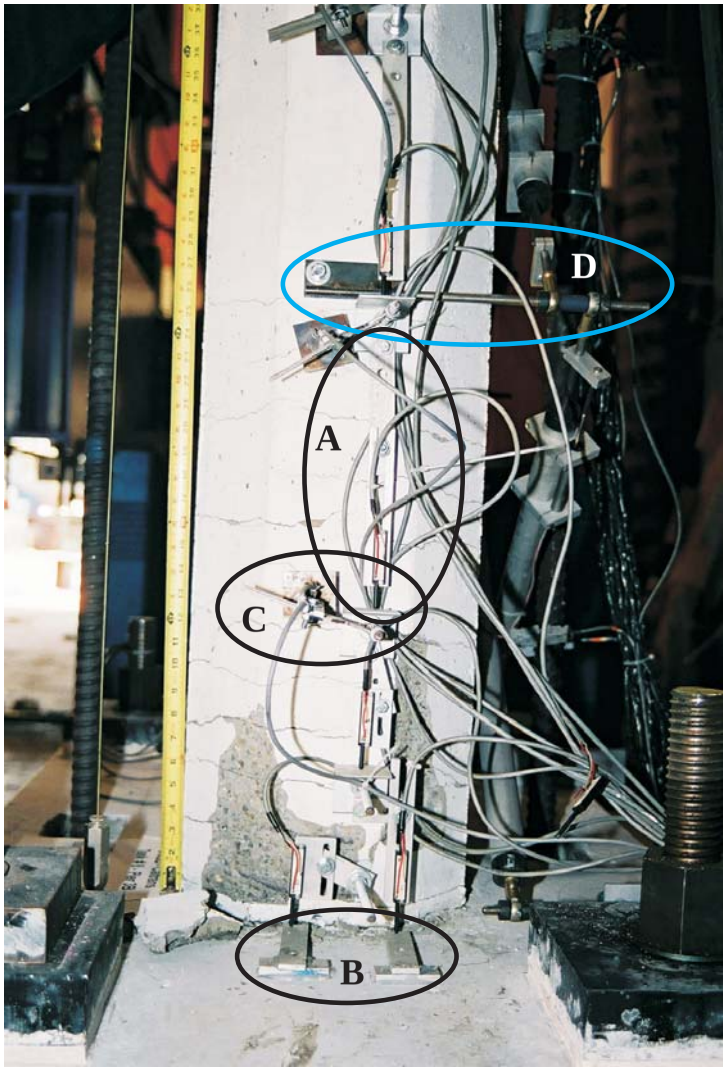

Figure 4.15: Test Unit 3B, elevation of lower north boundary element with instrumentation. A - "curvature" potentiometer. [152] and 2 in. [51] "curvature" potentiometer targets at column base. C - bar slip potentiometer and target. D - shear panel mounting bracket.

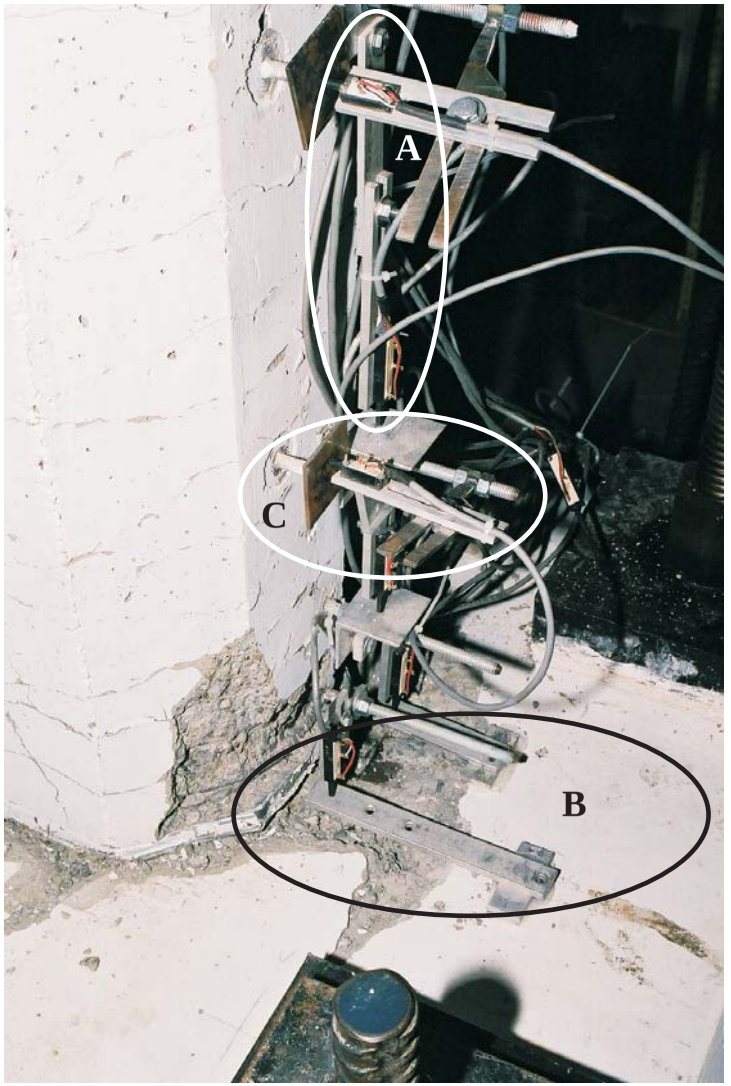

Figure 4.16: Test Unit 3B, aerial view of lower north boundary element with instrumentation. A - "curvature" potentiometer. B - 6 in. [152] and 2 in. [51] "curvature" potentiometer targets at column base. C - bar slip potentiometer and target.

4.4 Loading History

The test unit was subjected to the modified UCSD cyclic loading history shown in Figure 4.17. This particular loading history, in its simplicity, allows for comparison of damage and performance at specified displacement ductility levels. It is less severe in terms of energy demand on the test units than the standard UCSD loading history which cycles three times at each displacement ductility level.

Four initial cycles were run in load control up to theoretical first yield of the extreme longitudinal reinforcing bars. The remainder of the test was conducted in displacement control until failure of the test unit.

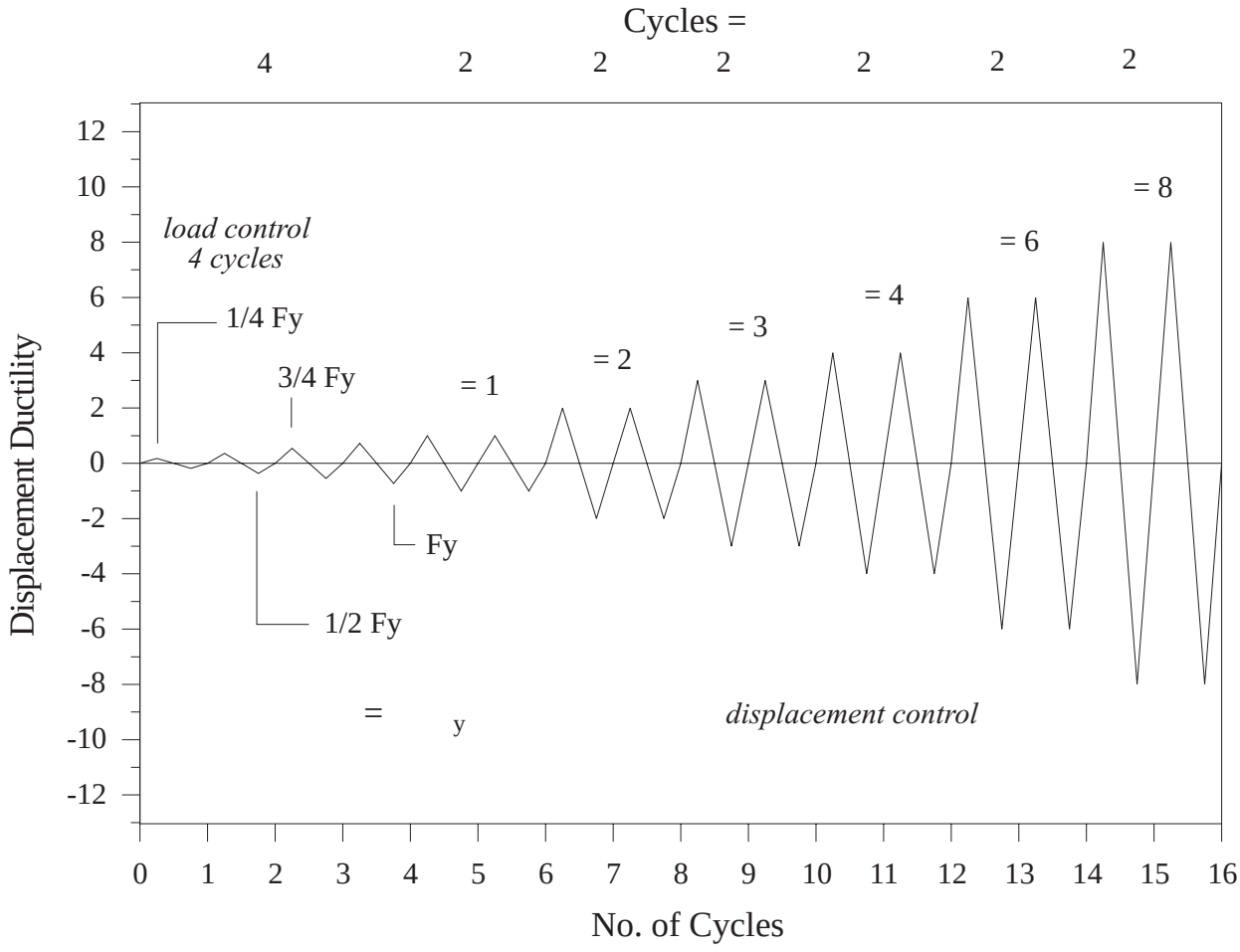

Figure 4.17: Loading history for the Phase III Web Crushing Test Units.

4.4.1 $\mu_\Delta = 1$

First yield, $F_{y'}$ of the extreme longitudinal reinforcing bars was calculated based on a moment curvature analysis of the given section, according to the theoretical first yield of the longitudinal reinforcing bars used in a given test unit. $F_{y'}$ was then determined by dividing the first yield moment, $M_{y'}$ from the moment-curvature analysis, by the column shear span. When the column reached first yield, the actual top displacement was used to calculate the experimental elastic bending stiffness.

$$K_e = F_{y',theory} /\quad _{y',exp} \tag{4.8}$$

This stiffness was then used in conjunction with the theoretical force at which either the extreme confined concrete fibers reached $\varepsilon_c = 0.0040$, or the extreme steel fiber in tension reached $\varepsilon_s = 0.015$, to determine the experimental ideal yield displacement, $\quad _y$ [7].

$$_y = F_{\varepsilon_c=0.004}/K_e \Longrightarrow \mu_\Delta = 1 \tag{4.9}$$

The ideal yield displacement was then defined as displacement ductility one, which marked the first excursion in displacement control. The ideal yield force, F_y was the experimental load required to bring the column to its ideal yield displacement.

4.5 Data Acquisition and Control

Lateral load was applied via a single +445 / -250 kip at 4000 psi [+1980 / -1113 kN, at 27.6 MPa], ± 18 in. [457 mm] stroke TJ Vickers, servo-controlled hydraulic actuator, controlled by an MTS *Flextest* digital controller. Strains and displacements were recorded as voltages and then converted to digital signals by a 16 bit analog to digital converter.

Chapter 5

Analytical Considerations and Test Predictions

5.1 Overview

Existing methods for predicting test unit response are described. The procedure for calculating force-deflection relationships from moment-curvature analysis results is described. Existing models for shear capacity are discussed. Moment-curvature and force-deflection predictions for each test unit are presented with web crushing capacity envelopes according to ACI pure shear provisions and according to the UCSD flexure-shear model.

5.2 Failure Mechanisms

The test units were expected to fail in shear by crushing of the critical compression struts at displacement ductility levels greater than $\mu_\Delta = 3$.

5.3 Moment-Curvature Analysis

The force-deflection curve for the Phase III Web Crushing Test Units predicted using results from a moment curvature analysis and an assumed equivalent plastic hinge length. The moment curvature analysis was conducted using non-linear material models for confined concrete, unconfined concrete and reinforcing steel. Architectural concrete blockouts were accounted for in all calculations of the column base moments by not including the cover concrete around the boundary elements. The steel stress-strain relationship was described by a linear elastic branch, followed by a yield plateau and ending in a strain hardening

branch, whose exponent was defined by the strain hardening modulus E_{sh}. The concrete model followed Mander's equations for confined and unconfined concrete [12].

5.3.1 Steel

Reinforcing steel stress strain behavior was calculated assuming that E = 29,000 ksi [200 GPa] up to the yield stress. The plastic region was assumed to have zero stiffness up to ε_{sh}, the strain at which hardening was assumed to begin. According to Mander's model for strain hardening of steel [13], the strain hardening region was then assumed to follow a power curve based on the modulus at first hardening that was calibrated to best fit the data. The equation for stress in the strain hardening region is given as

$$f_s = f_u - (f_u - f_y)\left(\frac{\varepsilon_{su} - \varepsilon_s}{\varepsilon_{su} - \varepsilon_{sh}}\right)^P \tag{5.1}$$

where f_s is the stress in the strain hardening region, f_u is the ultimate stress of the steel, f_y is the steel yield stress, ε_{su} is the ultimate steel strain, ε_s is the strain in the hardening region, and P is calculated as

$$P = E_{sh}\frac{\varepsilon_{su} - \varepsilon_{sh}}{f_u - f_y} \tag{5.2}$$

where E_{sh} is the elastic modulus of the steel at first strain hardening.

Effective Ultimate Steel Strain

Moment-Curvature analyses for all three test units terminated at an assumed effective ultimate steel strain. This strain was taken based on the method proposed by Dodd [14] as the extreme fiber steel strain from a moment-curvature analysis at the point when

$$\varepsilon_s + \varepsilon_c = 0.10 \tag{5.3}$$

where ε_s is the extreme fiber tensile steel strain and ε_c is the extreme fiber compressive confined concrete strain.

5.3.2 Concrete

The concrete constitutive relationship assumed in the moment curvature analysis was based on Mander's Model for confined and unconfined concrete [12] and is described briefly below.

Confined Concrete

The confined concrete stress strain relationship was assumed to follow the curve proposed by Popovics [15], which is written as

$$f_c = \frac{f'_{cc} x r}{r - 1 + x^r} \tag{5.4}$$

where, according to Mander [12],

$$f'_{cc} = f'_c \quad 2.254\sqrt{1 + \frac{7.94 f'_l}{f'_c}} - \frac{2 f'_l}{f'_c} - 1.254\Bigg) \tag{5.5}$$

$$x = \frac{\varepsilon_c}{\varepsilon_{cc}} \tag{5.6}$$

$$\varepsilon_{cc} = \varepsilon_{co}\left[1 + 5 \quad \frac{f'_{cc}}{f'_c} - 1\Bigg)\right] \tag{5.7}$$

$$r = \frac{E_c}{E_c - E_{sec}} \tag{5.8}$$

$$E_c = 57,000\sqrt{f'_c} \qquad (psi) \tag{5.9}$$

$$E_{sec} = \frac{f'_{cc}}{\varepsilon_{cc}} \tag{5.10}$$

$$f'_l = \frac{1}{2} k_e \rho_s f_y \tag{5.11}$$

and for circular columns

$$k_e = 0.9 \tag{5.12}$$

which is a simplification proposed by Priestley [7].

Figure 5.1 shows the stress-strain curves for confined and unconfined concrete.

Unconfined Concrete

The stress-strain curve for unconfined concrete is pictured in Figure 5.1. Typical concrete spalling strains range between $0.003 \leq \varepsilon_{sp} \leq 0.008$. Therefore ε_{sp} was set at the maximum 0.008 because the boundary element cover concrete was blocked out at the column base. The unconfined concrete stress-strain curve shown in Figure 5.1 peaks at a strain of $\varepsilon_{co} = 0.002$ and follows the Popovics curve until $\varepsilon_c = 2\varepsilon_{co} = 0.004$. At higher strains, the stress decreases linearly to zero.

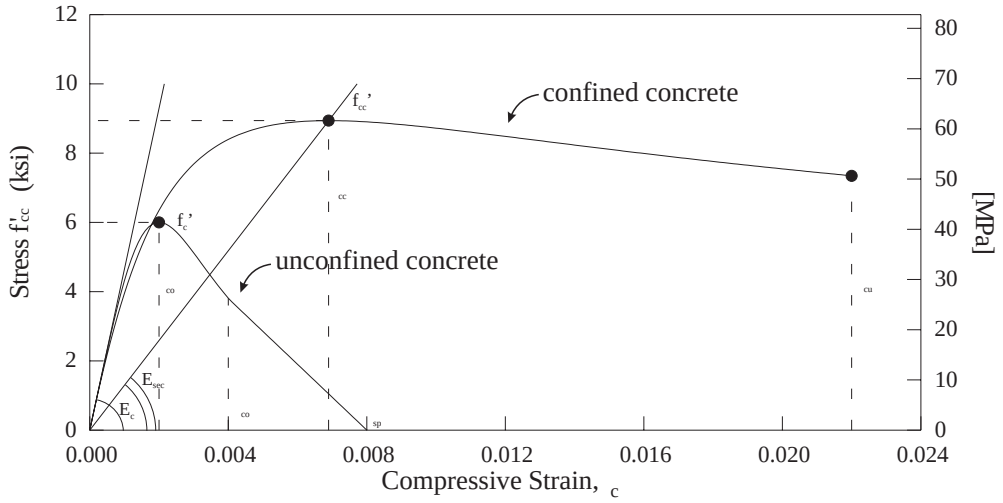

Figure 5.1: Concrete stress-strain curves used in the moment-curvature analysis.

5.4 Column Deflection

Column flexural displacement was calculated as the sum of elastic and plastic components, given as

$$_e + \Delta_p \tag{5.13}$$

Assuming that plastic rotation occurs about the column base, this may be written as

$$\frac{\phi_{y'} L^2}{3} \frac{M}{M_{y'}} + \quad \phi - \phi_{y'} \frac{M}{M_{y'}} \quad L_p L \tag{5.14}$$

$\Delta =$

where M is the moment at a given level of displacement, ϕ is the curvature at that displacement level, $M_{y'}$ is the theoretical first yield moment, $\phi_{y'}$ is the curvature at first yield, L is the column shear span, and L_p is the equivalent plastic hinge length, which was assumed simply to have the value $D/2$, where D is the total section depth.

5.5 Shear Equations

Shear capacity was evaluated based on a three component model (as opposed to the traditional two component model in the ACI Code) that is a function of the concrete, axial load and steel contributions.

$$V_n = V_c + V_p + V_s \tag{5.15}$$

The concrete contribution V_c, is a compilation of the shear resistance provided by aggregate interlock, dowel action of the longitudinal reinforcing bars, tension stiffening, and the compression toe. This component degrades according to the value γ with increasing ductility due to reduction in the effectiveness of aggregate interlock as the crack width increases with ductility [16]. The concrete component is given as

$$V_c = \alpha\beta\gamma\sqrt{f'_c}A_e \tag{5.16}$$

where A_e is the effective concrete area, taken typically as $A_e = 0.8A_g$ for circular and rectangular columns. In this report, A_e is taken as $A_e = 0.8Dt_w$, where D is the total section depth. This definition was thought to be overconservative but was used because it was consistent with the ACI definition A_e. Two different possibilities for A_e are shown as the shaded region in Figure 5.2. The definitions of α and β in the V_c component are given

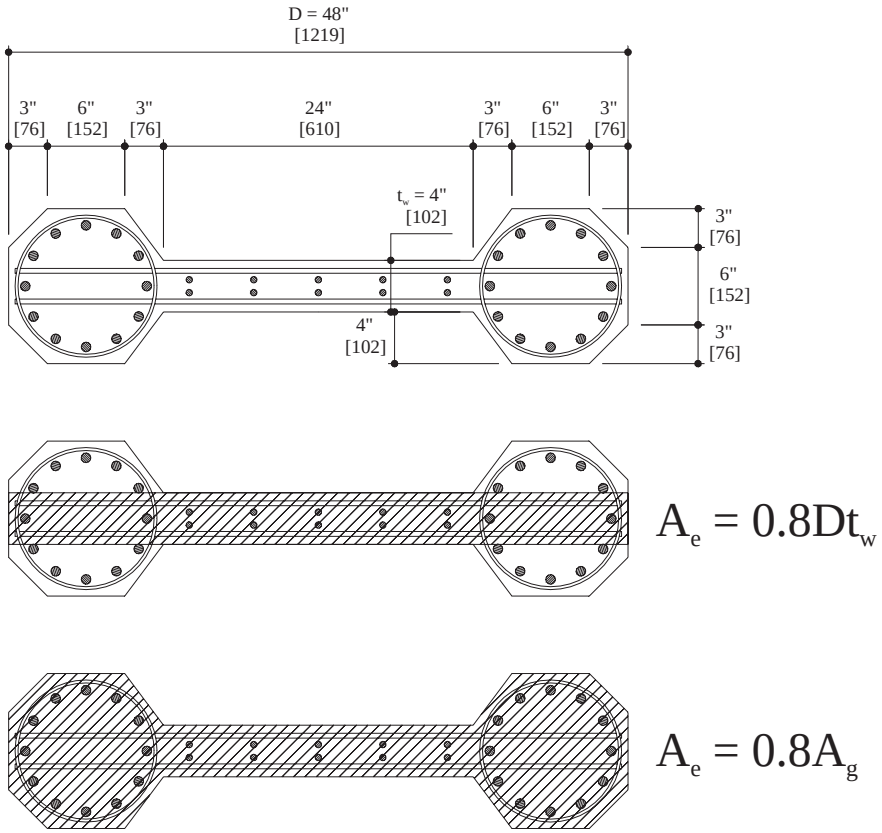

Figure 5.2: Effective area, A_e for test Unit 3A.

below.

$$1 \leq \alpha = 3 - M/VD \leq 1.5 \tag{5.17}$$

$$\beta = 0.5 + 20A_{st}/A_g \leq 1 \tag{5.18}$$

Values for γ as a function of curvature ductility are given in Figure 5.3. These curves have been simplified since [16] to consist of one descending slope instead of two [10].

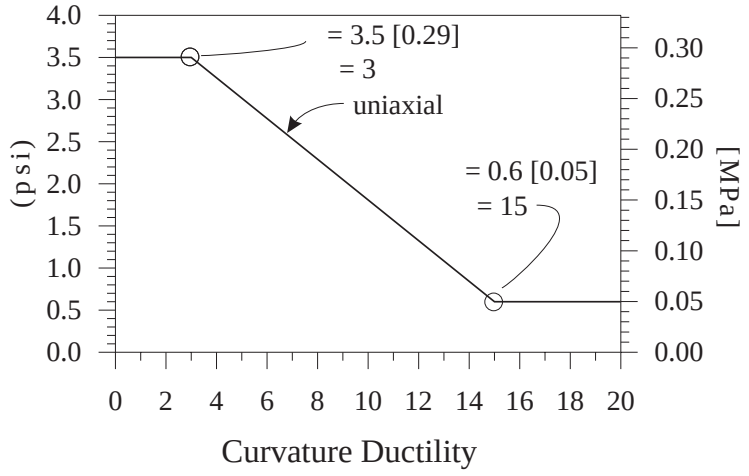

Figure 5.3: V_c parameter γ as a function of μ_ϕ [10].

The axial load contribution, V_p and the steel contribution, V_s to shear capacity were previously explained in Chapter 2.

5.6 Shear Displacements

Shear deformations were predicted simply as a percentage of flexural deformations calculated from the moment-curavture analysis. For all three tests, the shear deformation was assumed to equal 20% of the flexural deformation.

5.7 Moment-Curvature Predictions, Force-Deflection Predictions and Web Crushing Capacity Curves

Figure 5.5 shows the predicted moment-curvature responses of the test unit cross sections with architectural concrete blockouts. Figure 5.6 presents the flexural force-deflection curves

for the Phase III Web Crushing Test Units based on the simple equation for equivalent plastic hinge length introduced earlier and 20% shear displacements. Figures 5.7, 5.8 and 5.9 show force-displacement curves calculated with a variety of analytical tools along with the previously discussed ACI web crushing criteria and the UCSD flexure-shear web crushing assessment equation. The four force-displacement predictions in each figure represent the four independent analyses listed below.

1. Moment curvature analysis with plastic hinge length, $L_p = 0.5D$ and $\quad _s = 0.2\Delta_f$
2. Rechenbrett 2-D analysis [17], based on assumptions of pure flexure.
3. Response 2000 [18] analysis, assuming Mander's confined concrete properties [13] in the boundary elements and unconfined concrete properties in the wall.
4. 3-D non linear, Abaqus [19] monotonic finite element analysis with the ANACAP [20, 21] concrete model.

The meshes for the 3-D finite element analysis are shown in Figure 5.4.

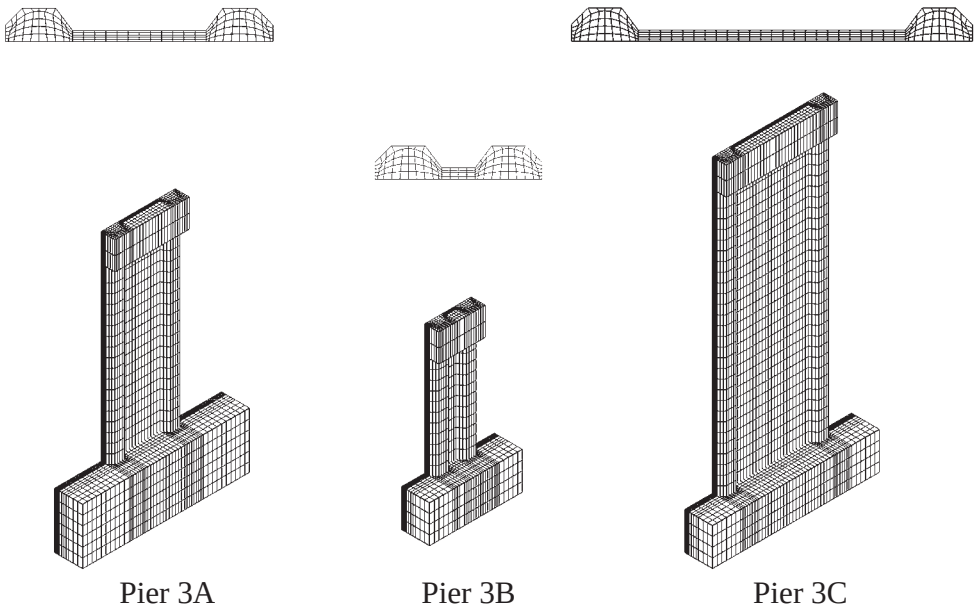

Figure 5.4: Test Units 3A, 3B and 3C, 3-D finite element meshes.

The flexure-shear web crushing curves were calculated according to the procedure outlined in Chapter 1, using Collins' 1978 model for compression softening. For this model, ε_0 was assumed to be 0.002 and γ_m was assumed to be the shear displacement divided by the column depth, implying that all shear deformation was assumed to occur within the plastic hinge region.

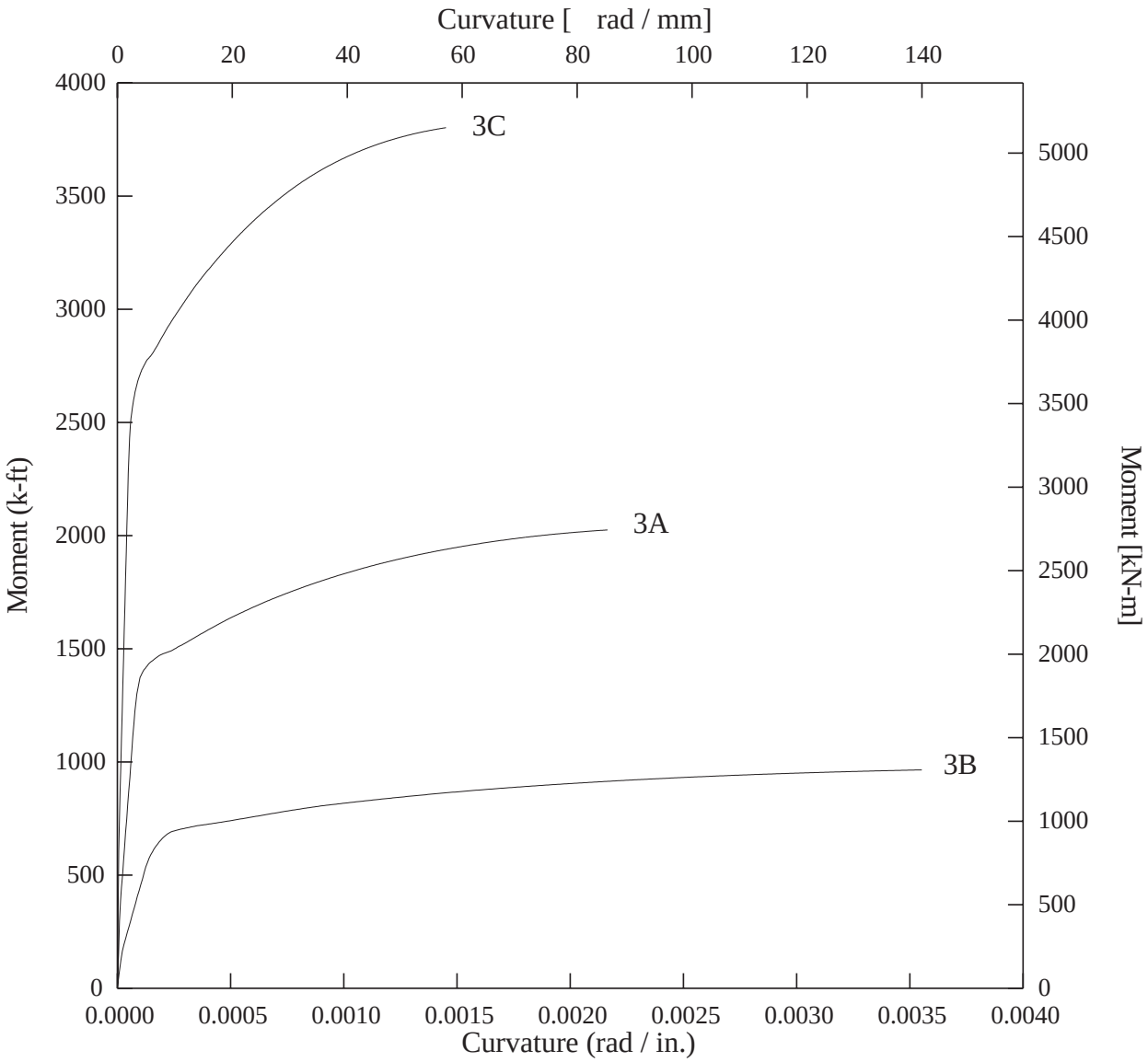

Figure 5.5: Test Units 3A, 3B and 3C, moment-curvature predictions.

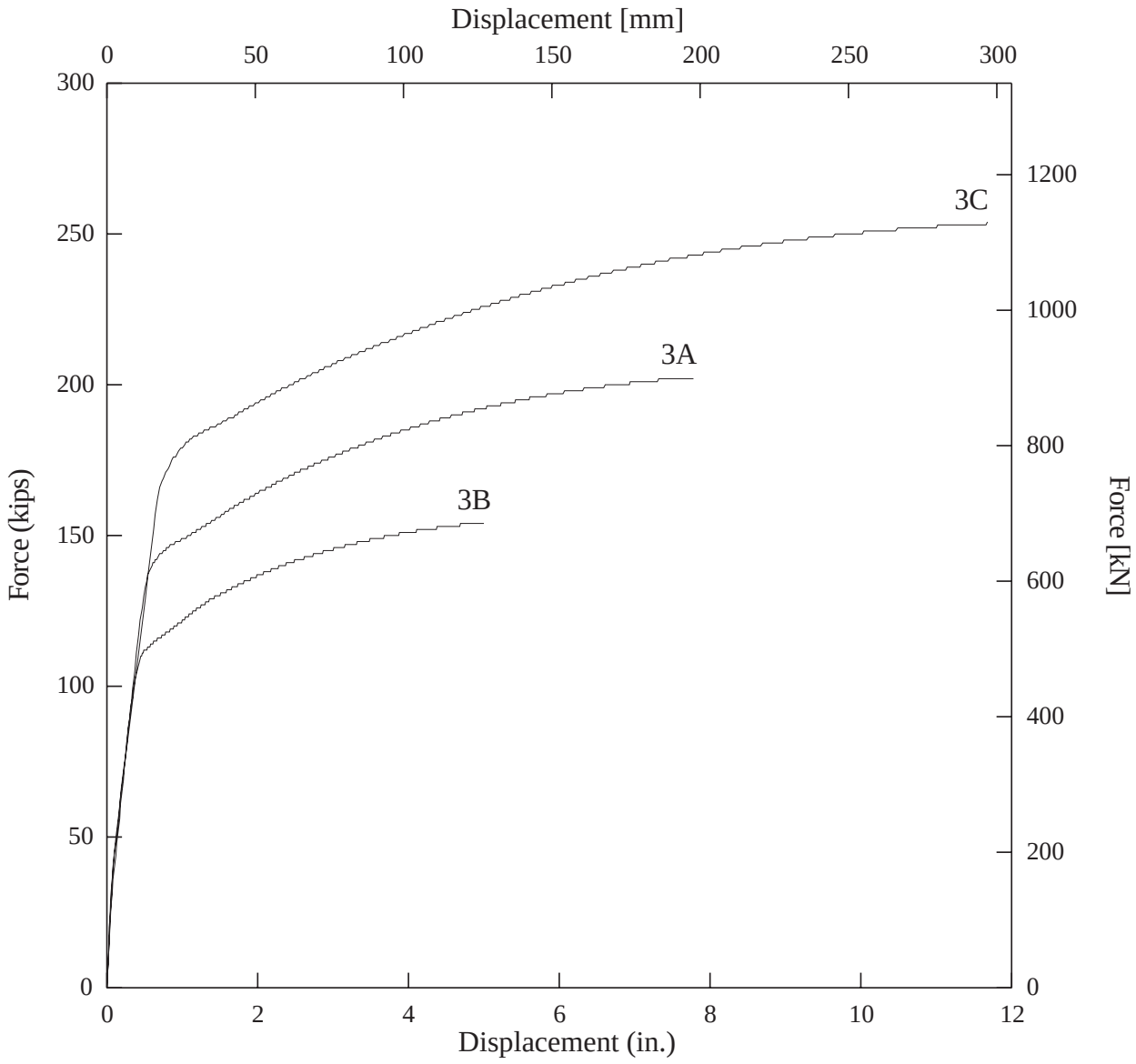

Figure 5.6: Test Units 3A, 3B and 3C, force-deflection predictions.

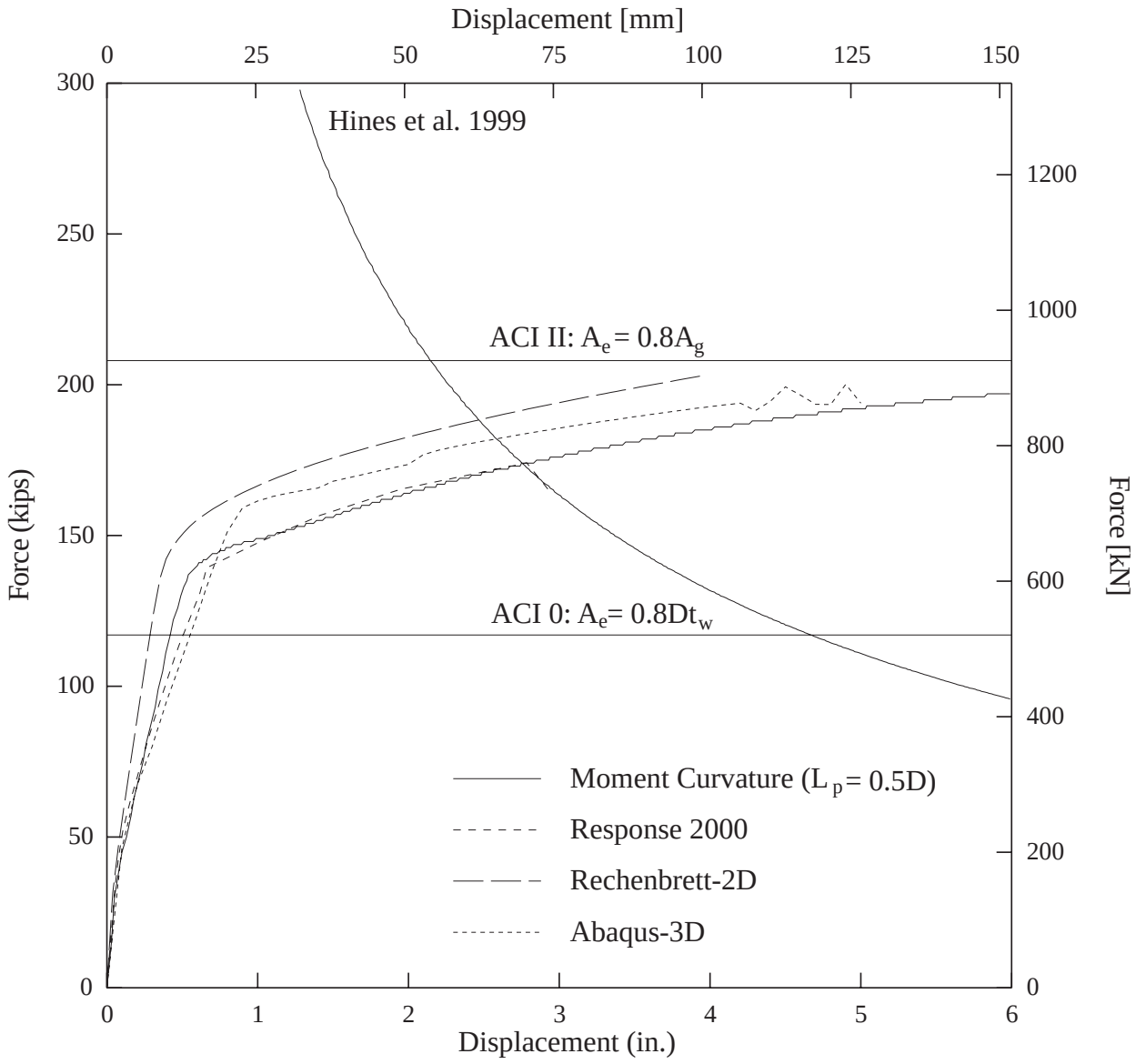

Figure 5.7: Test Unit 3A, force-deflection predictions with web crushing capacity envelopes.

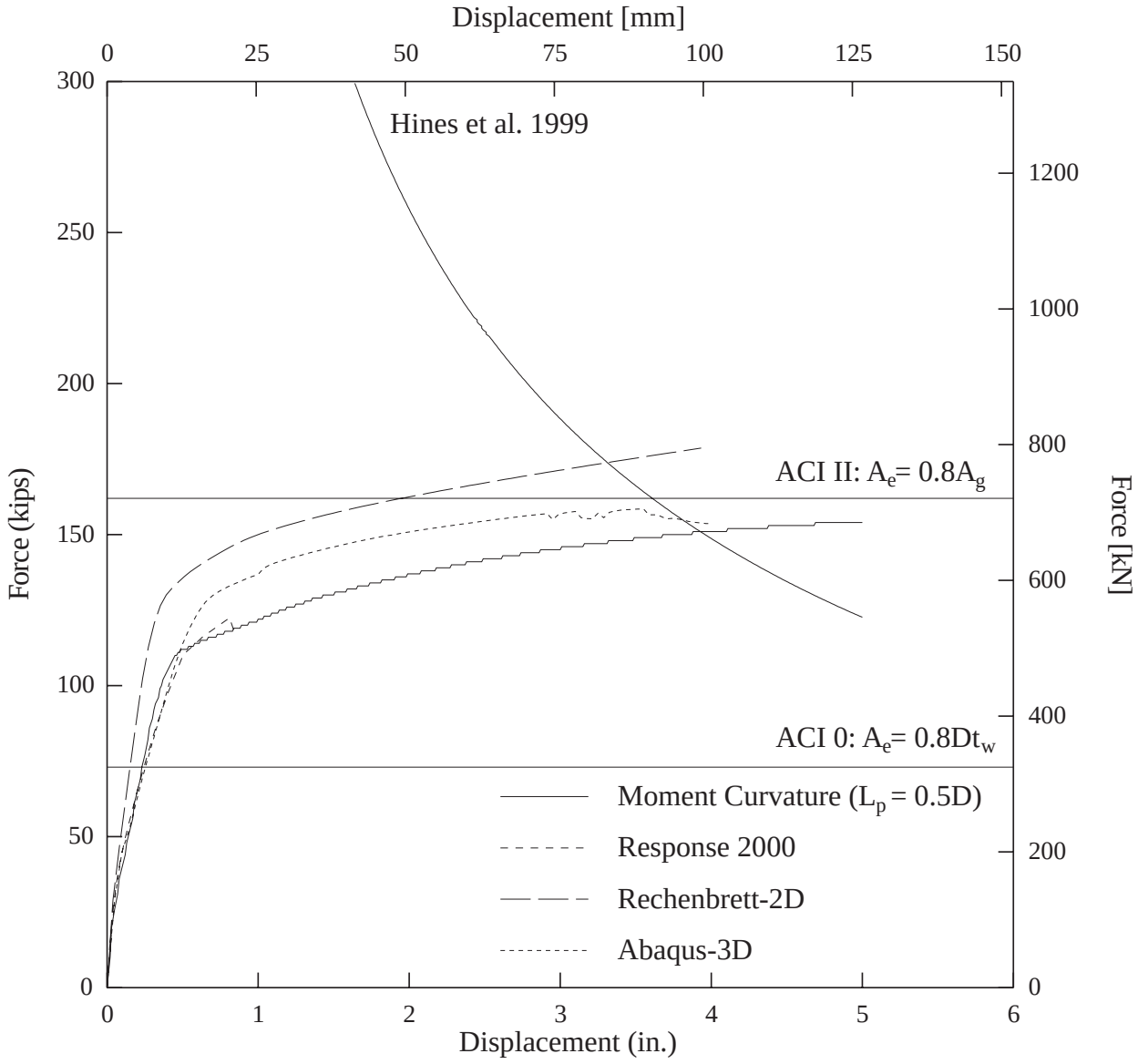

Figure 5.8: Test Units 3B, force-deflection predictions with web crushing capacity envelopes.

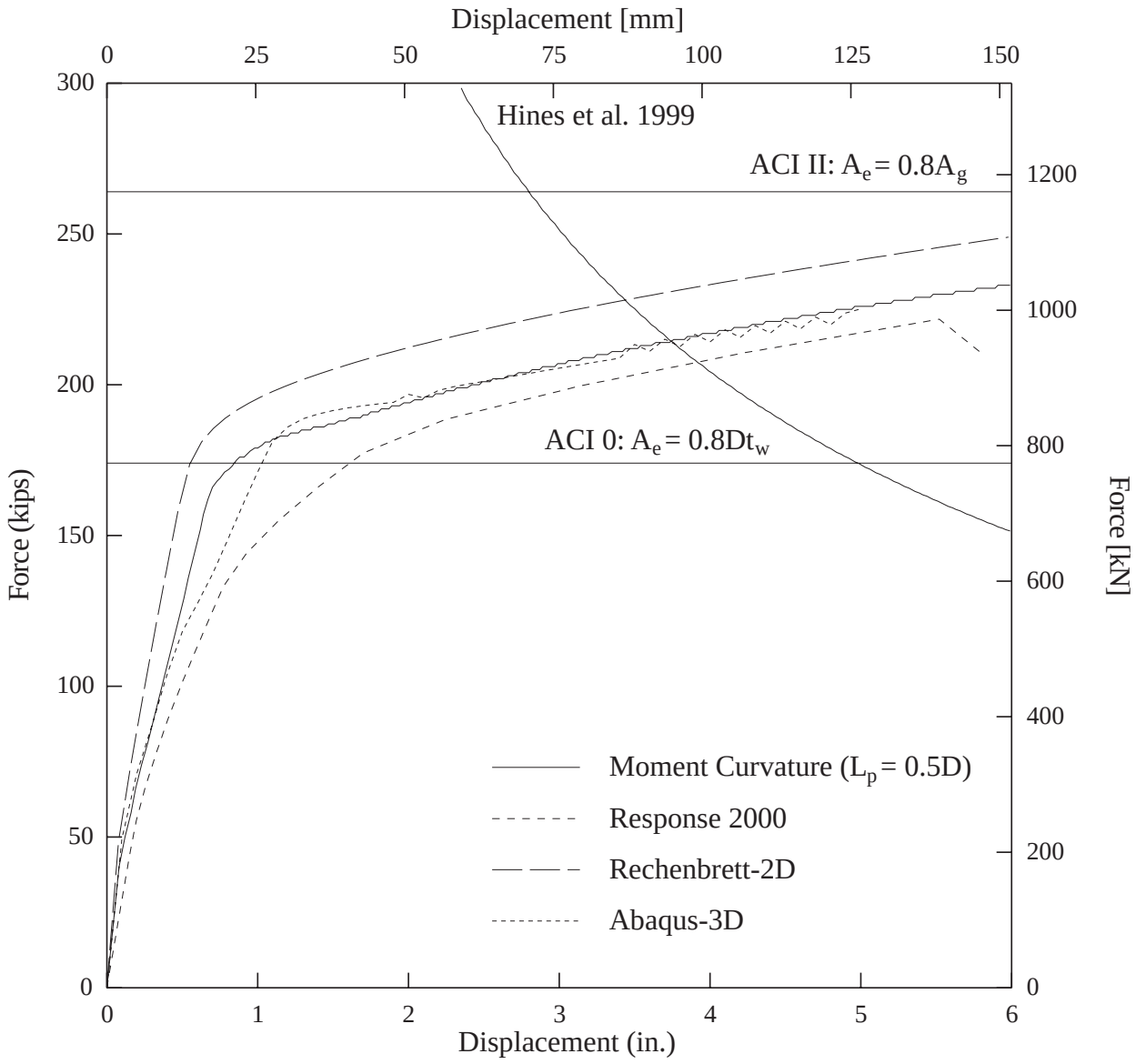

Figure 5.9: Test Unit 3C, force-deflection predictions with web crushing capacity envelopes.

Chapter 6

Test Observations

6.1 Overview

Test observations are presented for each level of displacement ductility. These observations refer to the photos in Appendix B. These observations refer to unmarked cracks on the east face of each test unit. Note that while all of the observations in this chapter were made on the test unit east faces, all of the data in Chapter 7 is reported as if looking at the west face of the test units. For scale, each test unit was marked with cross hairs at 12 in. [305] vertical intervals, 12 in. [305] horizontal intervals on the structural wall, and at the center of each boundary element, 6 in. [152] from the extreme end of the test unit. Specific cracks are singled out, and their widths at various locations along the section depth are given for the first positive excursion to each displacement ductility level and at zero load immediately following the excursion.

6.2 Crack Widths

Five representative cracks were monitored throughout each test. These cracks are shown in Figures 6.1, 6.2 and 6.3. Since the cracks were not always continuous through the tension boundary element, as with cracks #3 and #4 in Test Unit 3A, and since the cracks sometimes changed position at higher displacement levels, as with crack #1 in Test Unit 3A, the crack widths reported are representative of behavior but not as reliable as the other measured test data. Some cracks were extended or redefined at later ductility levels. This is was the case particularly for cracks #2 and #5 in Test Unit 3B.

The widths of these cracks were recorded on the test unit east face at specified horizontal

positions at each positive peak load and displacement level and at zero load immediately following the peak. The horizontal positions correspond to the position letters for the instrumentation layouts presented in Chapter 4. Test Units 3A and 3C had horizontal positions A - G for instrumentation. Therefore, the horizontal crack positions for Test Unit 3A corresponded exactly to the instrumentation positions. Test Unit 3C had two more horizontal crack positions than horizontal positions for instrumentation, however, so Positions C and E were flanked by positions C_N to the north of C and position E_S to the south of E. Furthermore, crack Position C was 3 in. [76 mm] south of gage Position C and crack position E was 3 in. [76 mm] north of gage Position E. Test Unit 3B had only positions A - E for instrumentation. Therefore, the two additional crack positions, were labeled D_S and D_N.

Tables 6.1 - 6.12 list the crack widths in both English and metric units. The columns of each table specify the horizontal position of the measurement. The rows are grouped into individual cracks, starting with Crack #1 at the bottom of the table and moving to Crack #5 at the top. For an individual crack, a given row refers either to the specified peak level or to the zero load level immediately following the peak. If no crack appeared at a given position, the space is left blank. If the crack closed completely, the width is listed as 0.000 in. [0.00]. The minimum measured crack width was 0.002 in. [0.05]. Cracks that appeared narrower than the minimum width appear labeled as $<$ 0.002 in. [$<$ 0.05].

6.3 Test Unit 3A

The test unit performed in a ductile manner up through $\mu_\Delta = 4$, on the first excursion to $\mu_\Delta = 5$ the web was observed to begin crushing at approximately $\mu_\Delta = 4.4$. At this point, the test was stopped immediately and ended after taking the column back to zero load.

6.3.1 First Cracking and First Yielding ($1/4F_y - \mu_\Delta = 1$)

Shear cracks first appeared in the wall at $1/2F_y$. At $3/4F_y$, hairline flexural cracks were observed to extend at regular intervals from the column base up to 72 in. [1829 mm] above the column base. Also at $3/4F_y$, shear cracks were observed to spread at regular intervals up the entire column height at an angle of 35° from the vertical. At F_y, the previously existing cracks opened further and no vertical splitting cracks were visible in the compression

boundary element.

Figure B.1 shows the east face of Test Unit 3A as it was pushed to the first positive excursion at $\mu_\Delta = 1$. Cracks in the column were difficult to see at this level and consequently do not appear clearly in the figure.

6.3.2 Initial Spread of Plasticity ($\mu_\Delta = 2.0 - 3.0$)

Figure B.2 shows the same view of the test unit at the first positive excursion to $\mu_\Delta = 2$. Figure B.1 shows a vertical splitting crack on the east face of the compression (south) boundary element at this level. Figure B.4 shows the same east view of the south boundary element in tension after the first positive excursion to $\mu_\Delta = 4$. No significant spalling occurred on the south boundary element during the entire test. A single concrete chunk, roughly 3 in. x 4 in. [76 x 102] did, however, come off of the north boundary element at $\mu_\Delta = 4$. This asymmetric behavior demonstrated the random nature of such spalling in architectural concrete with blockouts, where potientially the architectural concrete could remain completely intact if it were held on by tiewire. Such circumstances are meaningless from the point of view of structural behavior and repair, however it is important to note the significant decrease in spalling on such columns with blockouts as compared to the level of spalling seen in the Phase I and II columns by $\mu_\Delta = 4$ [1].

Figure B.5 shows the test unit west face at the first positive excursion to $\mu_\Delta = 3$. Nine 1.2 in. [30 mm] concrete gages are visible on the south side of the wall in this figure. These gages were applied after completing all cycles at $\mu_\Delta = 2$ to three of the compression struts expected to crush at a higher level of displacement ductility. In Figure B.23, much of the paint in this critical region can be seen to have flaked off, indicating increasingly high compression strains in the concrete at this displacement level. Furthermore, the cracks at the column base were observed to converge roughly 1 in. [25 mm] above the footing at the compression boundary element, indicating that the neutral axis had moved into the compression boundary element.

6.3.3 Further Spread of Plasticity and Web Crushing Failure ($\mu_\Delta = 4.0 - 5.0$)

Figure B.6 shows the test unit west face at the first positive excursion to $\mu_\Delta = 4$. At this level, more flaking of the paint on the wall was observed, however there was no indication that the concrete in this region was beginning to give way. The test unit survived two full cycles

at $\mu_\Delta = 4$, before failing by web crushing on the first positive excursion to $\mu_\Delta = 5$. Figure B.7 shows the level of damage in the wall after the second negative excursion to $\mu_\Delta = 4$. At this point, there appeared to be no signs of actual strength degradation, however the critical compression struts appeared more degraded than they had appeared during the first cycle at $\mu_\Delta = 4$.

The test unit finally failed on the first positive excursion to $\mu_\Delta = 5$ at a displacement ductility level of approximately $\mu_\Delta = 4.4$. Critical compression struts were first observed to crush in the wall next to the compression (south) boundary element between heights of 6 - 12 in. [152 - 305] above the footing. After these initial two struts crushed, the struts just above them began to slide downward along the interface between the compression boundary element and the wall, creating a vertical failure plane up to a height of roughly 36 in. [914] above the footing. Loading was halted as soon as the first struts were observed to crush, but under a constant displacement at this level, the sliding failure occurred in the higher struts until the load dropped by roughly 20%. At this point, the test unit was brought back to zero load and the test was ended.

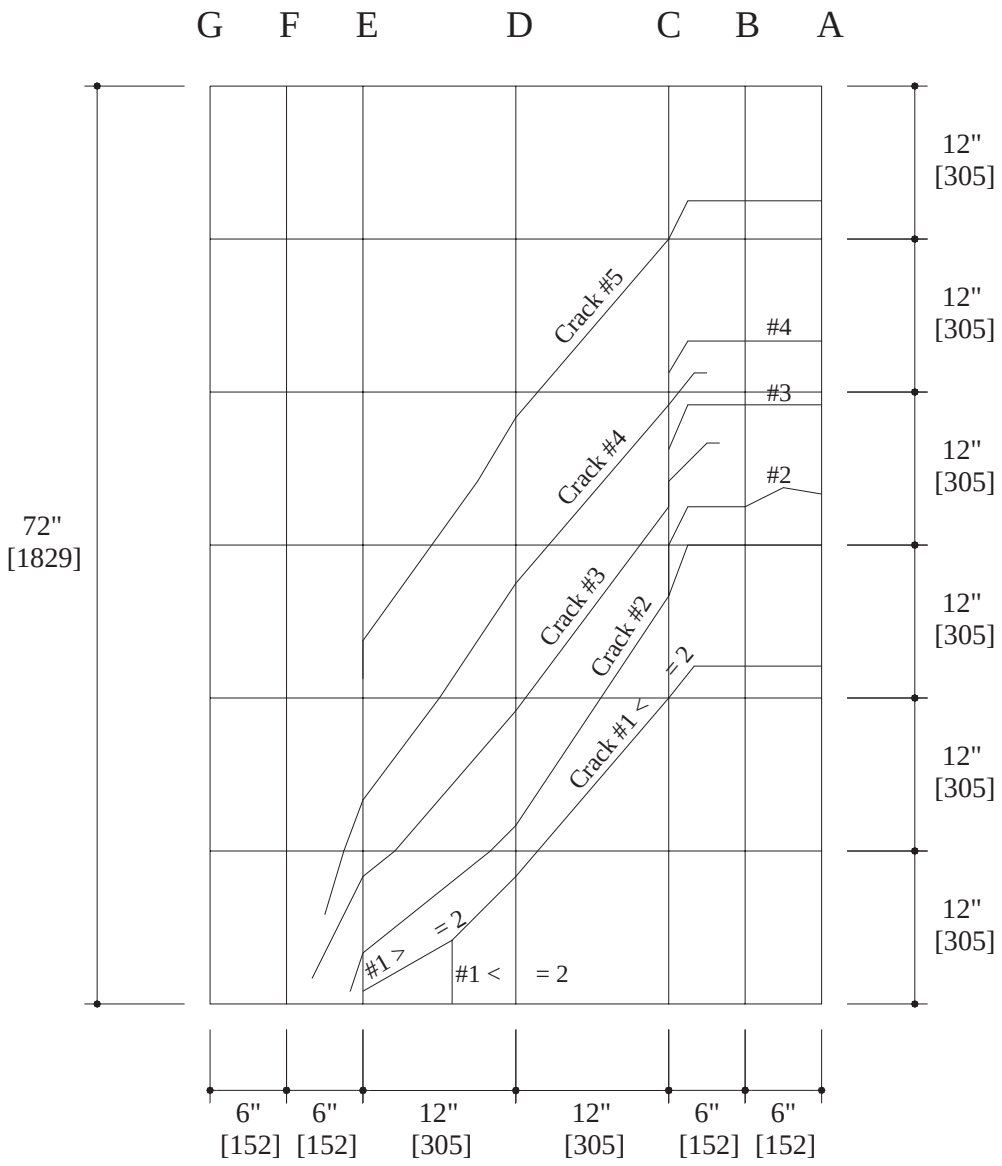

Figure 6.1: Test Unit 3A, Cracks 1 - 5.

	Load	E	D	C	B	A
Crack #5	1/4 Fy					
	Zero Load					
	1/2 Fy		0.002	< 0.002		
	Zero Load		0.000	0.000		
	Fy	0.004	0.008	0.006	0.002	0.002
	Zero Load	< 0.002	< 0.002	< 0.002	0.000	0.000
Crack #4	1/4 Fy					
	Zero Load					
	1/2 Fy		0.002	0.002		
	Zero Load		< 0.002	< 0.002		
	Fy	0.004	0.008	0.006	0.004	0.004
	Zero Load	< 0.002	< 0.002	< 0.002	0.000	0.000
Crack #3	1/4 Fy					
	Zero Load					
	1/2 Fy		0.002	0.002		
	Zero Load		< 0.002	< 0.002		
	Fy	0.002	0.008	0.006	0.002	0.002
	Zero Load	< 0.002	< 0.002	< 0.002	0.000	0.000
Crack #2	1/4 Fy					
	Zero Load					
	1/2 Fy		0.002	0.002		
	Zero Load		< 0.002	< 0.002		
	Fy	0.002	0.006	0.004	0.004	0.004
	Zero Load	< 0.002	< 0.002	< 0.002	0.000	0.000
Crack #1	1/4 Fy					
	Zero Load					
	1/2 Fy		0.002	0.002	< 0.002	< 0.002
	Zero Load		< 0.002	< 0.002	0.000	0.000
	Fy		0.006	0.004	0.004	0.006
	Zero Load		< 0.002	< 0.002	0.000	0.000

Table 6.1: Test Unit 3A crack widths at load levels up to F_y (in.).

	Load	E	D	C	B	A
Crack #5	1/4 Fy					
	Zero Load					
	1/2 Fy		0.05	< 0.05		
	Zero Load		0.00	0.00		
	Fy	0.10	0.20	0.15	0.05	0.05
	Zero Load	< 0.05	< 0.05	< 0.05	0.00	0.00
Crack #4	1/4 Fy					
	Zero Load					
	1/2 Fy		0.05	0.05		
	Zero Load		< 0.05	< 0.05		
	Fy	0.10	0.20	0.15	0.10	0.10
	Zero Load	< 0.05	< 0.05	< 0.05	0.00	0.00
Crack #3	1/4 Fy					
	Zero Load					
	1/2 Fy		0.05	0.05		
	Zero Load		< 0.05	< 0.05		
	Fy	0.05	0.20	0.15	0.05	0.05
	Zero Load	< 0.05	< 0.05	< 0.05	0.00	0.00
Crack #2	1/4 Fy					
	Zero Load					
	1/2 Fy		0.05	0.05		
	Zero Load		< 0.05	< 0.05		
	Fy	0.05	0.15	0.10	0.10	0.10
	Zero Load	< 0.05	< 0.05	< 0.05	0.00	0.00
Crack #1	1/4 Fy					
	Zero Load					
	1/2 Fy		0.05	0.05	< 0.05	< 0.05
	Zero Load		< 0.05	< 0.05	0.00	0.00
	Fy		0.15	0.10	0.10	0.15
	Zero Load		< 0.05	< 0.05	0.00	0.00

Table 6.2: Test Unit 3A crack widths at load levels up to F_y [mm].

	μ_Δ	E	D	C	B	A
Crack #5	1	0.006	0.008	0.008	0.003	0.002
	Zero Load	< 0.002	< 0.002	< 0.002	0.000	0.000
	2	0.006	0.010	0.006	0.004	0.004
	Zero Load	0.002	0.002	< 0.002	0.000	0.000
	3	0.006	0.010	0.006	0.004	0.004
	Zero Load	0.002	0.002	0.000	0.000	0.000
	4	0.012	0.012	0.008	0.004	0.004
	Zero Load	0.008	0.004	0.002	0.000	0.000
Crack #4	1	0.004	0.008	0.008	0.004	0.004
	Zero Load	< 0.002	< 0.002	< 0.002	0.000	0.000
	2	0.008	0.008	0.004	0.004	0.004
	Zero Load	0.002	0.002	< 0.002	0.000	0.000
	3	0.020	0.012	0.008	0.006	0.006
	Zero Load	0.006	0.004	0.002	0.000	0.000
	4	0.012	0.020	0.010	0.002	0.002
	Zero Load	0.010	0.006	0.002	0.000	0.000
Crack #3	1	0.004	0.008	0.006	0.002	0.002
	Zero Load	< 0.002	< 0.002	< 0.002	0.000	0.000
	2	0.004	0.012	0.008	0.004	0.004
	Zero Load	0.002	0.002	< 0.002	0.000	0.000
	3	0.012	0.016	0.006	0.004	0.004
	Zero Load	0.004	0.006	0.002	0.000	0.000
	4	0.008	0.031	0.012	0.004	0.004
	Zero Load	0.008	0.016	0.004	0.000	0.000
Crack #2	1	0.004	0.006	0.006	0.004	0.006
	Zero Load	< 0.002	< 0.002	< 0.002	0.000	0.000
	2	0.004	0.014	0.008	0.006	0.006
	Zero Load	0.002	0.002	< 0.002	0.000	0.000
	3	0.004	0.020	0.006	0.008	0.008
	Zero Load	0.002	0.016	0.002	0.000	0.000
	4	0.008	0.024	0.024	0.049	0.059
	Zero Load	0.008	0.020	0.016	0.031	0.031
Crack #1	1		0.004	0.006	0.006	0.008
	Zero Load		< 0.002	< 0.002	0.000	0.000
	2		0.016	0.008	0.008	0.008
	Zero Load		0.004	< 0.002	0.000	0.000
	3	< 0.002	0.031	0.031	0.031	0.059
	Zero Load	< 0.002	0.020	0.020	0.016	0.039
	4	0.002	0.039	0.031	0.059	0.071
	Zero Load	0.002	0.024	0.020	0.039	0.049

Table 6.3: Test Unit 3A crack widths at varying levels of μ_Δ (in.).

	μ_Δ	E	D	C	B	A
Crack #5	1	0.15	0.20	0.20	0.08	0.05
	Zero Load	< 0.05	< 0.05	< 0.05	0.00	0.00
	2	0.15	0.25	0.15	0.10	0.10
	Zero Load	0.05	0.05	< 0.05	0.00	0.00
	3	0.15	0.25	0.15	0.10	0.10
	Zero Load	0.05	0.05	0.00	0.00	0.00
	4	0.30	0.30	0.20	0.10	0.10
	Zero Load	0.20	0.10	0.05	0.00	0.00
Crack #4	1	0.10	0.20	0.20	0.10	0.10
	Zero Load	< 0.05	< 0.05	< 0.05	0.00	0.00
	2	0.20	0.20	0.10	0.10	0.10
	Zero Load	0.05	0.05	< 0.05	0.00	0.00
	3	0.50	0.30	0.20	0.15	0.15
	Zero Load	0.15	0.10	0.05	0.00	0.00
	4	0.30	0.50	0.25	0.05	0.05
	Zero Load	0.25	0.15	0.05	0.00	0.00
Crack #3	1	0.10	0.20	0.15	0.05	0.05
	Zero Load	< 0.05	< 0.05	< 0.05	0.00	0.00
	2	0.10	0.30	0.20	0.10	0.10
	Zero Load	0.05	0.05	< 0.05	0.00	0.00
	3	0.30	0.40	0.15	0.10	0.10
	Zero Load	0.10	0.15	0.05	0.00	0.00
	4	0.20	0.80	0.30	0.10	0.10
	Zero Load	0.20	0.40	0.10	0.00	0.00
Crack #2	1	0.10	0.15	0.15	0.10	0.15
	Zero Load	< 0.05	< 0.05	< 0.05	0.00	0.00
	2	0.10	0.35	0.20	0.15	0.15
	Zero Load	0.05	0.05	< 0.05	0.00	0.00
	3	0.10	0.50	0.15	0.20	0.20
	Zero Load	0.05	0.40	0.05	0.00	0.00
	4	0.20	0.60	0.60	1.25	1.50
	Zero Load	0.20	0.50	0.40	0.80	0.80
Crack #1	1		0.10	0.15	0.15	0.20
	Zero Load		< 0.05	< 0.05	0.00	0.00
	2		0.40	0.20	0.20	0.20
	Zero Load		0.10	< 0.05	0.00	0.00
	3	< 0.05	0.80	0.80	0.80	1.50
	Zero Load	< 0.05	0.50	0.50	0.40	1.00
	4	0.05	1.00	0.80	1.50	1.80
	Zero Load	0.05	0.60	0.50	1.00	1.25

Table 6.4: Test Unit 3A crack widths at varying levels of μ_Δ [mm].

6.4 Test Unit 3B

The test unit performed in a ductile manner up through $\mu_\Delta = 6$, where large shear cracks up to 0.04 in. [1 mm] wide were observed. On the first negative excursion to $\mu_\Delta = 6$ the web was observed to begin crushing at approximately $\mu_\Delta = -5.4$. At this point, the test was stopped immediately and ended after taking the column back to zero load.

6.4.1 First Cracking and First Yielding ($1/4F_y - \mu_\Delta = 1$)

Shear cracks were first observed to form at $1/2F_y$, with flexural cracks following immediately thereafter at $-1/2F_y$. By F_y flexure and shear cracks had formed up the entire column height, with the flexural cracks closing completely at zero load.

Figure B.10 shows the east face of Test Unit 3B as it was pushed to the first positive excursion at $\mu_\Delta = 1$. Cracks in the column were difficult to see at this level and consequently do not appear clearly in the figure.

6.4.2 Initial Spread of Plasticity ($\mu_\Delta = 2.0 - 3.0$)

Figure B.11 shows the same view of the test unit at the first positive excursion to $\mu_\Delta = 2$. Figure B.12 shows a vertical splitting crack on the east face of the compression (south) boundary element at this level. Figure B.13 shows the same east view of the south boundary element in tension after the first positive excursion to $\mu_\Delta = 4$.

Figure B.14 shows the test unit west face at the first positive excursion to $\mu_\Delta = 3$. Four 1.2 in. [30 mm] concrete gages are visible on the south side of the wall in this figure. These gages were applied after completing all cycles at $\mu_\Delta = 2$ to three of the compression struts expected to crush at a higher level of displacement ductility. Figure B.14 shows the paint in this critical region still to be relatively intact, compared with Test Units 3A and 3C at the same level of displacement ductility. Furthermore, several cracks were observed to penetrate 3 - 6 in. [76 - 152] from the wall into the compression boundary element.

6.4.3 Further Spread of Plasticity and Web Crushing Failure ($\mu_\Delta = 4.0 - 6.0$)

Figure B.15 shows the test unit west face at the first positive excursion to $\mu_\Delta = 4$. At this level, very little flaking of the paint on the wall was observed, and there was no indication

that the concrete in the critical region was close to giving way. The test unit survived two full cycles at $\mu_\Delta = 4$, and was then taken directly to $\mu_\Delta = 6$ (see Figure B.16), because it appeared that if a web crushing failure were to occur, it would occur very close to flexural failure of the column.

The test unit failed on the first negative excursion to $\mu_\Delta = 6$ at a displacement ductility level of approximately $\mu_\Delta = 5.4$ (see Figure B.17). Critical compression struts were first observed to crush in the wall next to the compression (south) boundary element between heights of 7 - 19 in. [178 - 483] above the footing. Figure B.18 shows that three struts hit the boundary element in this region, however only the top and bottom struts showed serious signs of crushing. Their crushing initiated as several splitting cracks formed parallel to the compression struts. After these initial two struts began to crush, the struts just above them began to slide downward along the interface between the compression boundary element and the wall, creating a vertical failure plane up to a height of roughly 43 in. [1092] above the footing. Loading was halted as soon as the first struts were observed to crush, but under a constant displacement at this level, the sliding failure occurred in the higher struts until the load dropped by roughly 20%. At this point, the test unit was brought back to zero load and the test was ended.

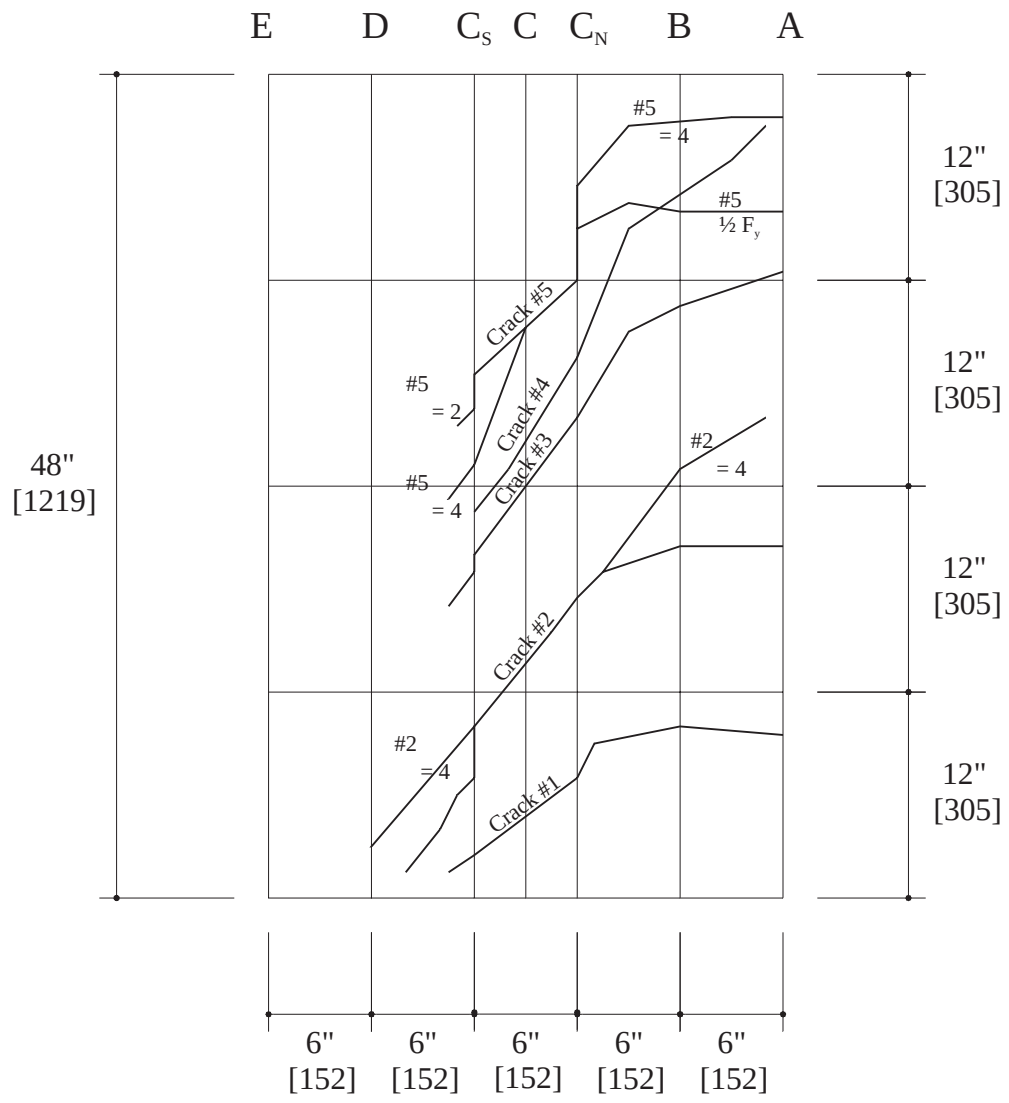

Figure 6.2: Test Unit 3B, Cracks 1 - 5.

	Load	C_s	C	C_s	B	A
Crack #5	1/4 Fy					
	Zero Load					
	1/2 Fy	< 0.002	< 0.002	< 0.002		
	Zero Load	0.000	0.000	0.000		
	Fy	0.004	0.004	0.004	0.002	0.002
	Zero Load	< 0.002	< 0.002	< 0.002	0.000	0.000
Crack #4	1/4 Fy					
	Zero Load					
	1/2 Fy					
	Zero Load					
	Fy					
	Zero Load					
Crack #3	1/4 Fy					
	Zero Load					
	1/2 Fy					
	Zero Load					
	Fy	0.004	0.004	0.004	0.002	0.002
	Zero Load	< 0.002	< 0.002	< 0.002	0.000	0.000
Crack #2	1/4 Fy					
	Zero Load					
	1/2 Fy	< 0.002	< 0.002	< 0.002		
	Zero Load	0.000	0.000	0.000		
	Fy	0.004	0.004	0.004	0.004	0.004
	Zero Load	< 0.002	< 0.002	< 0.002	0.000	0.000
Crack #1	1/4 Fy					
	Zero Load					
	1/2 Fy					
	Zero Load					
	Fy					
	Zero Load					

Table 6.5: Test Unit 3B crack widths at load levels up to F_y (in.).

	Load	C_S	C	C_N	B	A
Crack #5	1/4 Fy					
	Zero Load					
	1/2 Fy	<0.05	< 0.05	< 0.05		
	Zero Load	0.00	0.00	0.00		
	Fy	0.10	0.10	0.10	0.05	0.05
	Zero Load	< 0.05	< 0.05	< 0.05	0.00	0.00
Crack #4	1/4 Fy					
	Zero Load					
	1/2 Fy					
	Zero Load					
	Fy					
	Zero Load					
Crack #3	1/4 Fy					
	Zero Load					
	1/2 Fy					
	Zero Load					
	Fy	0.10	0.10	0.10	0.05	0.05
	Zero Load	< 0.05	< 0.05	< 0.05	0.00	0.00
Crack #2	1/4 Fy					
	Zero Load					
	1/2 Fy	< 0.05	< 0.05	< 0.05		
	Zero Load	0.00	0.00	0.00		
	Fy	0.10	0.10	0.10	0.10	0.10
	Zero Load	< 0.05	< 0.05	< 0.05	0.00	0.00
Crack #1	1/4 Fy					
	Zero Load					
	1/2 Fy					
	Zero Load					
	Fy					
	Zero Load					

Table 6.6: Test Unit 3B crack widths at load levels up to F_y [mm].

	μ_Δ	C_s	C	C_N	B	A
Crack #5	1	0.006	0.006	0.008	0.002	0.002
	Zero Load	< 0.002	< 0.002	< 0.002	0.000	0.000
	2	0.006	0.010	0.010	0.004	0.004
	Zero Load	< 0.002	0.002	0.002	0.000	0.000
	3	0.002	0.016	0.012	0.002	0.004
	Zero Load	0.000	0.004	0.002	0.000	0.000
	4	0.002	0.024	0.014	0.004	0.004
	Zero Load	0.004	0.010	0.004	0.000	0.000
	6	0.016	0.031	0.016	0.004	0.006
	Zero Load	0.008	0.008	0.008	0.000	0.000
Crack #4	1					
	Zero Load					
	2		0.004	0.008	0.004	
	Zero Load		< 0.002	< 0.002	0.000	
	3	0.002	0.010	0.012	0.006	
	Zero Load	0.000	0.004	0.002	0.000	
	4	0.002	0.020	0.010	0.008	
	Zero Load	0.000	0.008	0.002	0.000	
	6	0.012	0.031	0.016	0.008	
	Zero Load	0.006	0.020	0.004	0.002	
Crack #3	1	0.004	0.010	0.006	0.004	0.004
	Zero Load	< 0.002	< 0.002	< 0.002	0.000	0.000
	2	0.008	0.010	0.008	0.004	0.004
	Zero Load	0.002	0.002	0.002	0.000	0.000
	3	0.012	0.012	0.010	0.006	0.004
	Zero Load	0.004	0.006	0.004	0.000	0.000
	4	0.010	0.020	0.012	0.010	0.006
	Zero Load	0.004	0.012	0.004	0.000	0.000
	6	0.016	0.031	0.016	0.008	0.004
	Zero Load	0.010	0.020	0.006	0.002	0.000
Crack #2	1	0.008	0.008	0.008	0.004	0.004
	Zero Load	< 0.002	< 0.002	< 0.002	0.000	0.000
	2	0.010	0.012	0.010	0.004	0.006
	Zero Load	0.002	0.004	0.002	0.000	0.000
	3	0.016	0.016	0.012	0.014	0.020
	Zero Load	0.006	0.004	0.002	0.004	0.006
	4	0.024	0.024	0.024	0.031	0.031
	Zero Load	0.008	0.012	0.008	0.020	0.020
	6	0.039	0.039	0.039	0.039	0.039
	Zero Load	0.031	0.031	0.024	0.031	0.031
Crack #1	1	0.002	0.002	0.004	0.004	0.004
	Zero Load	< 0.002	< 0.002	< 0.002	0.000	0.000
	2	0.004	0.008	0.016	0.020	0.020
	Zero Load	0.004	0.004	0.006	0.008	0.012
	3	0.016	0.031	0.039	0.035	0.024
	Zero Load	0.010	0.016	0.020	0.024	0.016
	4	0.024	0.031	0.039	0.049	0.035
	Zero Load	0.016	0.012	0.020	0.039	0.024
	6	0.039	0.039	0.049	0.049	0.059
	Zero Load	0.031	0.024	0.039	0.039	0.049

Table 6.7: Test Unit 3B crack widths at varying levels of μ_Δ (in.).

	μ_Δ	C_s	C	C_N	B	A
Crack #5	1	0.15	0.15	0.20	0.05	0.05
	Zero Load	< 0.05	< 0.05	< 0.05	0.00	0.00
	2	0.15	0.25	0.25	0.10	0.10
	Zero Load	< 0.05	0.05	0.05	0.00	0.00
	3	0.05	0.40	0.30	0.05	0.10
	Zero Load	0.00	0.10	0.05	0.00	0.00
	4	0.05	0.60	0.35	0.10	0.10
	Zero Load	0.10	0.25	0.10	0.00	0.00
	6	0.40	0.80	0.40	0.10	0.15
	Zero Load	0.20	0.20	0.20	0.00	0.00
Crack #4	1					
	Zero Load					
	2		0.10	0.20	0.10	
	Zero Load		< 0.05	< 0.05	0.00	
	3	0.05	0.25	0.30	0.15	
	Zero Load	0.00	0.10	0.05	0.00	
	4	0.05	0.50	0.25	0.20	
	Zero Load	0.00	0.20	0.05	0.00	
	6	0.30	0.80	0.40	0.20	
	Zero Load	0.15	0.50	0.10	0.05	
Crack #3	1	0.10	0.25	0.15	0.10	0.10
	Zero Load	< 0.05	< 0.05	< 0.05	0.00	0.00
	2	0.20	0.25	0.20	0.10	0.10
	Zero Load	0.05	0.05	0.05	0.00	0.00
	3	0.30	0.30	0.25	0.15	0.10
	Zero Load	0.10	0.15	0.10	0.00	0.00
	4	0.25	0.50	0.30	0.25	0.15
	Zero Load	0.10	0.30	0.10	0.00	0.00
	6	0.40	0.80	0.40	0.20	0.10
	Zero Load	0.25	0.50	0.15	0.05	0.00
Crack #2	1	0.20	0.20	0.20	0.10	0.10
	Zero Load	< 0.05	< 0.05	< 0.05	0.00	0.00
	2	0.25	0.30	0.25	0.10	0.15
	Zero Load	0.05	0.10	0.05	0.00	0.00
	3	0.40	0.40	0.30	0.35	0.50
	Zero Load	0.15	0.10	0.05	0.10	0.15
	4	0.60	0.60	0.60	0.80	0.80
	Zero Load	0.20	0.30	0.20	0.50	0.50
	6	1.00	1.00	1.00	1.00	1.00
	Zero Load	0.80	0.80	0.60	0.80	0.80
Crack #1	1	0.05	0.05	0.10	0.10	0.10
	Zero Load	< 0.05	< 0.05	< 0.05	0.00	0.00
	2	0.10	0.20	0.40	0.50	0.50
	Zero Load	0.10	0.10	0.15	0.20	0.30
	3	0.40	0.80	1.00	0.90	0.60
	Zero Load	0.25	0.40	0.50	0.60	0.40
	4	0.60	0.80	1.00	1.25	0.90
	Zero Load	0.40	0.30	0.50	1.00	0.60
	6	1.00	1.00	1.25	1.25	1.50
	Zero Load	0.80	0.60	1.00	1.00	1.25

Table 6.8: Test Unit 3B crack widths at varying levels of μ_Δ [mm].

6.5 Test Unit 3C

The test unit performed in a ductile manner up to $\mu_\Delta = 4$, whereupon it withstood two positive excursions and one negative excursion to this level, finally failing in web crushing close the the peak of the second negative excursion.

6.5.1 First Cracking and First Yielding ($1/4F_y - \mu_\Delta = 1$)

Shear cracks first appeared in the wall at $1/4F_y$. These cracks did not extend through the tension boundary element as flexural cracks until $3/4F_y$. At F_y, hairline vertical splitting cracks with an average width of 0.002 in. [0.05 mm] became visible at the base of the compression boundary element.

Figure B.19 shows the east face of Test Unit 3C as it was pushed to the first positive excursion at $\mu_\Delta = 1$. Cracks in the column were difficult to see at this level and consequently do not appear clearly in the figure.

6.5.2 Spalling and Initial Spread of Plasticity ($\mu_\Delta = 2.0 - 3.0$)

Figure B.20 shows the same view of the test unit at the first positive excursion to $\mu_\Delta = 2$. Figure B.21 shows a vertical splitting crack on the west face of the compression (south) boundary element at this level, having grown from its previously innocuous size at F_y. Figure B.22 shows the same west view of the south boundary element in tension after the first negative excursion to $\mu_\Delta = 3$. At this level the architectural concrete covering the pictured region was lifted off by hand in one piece. During the entire test, this was the only significant chunk of architectural concrete to come off the column. The rest of the south boundary element and the entire north boundary element remained relatively intact by comparison. When architectural concrete did come off, it was typically when the boundary element went into tension after a compression cycle with substantial vertical splitting. The vertical splitting cracks and the horizontal flexural cracks formed a cracked grid on the boundary elements, out of which large pieces could fall. Many pieces stayed connected to the core concrete simply by the tiewire that had held the spirals and the longitudinal bars together during construction.

Figure B.23 shows the test unit west face at the first positive excursion to $\mu_\Delta = 3$. Nine 1.2

in. [30 mm] concrete gages are visible on the south side of the wall in this figure. These gages were applied after completing all cycles at $\mu_\Delta = 2$ to the three compression struts expected to crush at a higher level of displacement ductility. In Figure B.23, much of the paint in this critical region can be seen to have flaked off, indicating increasingly high compression strains in the concrete at this displacement level. Furthermore, the cracks at the column base were observed to converge roughly 3 in. [76] above the footing at the compression boundary element, indicating that the neutral axis had moved into the compression boundary element.

6.5.3 Further Spread of Plasticity and Web Crushing Failure ($\mu_\Delta = 4.0 - 5.0$)

Figure B.24 shows the test unit west face at the first positive excursion to $\mu_\Delta = 4$. At this level, more flaking of the paint on the wall was observed, however there was no indication that the concrete in this region was beginning to give way. The test unit survived two positive excursions and one negative excursion to $\mu_\Delta = 4$, before failing by web crushing near the peak of the second negative excursion at a load of -199 kips [-886 kN] and a displacement of -4.4 in. [-112] . The failure is shown in Figures B.25 and B.26, where it is evident that both a horizontal and a vertical failure plane developed. The first strut to give way hit the compression boundary element between roughly 8 - 10 in. [203 -254] above the footing. The crushing of this strut set in action a domino effect on several higher struts, and a vertical failure plane was observed to propagate up the column to a height of roughly 27 in. [686]. Simultaneously, an almost horizontal sliding plane was observed to develop across the entire wall. At the compression boundary element, this plane developed just under the first strut to crush. It angled slightly upward into the wall and met the tension boundary element at a height of roughly 18 in. [457] above the footing.

After the initial crushing, the wall degraded and diminished in strength rapidly. Large diamond-shaped chunks of concrete fell out of the unconfined wall as the test unit was pushed further. After cycling to the second negative peak at $\mu_\Delta = 4$, the test unit was cycled for a single positive excursion to $\mu_\Delta = 5$. At the previous peak, and during this last excursion, the test unit continued to degrade, until it began to look and behave more like a frame than a wall, with the boundary elements acting as two columns. Figure B.27 shows that by the peak displacement at $\mu_\Delta = 5$, the vertical failure planes on both sides of the wall had reached a 60 in. [1524] height above the footing. The bottom of the horizontal sliding plane stayed

at 12 in. [305] above the footing, and all three failure planes reached widths of 6 - 12 in. [152 - 305], wherein vertical and transverse reinforcing bars became exposed and were observed to buckle significantly. By the end of the test, as Figure B.27 shows, enough concrete had fallen out to allow a clear view through the wall in several places.

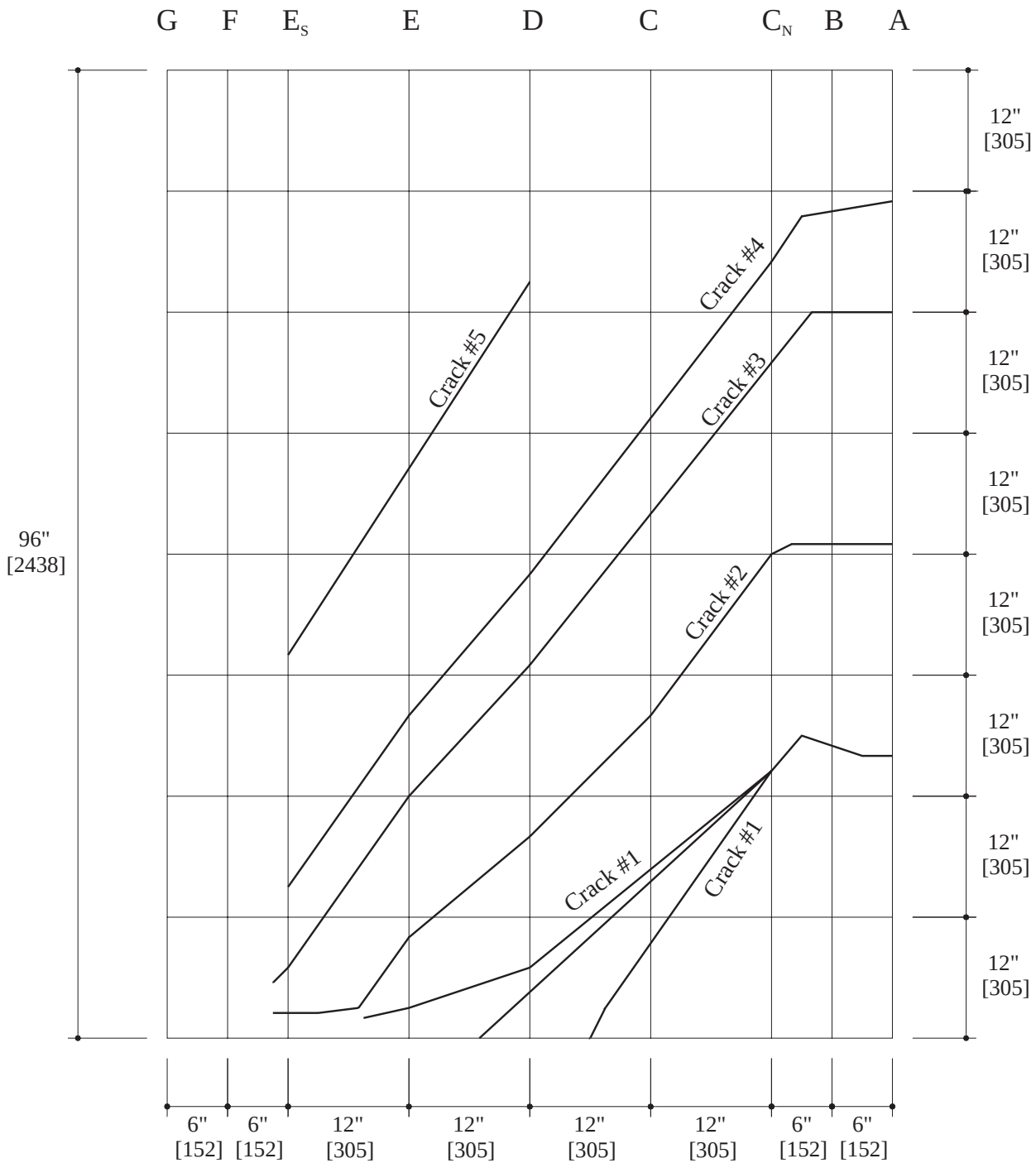

Figure 6.3: Test Unit 3C, Cracks 1 - 5.

	Load	E_s	E	D	C	C_N	B	A
Crack #5	1/4 Fy							
	Zero Load							
	1/2 Fy							
	Zero Load							
	Fy							
	Zero Load							
Crack #4	1/4 Fy							
	Zero Load							
	1/2 Fy							
	Zero Load							
	Fy		0.004	0.008	0.012	0.004	< 0.002	< 0.002
	Zero Load		< 0.002	< 0.002	0.002	< 0.002	0.000	0.000
Crack #3	1/4 Fy							
	Zero Load							
	1/2 Fy				< 0.002	0.002		
	Zero Load				< 0.002	< 0.002		
	Fy	< 0.002	0.006	0.008	0.008	0.004	< 0.002	
	Zero Load	0.000	< 0.002	< 0.002	0.002	0.002	0.000	
Crack #2	1/4 Fy							
	Zero Load							
	1/2 Fy			< 0.002	0.004	0.002		
	Zero Load			< 0.002	< 0.002	< 0.002		
	Fy		< 0.002	0.006	0.010	0.004	< 0.002	0.004
	Zero Load		0.000	0.000	0.002	< 0.002	0.000	0.000
Crack #1	1/4 Fy				0.002	0.002		
	Zero Load				< 0.002	< 0.002		
	1/2 Fy				0.004	0.004		
	Zero Load				0.002	< 0.002		
	Fy				0.008	0.008	< 0.002	0.004
	Zero Load				0.002	< 0.002	0.000	0.000

Table 6.9: Test Unit 3C crack widths at load levels up to F_y (in.).

	Load	E_S	E	D	C	C_N	B	A
Crack #5	1/4 Fy							
	Zero Load							
	1/2 Fy							
	Zero Load							
	Fy							
	Zero Load							
Crack #4	1/4 Fy							
	Zero Load							
	1/2 Fy							
	Zero Load							
	Fy		0.10	0.20	0.30	0.10	< 0.05	< 0.05
	Zero Load		< 0.05	< 0.05	0.05	< 0.05	0.00	0.00
Crack #3	1/4 Fy							
	Zero Load							
	1/2 Fy				< 0.05	0.05		
	Zero Load				< 0.05	< 0.05		
	Fy	< 0.05	0.15	0.20	0.20	0.10	< 0.05	
	Zero Load	0.00	< 0.05	< 0.05	0.05	0.05	0.00	
Crack #2	1/4 Fy							
	Zero Load							
	1/2 Fy			< 0.05	0.10	0.05		
	Zero Load			< 0.05	< 0.05	< 0.05		
	Fy		< 0.05	0.15	0.25	0.10	< 0.05	0.10
	Zero Load		0.00	0.00	0.05	< 0.05	0.00	0.00
Crack #1	1/4 Fy				0.05	0.05		
	Zero Load				< 0.05	< 0.05		
	1/2 Fy				0.10	0.10		
	Zero Load				0.05	< 0.05		
	Fy				0.20	0.20	< 0.05	0.10
	Zero Load				0.05	< 0.05	0.00	0.00

Table 6.10: Test Unit 3C crack widths at load levels up to F_y [mm].

	μ_Δ	E_s	E	D	C	C_N	B	A
Crack #5	1							
	Zero Load							
	2	0.002	0.008	0.010				
	Zero Load	0.002	0.002	0.002				
	3	0.004	0.008	0.012				
	Zero Load	0.002	0.002	0.002				
	4	0.002	0.012	0.010				
	Zero Load	0.002	0.002	0.002				
Crack #4	1	< 0.002	0.006	0.010	0.014	0.008	0.002	0.004
	Zero Load	< 0.002	0.002	0.002	0.002	< 0.002	0.000	0.000
	2	0.004	0.012	0.016	0.014	0.004	0.004	0.006
	Zero Load	0.002	0.002	0.002	0.002	0.000	0.000	0.000
	3	0.002	0.016	0.020	0.016	0.008	0.004	0.008
	Zero Load	0.002	0.006	0.002	0.002	< 0.002	0.000	0.000
	4	0.002	0.016	0.020	0.014	0.010	0.004	0.004
	Zero Load	0.004	0.006	0.010	0.002	0.000	0.000	0.000
Crack #3	1	0.002	0.008	0.012	0.012	0.008	0.004	0.006
	Zero Load	< 0.002	0.002	0.002	0.002	0.002	0.000	0.000
	2	0.006	0.014	0.016	0.012	0.008	0.006	0.006
	Zero Load	0.002	0.004	0.004	0.002	0.002	0.000	0.000
	3	0.012	0.020	0.020	0.016	0.008	0.004	0.006
	Zero Load	0.004	0.008	0.004	0.002	0.002	0.000	0.000
	4	0.008	0.024	0.031	0.024	0.010	0.006	0.008
	Zero Load	0.000	0.008	0.012	0.010	0.002	0.000	0.000
Crack #2	1		0.004	0.004	0.014	0.006	0.004	0.004
	Zero Load		< 0.002	< 0.002	0.002	0.002	0.000	0.000
	2	< 0.002	0.012	0.016	0.016	0.012	0.006	0.004
	Zero Load	0.000	0.008	0.004	0.004	0.002	0.000	0.000
	3	0.002	0.031	0.039	0.049	0.031	0.031	0.031
	Zero Load	0.002	0.016	0.016	0.024	0.014	0.031	0.020
	4	0.002	0.031	0.039	0.059	0.039	0.031	0.020
	Zero Load	0.000	0.020	0.035	0.035	0.020	0.024	0.024
Crack #1	1			0.002	0.008	0.012	0.004	0.004
	Zero Load			0.000	< 0.002	0.002	0.000	0.000
	2		0.016	0.024	0.024	0.031	0.024	0.031
	Zero Load		0.012	0.016	0.016	0.020	0.016	0.016
	3		0.020	0.039	0.049	0.049	0.035	0.049
	Zero Load		0.012	0.031	0.031	0.039	0.031	0.031
	4	0.020	0.020	0.049	0.059	0.059	0.039	0.059
	Zero Load	0.000	0.012	0.039	0.039	0.039	0.024	0.049

Table 6.11: Test Unit 3C crack widths at varying levels of μ_Δ (in.).

	μ_Δ	E_S	E	D	C	C_N	B	A
Crack #5	1							
	Zero Load							
	2	0.05	0.20	0.25				
	Zero Load	0.05	0.05	0.05				
	3	0.10	0.20	0.30				
	Zero Load	0.05	0.05	0.05				
	4	0.05	0.30	0.25				
	Zero Load	0.05	0.05	0.05				
Crack #4	1	< 0.05	0.15	0.25	0.35	0.20	0.05	0.10
	Zero Load	< 0.05	0.05	0.05	0.05	< 0.05	0.00	0.00
	2	0.10	0.30	0.40	0.35	0.10	0.10	0.15
	Zero Load	0.05	0.05	0.05	0.05	0.00	0.00	0.00
	3	0.05	0.40	0.50	0.40	0.20	0.10	0.20
	Zero Load	0.05	0.15	0.05	0.05	< 0.05	0.00	0.00
	4	0.05	0.40	0.50	0.35	0.25	0.10	0.10
	Zero Load	0.10	0.15	0.25	0.05	0.00	0.00	0.00
Crack #3	1	0.05	0.20	0.30	0.30	0.20	0.10	0.15
	Zero Load	< 0.05	0.05	0.05	0.05	0.05	0.00	0.00
	2	0.15	0.35	0.40	0.30	0.20	0.15	0.15
	Zero Load	0.05	0.10	0.10	0.05	0.05	0.00	0.00
	3	0.30	0.50	0.50	0.40	0.20	0.10	0.15
	Zero Load	0.10	0.20	0.10	0.05	0.05	0.00	0.00
	4	0.20	0.60	0.80	0.60	0.25	0.15	0.20
	Zero Load	0.00	0.20	0.30	0.25	0.05	0.00	0.00
Crack #2	1		0.10	0.10	0.35	0.15	0.10	0.10
	Zero Load		< 0.05	< 0.05	0.05	0.05	0.00	0.00
	2	< 0.05	0.30	0.40	0.40	0.30	0.15	0.10
	Zero Load	0.00	0.20	0.10	0.10	0.05	0.00	0.00
	3	0.05	0.80	1.00	1.25	0.80	0.80	0.80
	Zero Load	0.05	0.40	0.40	0.60	0.35	0.80	0.50
	4	0.05	0.80	1.00	1.50	1.00	0.80	0.50
	Zero Load	0.00	0.50	0.90	0.90	0.50	0.60	0.60
Crack #1	1			0.05	0.20	0.30	0.10	0.10
	Zero Load			0.00	< 0.05	0.05	0.00	0.00
	2		0.40	0.60	0.60	0.80	0.60	0.80
	Zero Load		0.30	0.40	0.40	0.50	0.40	0.40
	3		0.50	1.00	1.25	1.25	0.90	1.25
	Zero Load		0.30	0.80	0.80	1.00	0.80	0.80
	4	0.50	0.50	1.25	1.50	1.50	1.00	1.50
	Zero Load	0.00	0.30	1.00	1.00	1.00	0.60	1.25

Table 6.12: Test Unit 3C crack widths at varying levels of μ_Δ [mm].

Chapter 7

Discussion of Test Results

7.1 Overview

Results are presented as if looking at the test unit west faces, occasionally referring to figures in Appendix C. The west face perspective of the test results contrasts with the east face perspective of the test observations presented in Chapter 6, however it is consistent with the instrumentation drawings in Chapter 4 and with the notion that positive displacement values are plotted on the right hand side of a graph. Test unit hysteretic behavior is evaluated in terms of overall load-deflection response and independent flexural and shear displacements. Shear performance is explored based on transverse bar strains, spiral strains and the slippage of the transverse bars.

7.2 Test Unit 3A

7.2.1 Hysteretic Behavior

Test Unit 3A performed in a ductile manner up through two cycles at $\mu_\Delta = 4$ until it failed on the first positive excursion to $\mu_\Delta = 5$ (see Figure 7.1). The test unit reached a maximum displacement ductility of $\mu_\Delta = 4.4$ before failing in web crushing. The column failed by crushing of the critical compression struts inside the plastic hinge region and subsequent vertical slippage of the compression struts against the compression boundary element immediately above the critical struts.

Until failure, the test unit exibited stable hysteretic behavior with minimal pinching. The test unit's flexibility in shear contributed significantly to its overall initial flexibility. After reaching its ideal yield displacement at $\mu_\Delta = 1$, however, the test unit continued to

gain strength up through $\mu_\Delta = 4$ maintaining enough shear stiffness to develop some strain hardening in the longitudinal reinforcement. Figure 5.7 compares the test results with the predictions given in Chapter 5.

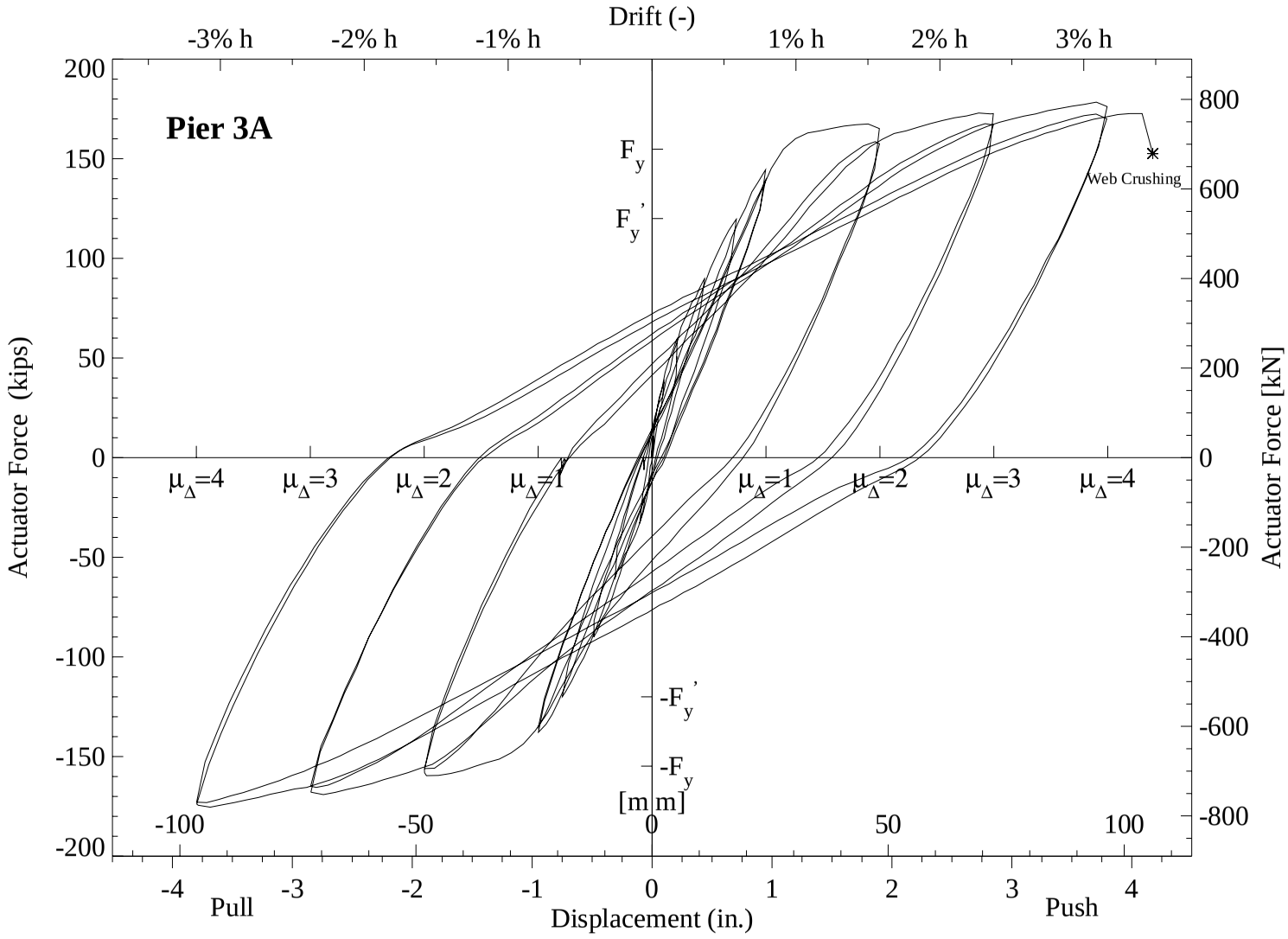

Figure 7.1: Test Unit 3A, measured experimental hysteretic response.

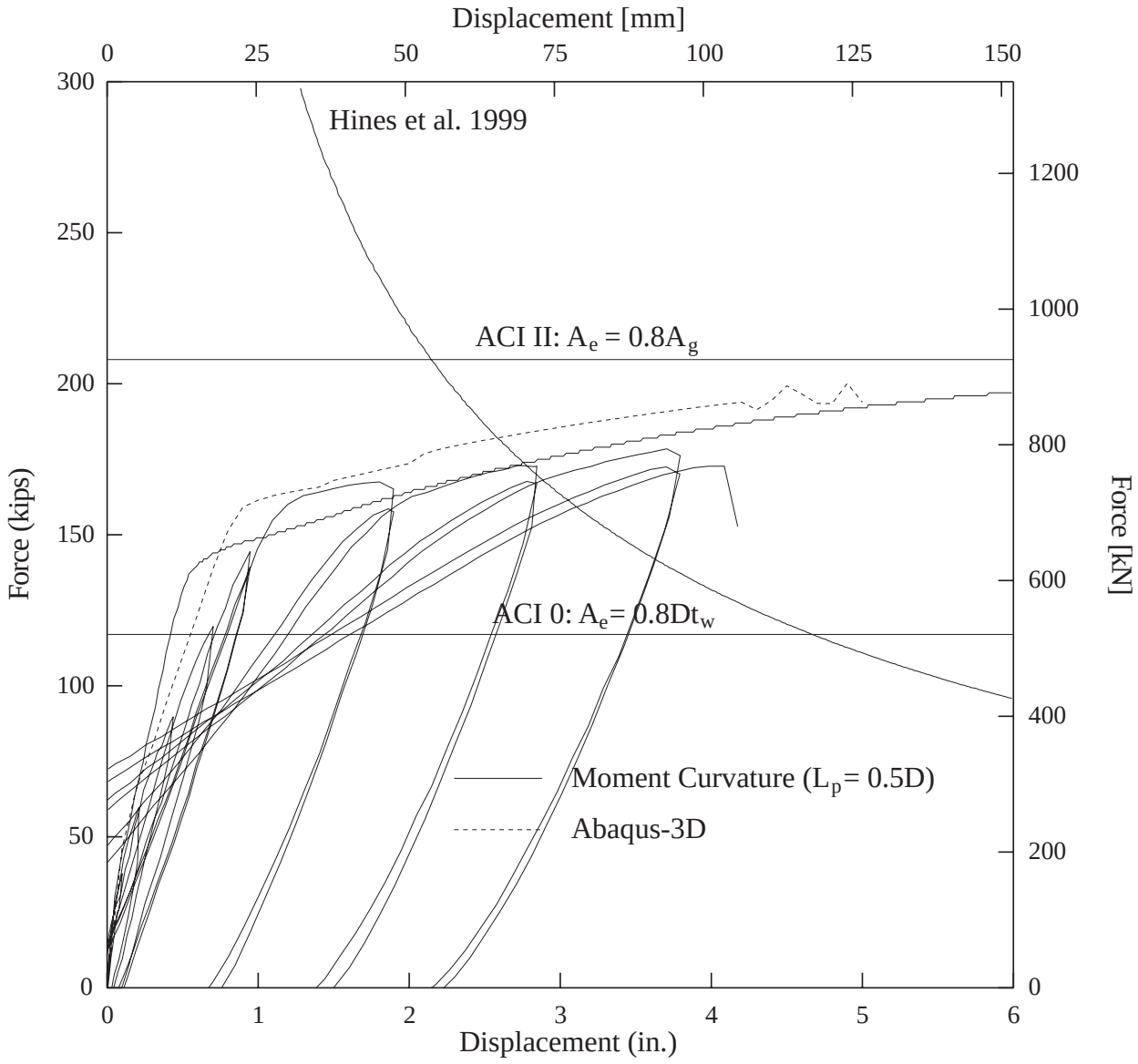

Figure 7.2: Test Unit 3A, force-deflection predictions with web crushing capacity envelopes and test results.

7.2.2 Flexural and Shear Displacements

Figures 7.3 and 7.4 give the flexural and shear hysteretic behavior of Test Unit 3A as calculated from the curvature and shear instrumentation discussed in Chapter 4. Figures 7.5 and 7.7 give favorable comparisons between the flexural + shear hysteretic response and the measured hysteretic response of the column, implying that the flexure and shear displacement values calculated from test data were reasonably accurate.

The clear difference between the shape of the flexural and shear hysteresis loops underlines the difference between the two mechanisms of deformation. Pinching occurred almost entirely in the shear hysteretic response. This may have been due to sliding along wide-open flexural cracks in the plastic hinge region. Regardless of the difference in shape, it is useful to note that at the peaks, the ratio between shear and flexural displacement remained relatively constant. Figure 7.6 shows this in a plot of shear displacement as a function of flexural displacement, where a straight line corresponding to $_s/\ _f = 0.30$ matches the trend in peak displacements fairly well. Therefore, it might be reasonable to assume shear displacements to be roughly 30% of the flexural displacements when conducting a simple moment-curvature based force-deflection prediction of such a column. This value is one and a half times the value of 20% assumed for the prediction in Chapter 5.

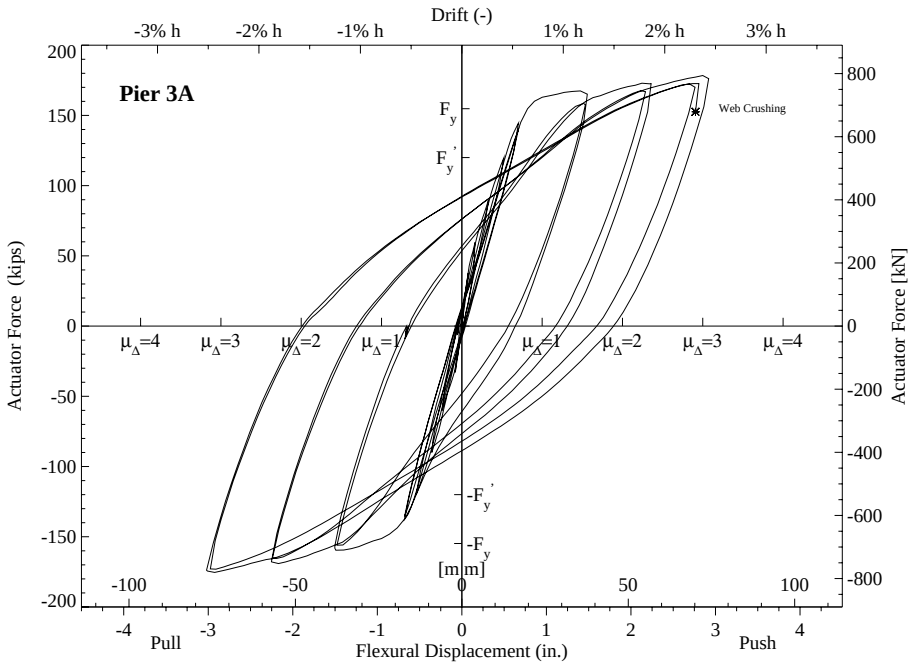

Figure 7.3: Test Unit 3A, calculated experimental flexural hysteretic response.

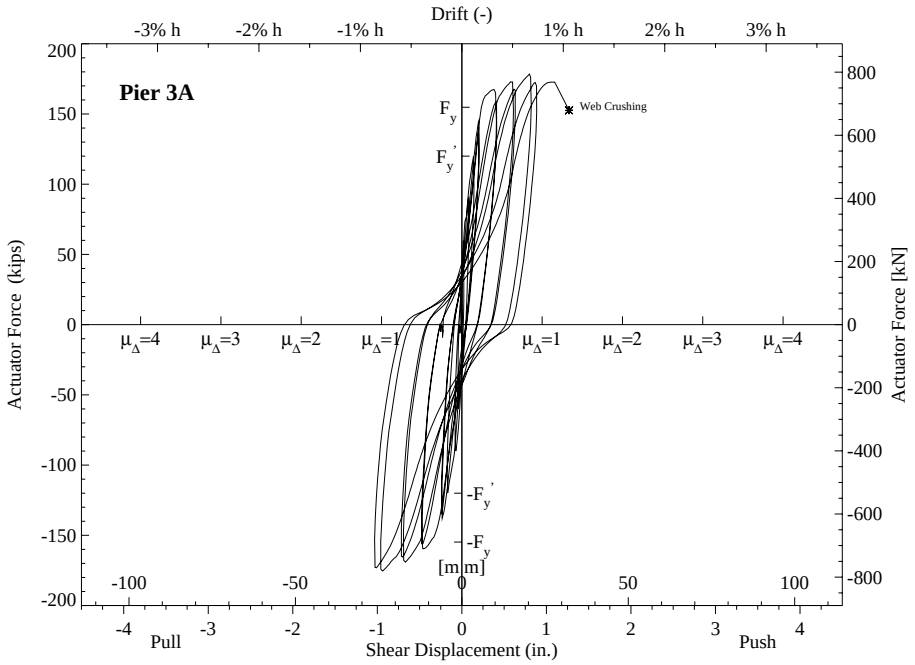

Figure 7.4: Test Unit 3A, calculated experimental shear hysteretic response.

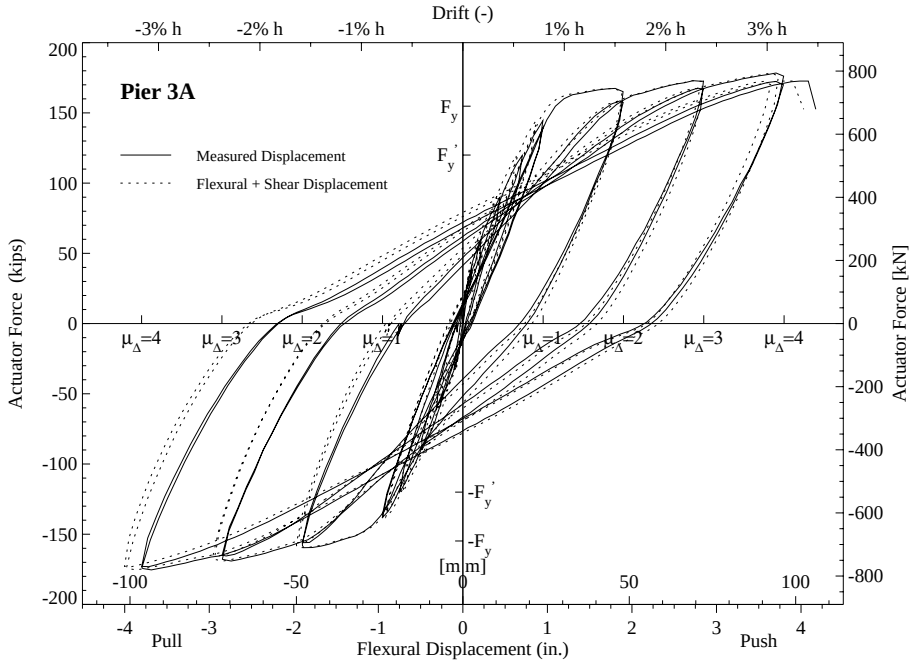

Figure 7.5: Test Unit 3A, calculated experimental flexure + shear hysteretic response compared to the measured hysteretic response.

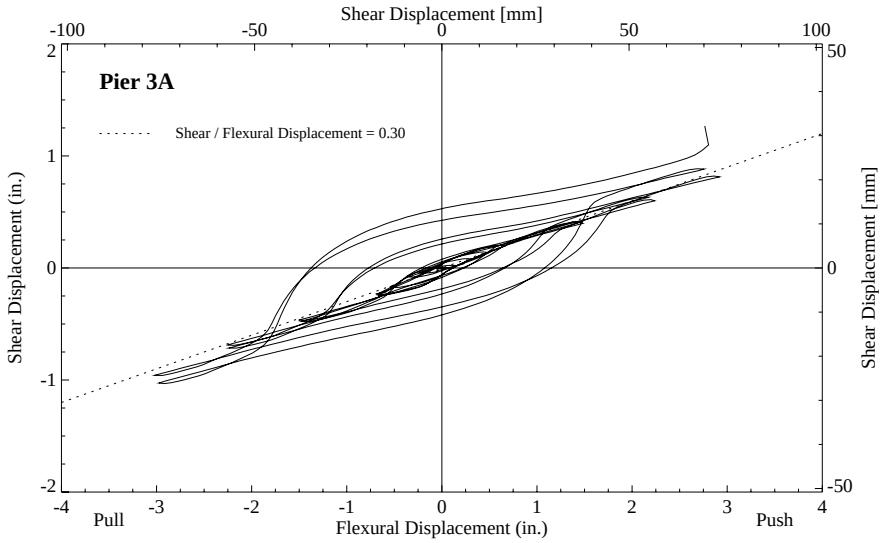

Figure 7.6: Test Unit 3A, shear displacements as a function of the flexural displacements.

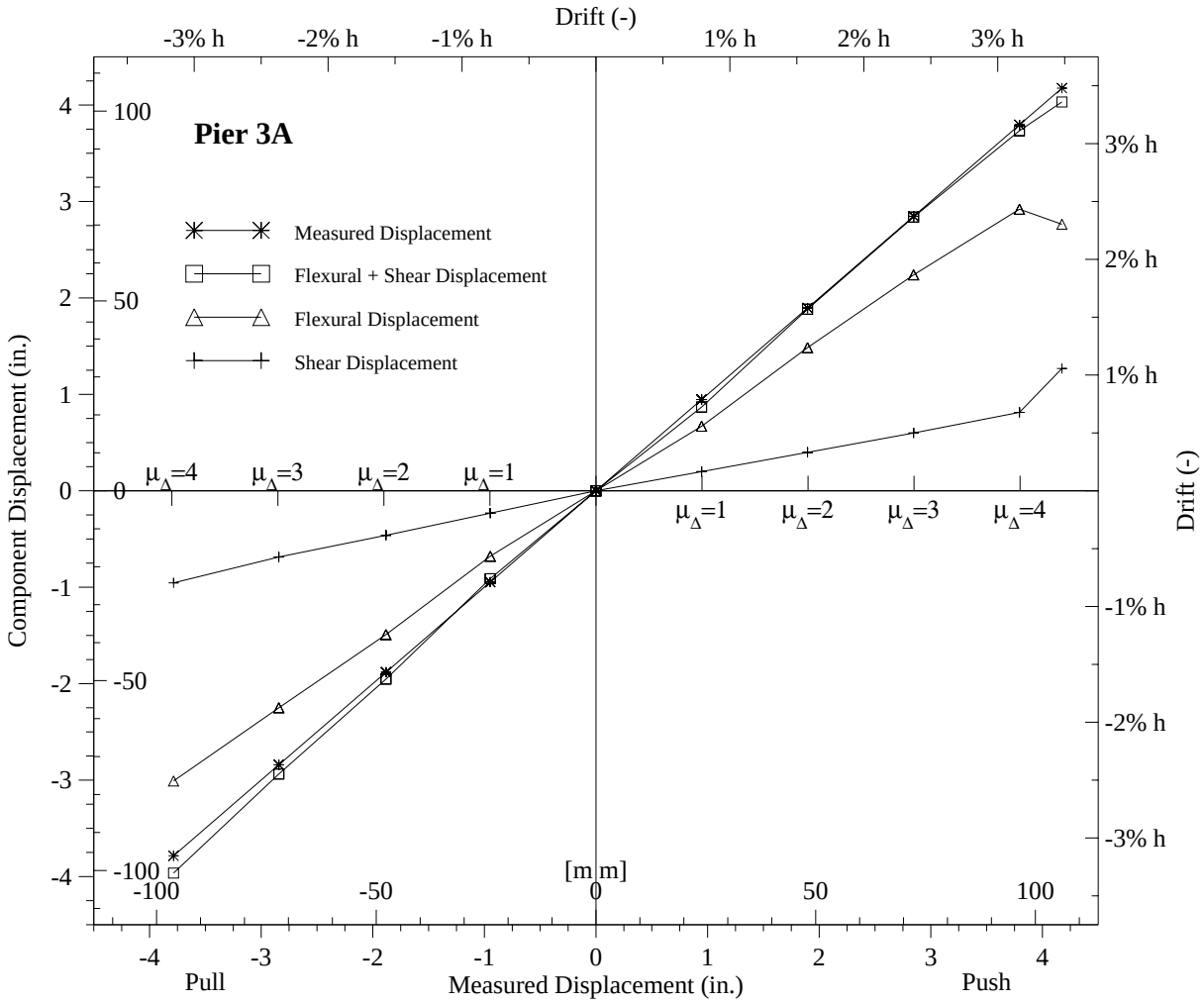

Figure 7.7: Test Unit 3A, calculated and measured experimental displacement peak values.

7.2.3 Performance of the Transverse Reinforcement

Designed according to the method outlined in Chapter 2, the transverse reinforcement remained below yield for most of the test and experienced yield at some locations in the wall ranging from 12 in. [305] to at least 72 in. [1829] above the footing at higher levels of displacement ductility. Figure 7.8 shows strain profiles of six transverse bars spaced on 12 in. [305] vertical intervals from 12 in. [305] to 72 in. [1829] above the footing.

Figure 7.9 compares spiral strains to transverse bar strains at position B inside the north boundary element. Figures C.7 - ?? in Appendix C make the same comparison at other locations in the test unit cross section. The transverse bars generally reached higher strain levels than the spirals, and neither the transverse bars nor the spirals yielded when the boundary element was in tension. As a rough approximation, the transverse bar strains of 1000 $\mu\varepsilon$ - 2000 $\mu\varepsilon$ could be added to the corresponding spiral strains of 250 $\mu\varepsilon$ - 1000 $\mu-\varepsilon$ to reach an equivalent yield strain. This would imply that if the spirals were not included in the V_s component, the transverse bars could be assumed capable of reaching yield, since the size and spacing of the spirals and transverse bars were roughly the same. Since the transverse bars were observed to strain past their yield point in the wall, as shown in Figure 7.8, it is unreasonable to assume that the spirals and the transverse bars would both reach their yield strain in the tension boundary element. The method for computing the V_s component in Chapter 2 was therefore unrealistic, and should be modified to include only the transverse bars. The extra shear capacity should therefore be attributed, not to the transverse bars and spirals, but to a stronger V_c component, resulting from the boundary element confinement effects on the compression toe and dowel action.

Figures 7.10 and 7.11 show the relationship between measured bar slip and measured strain inside of the north boundary element for four bars spaced on 12 in. [305] vertical intervals from 12 in. [305] to 48 in. [1219] above the footing. The north boundary element experienced tension when the column was pushed to positive displacements. For each bar, the slippage was observed to affect directly the ability of the bar to develop its full strain at peak load. The bars at 12 in. [305] and 24 in. [610] in Figure 7.10, for instance, slipped up to 0.08 in. [2] as shown in the left hand plots. The middle plots, show the gages at position B, to hit peak strains at zero displacement and then to decrease with increasing displacement.

The plots on the far right show the direct relationship between the bar slippage at position A and the strain at position B. Both of the plots on the far right, show strain increasing at position B up to a certain point and then decreasing with increasing slippage. Figure 7.11 shows the bars at 36 in. [914] and 48 in. [1219] to have slipped less than the lower bars. The bar at 48 in. [1219], for instance, slipped only 0.004 in. [0.1] and experienced no loss in strain capacity at position B. This can be seen in the middle and right hand top plots. These results suggest that while slippage and subsequent loss of strain capacity was likely to occur in transverse bars located inside the plastic hinge region, where large cracks were highly concentrated, significant slippage resulting in loss of strain capacity was unlikely to occur outside of the plastic region because the boundary element concrete was highly-confined and the flexural cracks are very small. The effect of bar slippage on strain capacity at Position C, just inside the wall, can be seen in Figures C.3 and C.13 to have been present but minimal inside of the plastic hinge region. The effect of bar slippage on strain capacity at Position D, in the middle of the wall, can be seen in Figures C.4 and C.14 to have been practically non-existent inside of the plastic hinge region. Finally, slippage resulting in loss of capacity was only observed to occur at higher levels of displacement ductility and never before development of the longitudinal reinforcement yield strength. This fact supports the idea that slippage only occurred in the presence of well developed, wide flexural cracks.

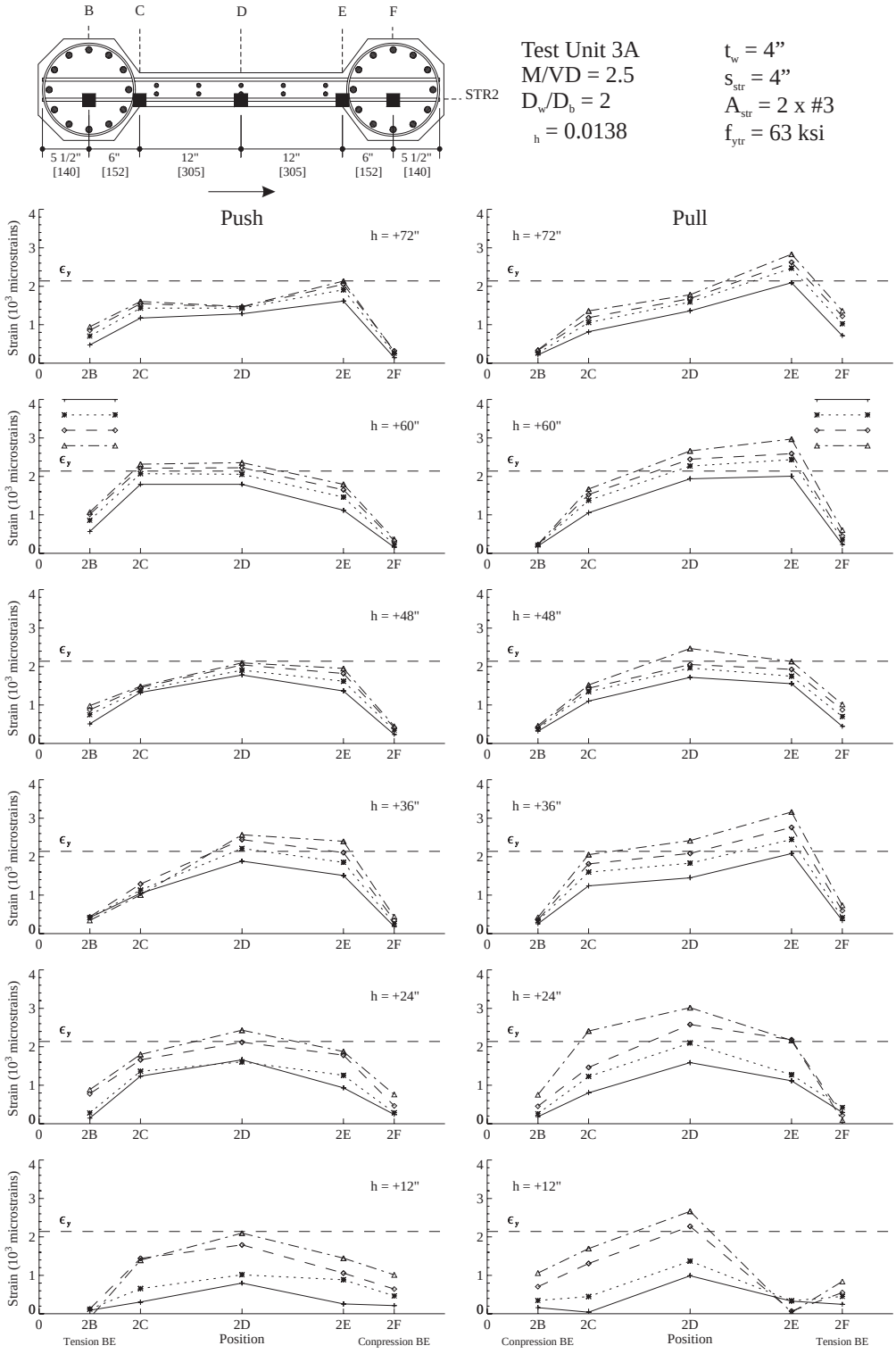

Figure 7.8: Test Unit 3A, transverse bar strain profiles.

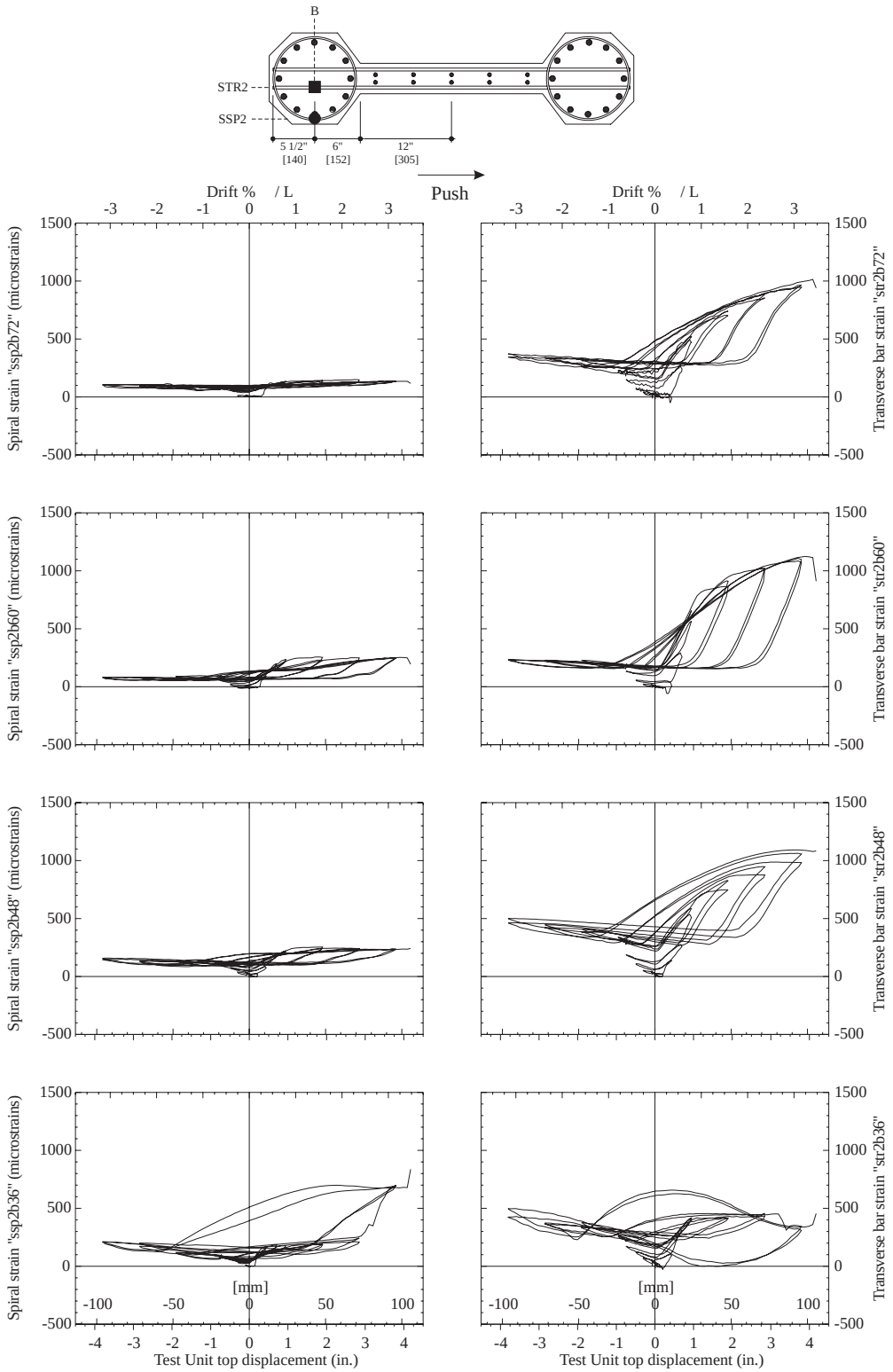

Figure 7.9: Test Unit 3A, spiral strains and transverse bar strains at Position B, for heights 36 in. [914], 48 in. [1219], 60 in. [1524] and 72 in. [1829] above the footing.

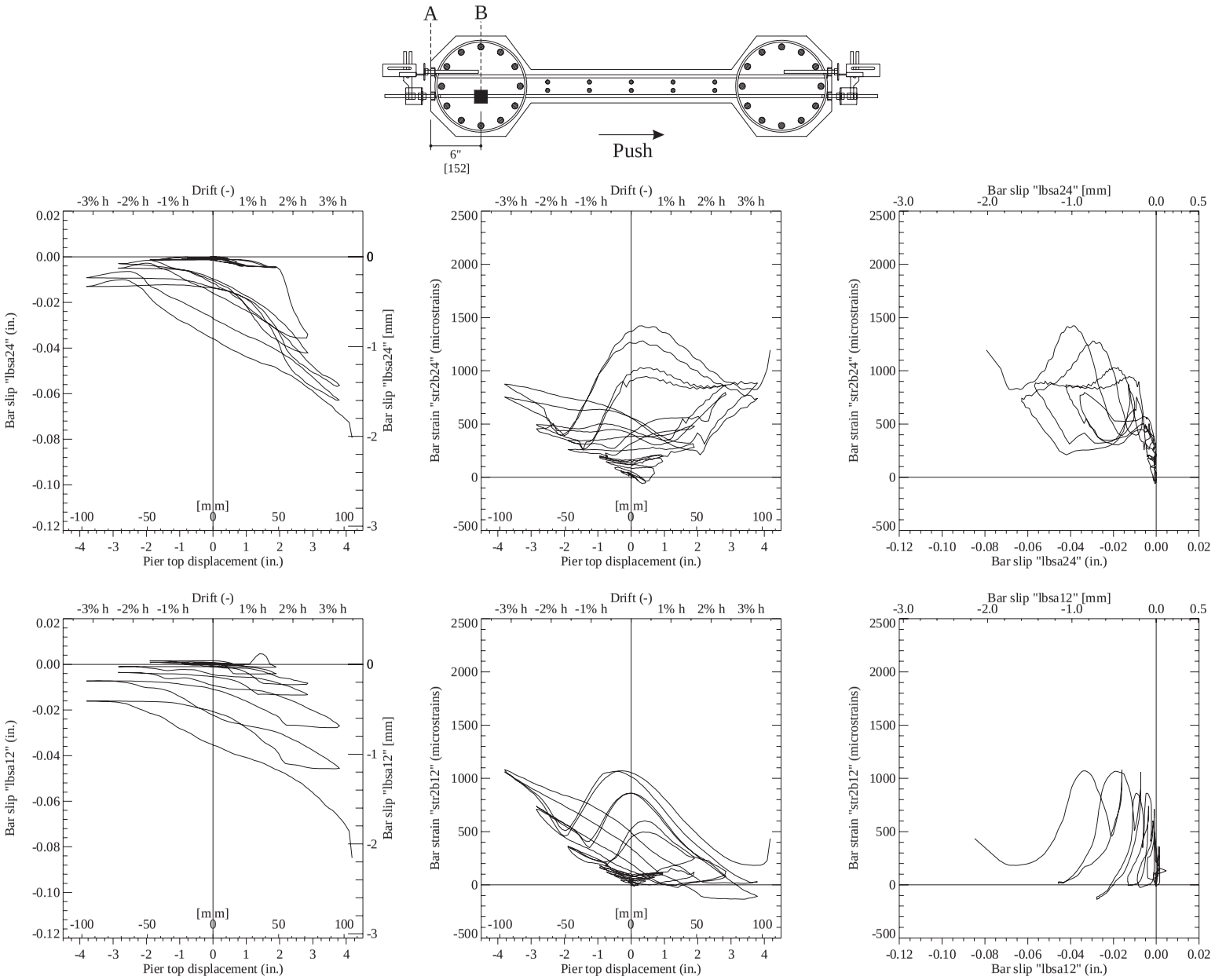

Figure 7.10: Test Unit 3A bar slip and transverse bar strain histories at positions A and B, 12 in. [305] and 24 in. [610] above the footing. Push (positive) direction is south.

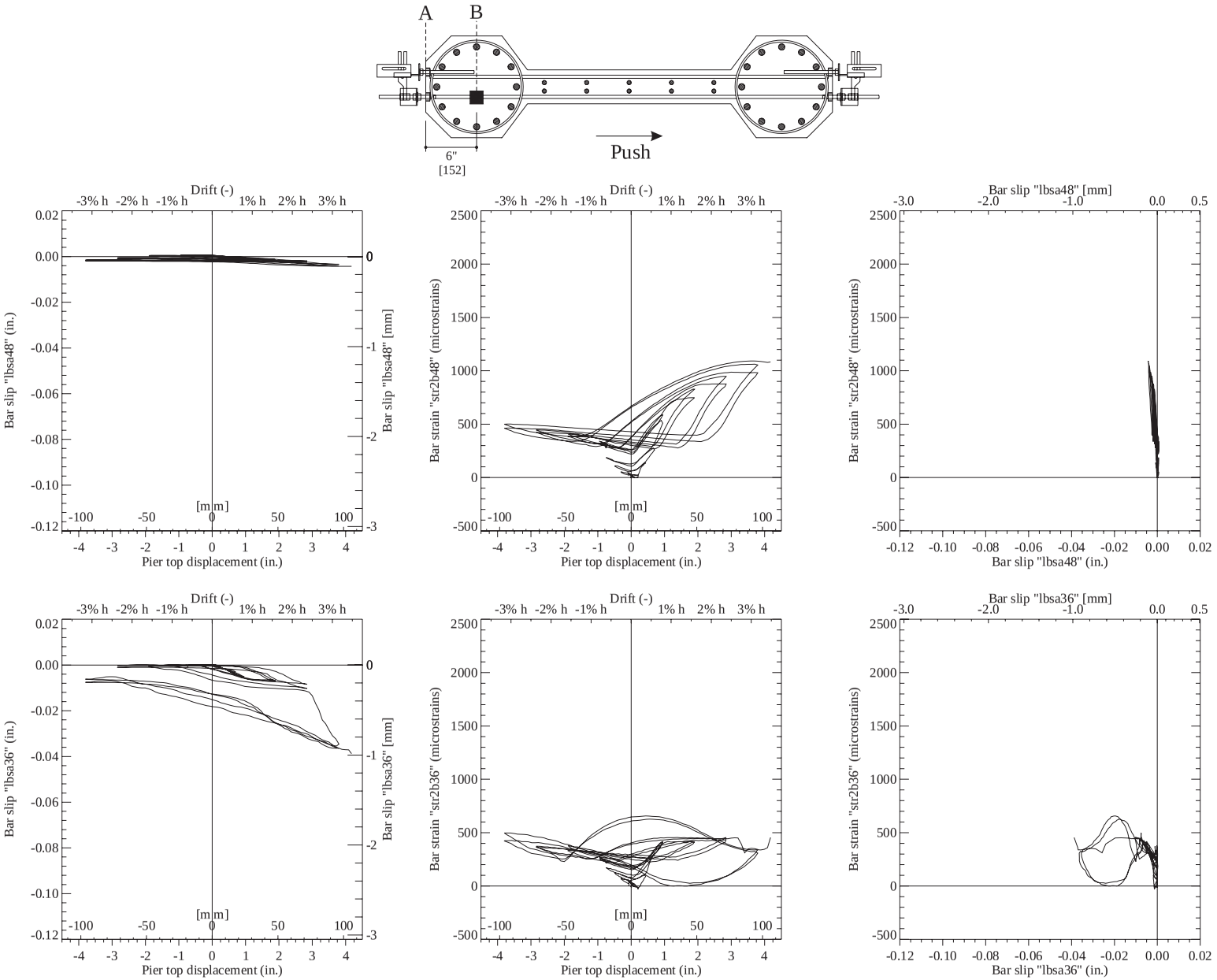

Figure 7.11: Test Unit 3A bar slip and transverse bar strain histories at positions A and B, 36 in. [914] and 48 in. [1219] above the footing. Push (positive) direction is south.

7.3 Test Unit 3B

7.3.1 Hysteretic Behavior

Test Unit 3B performed in a ductile manner up through the first positive excursion to $\mu_\Delta = 6$ whereafter it failed on the first negative excursion to $\mu_\Delta = 6$ (see Figure 7.12). The test unit reached a maximum negative displacement ductility of $\mu_\Delta = 5.4$ before failing in web crushing. The column failed by crushing of the critical compression struts inside the plastic hinge region and subsequent vertical slippage of the compression struts against the compression boundary element immediately above the critical struts. As the critical compression struts began to fail, multiple splitting cracks were observed to form in each strut. The shear cracks running perpendicular to the struts that failed had reached widths of 0.024 - 0.031 in. [0.6 - 0.8 mm] on the previous positive excursion to $\mu_\Delta = 6$. It was therefore possible that the individual diamond-shaped chunks of concrete composing the strut did not line up perfectly before going back into compression and the strut began to split under the stress concentrations on the interfaces of the chunks. Even at the positive peak of $\mu_\Delta = 6$ the struts appeared to be holding up very well, showing no sign of imminent crushing, such as excessive flaking of the paint. This behavior appeared somewhat different than Test Units 3A and 3C. Test Unit 3B seemed to fail almost simultaneously on several different struts higher up the wall than the two critical struts. As explained in Chapter 2, Test Unit 3B was designed with transverse steel that did not meet the strength of the required V_s component. This low amount of transverse steel allowed high transverse strains and therefore large crack widths throughout the wall, weakening all of the compression struts in the wall. The failure of Test Unit 3B, therefore not only proved that the concrete compression struts weaken with increasing shear displacements, but also that the struts weaken under cyclic loading, where they are cracked in tension and then forced to fit back together to carry compression.

Until failure, the test unit exibited stable hysteretic behavior with minimal pinching. The test unit's flexibility in shear contributed to its overall initial flexibility. After reaching its ideal yield displacement at $\mu_\Delta = 1$, however, the test unit continued to gain strength up through $\mu_\Delta = 6$ maintaining enough shear stiffness to develop some strain hardening in the longitudinal reinforcement. Figure 7.13 compares the test results to the predictions given in Chapter 5.

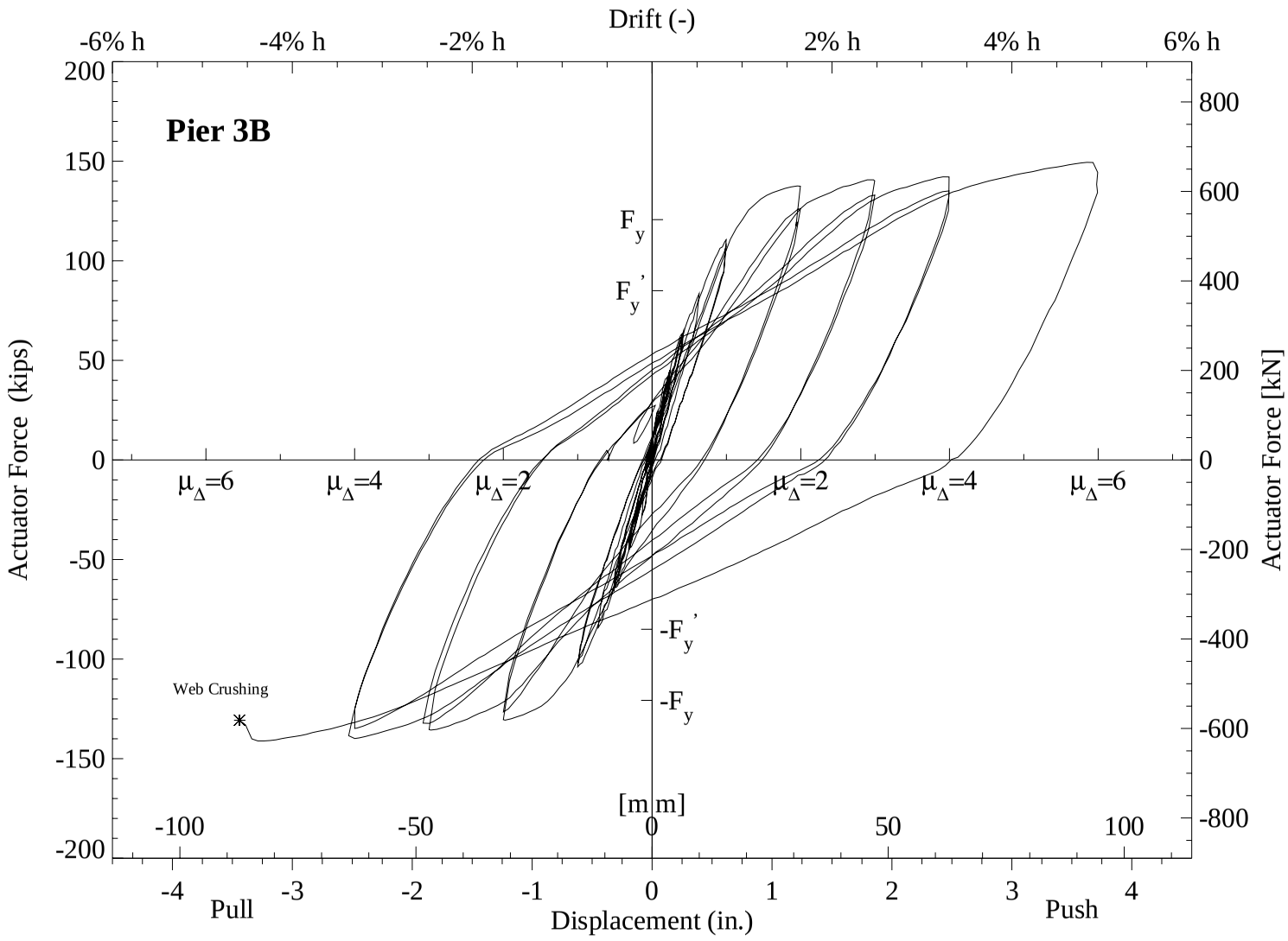

Figure 7.12: Test Unit 3B, measured experimental hysteretic response.

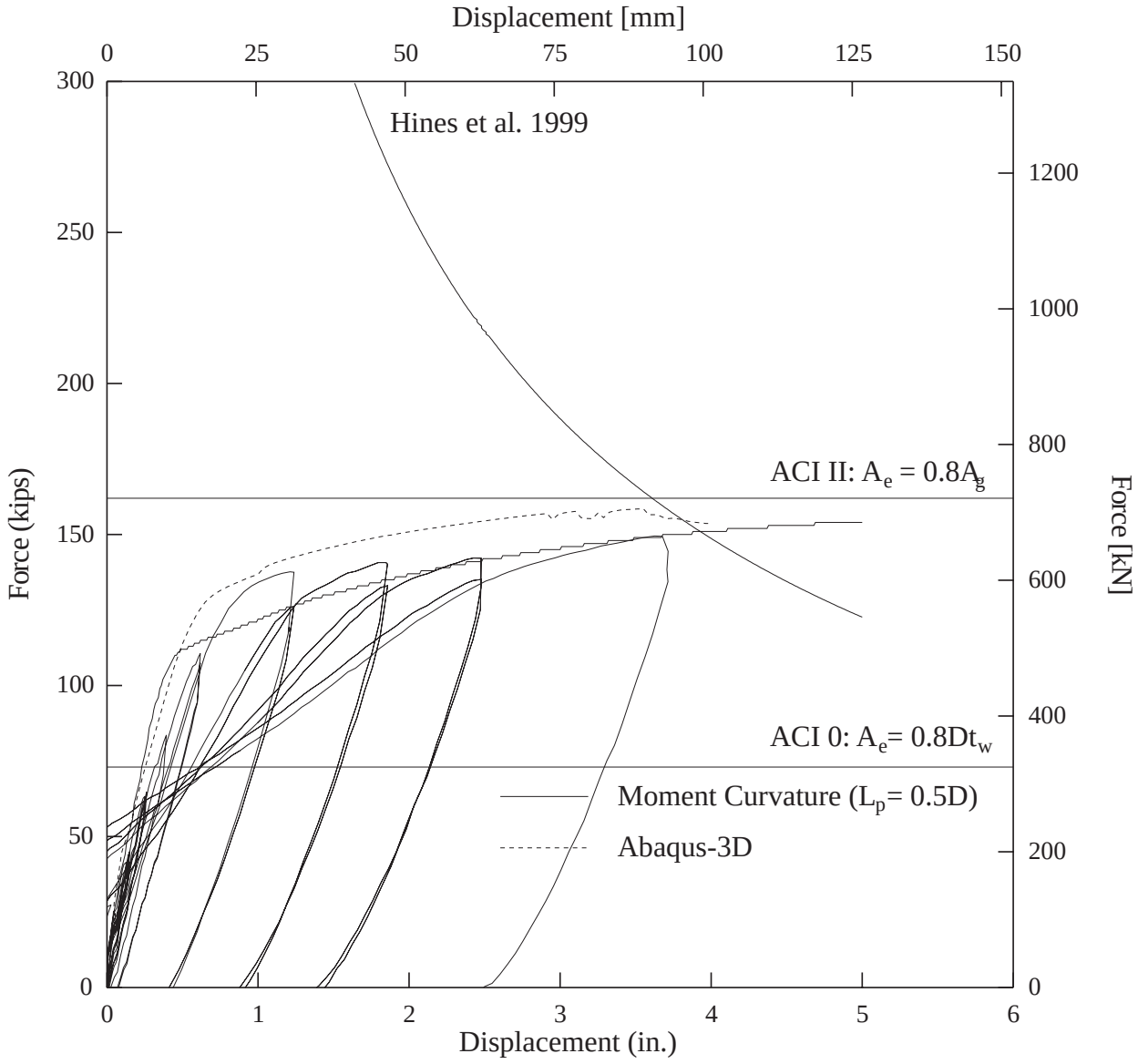

Figure 7.13: Test Unit 3B, force-deflection predictions with web crushing capacity envelopes and test results.

7.3.2 Flexural and Shear Displacements

Figures 7.14 and 7.15 give the flexural and shear hysteretic behavior of Test Unit 3B as calculated from the curvature and shear instrumentation discussed in Chapter 4. Figures 7.16 and 7.18 give favorable comparisons between the flexural + shear hysteretic response and the measured hysteretic response of the column, implying that the flexure and shear displacement values calculated from test data were reasonably accurate with the exception of the first positive excursion to $\mu_\Delta = 6$ where the shear displacements appeared unrealistically large.

The clear difference between the shape of the flexural and shear hysteresis loops underlines the difference between the two mechanisms of deformation. Pinching occurred almost entirely in the shear hysteretic response. This may have been due to the minor vertical slippage observed along the interface of the wall and compression boundary element in the the plastic hinge region. Regardless of the difference in shape, it is useful to note that at the peaks, the ratio between shear and flexural displacement remained relatively constant, again with the exception of the first peak at $\mu_\Delta = 6$, where the shear displacements appeared urealistically large. Figure 7.17 shows this in a plot of shear displacement as a function of flexural displacement, where a straight line corresponding to $_s/\ _f = 0.30$ matches the trend in peak displacements fairly well. Therefore, as with Test Unit 3A it might be reasonable to assume shear displacements to be roughly 30% of the flexural displacements when conducting a simple moment-curvature based force-deflection prediction of such a column. This value is one and a half times the value of 20% assumed for the prediction in Chapter 5.

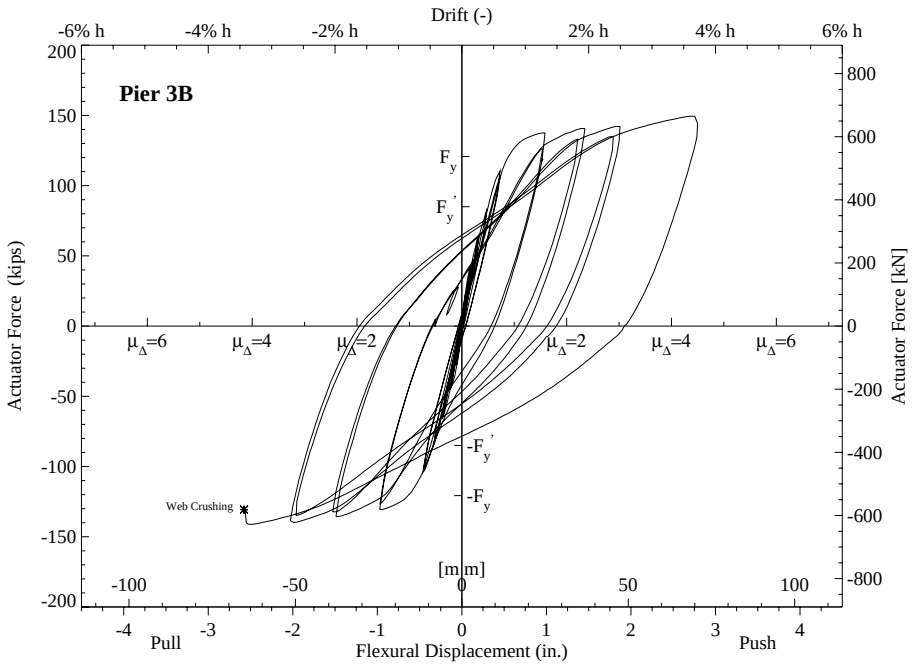

Figure 7.14: Test Unit 3F, calculated experimental flexural hysteretic response.

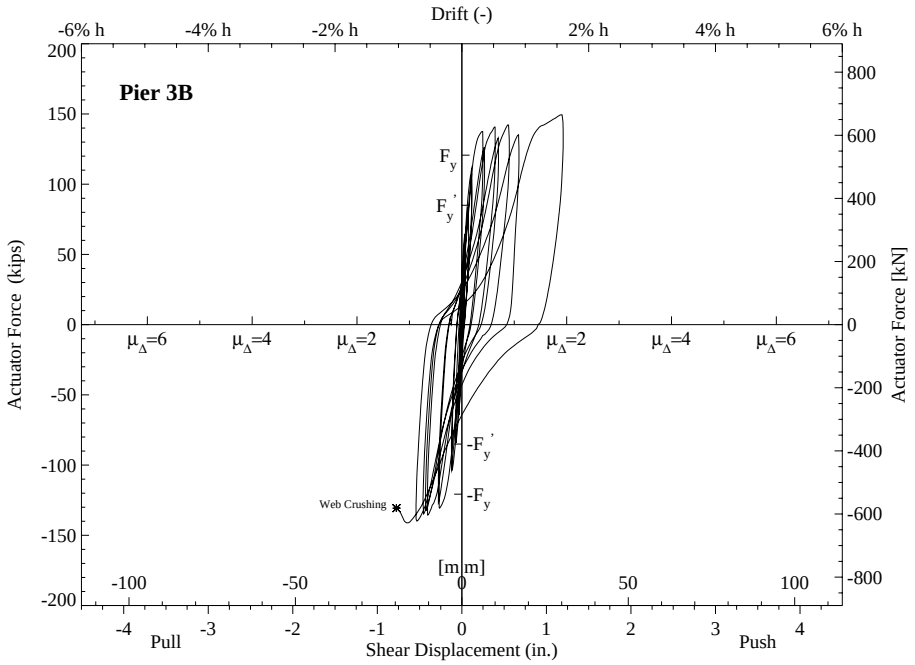

Figure 7.15: Test Unit 3B, calculated experimental shear hysteretic response.

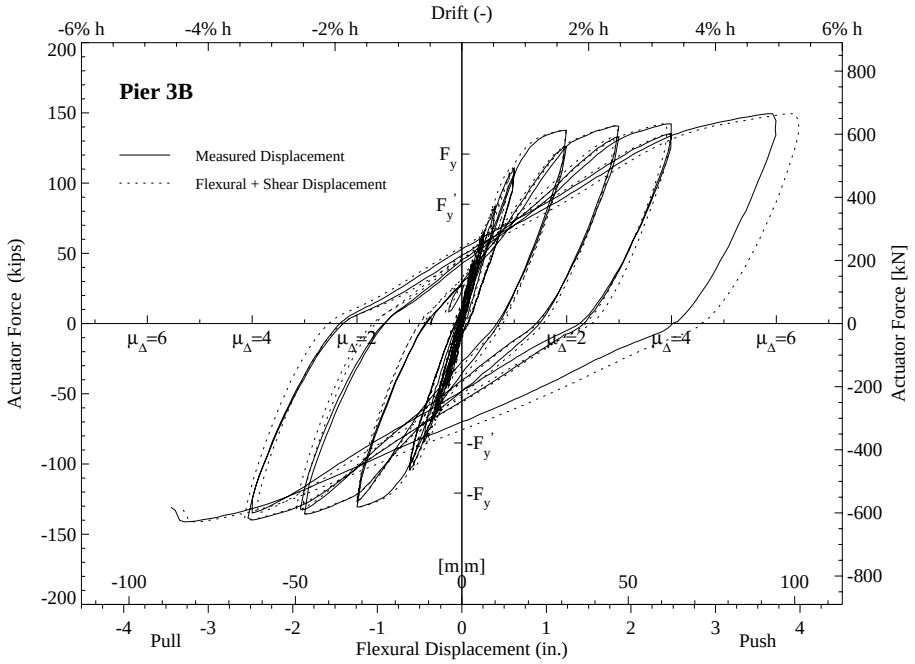

Figure 7.16: Test Unit 3B, calculated experimental flexure + shear hysteretic response compared to the measured hysteretic response.

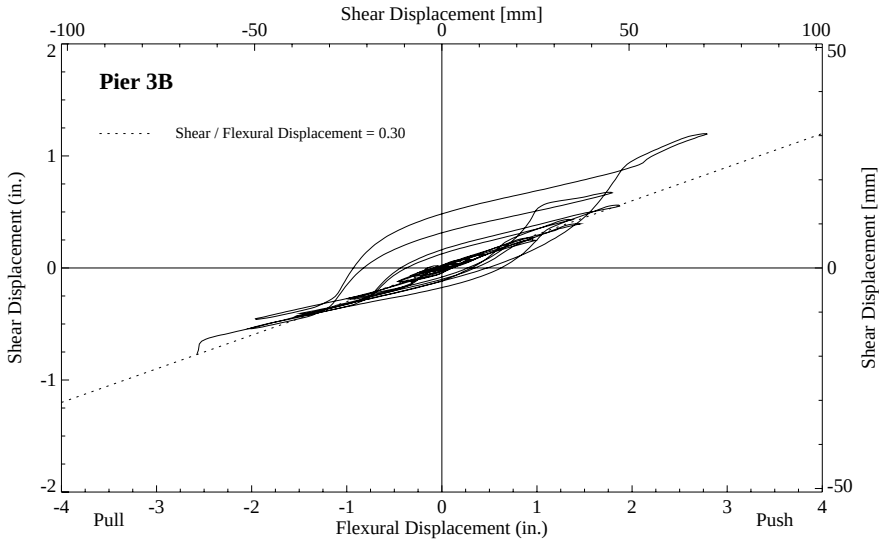

Figure 7.17: Test Unit 3B, shear displacements as a function of the flexural displacements.

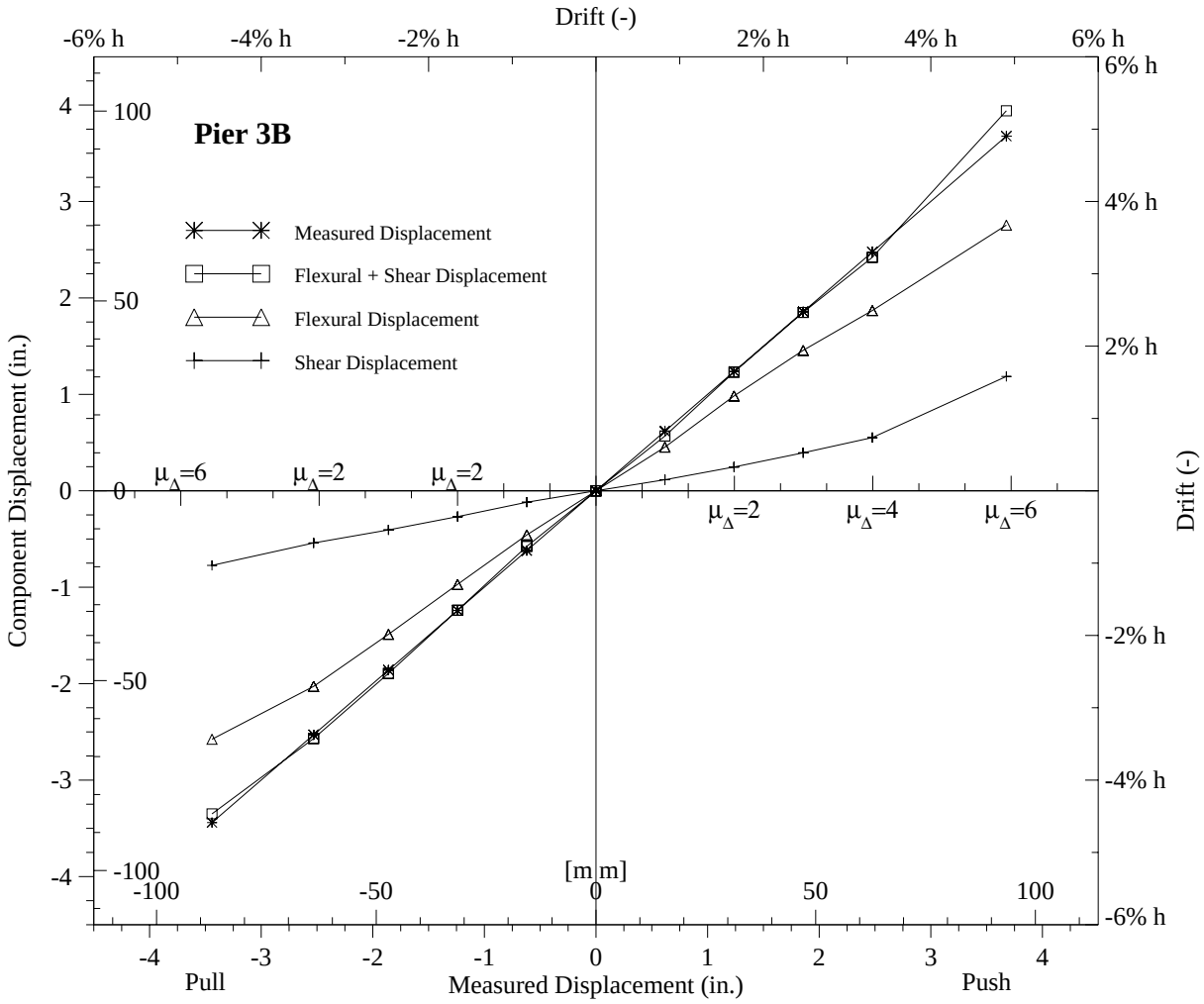

Figure 7.18: Test Unit 3B, calculated and measured experimental displacement peak values.

7.3.3 Performance of the Transverse Reinforcement

Designed to have the same transverse reinforcement ratio as 3A and 3C, it was clear that Test Unit 3B, lacked adequate transverse reinforcement to satisfy the design equations outlined in Chapter 2. This had been acceptable because it was thought that with lower transverse reinforcement and with the boundary elements so close together, the spirals would play a greater role in resisting the shear. The large shear cracks in the wall and the resulting web crushing under cyclic loading made clear that this was not the case. Figure 7.19 shows strain profiles of four transverse bars spaced on 12 in. [305] vertical intervals from 12 in. [305] to 48 in. [1219] above the footing. These high strains in the wall, compared to the boundary elements speaks to the great difference in stiffness between the wall and the boundary elements.

Figure 7.19 compares the spiral strains to the transverse bar strains at Position B in the north boundary element. These strains are compared for other positions on the cross section in Figures C.21 - C.24. Compared to the very large strains of up to 15,000 $\mu\varepsilon$ observed in the wall at Position C, the boundary element strains were all very low. None of the gages at Positions B and D reached yield, although they recorded slightly higher strains than the gages at the same positions in Test Unit 3A. Test Unit 3B had been designed with a low amount of transverse reinforcement on purpose, in order to see if the boundary element steel would contribute more substantially to the shear resistance. From the strain gage readings, the increase was only minimal and most of the transverse strain still wound up happening in the structural wall, which was much more flexible, due to its lower amount of steel, concrete and confinement than the boundary elements. As with Test Unit 3A, the width of shear cracks in the wall could have been mitigated, had the V_s component only consisted of the transverse reinforcement. In addition, the V_c component could have been increased slightly due to the strength that the boundary elements added to the compression toe and dowel action.

Figures 7.21 and 7.22 show the relationship between measured bar slip and measured strain inside of the north boundary element for four bars spaced on 12 in. [305] vertical intervals from 12 in. [305] to 48 in. [1219] above the footing. The north boundary element experienced tension when the column was pushed to positive displacements. For each bar,

the slippage was observed to affect directly the ability of the bar to develop its full strain at peak load. The bars at 12 in. [305] and 24 in. [610] in Figure 7.21, for instance, slipped up to 0.08 in. [2] as shown in the left hand plots. The lower middle plot, shows the gage at position B, 12 in. [305] above the footing, to hit peak strains at roughly zero displacement and then to decrease with increasing displacement. This was not the case, however with the gage at B 24 in. [610] above the footing (shown in the upper middle plot), which slipped, but then continued to develop strains at B. The plots on the far right show the direct relationship between the bar slippage at position A and the strain at position B. Both of the plots on the far right, show strain increasing at position B up to a certain point and then either decreasing with increasing slippage or plateauing and then increasing further. Figure 7.22 shows the bars at 36 in. [914] and 48 in. [1219] to have slipped less than the lower bars and to have experienced no loss in strain capacity at position B. This can be seen in the middle and right hand plots. Similar to the results from Test Unit 3A, these results suggest that while slippage and subsequent loss of strain capacity was likely to occur in transverse bars located inside the plastic hinge region, where large cracks are highly concentrated, significant slippage resulting in loss of strain capacity was unlikely to occur outside of the plastic region because the boundary element concrete was highly-confined and the flexural cracks were very small. The bars at 36 in. [914] above the footing in Test Unit 3B slipped less than those in 3A, simply because the plasticity in 3B did not spread up to that height. The effect of bar slippage on strain capacity at Position C, in the middle of the wall, can be seen in Figures C.19 and C.27 to have been practically non-existent inside of the plastic hinge region.

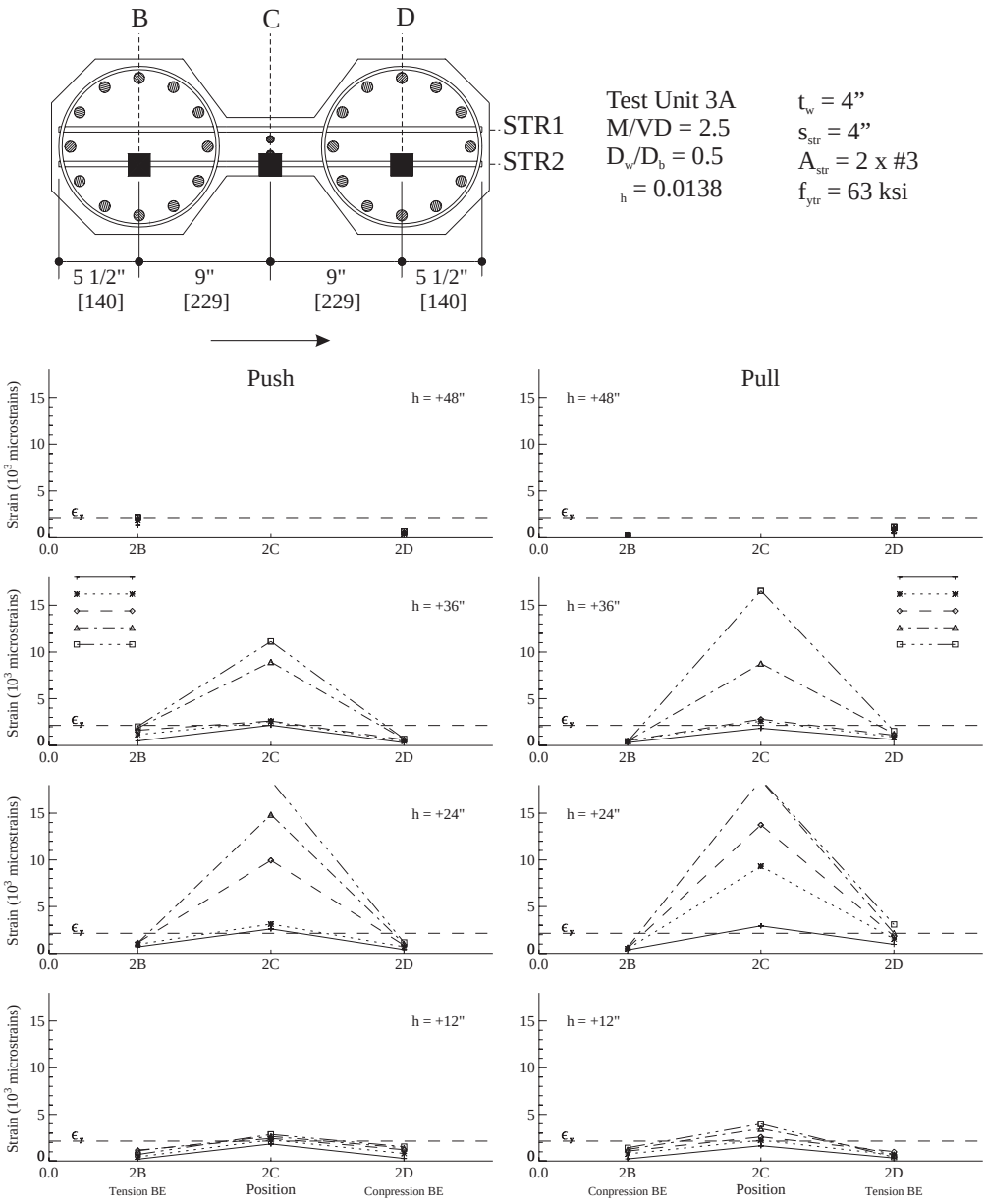

Figure 7.19: Test Unit 3B, transverse bar strain profiles.

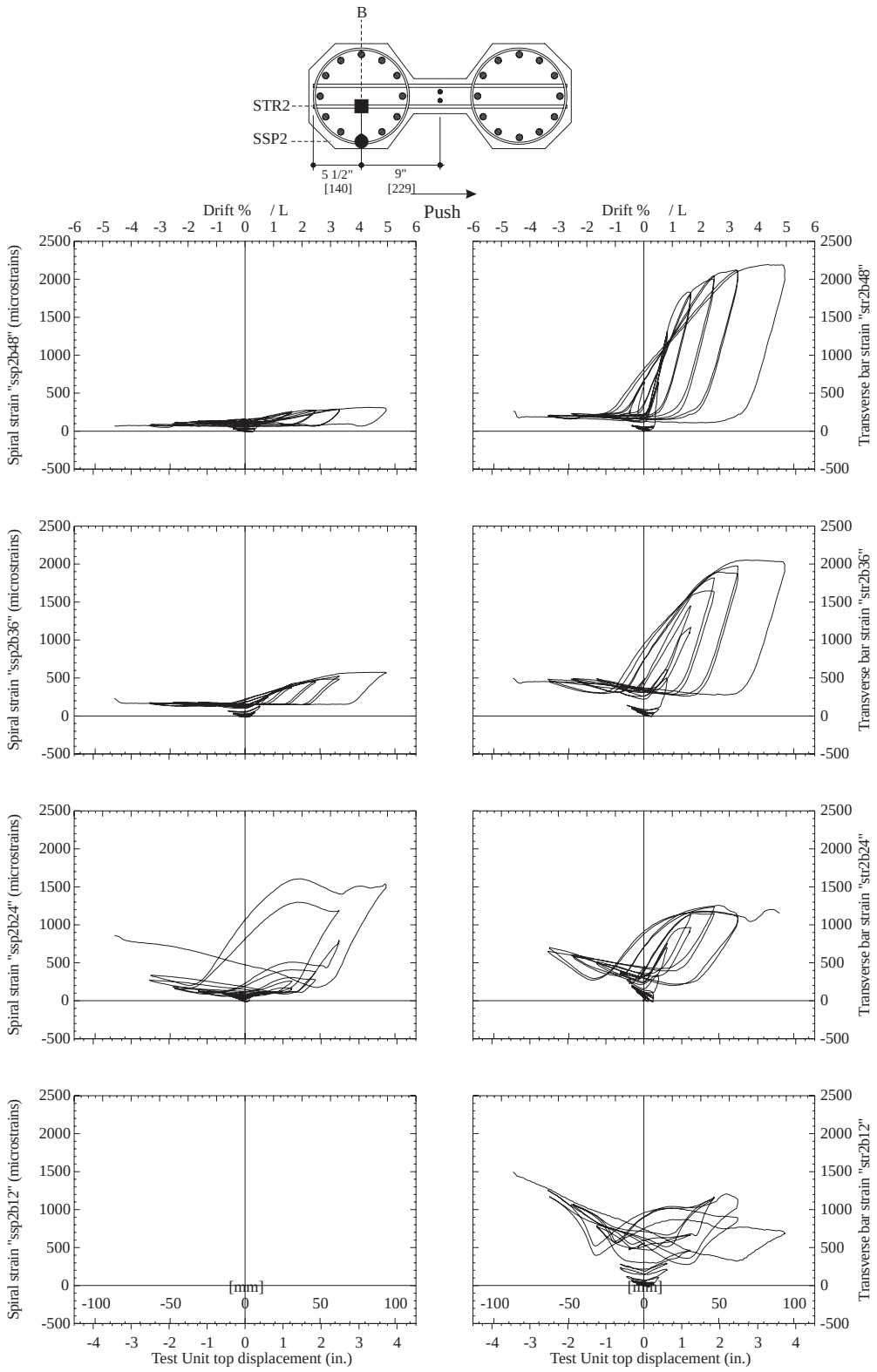

Figure 7.20: Test Unit 3B, spiral strains and transverse bar strains at Position B, for heights 12 in. [305], 24 in. [610], 36 in. [914] and 48 in. [1219] above the footing.

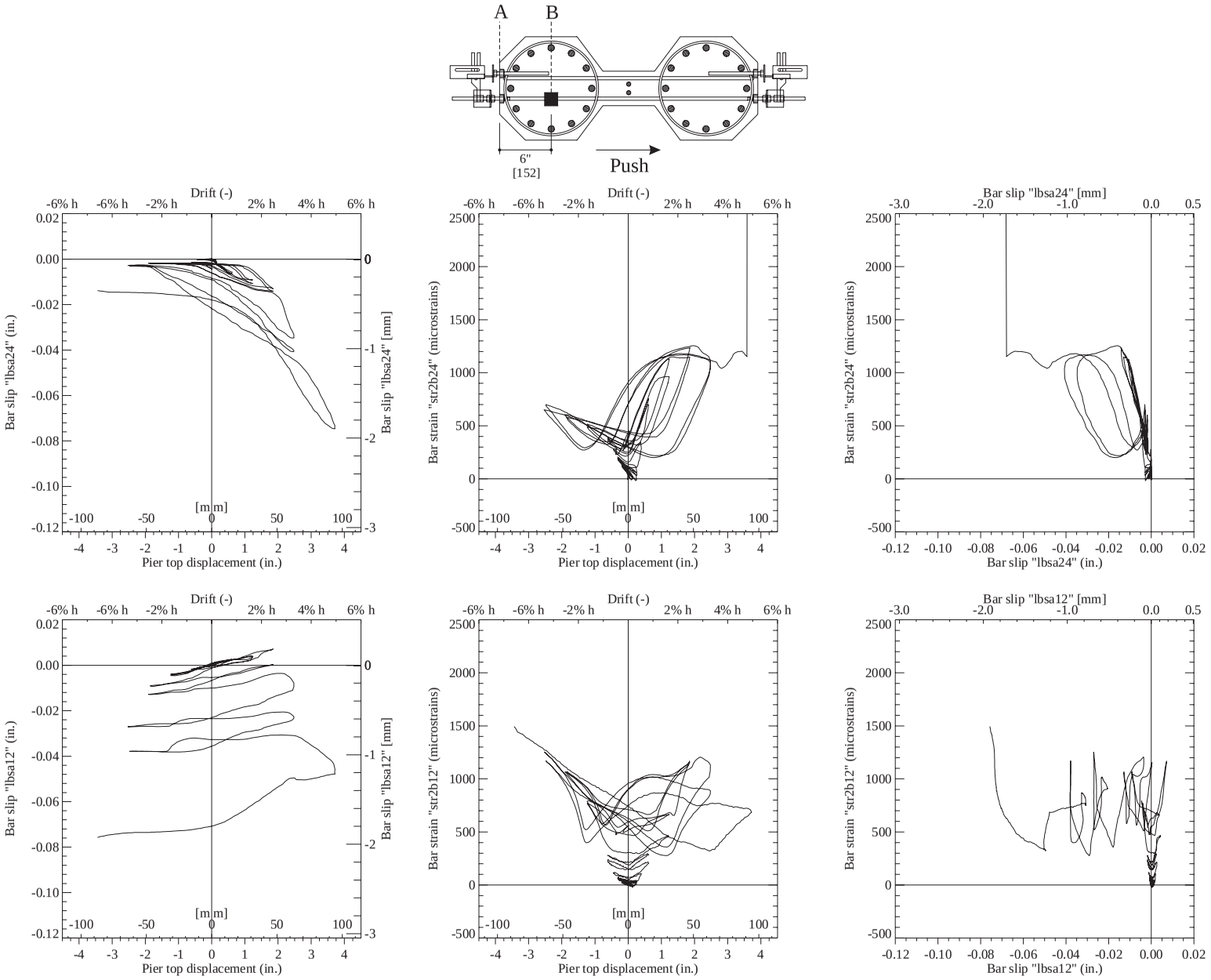

Figure 7.21: Test Unit 3B bar slip and transverse bar strain histories at positions A and B, 12 in. [305] and 24 in. [610] above the footing. Push (positive) direction is south.

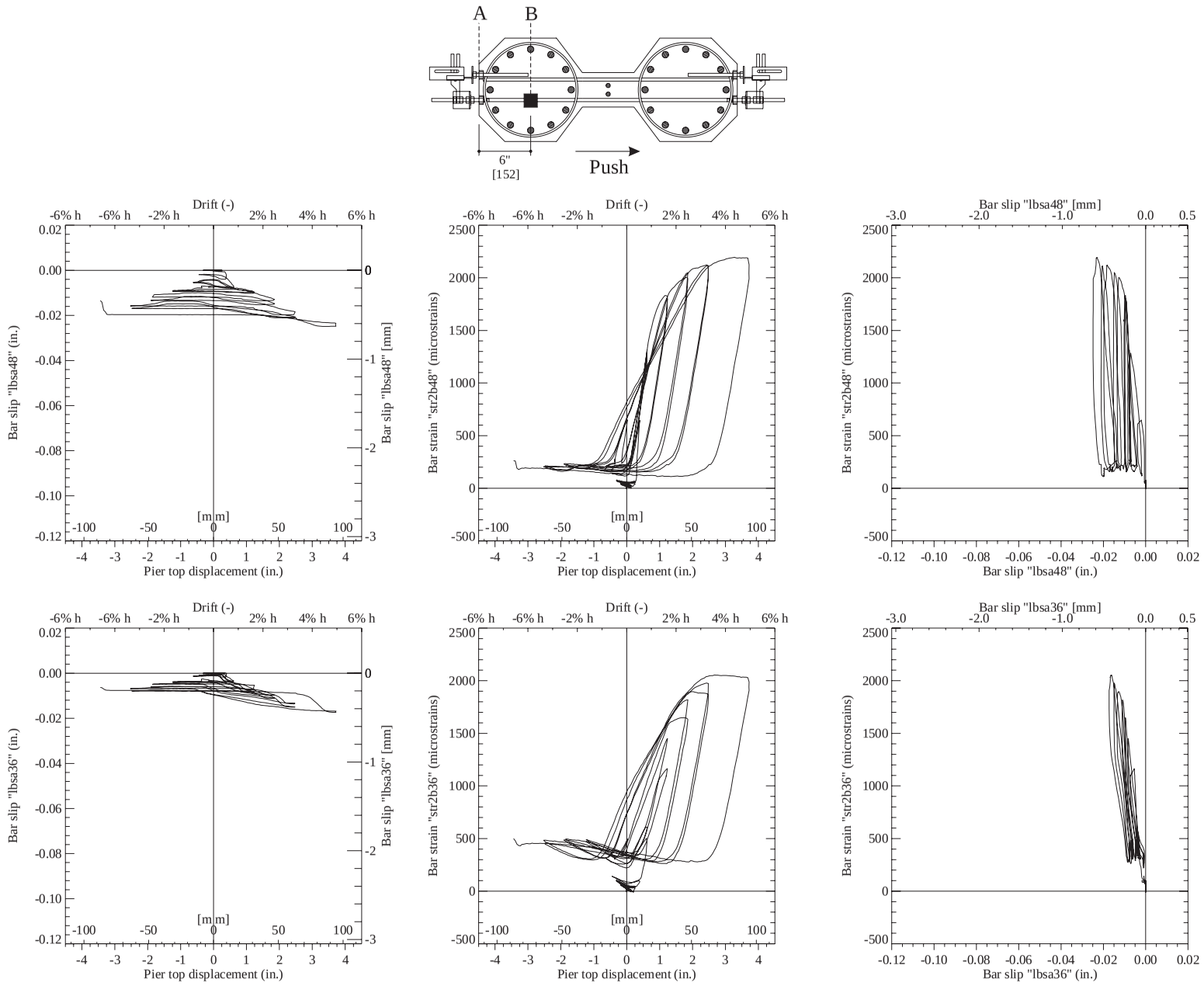

Figure 7.22: Test Unit 3B bar slip and transverse bar strain histories at positions A and B, 36 in. [914] and 48 in. [1219] above the footing. Push (positive) direction is south.

7.4 Test Unit 3C

7.4.1 Hysteretic Behavior

Test Unit 3C performed in a ductile manner up through one and a half cycles at $\mu_\Delta = 4$ until it failed on the second negative excursion to $\mu_\Delta = 4$ (see Figure 7.23). The column failed by crushing of the critical compression struts inside the plastic hinge region and subsequent vertical slippage of the compression struts against the compression boundary element immediately above the critical struts. In addition to a vertical failure plane, a horizontal failure plane at the height of the lowest critical compression strut was also observed to form. After the initial failure occurred, the test unit was cycled through the second negative excursion to $\mu_\Delta = 4$ and then pushed once to $\mu_\Delta = 5$ in the positive direction in order to observe and measure its post web crushing behavior.

Until failure, the test unit exibited stable hysteretic behavior with minimal pinching. The test unit's flexibility in shear contributed significantly to its overall initial flexibility. After reaching its ideal yield displacement at $\mu_\Delta = 1$, however, the test unit continued to gain strength up through $\mu_\Delta = 4$ maintaining enough shear stiffness to develop some strain hardening in the longitudinal reinforcement. Figure 7.24 compares the test results to the predictions given in Chapter 5.

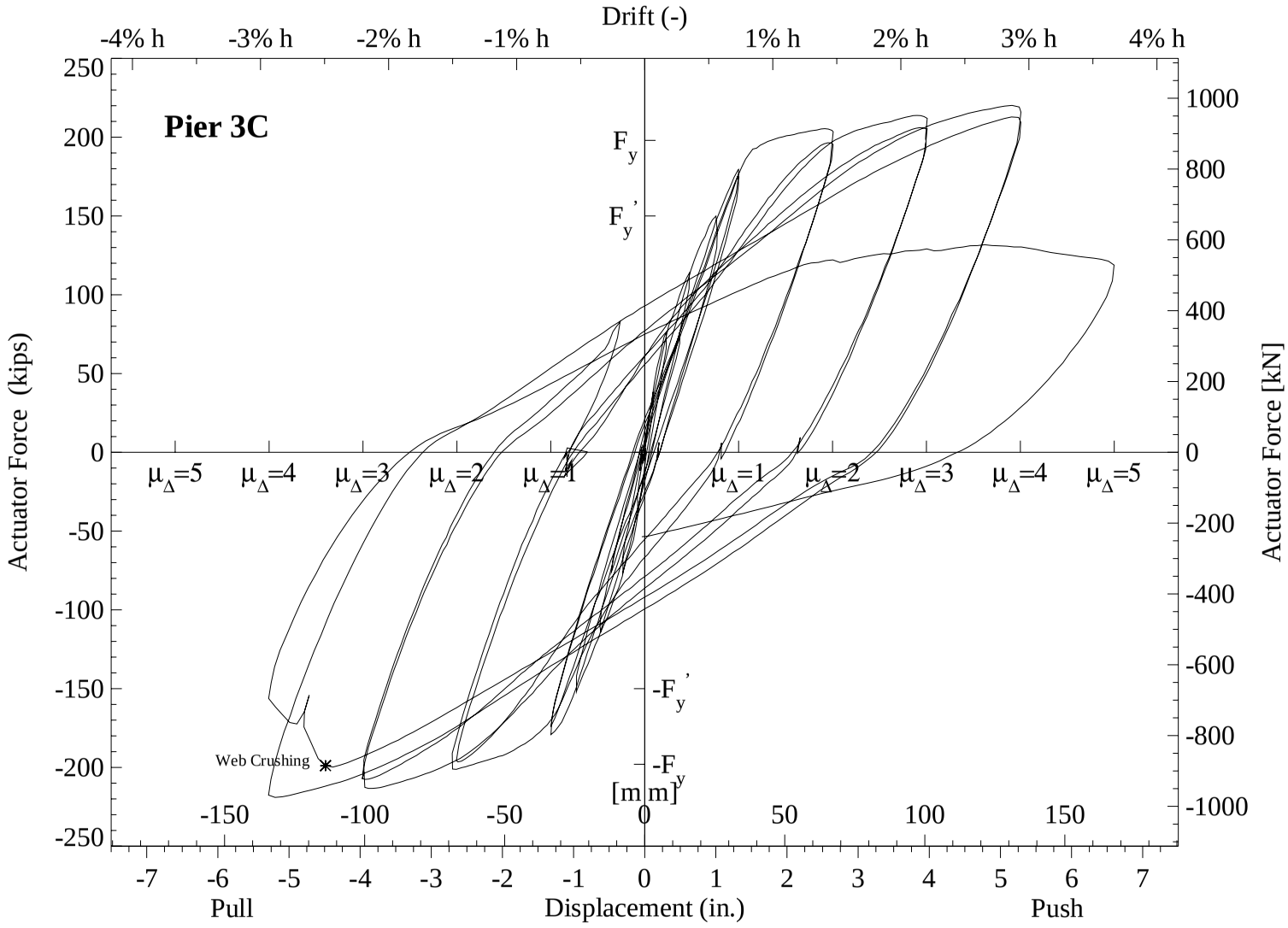

Figure 7.23: Test Unit 3C, measured experimental hysteretic response.

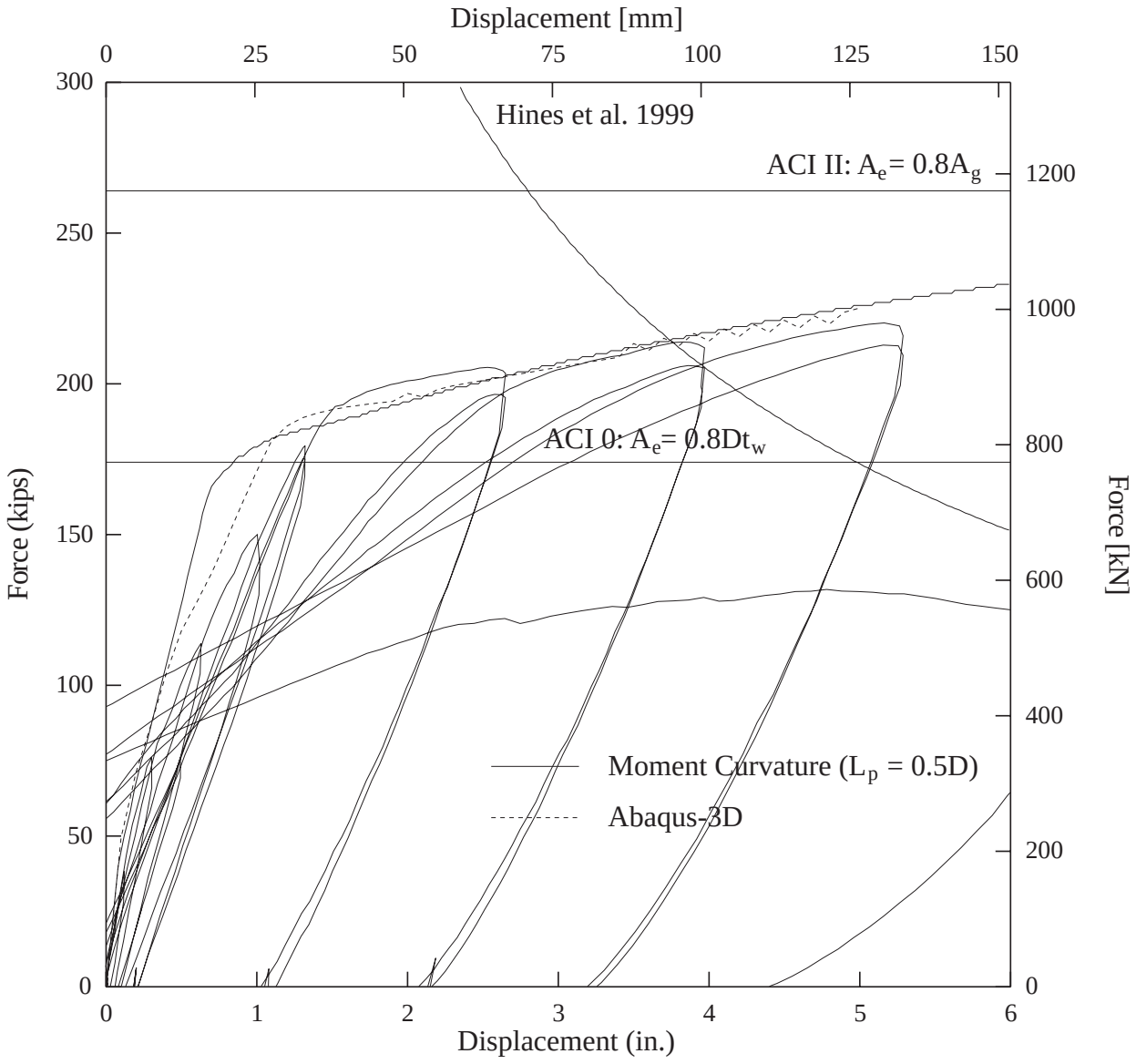

Figure 7.24: Test Unit 3C, force-deflection predictions with web crushing capacity envelopes and test results.

7.4.2 Flexural and Shear Displacements

Due to an electrical malfunction in one of the data acquisition cabinets for some selected curvature potentiometers, the second cycle of $\mu_\Delta = 2$ and the first cycle of $\mu_\Delta = 3$ were not recorded with a reasonable degree of accuracy. For this reason, the scans 750 - 1245 corresponding to these two cycles were omitted in plots of the flexural and shear displacements. Additionally, Figure 7.29, which reports data from first cycle peaks, does not show any data at $\mu_\Delta = 3$.

Figures 7.25 and 7.26 give the flexural and shear hysteretic behavior of Test Unit 3C as calculated from the curvature and shear instrumentation discussed in Chapter 4. Figures 7.27 and 7.29 give favorable comparisons between the flexural + shear hysteretic response and the measured hysteretic response of the column, implying that the flexure and shear displacement values calculated from test data were reasonably accurate. Furthermore, the large increase in shear displacement and the corresponding decrease in flexural displacement in the last half cycle at $\mu_\Delta = 5$ confirm the accuracy of the apparatus and methods used to measure flexural and shear displacements. When the column began to behave as a frame, deforming primarily in shear, the instruments captured the phenomenon.

The clear difference between the shape of the flexural and shear hysteresis loops underlines the difference between the two mechanisms of deformation. Pinching occurred almost entirely in the shear hysteretic response. Regardless of the difference in shape, it is useful to note that at the peaks, the ratio between shear and flexural displacement remained relatively constant. Figure 7.28 shows this in a plot of shear displacement as a function of flexural displacement, where a straight line corresponding to $_s/\ _f = 0.25$ matches the trend in peak displacements fairly well. Therefore, it might be reasonable to assume shear displacements to be roughly 25% of the flexural displacements when conducting a simple moment-curvature based force-deflection prediction of such a column. Additionally, since Test Unit 3C was cycled past its web crushing displacement (which was not the case for Test Units 3A and 3B), Figure 7.26 reveals that after web crushing, the column deformed primarily in shear in order to reach the $\mu_\Delta = 4$ displacement level. Figure 7.25 supports this finding, by showing that the column deformed only a small amout further in flexure after failing in web crushing.

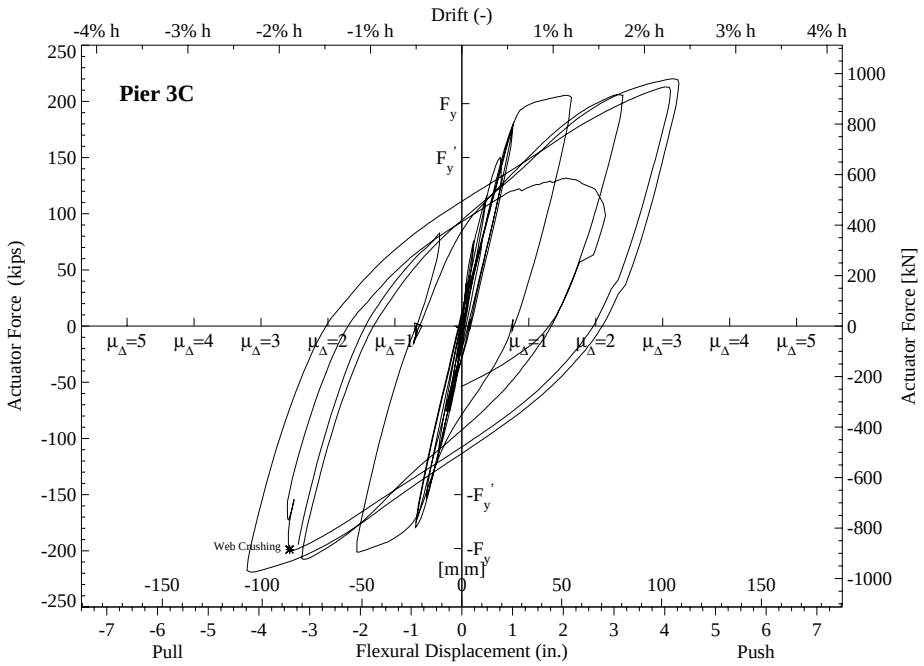

Figure 7.25: Test Unit 3C, calculated experimental flexural hysteretic response.

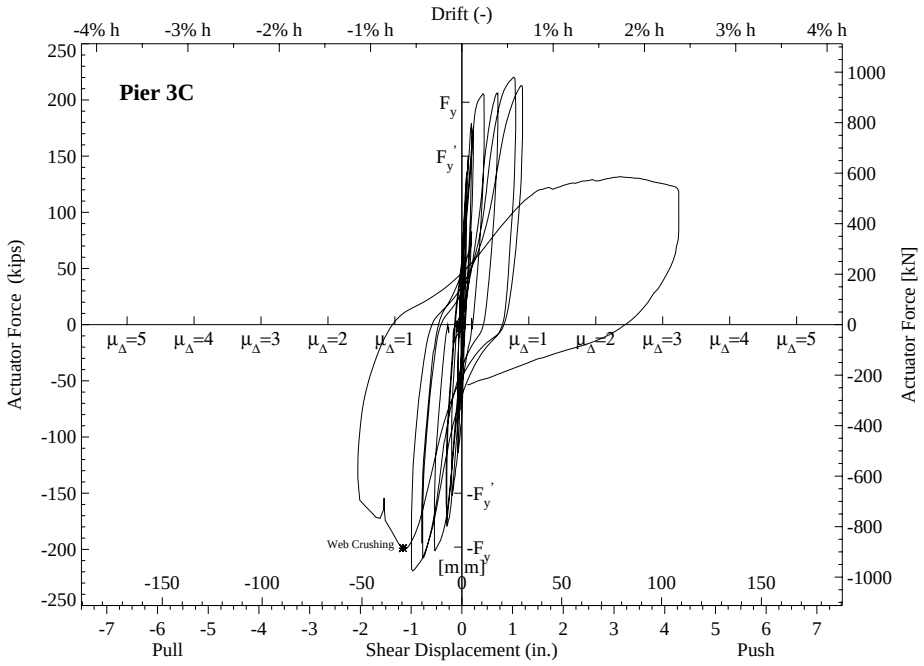

Figure 7.26: Test Unit 3C, calculated experimental shear hysteretic response.

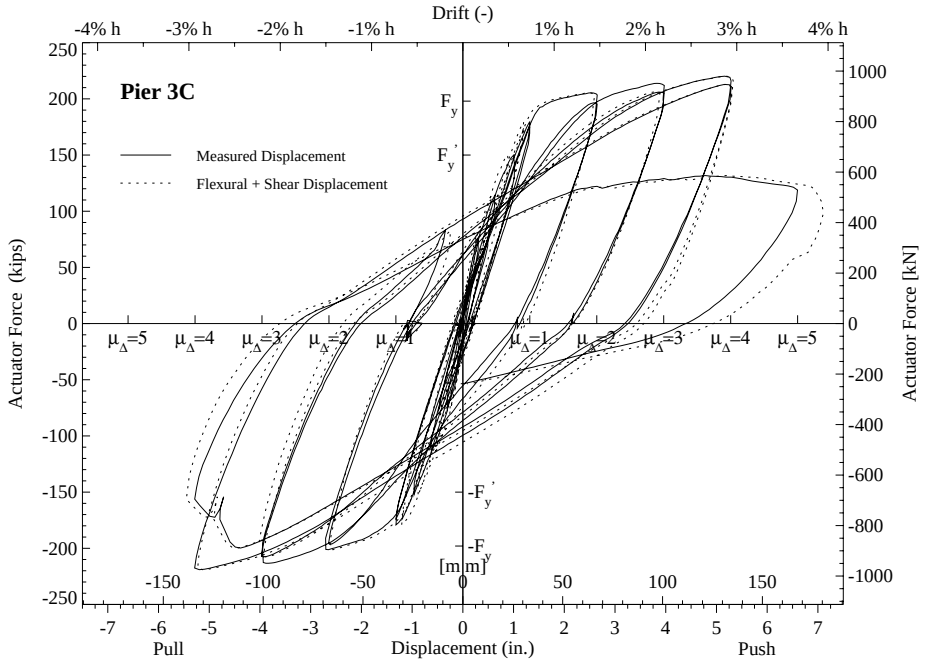

Figure 7.27: Test Unit 3C, calculated experimental flexure + shear hysteretic response compared to the measured hysteretic response.

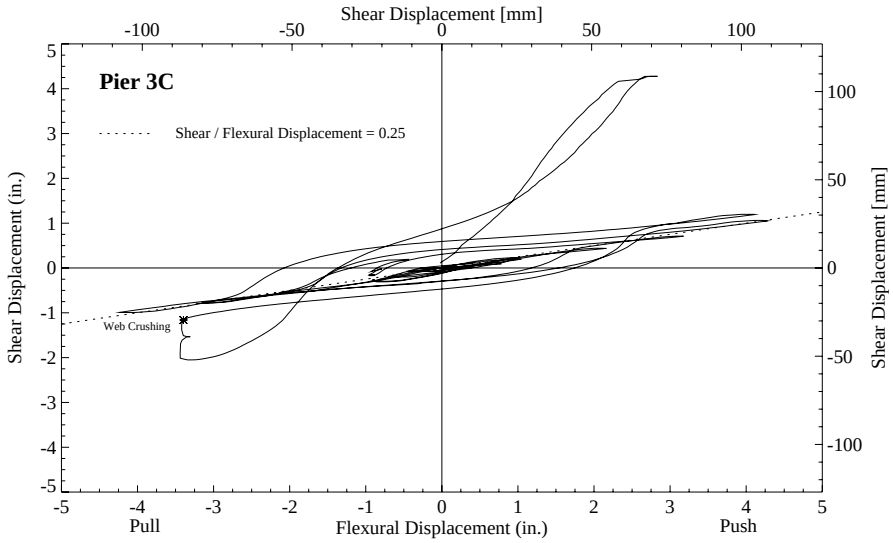

Figure 7.28: Test Unit 3C, shear displacements as a function of the flexural displacements.

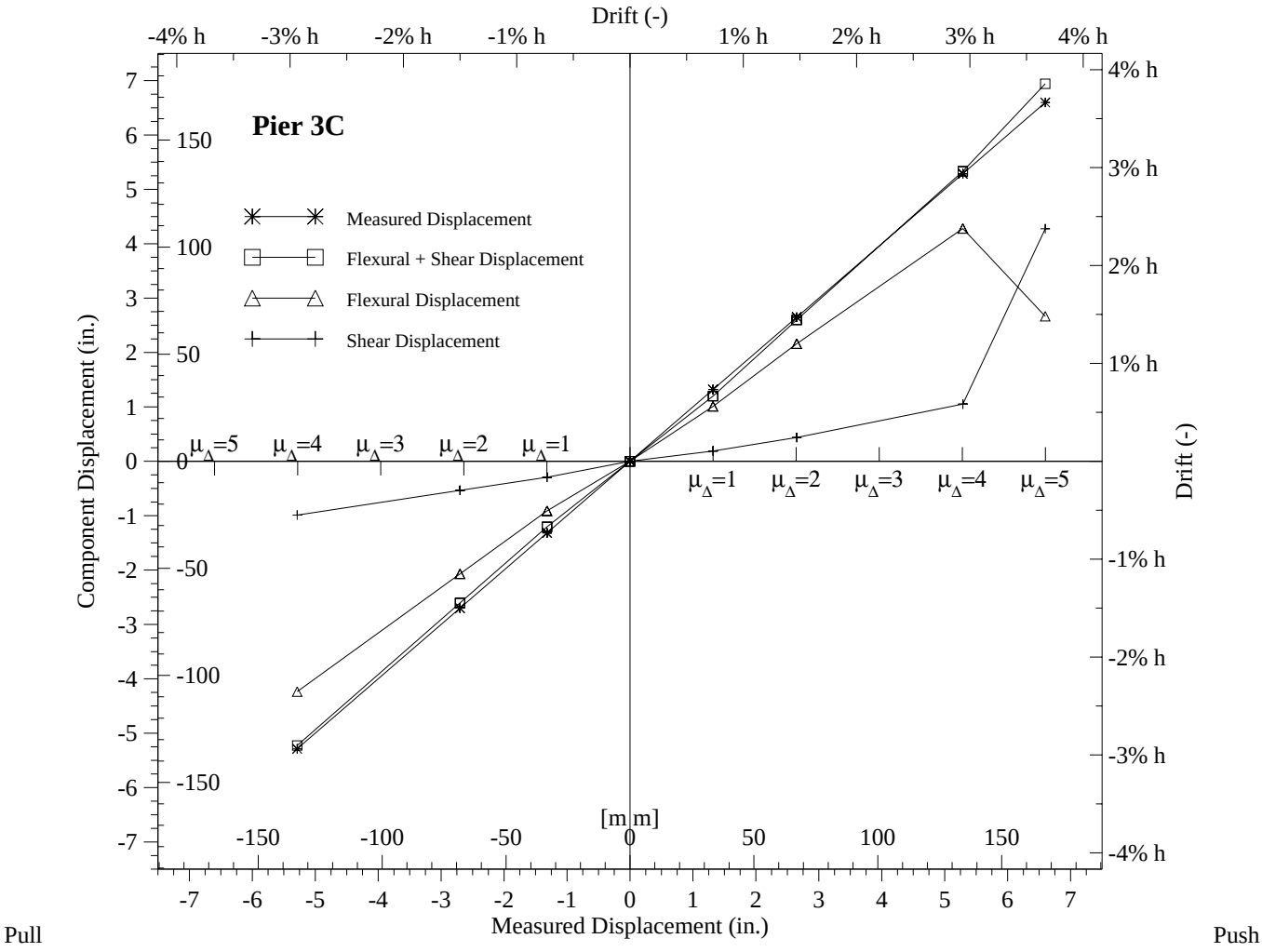

Figure 7.29: Test Unit 3C, calculated and measured experimental displacement peak values.

7.4.3 Performance of the Transverse Reinforcement

Designed according to the method outlined in Chapter 2, the transverse reinforcement remained below yield for most of the test with the exception of the transverse bars at 36 in. [914 mm] above the footing. Figures 7.30 and 7.31 shows strain profiles of eight transverse bars spaced on 12 in. [305] vertical intervals from 12 in. [305] to 96 in. [2438] above the footing.

Figure 7.32 compares spiral strains to transverse bar strains at position B inside the north boundary element. Figures C.36 - C.39 in Appendix C make the same comparison at other locations in the test unit cross section. The transverse bars generally reached higher strain levels than the spirals, and neither the transverse bars nor the spirals yielded when the north boundary element was in tension. The strains in the spirals and transverse bars in these positions support the conclusions drawn earlier about the V_s component of shear capacity from the Test Unit 3A data.

Figures 7.33 and 7.34 show the relationship between measured bar slip and measured strain inside of the north boundary element for four bars spaced on 12 in. [305] vertical intervals from 12 in. [305] to 48 in. [1219] above the footing. The north boundary element experienced tension when the column was pushed to positive displacements. For each bar, slippage of 0.02 in. [0.5 mm] or more was observed to affect directly the ability of the bar to develop its full strain at peak load. These results suggest that while slippage and subsequent loss of strain capacity was likely to occur in transverse bars located inside the plastic hinge region, where large cracks are highly concentrated, significant slippage resulting in loss of strain capacity was unlikely to occur outside of the plastic region because the boundary element concrete was highly-confined and the flexural cracks were very small. The effect of bar slippage on strain capacity at Position C, just inside the wall, can be seen in Figures C.32 and C.42. The effect of bar slippage on strain capacity at Position D, in the middle of the wall, can be seen in Figures C.33 and C.43.

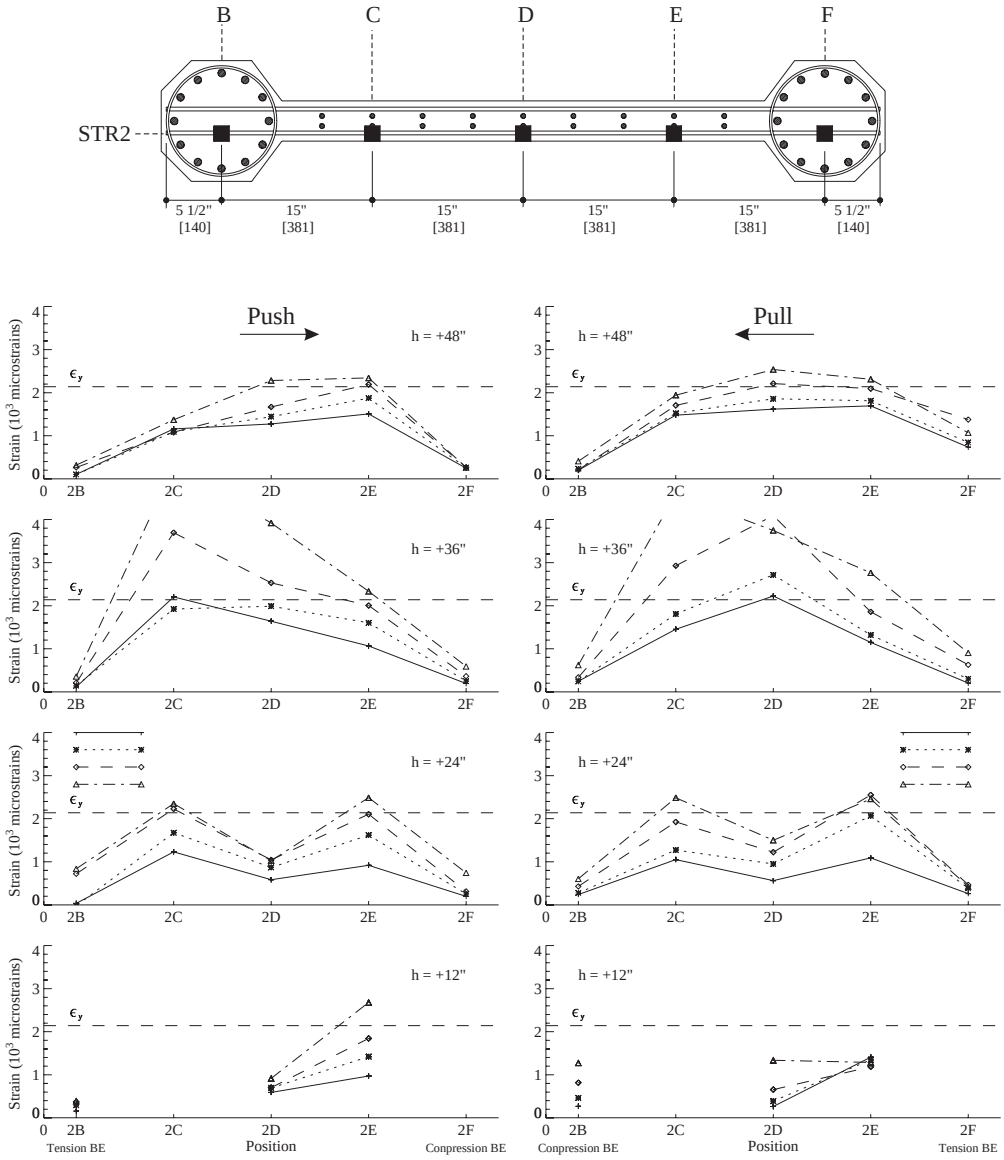

Figure 7.30: Test Unit 3C, lower transverse bar strain profiles.

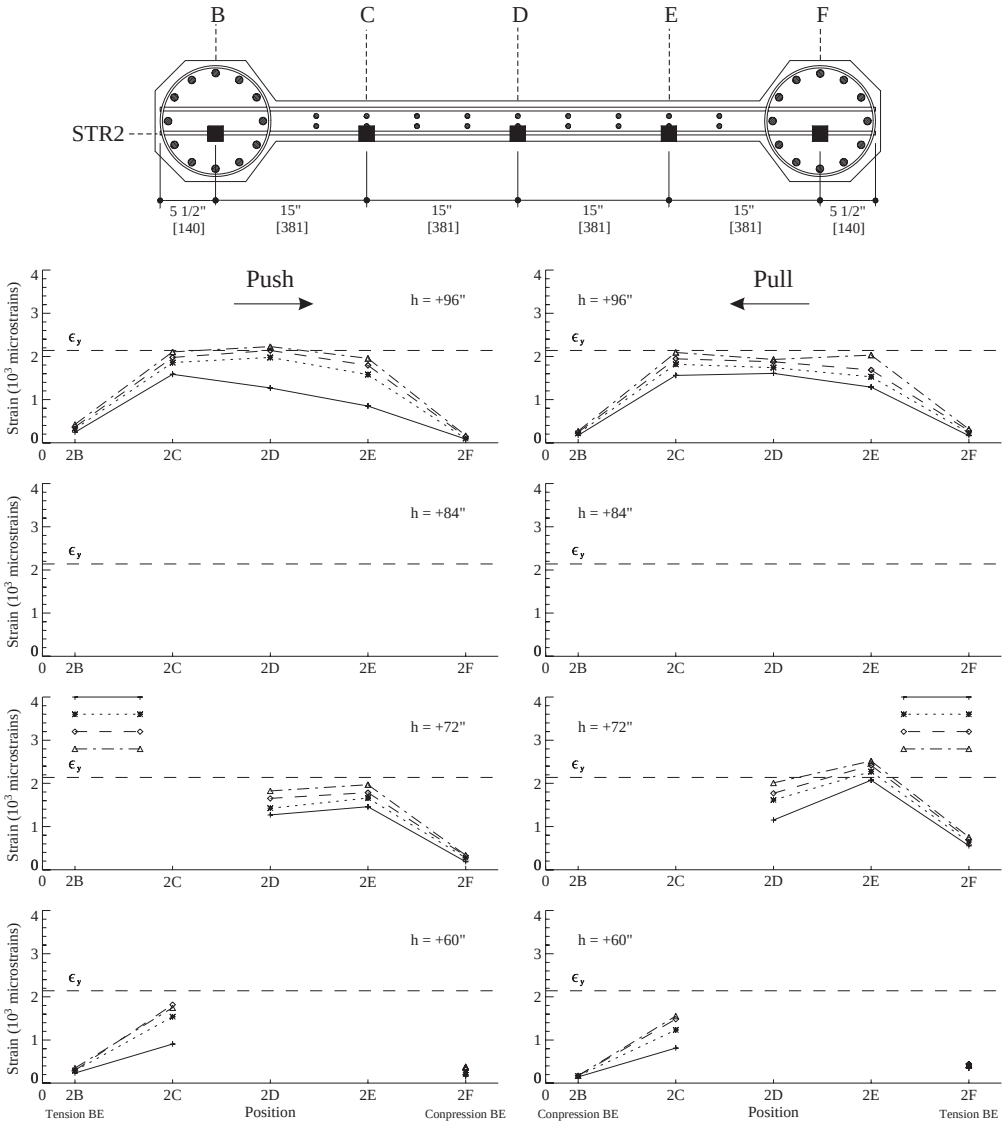

Figure 7.31: Test Unit 3C, upper transverse bar strain profiles.

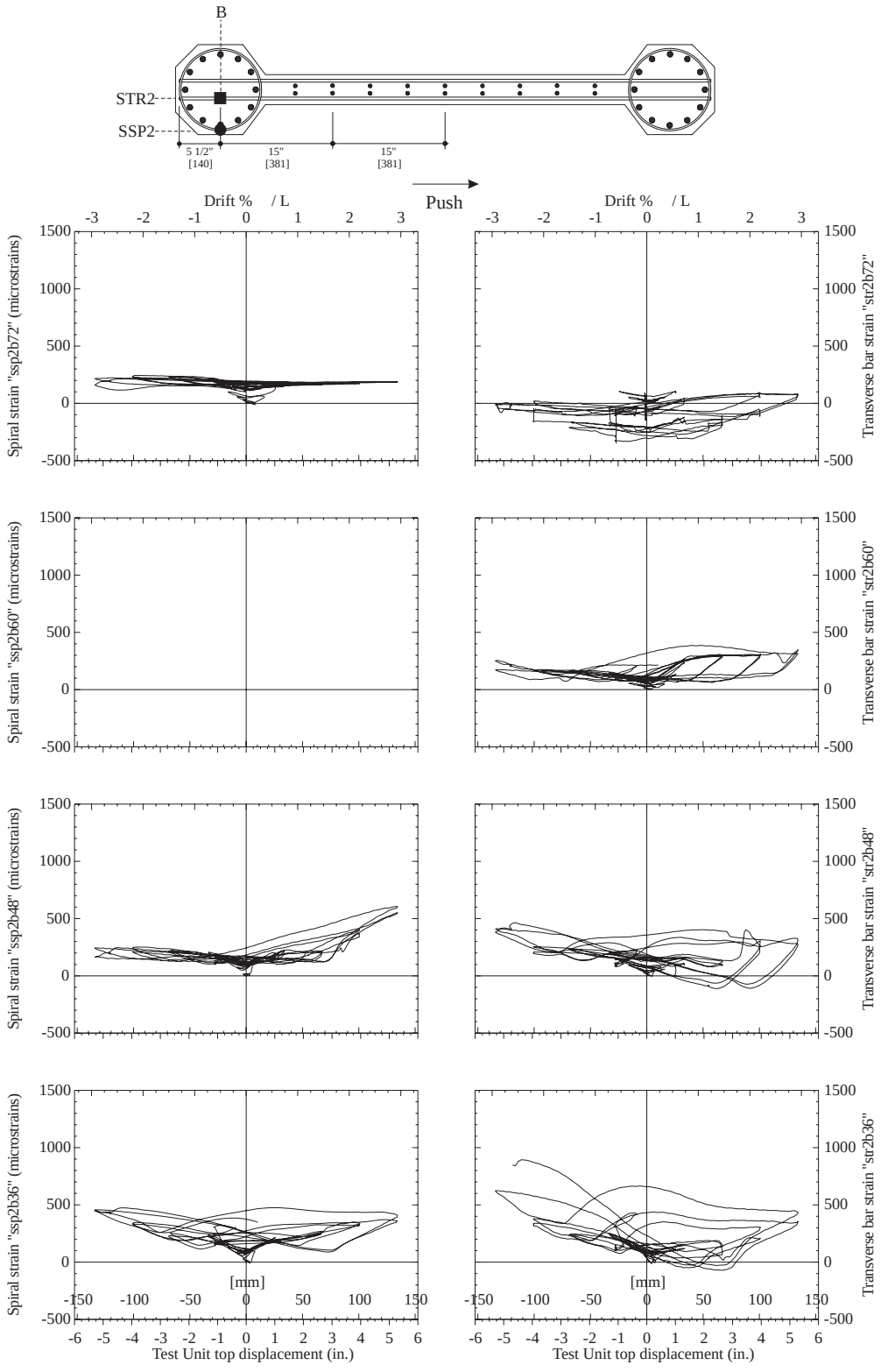

Figure 7.32: Test Unit 3C, spiral strains and transverse bar strains at Position B, for heights 36 in. [914], 48 in. [1219], 60 in. [1524] and 72 in. [1829] above the footing.

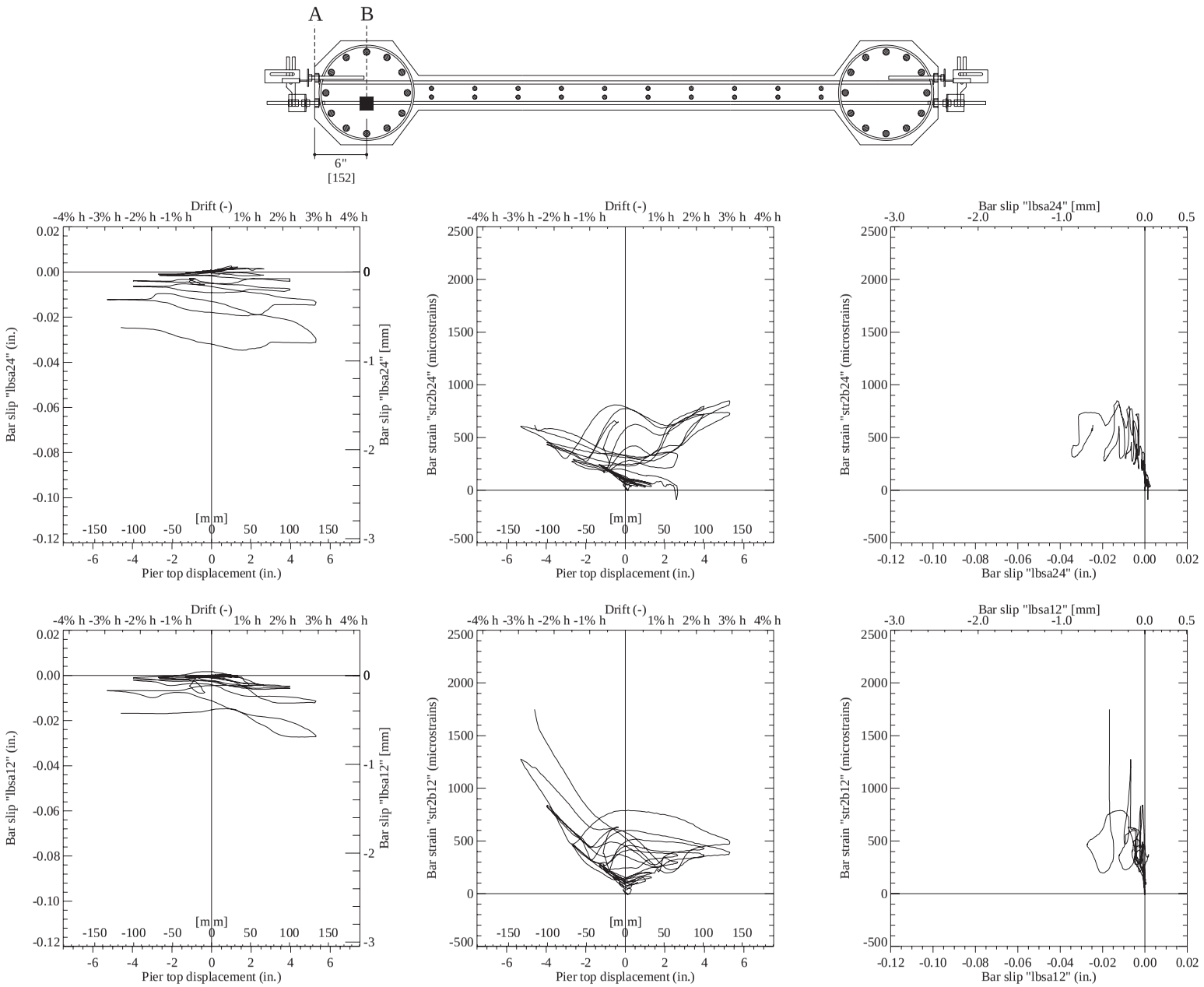

Figure 7.33: Test Unit 3C bar slip and transverse bar strain histories at positions A and B, 12 in. [305] and 24 in. [610] above the footing. Push (positive) direction is south.

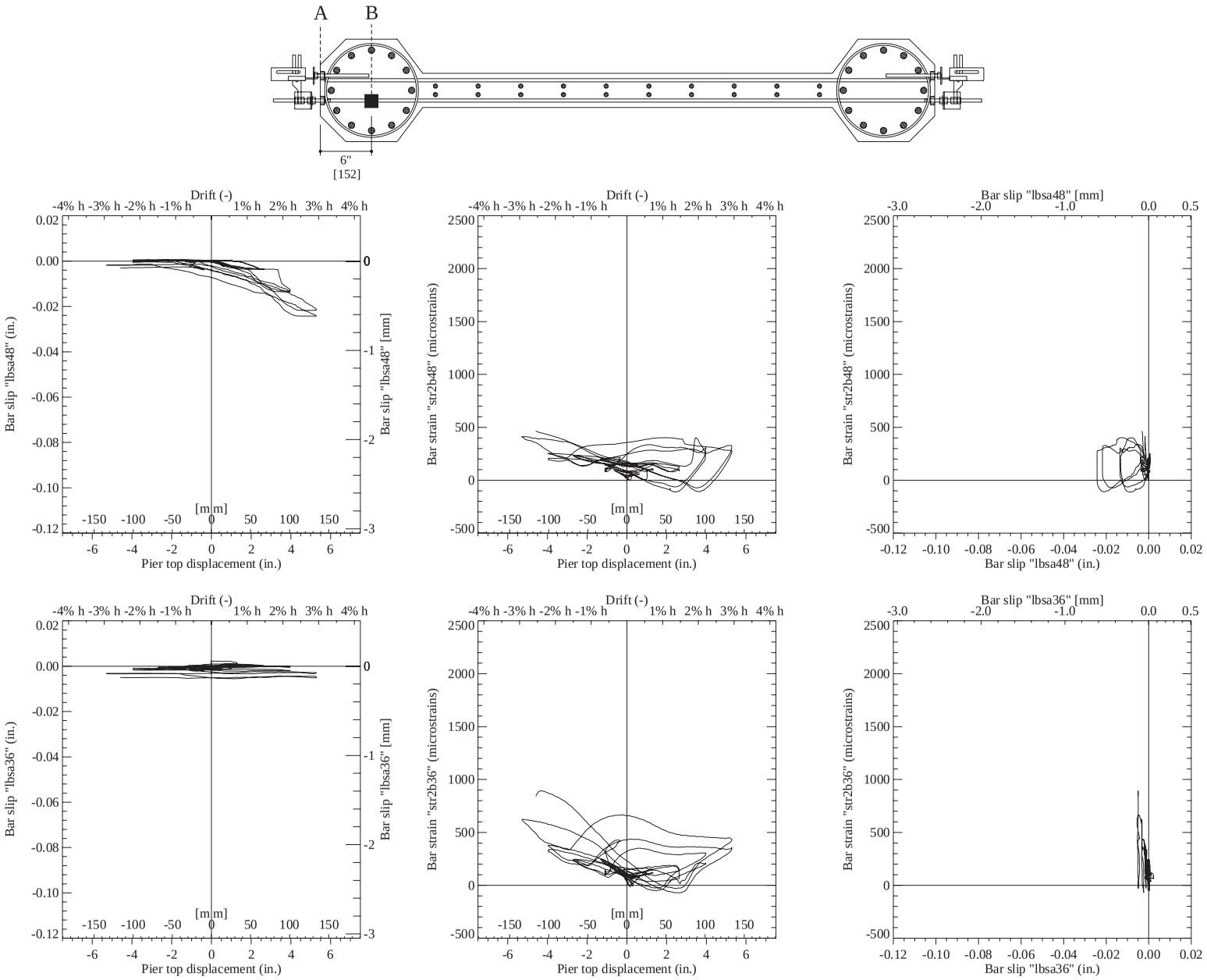

Figure 7.34: Test Unit 3C bar slip and transverse bar strain histories at positions A and B, 36 in. [914] and 48 in. [1219] above the footing. Push (positive) direction is south.

Chapter 8

Conclusions

8.1 Overview

Design and analysis issues are discussed on the basis of the test results from this Phase III report and from the report covering Phases I and II [1]. Design recommendations are given where possible and key issues for future research are highlighted.

8.2 Failure Mechanisms

The eight structural walls with highly-confined boundary elements that have been tested under this task (five from Phases I and II [1] and three from Phase III, reported herein) have each failed in one of three ways. For each failure mode, the wall and boundary elements performed to at least a displacement ductility level of $\mu_\Delta = 4$ before failing. Simple moment-curvature analyses and assumed plastic hinge lengths predicted the force-deflection behavior of all eight test units with sufficient accuracy. These simple predictions were regularly at least as accurate as predictions based on three dimensional, non-linear finite element models.

1. Flexural Failure: The wall and boundary elements exhibited a high ductility capacity as an integral section up through the third cycle of $\mu_\Delta = 6$ or the first cycle of $\mu_\Delta = 8$. The test units finally failed by buckling and fracture of the longitudinal reinforcement. Spirals were generally not observed to fracture, because of their high volumetric confinement ratio. When the spirals were observed to strain significantly, their strains were due more to buckling of the longitudinal bars than to expansion of the confined concrete. This behavior implied that flexural strain limit states for the boundary element

confined concrete should be based on steel strains rather than concrete strains. The exact nature of these steel strains still has to be investigated, as it is intimately linked to their buckling behavior. Several researchers have already begun to address this issue [22, 23, 17].

2. Tensile Shear Failure: The wall and boundary elements exhibited a high ductility capacity as an integral section, with post yield strains in the wall transverse reinforcement. These high strains in the wall accounted for increased shear deformations and large shear cracks in the wall. While cycling at $\mu_\Delta = 8$, the shear cracks in the wall grew large enough to allow the individual diamond-shaped concrete chunks in the wall at column midheight to crumble and fall out, leaving the once integral section to behave more similarly to a frame. The steel itself did not fracture before the wall literally fell apart under the cyclic loading. This failure mode resulted in a somewhat lower overstrength than the flexural failure mode, where the shear cracking was kept to a lower level. The failure was more gradual than catastrophic and still allowed the column to reach the same level of displacement ductility as a column that failed in flexure.

3. Compressive Shear Failure (Web Crushing Failure): The wall and the boundary elements exhibited a substantial ductility capacity as an integral section before the compression struts inside the plastic hinge region began to crush. After the first struts began to crush, the struts immediately above them slid downward along a vertical failure plane that grew between the wall and the compression boundary element. This resulted in a sudden drop in load capacity, until the column had formed an entirely new mechanism that acted like a frame with an average height of roughly 72 in. [1829] regardless of section depth. Until web crushing occurred, the test units exhibited stable hysteretic behavior, exceeding the allowable shear stresses defined by the ACI provisions [2].

These observed failures led to the conclusion that walls with highly-confined boundary elements exhibit a great degree of toughness, and are very unlikely to experience brittle shear failure. Even when the walls were designed with extremely thin webs or an extremely low amount of transverse reinforcement, a shear failure only occurred after the wall had reached a displacement ductility level of at least $\mu_\Delta = 4$, which was generally beyond the displacement capacity level required to resist a maximum credible earthquake event.

8.3 Web Crushing Strength

The three test units presented in this report designed to fail in web crushing failed at displacement ductility levels ranging from $\mu_\Delta = 4$ to $\mu_\Delta = 6$. Each test unit successfully carried average shear stresses higher than the $10\sqrt{f'_c}$ specified by ACI provisions [2]. Furthermore, the failure of each test unit was more dependent on displacement level than on force level, and the failures were uniformly observed to begin in the critical region discussed in Chapter 1. These two facts support the idea advanced in Chapter 1 that web crushing of such members should be evaluated according to a flexure-shear model of the test unit behavior, focusing on a critical region of the fanning crack pattern. Once the critical compression struts are identified and the demand on them has been estimated, their capacity can be evaluated based on the level of shear deformation they are expected to see. If shear displacements are assumed to be linearly proportional flexural displacements and the majority of shear deformation is assumed to occur inside the plastic hinge region, then the web crushing capacity can be evaluated simply as a function of flexural displacement. This was the case for the predictions presented in Chapter 5. The flexure-shear model for web crushing could be refined further, with a more accurate assessment of the demand on the critical compression struts and their capacity, however the model presented in Chapter 1 proved adequate for the suite of tests reported here (see Figures 7.2, 7.13 and 7.24), and might therefore serve, in its current form, as a useful tool in assessing the flexure-shear web crushing strength of structural walls with boundary elements for a wide variety of relative depth ratios. It is important to exercise caution when evaluating the concrete strength. Little data exist for such failures at higher concrete strengths, and it is doubtful that the relationship between web crushing strength and concrete strength is perfectly linear, since much of the breakdown in strength can be attributed to shear cracking and cyclic demands on the compression struts. For this reason, it is prudent to limit the maximum conceivable compression strut strength to $f'_c = 6000$ psi [41.4 MPa], even if a higher concrete strength is used in the pier, until tests are completed that validate the linear proportionality of flexure-shear web crushing strength to concrete strength.

8.4 Architectural Concrete

Blockouts provided in the architectural concrete at the base of the boundary elements for all three test units mitigated the overall damage to the boundary element architectural concrete due to spalling. The test units, reaching displacement ductility levels of $\mu_\Delta = 4$ and greater, experienced less spalling than their counterparts that had been tested without architectural concrete blockouts [1]. What little spalling of the architectural concrete did occur, resulted from the interesection of vertical splitting cracks and horizontal flexural cracks. These cracks formed a grid from which some chunks of concrete then fell off when a boundary element experienced tension. More cycling loosened up the chunks to a greater degree. This issue of protecting the architectural concrete has been dealt with more thoroughly in other documents discussing the seismic performance of flared bridge columns [24, 25].

8.5 Transverse Reinforcement and Shear Capacity

Transverse reinforcement for Test Unit 3A, which was designed according to model outlined in Chapter 2, was observed to yield only slightly in the wall at $\mu_\Delta = 4$. Transverse reinforcement for Test Unit 3B, which was underreinforced was observed to strain as high as 15,000 $\mu\varepsilon$ in the wall, without yielding either the transverse bars or the spirals in the tension boundary element. Furthermore, no tension boundary element spirals acting in shear in any of the Phase I, II, or III test units were observed to yield at any level of displacement ductility, casting doubt on the assumption that these bars can be included at their yield stress as part of the V_s component of shear capacity. Transverse bars and spirals gaged at the same location in the middle of the tension boundary element were observed in Test Units 3A and 3B to reach strains that added up roughly to an equivalent yield strain. Since both the spirals and the transverse bars were #3 [#10] bars in the Phase III test units, it was convenient to assume that the transverse bars were capable of reaching their yield capacity if the spirals were not included in the calculation of the V_s component. It is recommended that a conservative estimation of the V_s component be calculated as

$$V_s = A_{str} f_{ytr} \frac{w_T}{s_{tr}} cot 35^\circ \tag{8.1}$$

where A_{str} is the total area of transverse reinforcement at a given vertical level, f_{ytr} is the yield stress of the transverse reinforcement, w_T is the distance between the neutral axis and the centroid of tension (which can be assumed to act approximately at the center of the tension boundary element), s_{tr} is the vertical spacing of transverse reinforcement and 35° is taken from the vertical axis.

In light of this reduction in the effectiveness of transverse reinforcement from the model assumed in Chapter 2, the high shear capacity of the test units with or without large shear cracks in the wall should still be reflected in an increased V_c component. This increase was attributed to the high level of confinement in the boundary elements, which both strengthened the compression toe and increased the effectiveness of aggregate interlock and dowel action in the tension boundary element. The V_c component can therefore be calculated as

$$V_c = \alpha\beta\gamma\sqrt{f'_c}A_e \tag{8.2}$$

where

$$A_e = 0.8A_g \tag{8.3}$$

and where α, β and γ are explained in Chapter 5. A_g in Equation 8.3 should be taken as the gross area of the section acting in plane, including the boundary elements. Under this assumption, the V_c component will provide a proportionally greater contribution to column shear strength as the relative depth ratio (D_w/D_b) decreases. This is consistent with test observations that the boundary elements appeared to offer greater a contribution to the total shear strength in Test Unit 3B than in Test Unit 3C.

8.6 Anchorage Details

No anchorage details were provided on the transverse bars in the Phase III test units in order to answer questions about their ability to develop yield capacity inside of the tension boundary element. Confirming results reported for Phase I [1], the transverse bars were observed to slip significantly only inside of the plastic region, where flexural crack widths exceeded 0.008 in. [0.2]. In this region, slightly less than one section depth above the footing, slippage of the transverse bars was observed to cause direct losses in strain capacity at the center of the boundary element. Outside of the plastic region and prior to plastic deformations,

however, the transverse bars slipped much less and this little amount of slippage appeared not to affect their ability to develop strains. Since the transverse reinforcement inside the plastic hinge region is generally not as critical to overall test unit behavior as the transverse reinforcement higher up the column, the slippage inside of the plastic region was considered acceptable and not detrimental to the overall performance of the column. Leaving the transverse reinforcing bars straight greatly eased the construction process without impairing the columns from performing as expected.

Since the boundary elements of such columns were generally well confined, both by the spiral reinforcement and the longitudinal reinforcing bar cage, an equation for development length was developed that assumed an average ultimate bond stress of $14\sqrt{f'_c}$. This value was assumed sufficiently conservative for anchoring longitudinal reinforcement into bent caps [7] where average ultimate bond stresses had been observed to be as high as $30\sqrt{f'_c}$. Assuming uniformly distributed bond stresses, an acceptable development length of transverse bars in confined tension boundary elements outside of the plastic hinge region can be written as

$$l_b = \frac{0.018 d_b f_y}{\sqrt{f'_c}} \qquad (psi) \tag{8.4}$$

which has a slightly lower coefficient than the Equation developed for cap beams assuming the same bond stress, because the overstrength of the transverse bars was considered irrelevant, since such bars are designed not to strain beyond their yield point. For the #3 [#10] transverse bars in the Phase III test units, with $f'_c = 5930$ psi [40.9 MPa] and $f_y = 63{,}000$ psi [434 MPa], Equation 8.4 gives a development length of 5.5 in. [140], obtaining yield capacity close to the center of the tension boundary element. The corresponding ACI Equation 12.2.3 [2], assuming α, β, γ and λ all equal to one, gives

$$l_b = \frac{0.030 d_b f_y}{\sqrt{f'_c}} \qquad .(psi) \tag{8.5}$$

which for the same bar gives a development length of 9.1 in. [232] and an average ultimate bond stress of $8.4\sqrt{f'_c}$.

8.7 Final Remarks

The walls tested in Phase III of this research project on the seismic performance of hollow rectangular reinforced concrete piers with highly-confined boundary elements have given

more complete insight into the shear capacity of such piers. The web crushing failures observed in this Phase III occurred at a level of displacement ductility that exceeded the expected response under a maximum credible earthquake, and proved that even when such piers are expected to fail in shear, they still exhibit substantial toughness. The columns' failures in web crushing inside the critical region introduced in Chapter 1 and the dependence of these failures on column deformation more than applied shear force validated the assumptions on which the flexure-shear model discussed in Chapter 1 for web crushing was based. More work is needed to establish the true relationship between flexure-shear web crushing strength and concrete strength. This reflects a general need in seismic research to investigate further the application of high strength concrete to seismic design.

Spiral and transverse bar strains in the tension boundary elements provided sufficient insight into the steel component of shear resistance, to define a conservative approach for calculating V_s and V_c. Transverse bar slippage measurements and transverse bars strains in the tension boundary elements showed that transverse bars without special anchorage details slipped only inside the plastic zone, roughly one section depth high above the footing, where they are not needed to develop their full shear capacity. It was therefore thought sufficient to assume a rather high value of average ultimate bond stress ($14\sqrt{f'_c}$ (psi)) in calculating their development length, resulting in 40% less development length than required by ACI [2] for a fully-confined section.

Results from the in-plane behavior of the test units reported for Phases I and II [1] and in this third phase, should be generalized to assess the three dimensional behavior of hollow piers with highly-confined boundary elements. Assuming that the shear requirements discussed in this report are satisfied, the force-deflection behavior of such piers could be modeled with reasonable accuracy in the bridge longitudinal and transverse directions based on moment-curvature analyses, with assumed plastic hinge lengths, conservative steel strain limit states and assumed shear displacements that are proportional to the flexural displacements.

Appendix A

Photos of Construction

This appendix contains photos taken during the construction. Chapter 3 refers to these photos in explaining the construction process of the Phase III Web Crushing Test Units.

Figure A.1: Typical boundary element reinforcement cages.

Figure A.2: Iron workers tie the footing cages of Units 3A and 3B.

Figure A.4: The column reinforcement cage of Test Unit 3A.

Figure A.3: The footing reinforcement cage of Test Unit 3A.

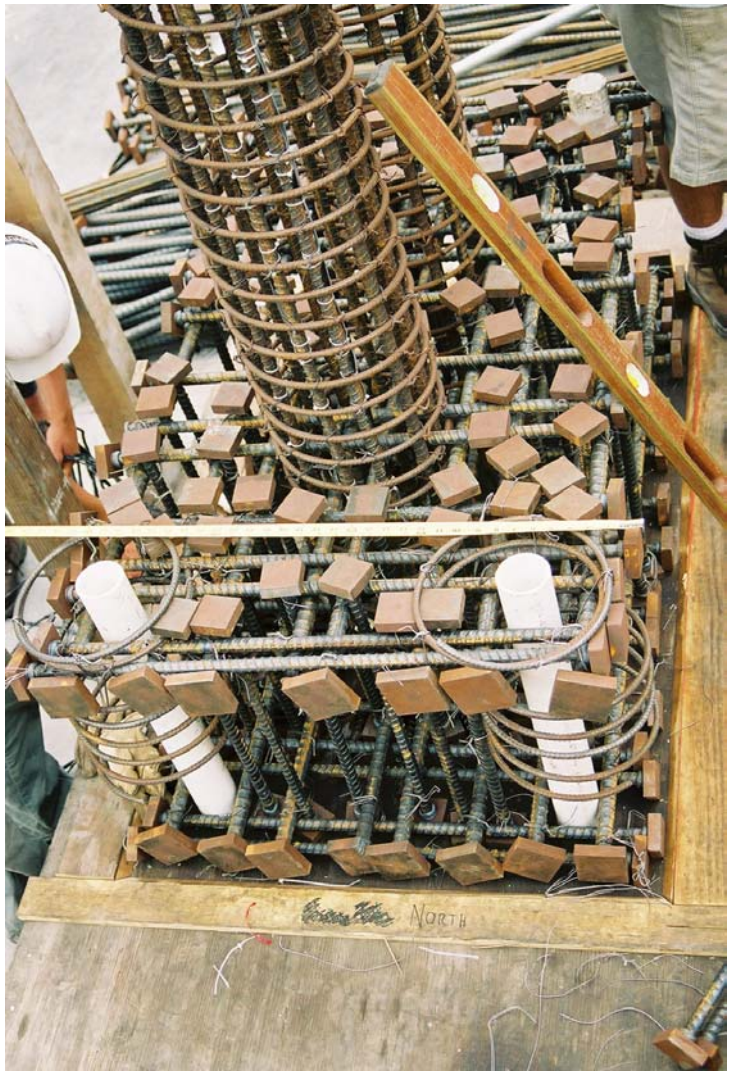

Figure A.5: The footing reinforcement cage of Test Unit 3B.

Figure A.6: The column reinforcement cage of Test Unit 3B.

Figure A.7: Iron workers align vertically the boundary elements of Test Unit 3C.

Figure A.8: The column reinforcement cage of Test Unit 3C.

Figure A.9: From left to right, Test Units 3B, 3A and 3C assembled in the laboratory with footings poured and some transverse reinforcement tied.

Figure A.10: Typical architectural concrete blockout at the base of a column boundary element.

Figure A.11: Arial view of the three test units before pouring the columns and load stubs.

Figure A.12: An indefatigable construction crew stands atop their scaffolding for Column 3C.

Appendix B

Test Photos

This appendix contains photos taken during the test. Chapter 6 refers to these photos in explaining the test observations for test units 3A, 3B and 3C.

B.1 Test Unit 3A

Figure B.1: μ_Δ 1 x +1; Test Unit 3A, east face. Push (positive) direction is south.

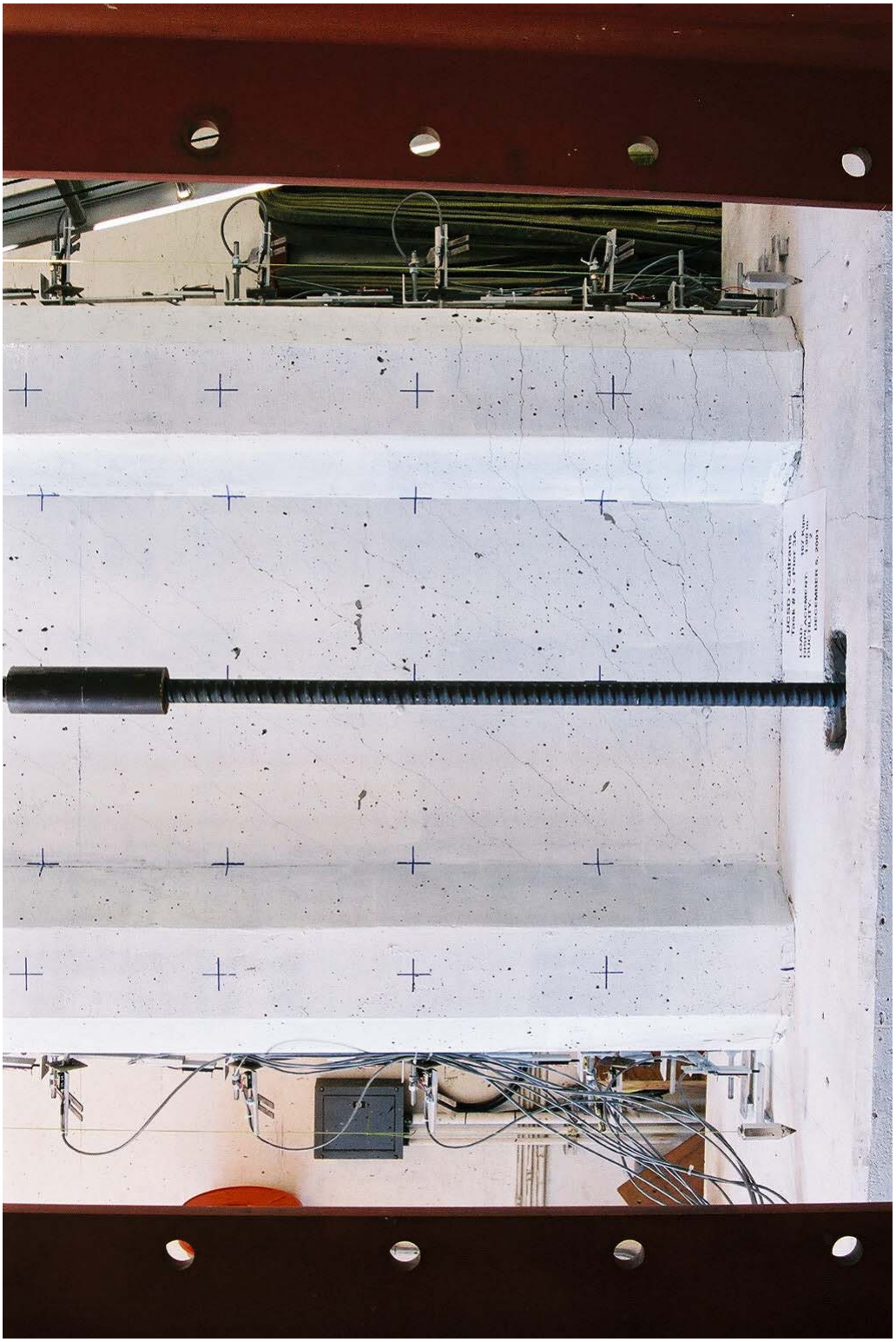

Figure B.2: μ_Δ 2 x +1; Test Unit 3A, east face. Push (positive) direction is south.

Figure B.3: μ_Δ 2 x +1; Test Unit 3A, splitting cracks on compression (south) boundary element.

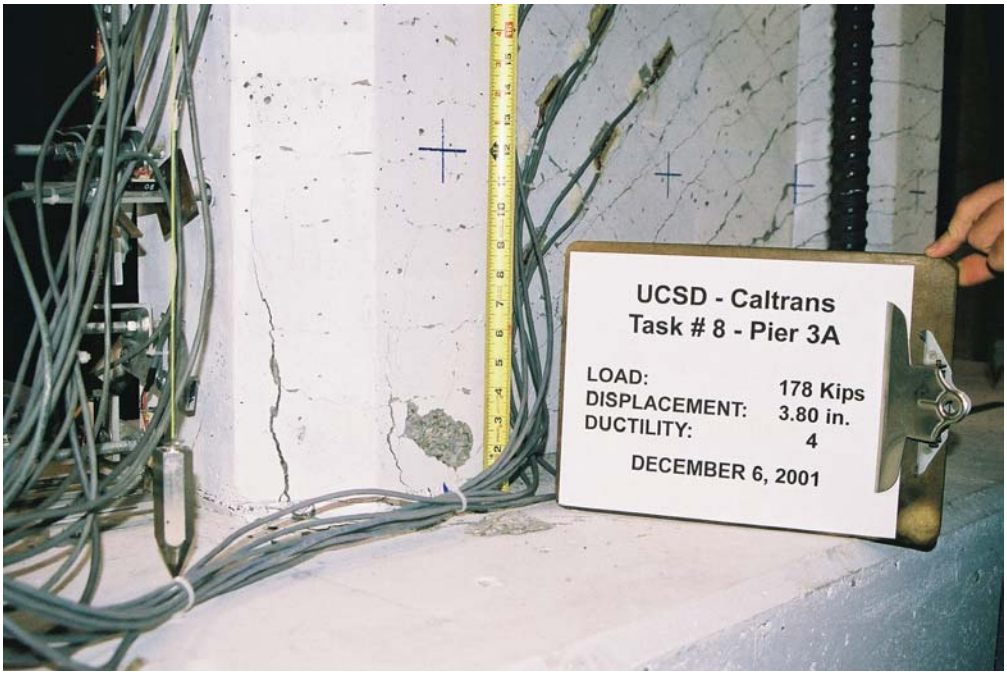

Figure B.4: μ_Δ 4 x +1; Test Unit 3A, splitting cracks and spalling on compression (south) boundary element.

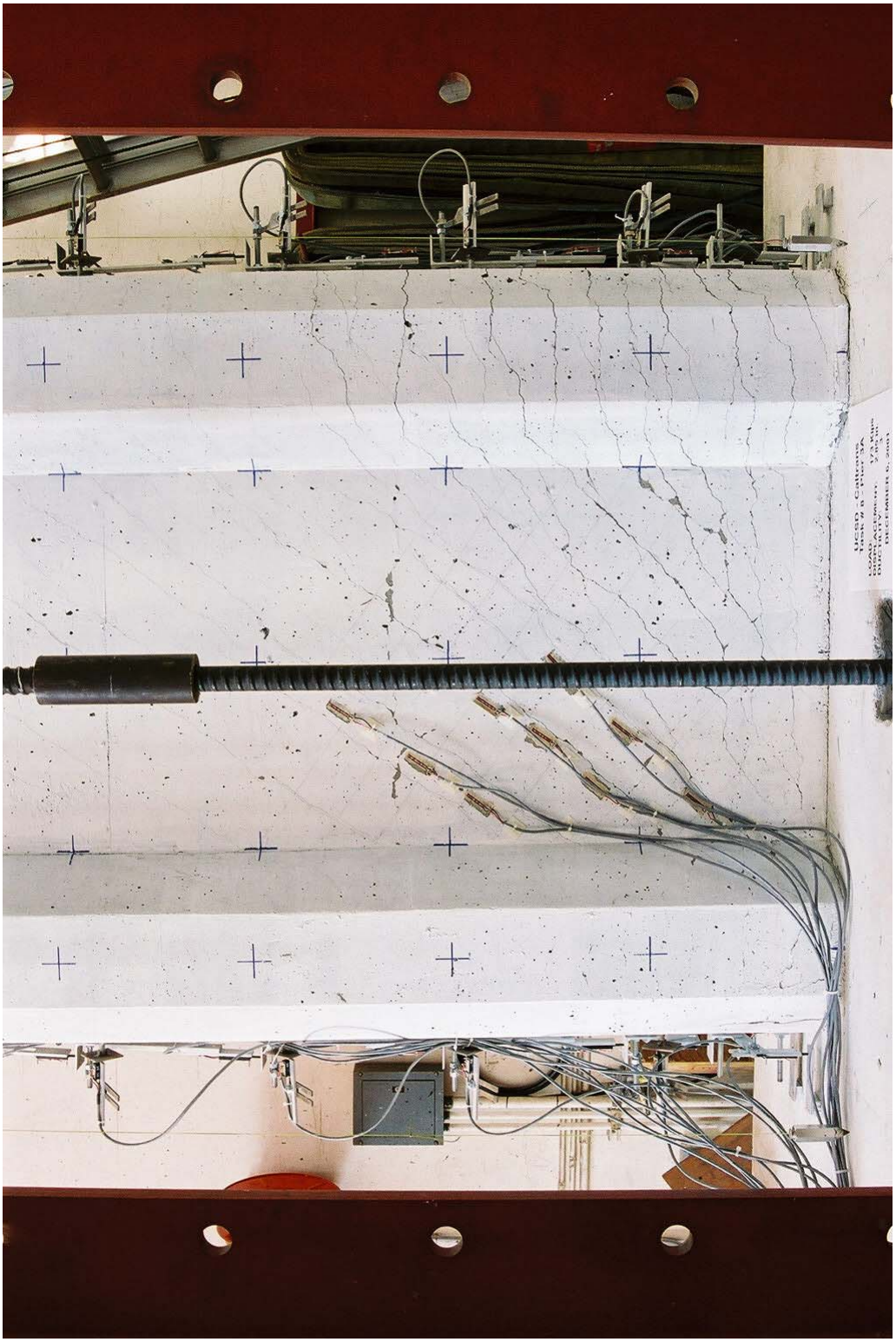

Figure B.5: μ_Δ 3 x +1; Test Unit 3A, east face. Push (positive) direction is south.

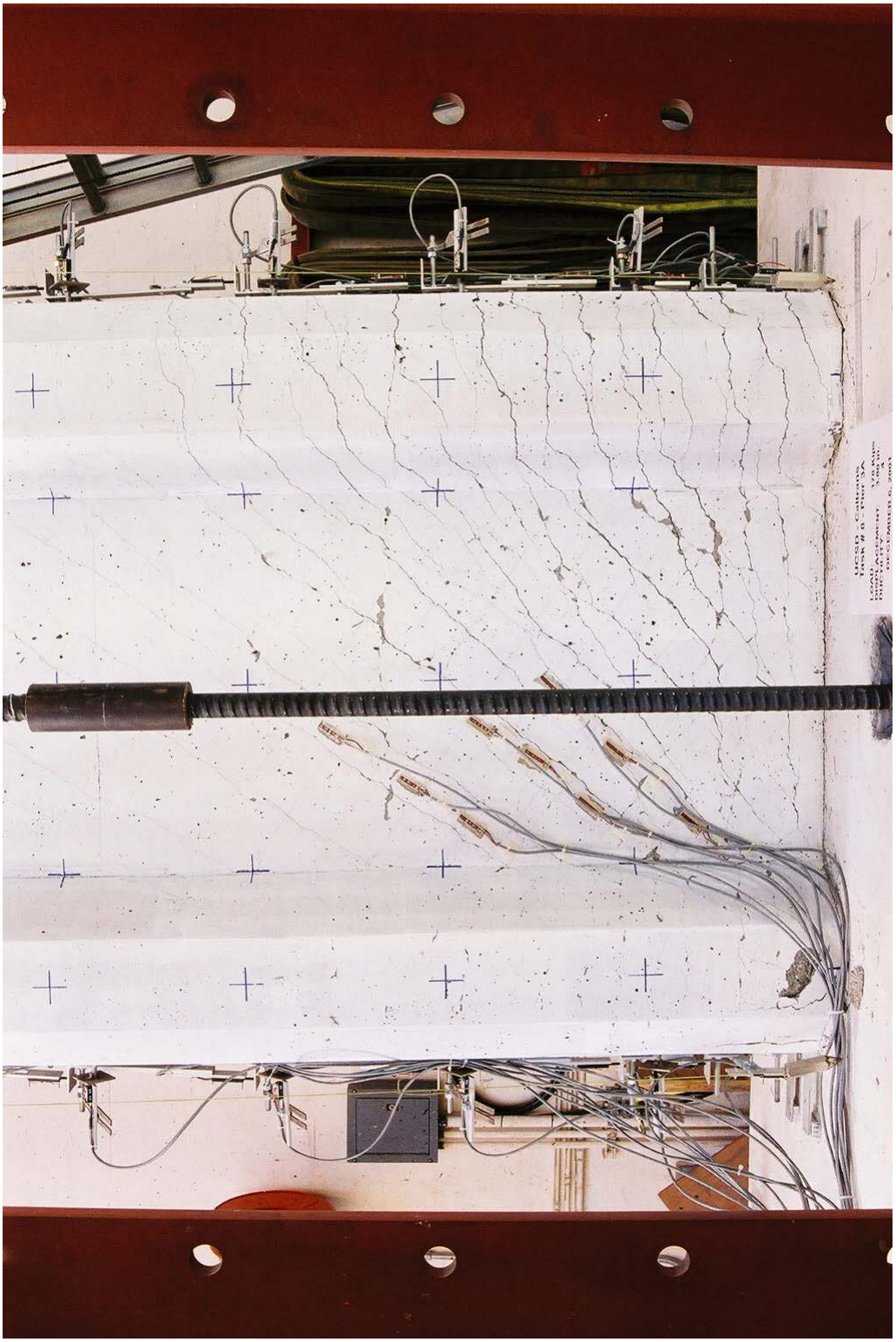

Figure B.6: μ_Δ 4 x +1; Test Unit 3A, east face. Push (positive) direction is south.

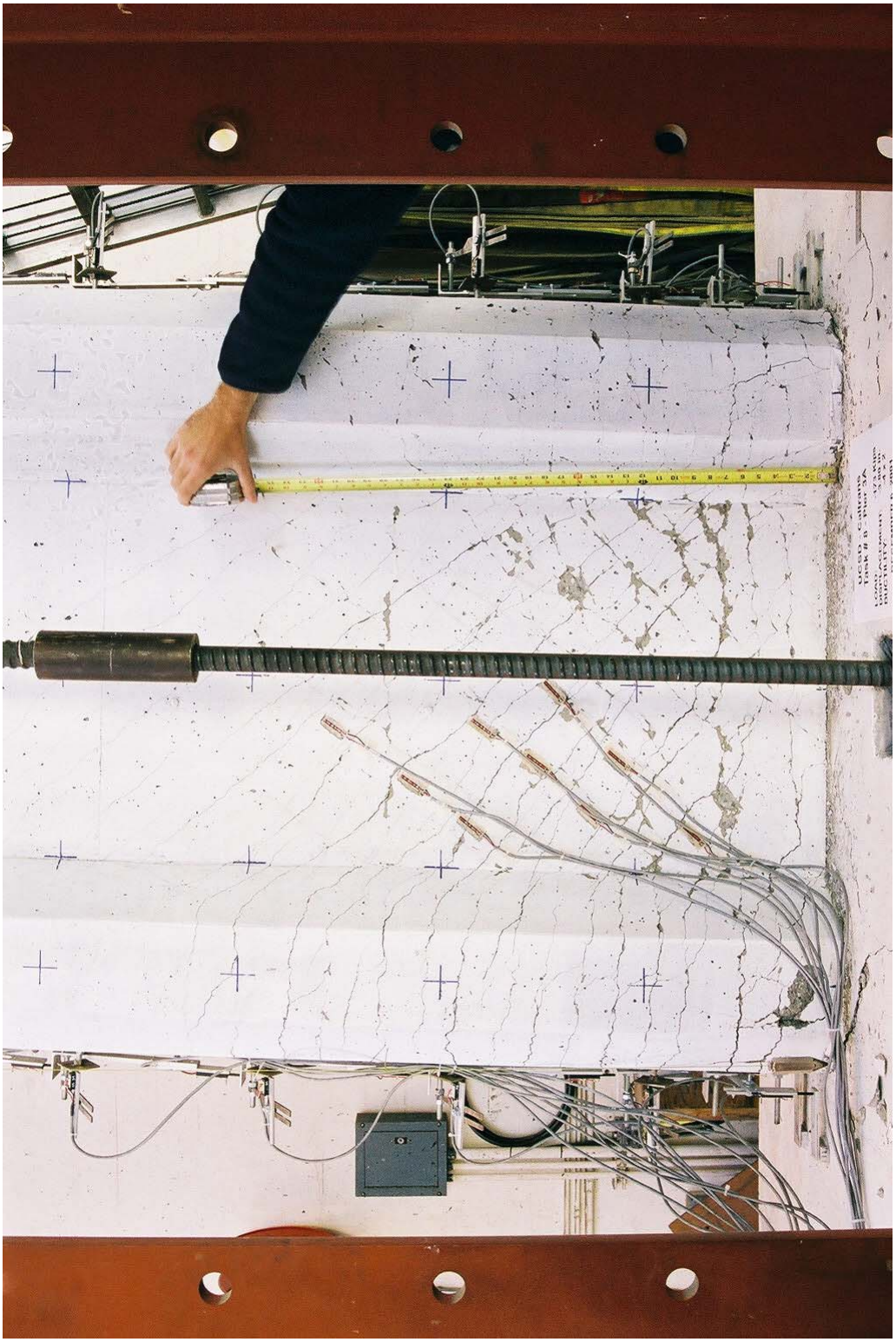

Figure B.7: μ_Δ 4 x -2; Test Unit 3A, east face. Push (positive) direction is south.

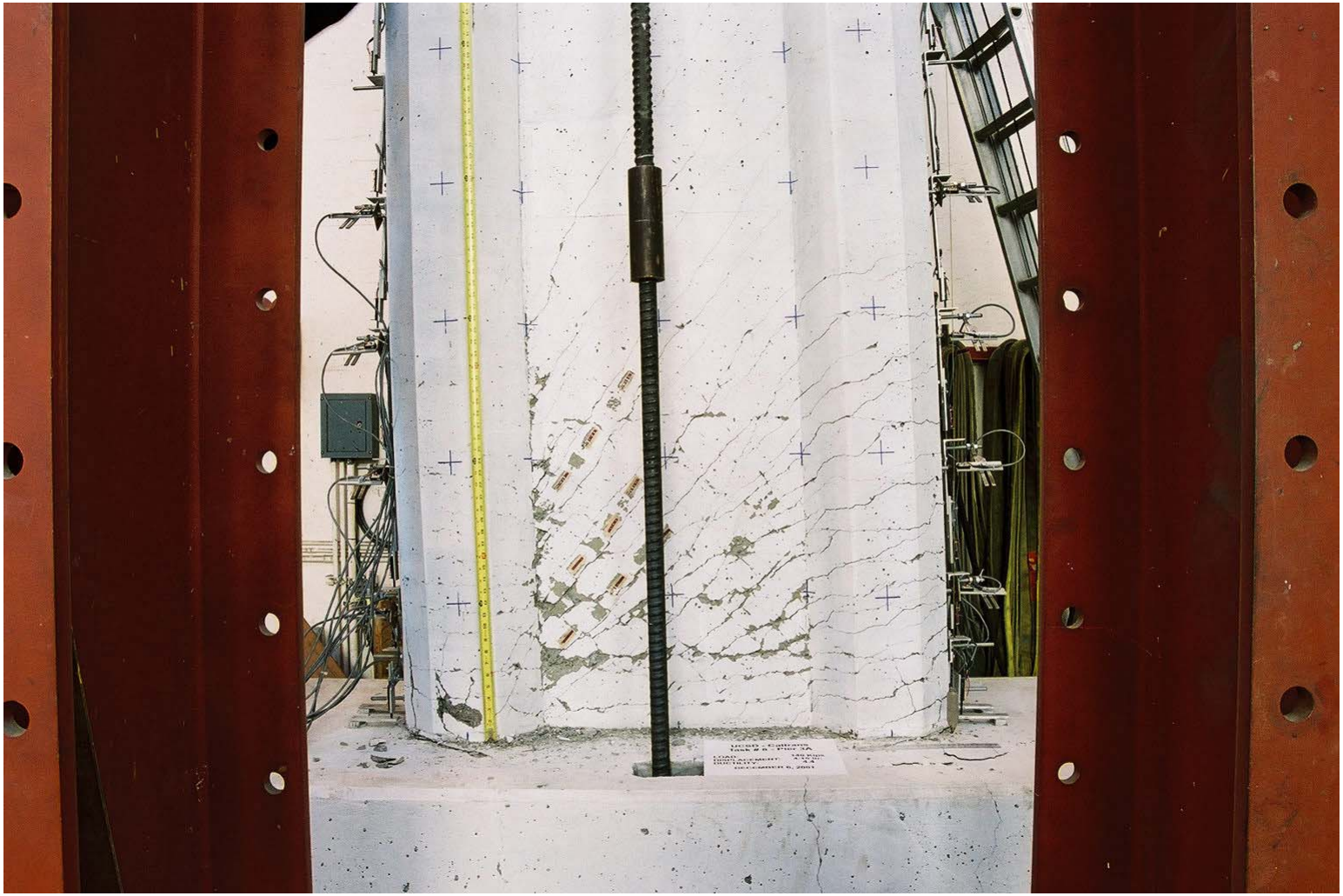

Figure B.8: μ_Δ .4 x +1 Test Unit 3A, east face. Push (positive) direction is south.

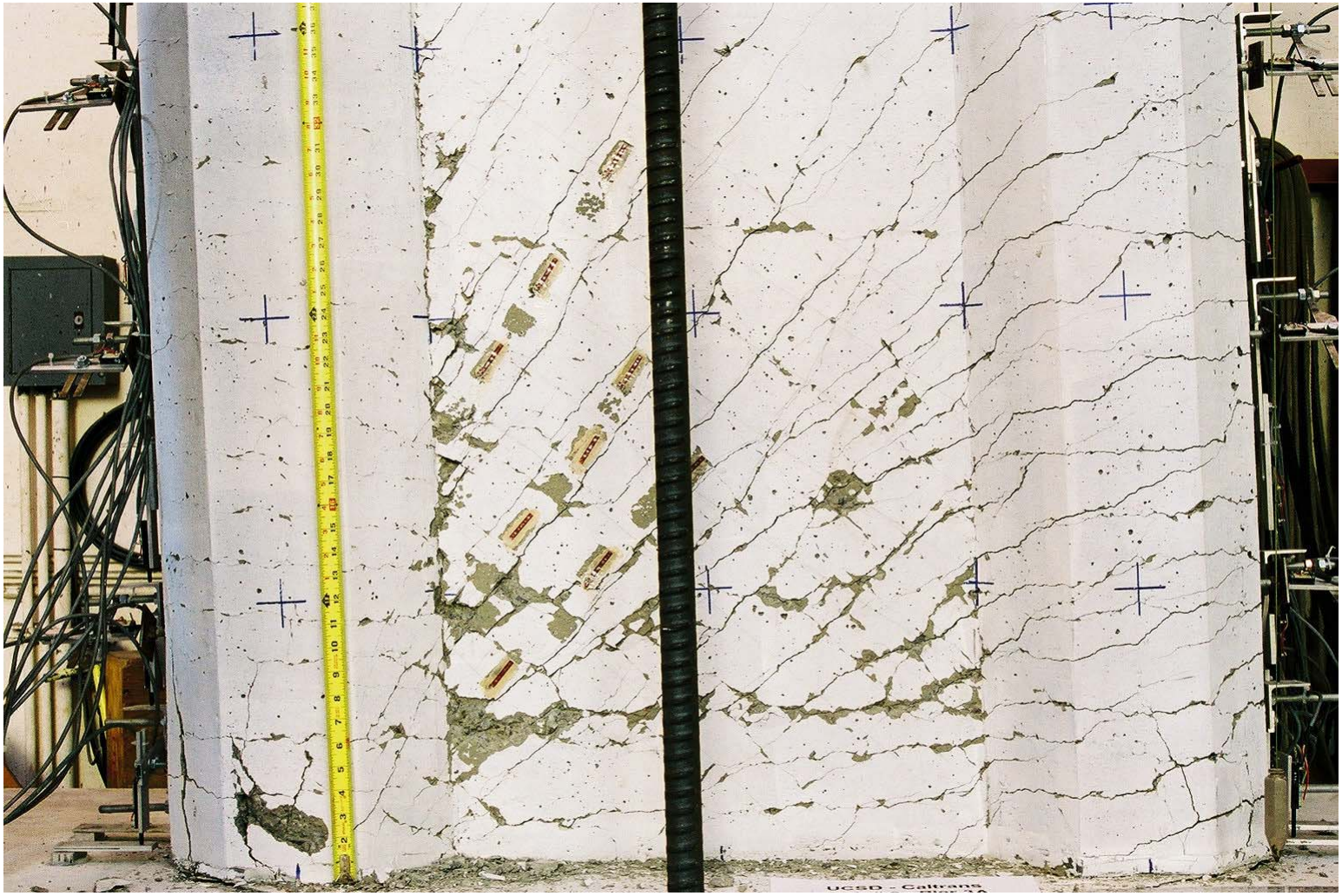

Figure B.9: μ_Δ .4 x +1 Test Unit 3A, closeup of east face. Push (positive) direction is south.

B.2 Test Unit 3B

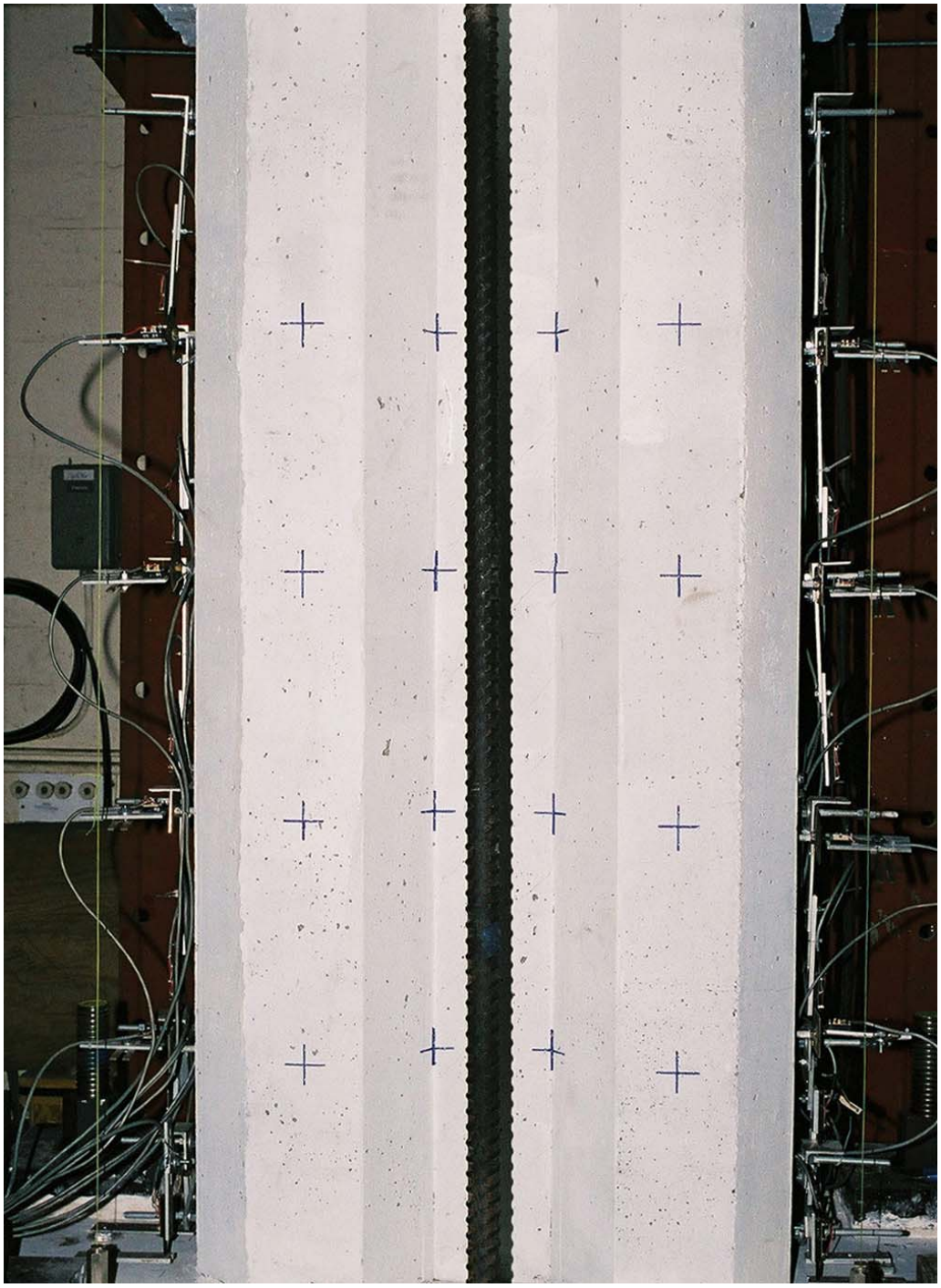

Figure B.10: μ_Δ 1 x +1; Test Unit 3B, east face. Push (positive) direction is south.

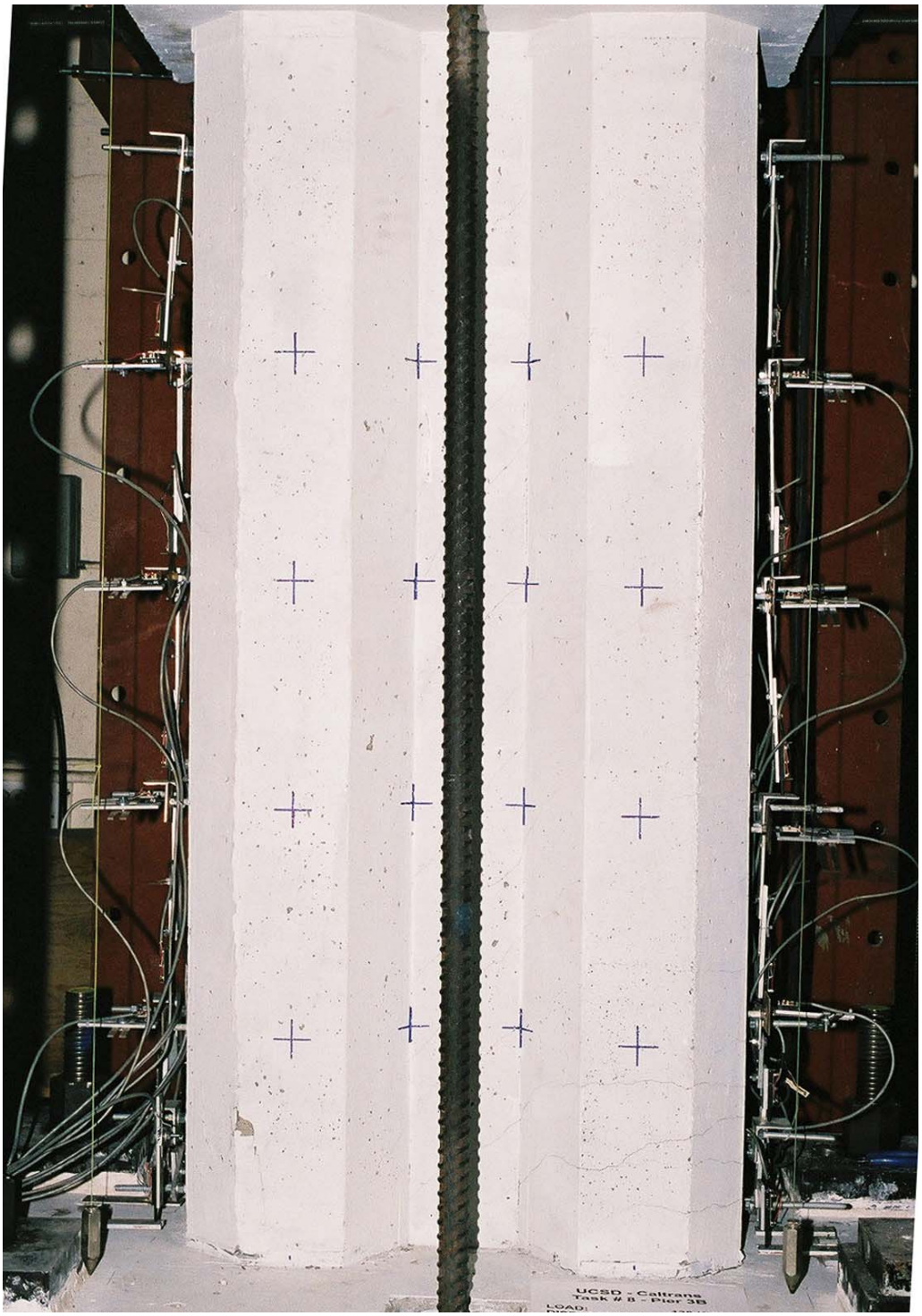

Figure B.11: μ_Δ 2 x +1; Test Unit 3B, east face. Push (positive) direction is south.

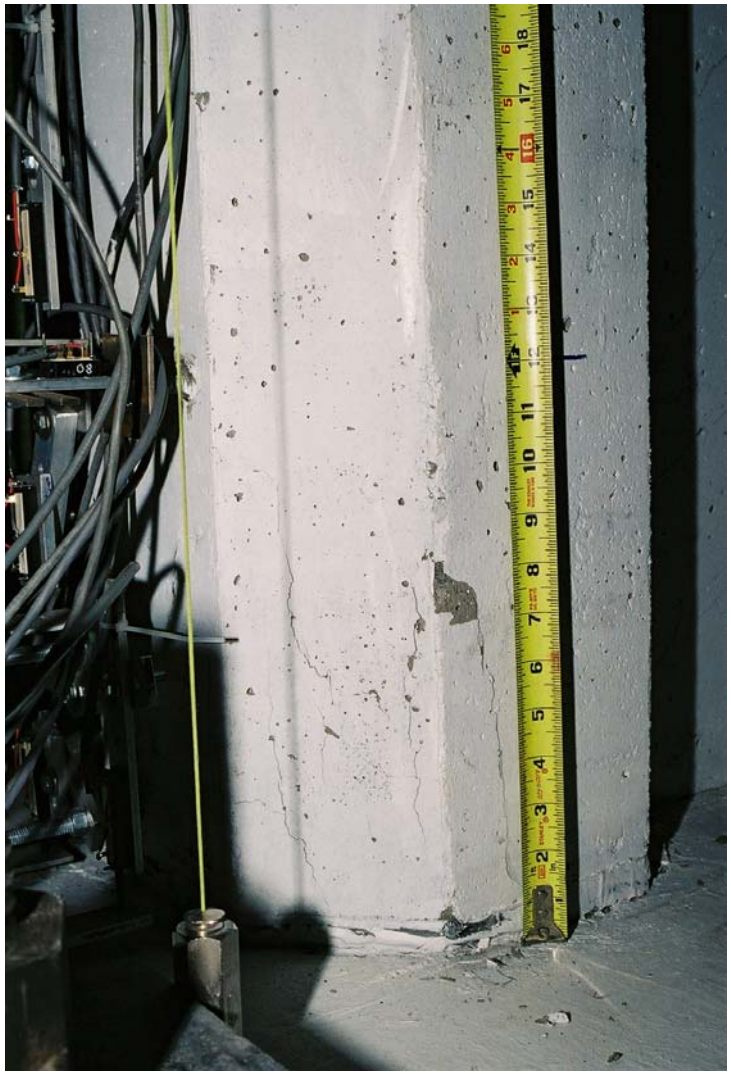

Figure B.12: μ_Δ 2 x +1; Test Unit 3B, vertical splitting crac est face of compression (south) boundary element. Push (positive) direction is south.

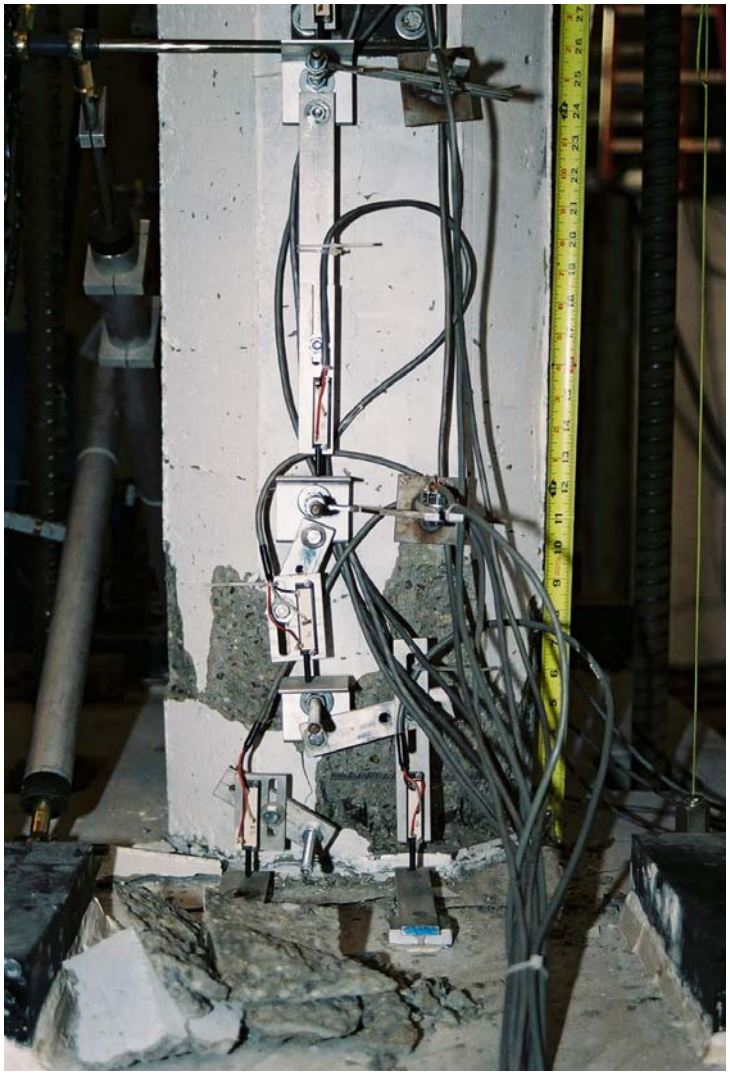

Figure B.13: μ_Δ 4 x 1; Test Unit 3B, spalled region on west face of tension (south) boundary element. Push (positive) direction is south.

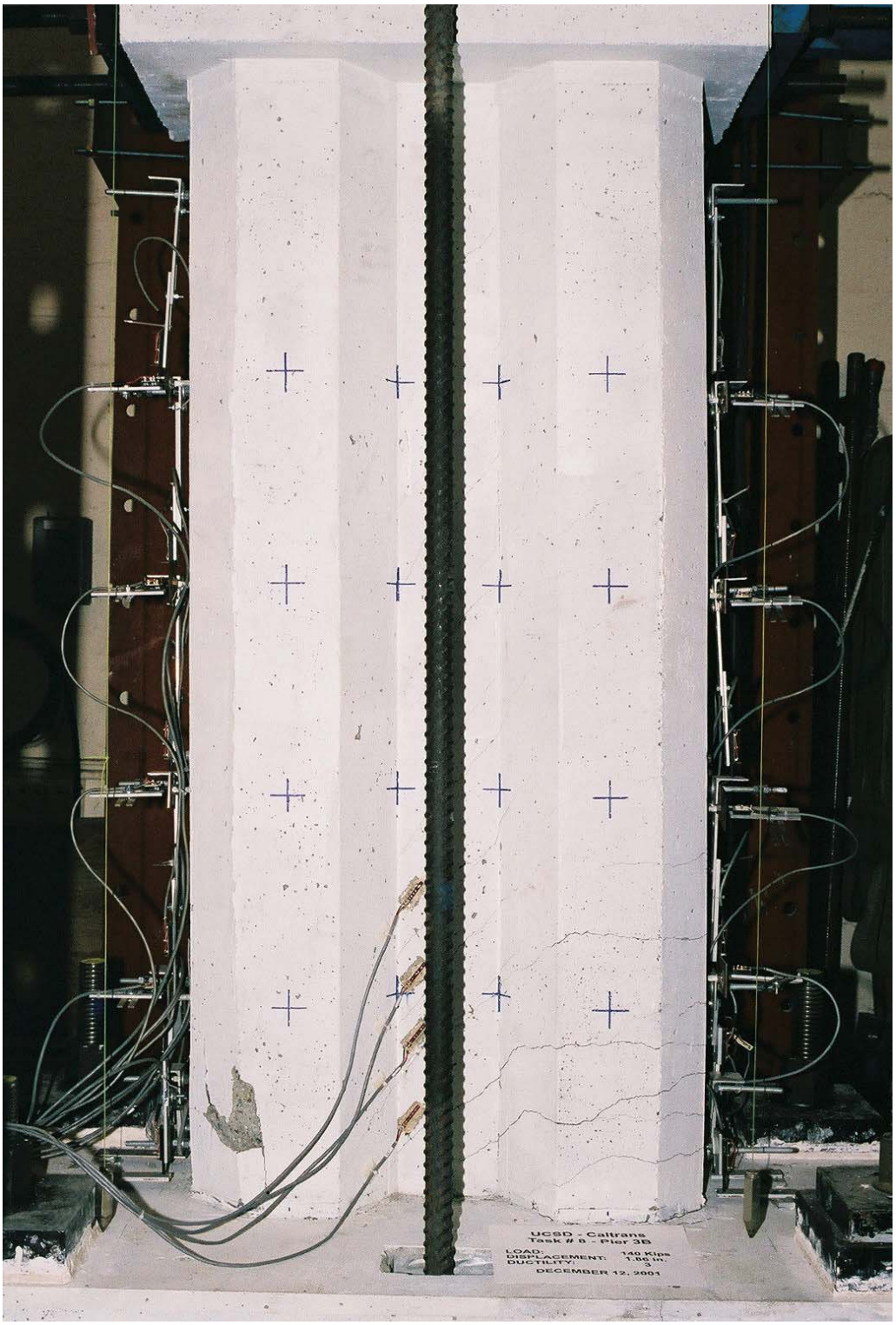

Figure B.14: μ_Δ 3 x +1; Test Unit 3B, east face. Push (positive) direction is south.

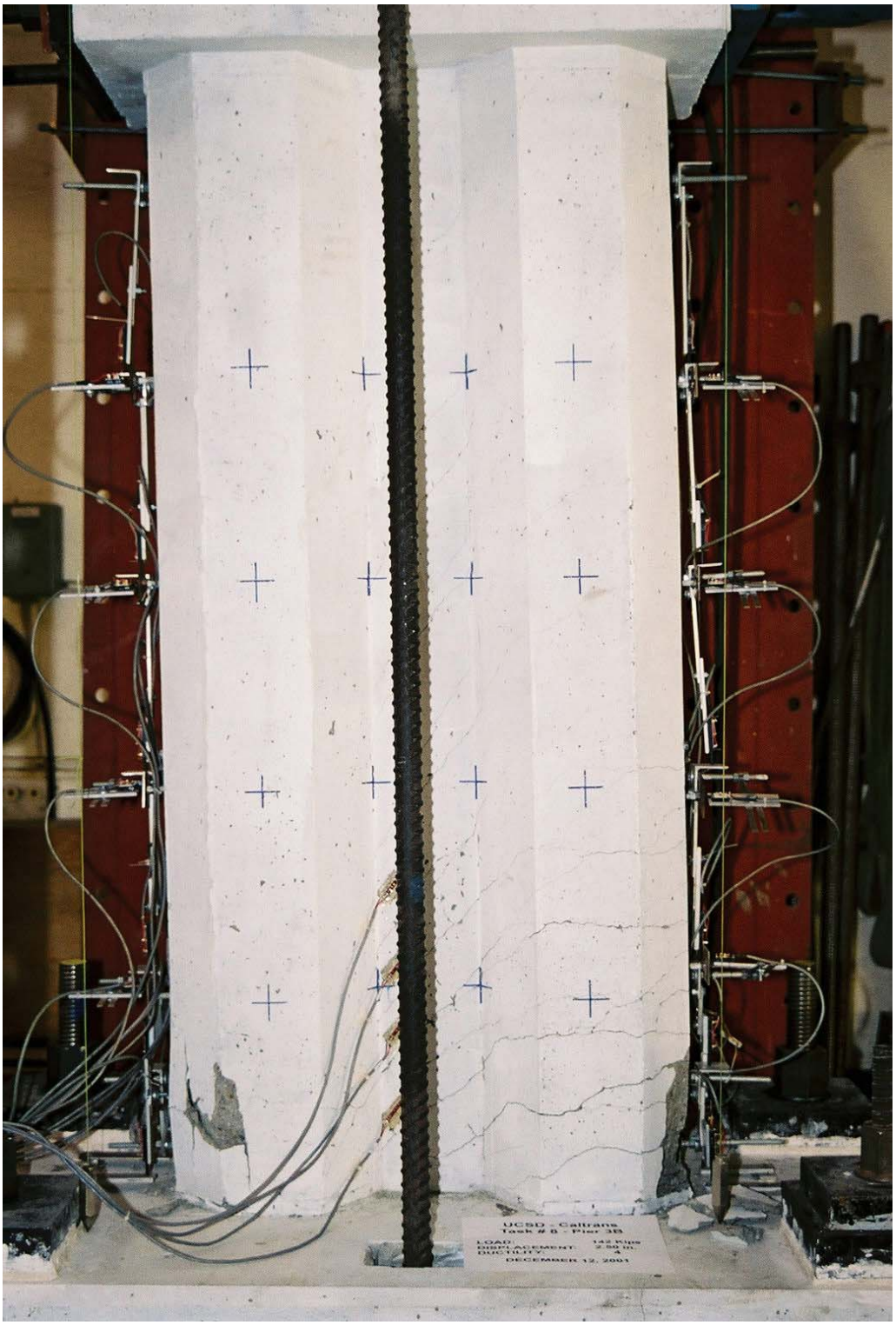

Figure B.15: μ_Δ 4 x +1; Test Unit 3B, east face. Push (positive) direction is south.

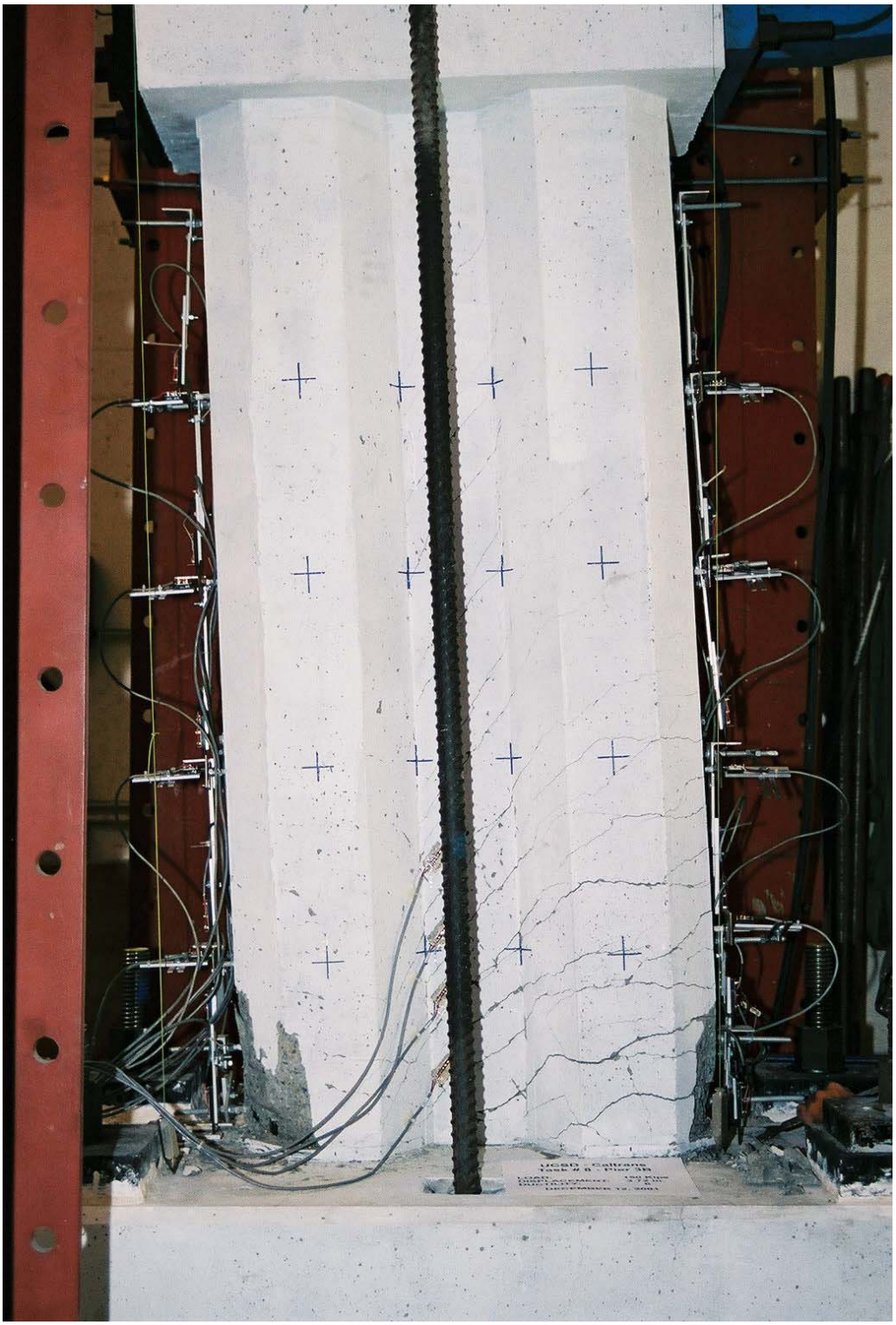

Figure B.16: μ_Δ 6 x +1; Test Unit 3B, east face. Push (positive) direction is south.

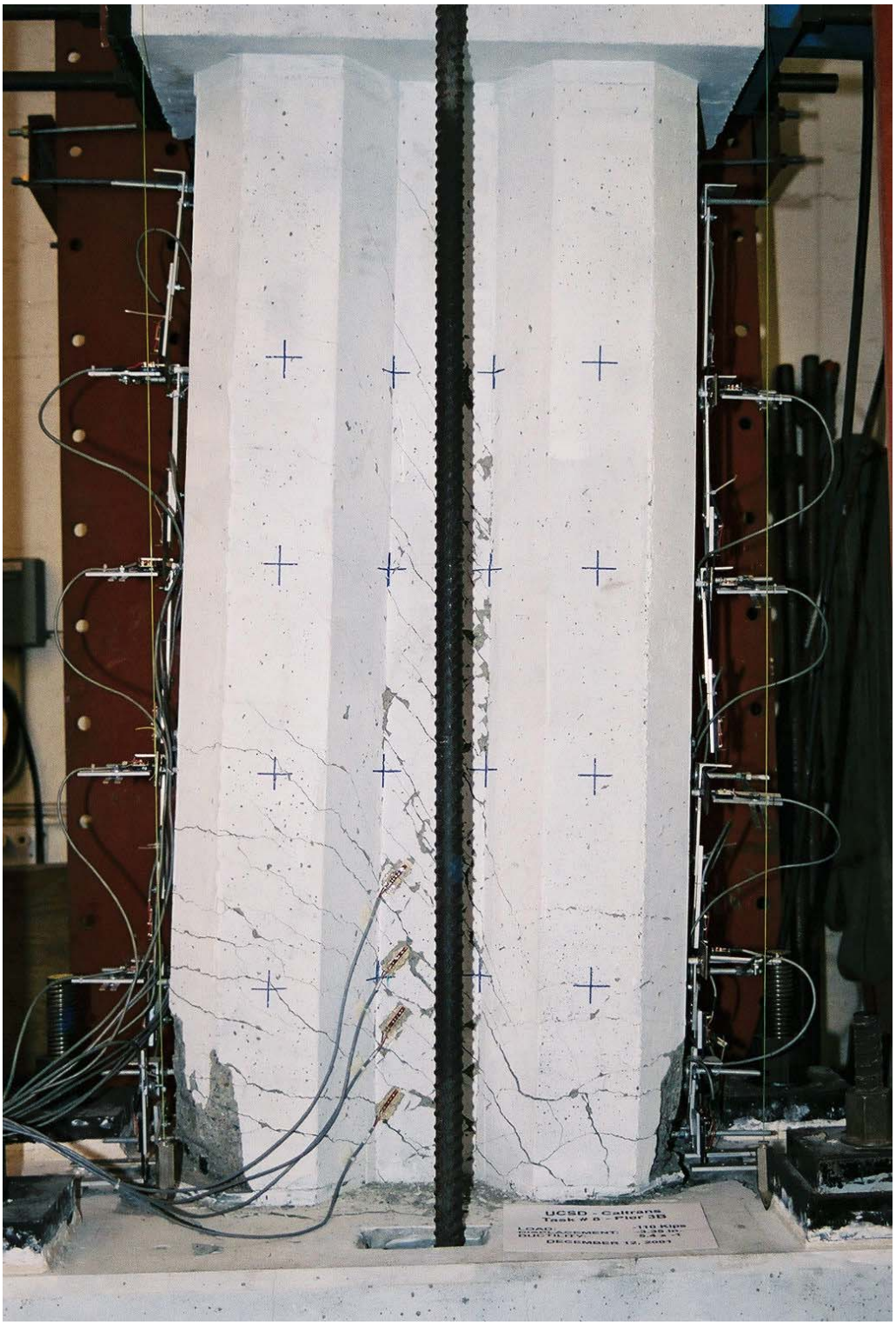

Figure B.17: μ_Δ 5.4 x -1; Test Unit 3B, east face. Push (positive) direction is south.

Figure B.18: μ_Δ 5.4 x -1; Test Unit 3B, closeup of east face. Push (positive) direction is south.

B.3 Test Unit 3C

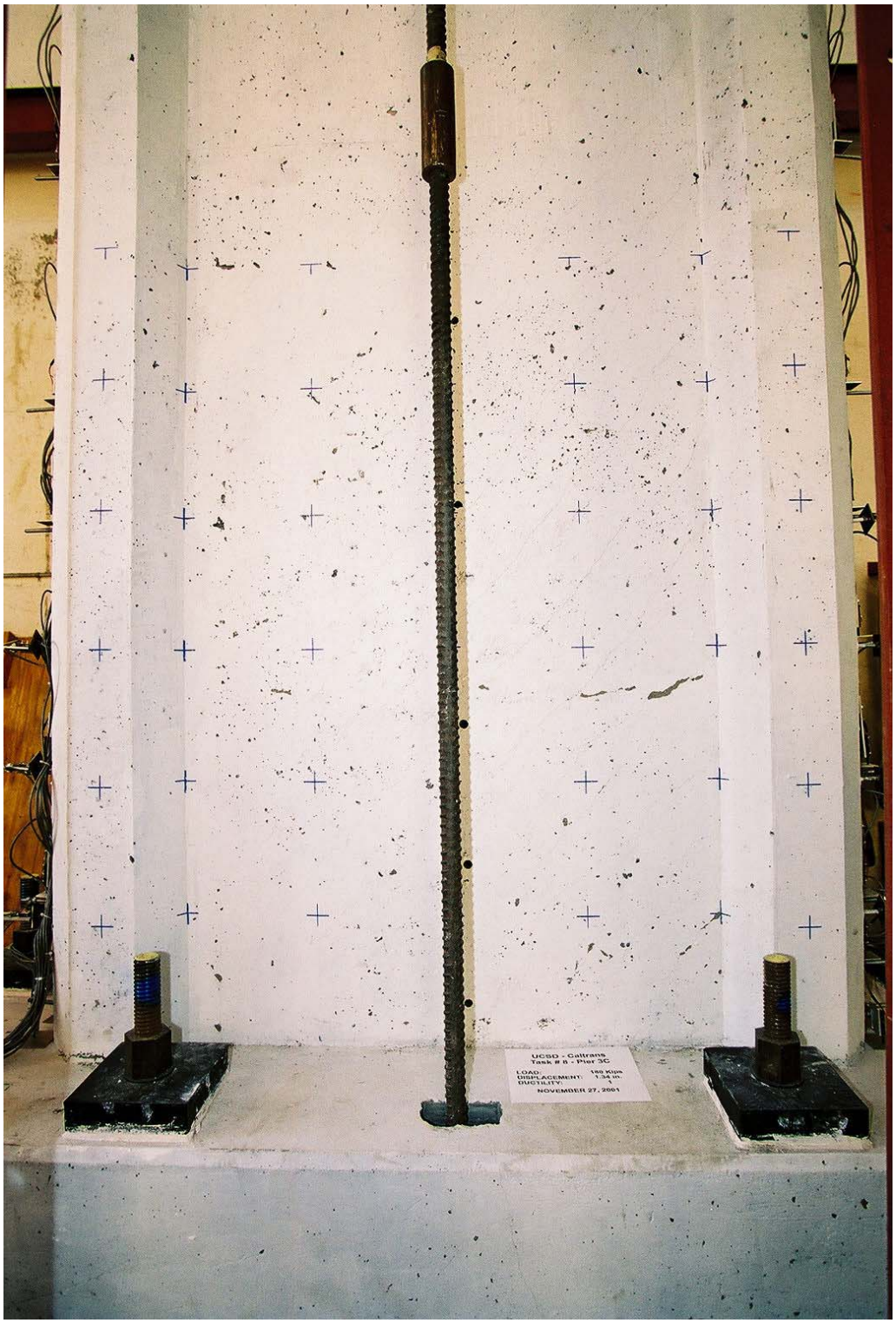

Figure B.19: μ_Δ 1 x +1; Test Unit 3C, east face. Push (positive) direction is south.

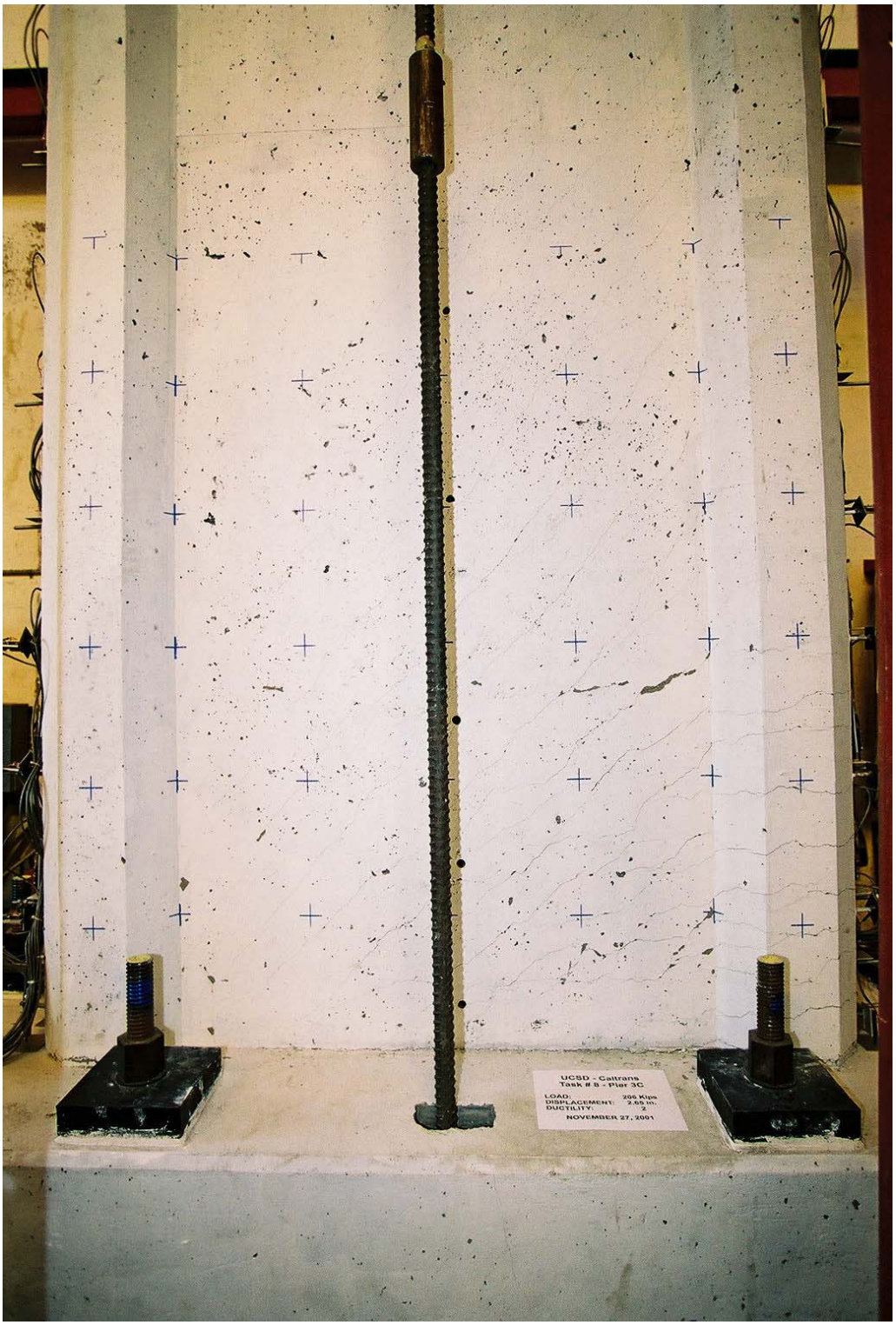

Figure B.20: μ_Δ 2 x +1; Test Unit 3C, east face. Push (positive) direction is south.

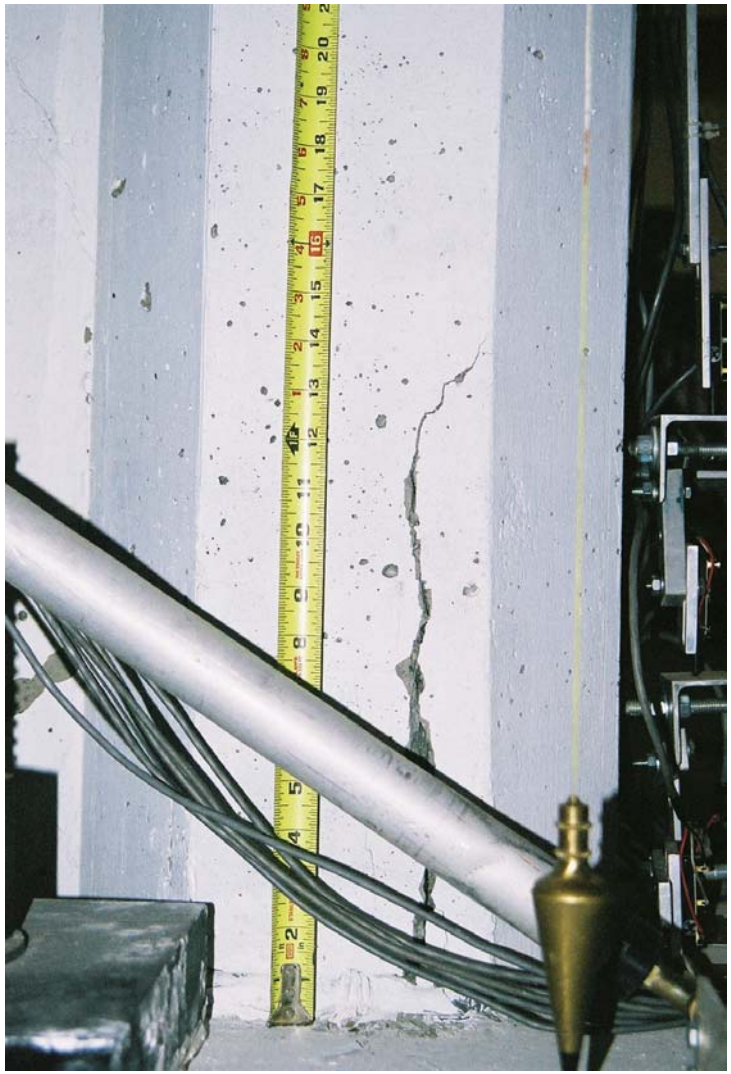

Figure B.21: μ_Δ 2 x +1; Test Unit 3C, vertical splitting crac est face of compression (south) boundary element. Push (positive) direction is south.

Figure B.22: μ_Δ 3 x -1; Test Unit 3C, spalled region on west face of tension (south) boundary element. Push (positive) direction is south.

Figure B.23: μ_Δ 3 x +1; Test Unit 3C, east face. Push (positive) direction is south.

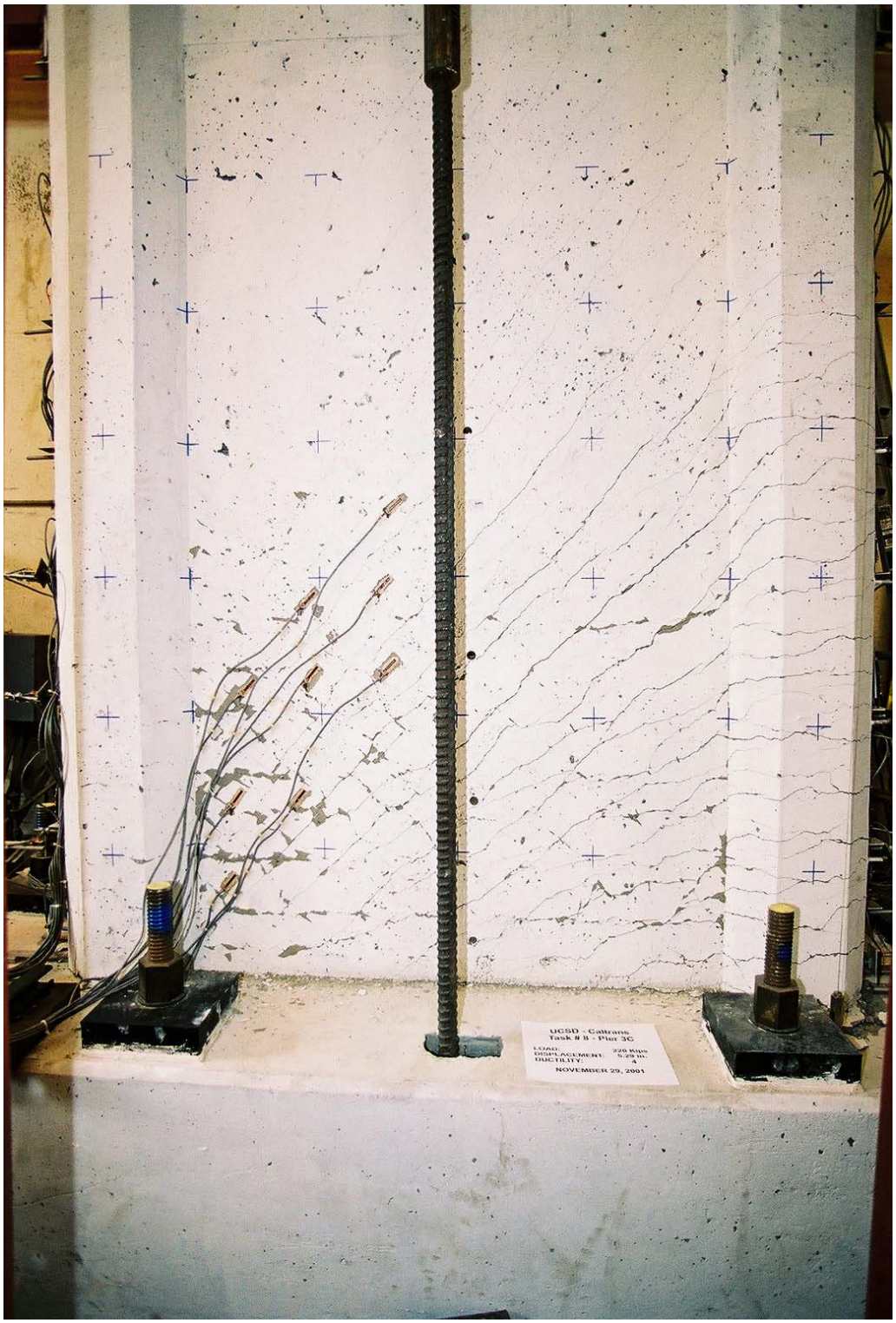

Figure B.24: μ_Δ 4 x +1; Test Unit 3C, east face. Push (positive) direction is south.

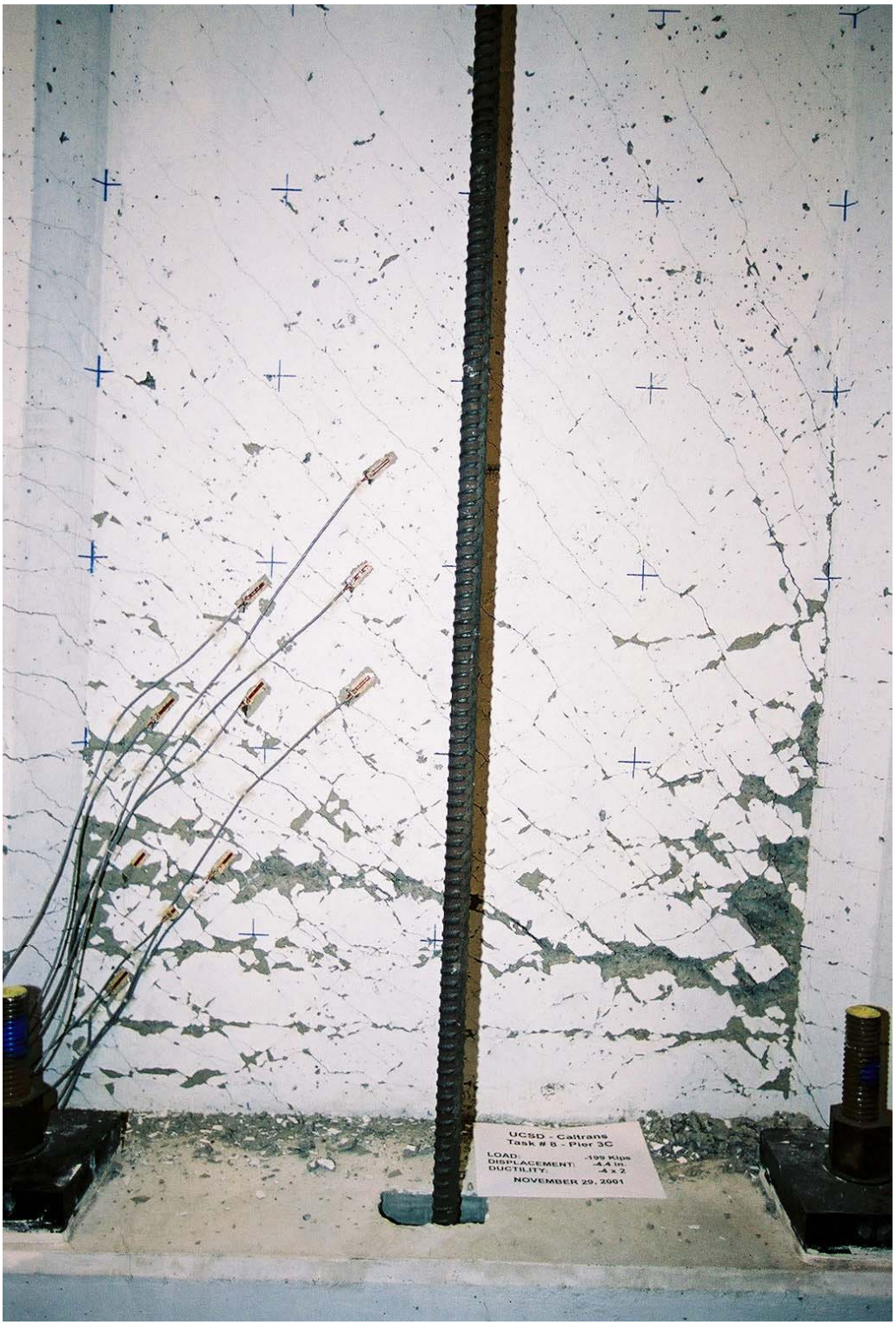

Figure B.25: Cycling to μ_Δ x -2 Test Unit 3C,web crushing failure, east face. Push =4 (positive) direction is south.

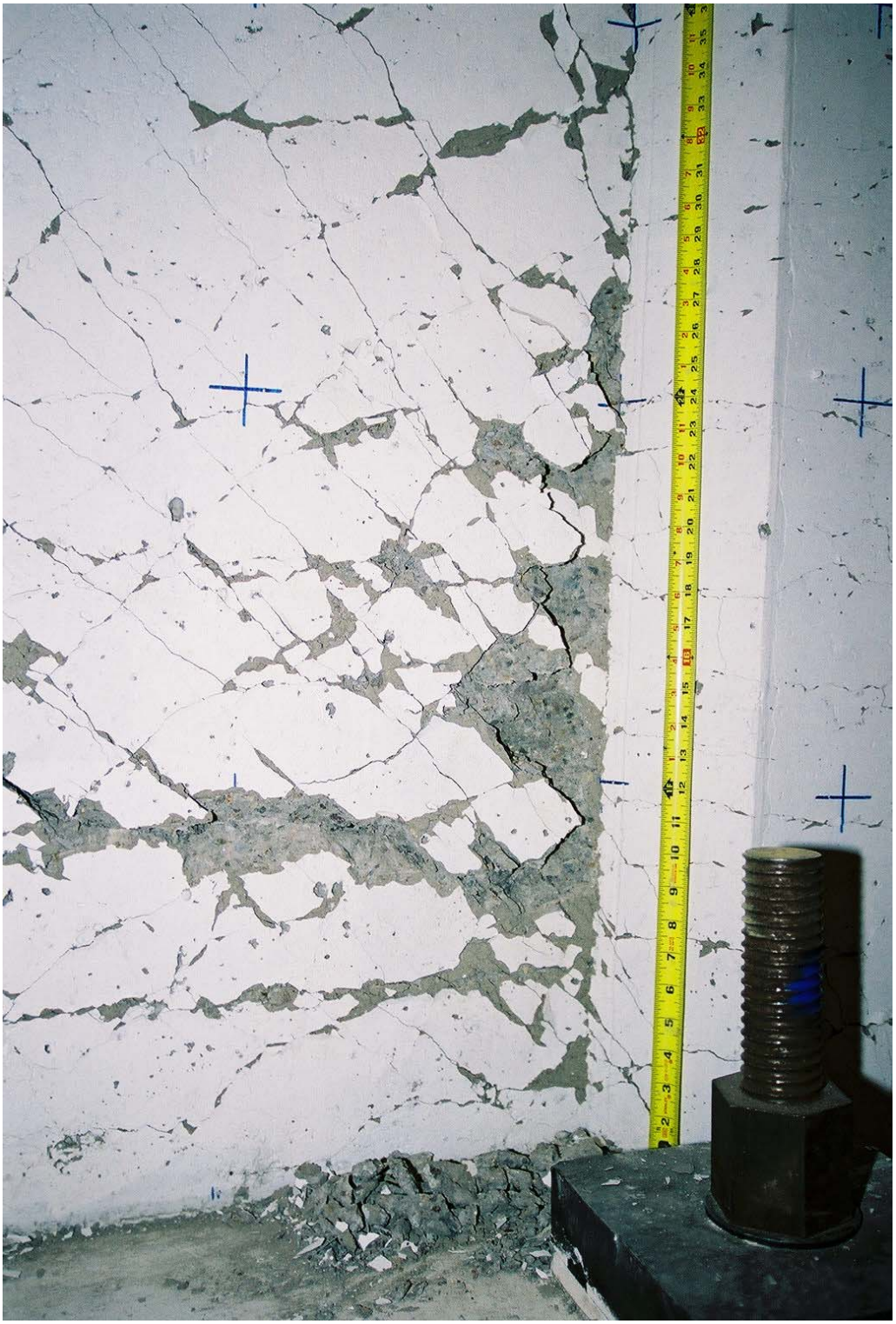

Figure B.26: Cycling to μ_Δ x -2 Test Unit 3C, closeup of the web crushing failure on the the interface between the wall and the compression (north) boundary element, east face . Push (positive) direction is south.

Figure B.27: μ_Δ 5 x +1; Test Unit 3C, end of test, east face. Push (positive) direction is south.

Appendix C

Test Results

C.1 Test Unit 3A

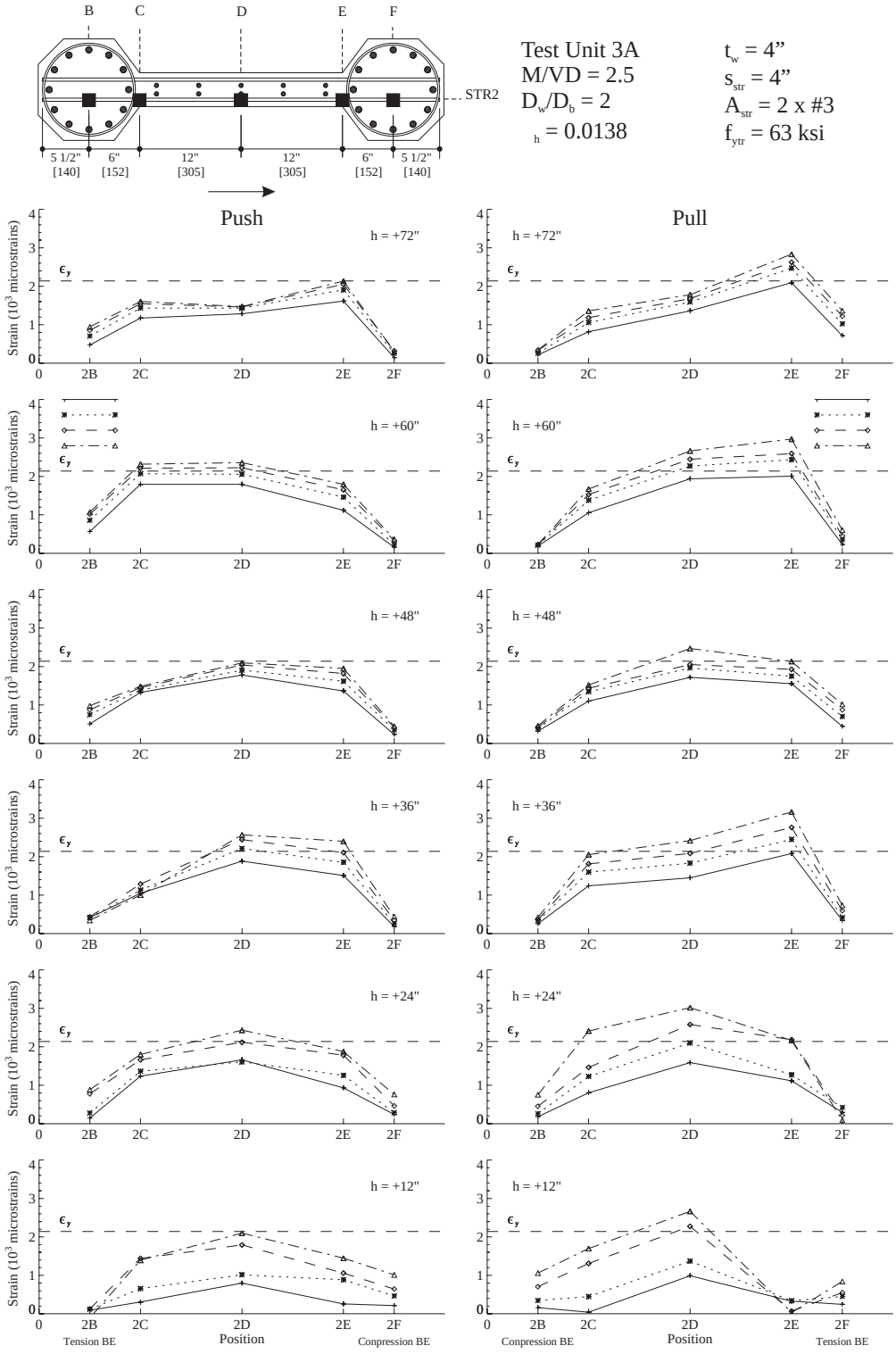

Figure C.1: Test Unit 3A, transverse bar strain profiles for bar STR2.

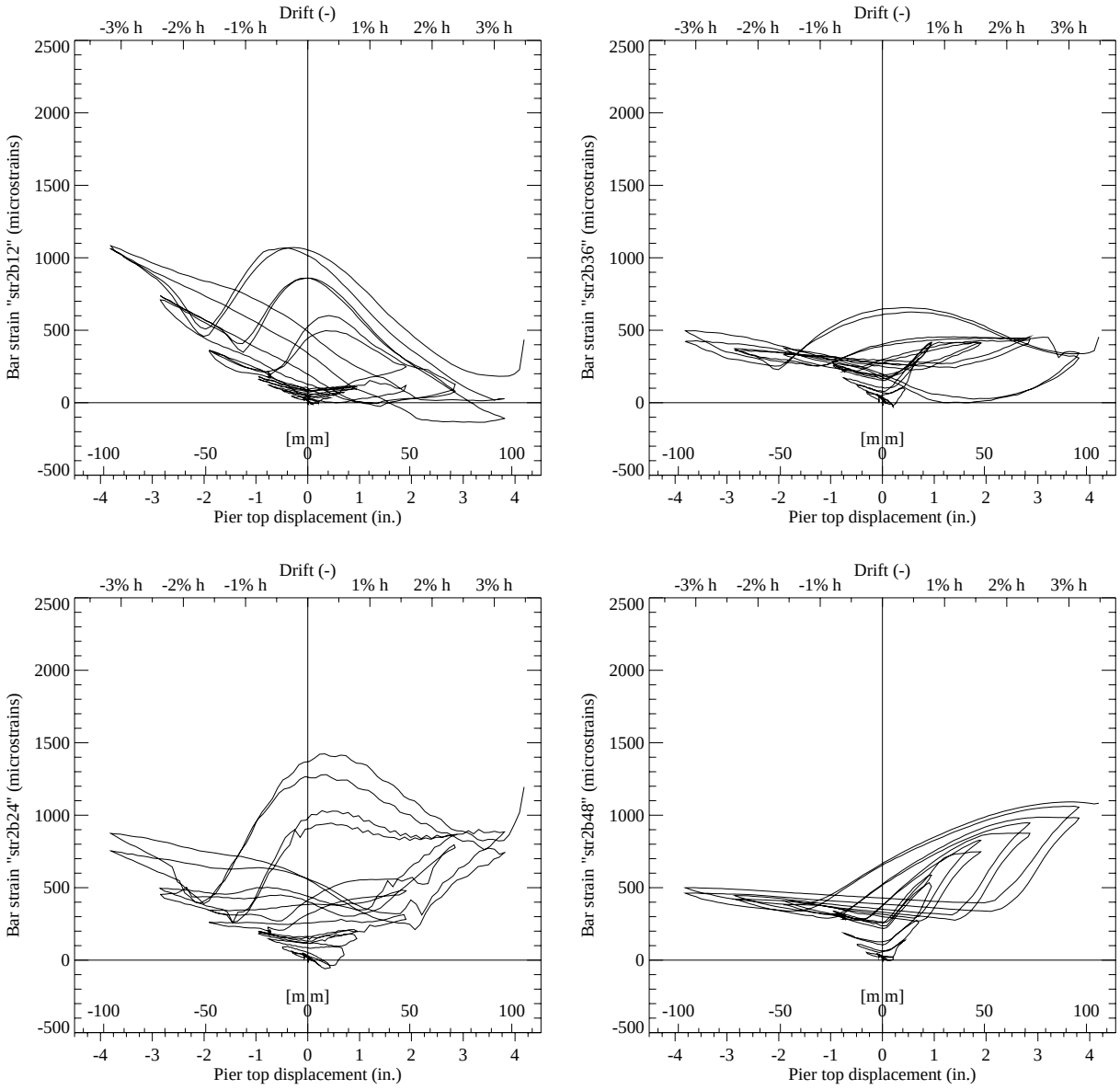

Figure C.2: Test Unit 3A, transverse bar strain hysteresis for gages STR2B12, STR2B24, STR2B36, STR2B48.

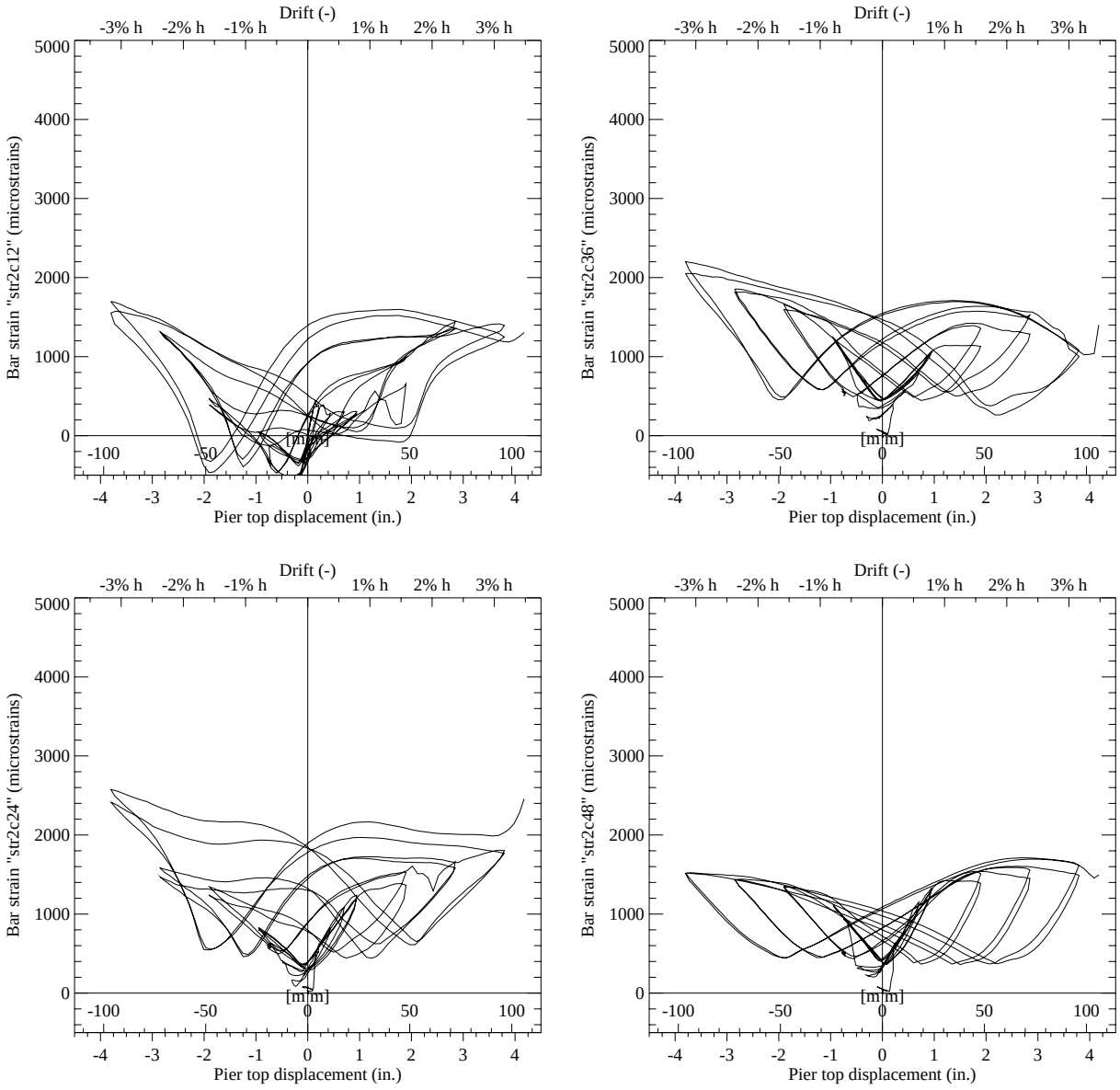

Figure C.3: Test Unit 3A, transverse bar strain hysteresis for gages STR2C12, STR2C24, STR2C36, STR2C48.

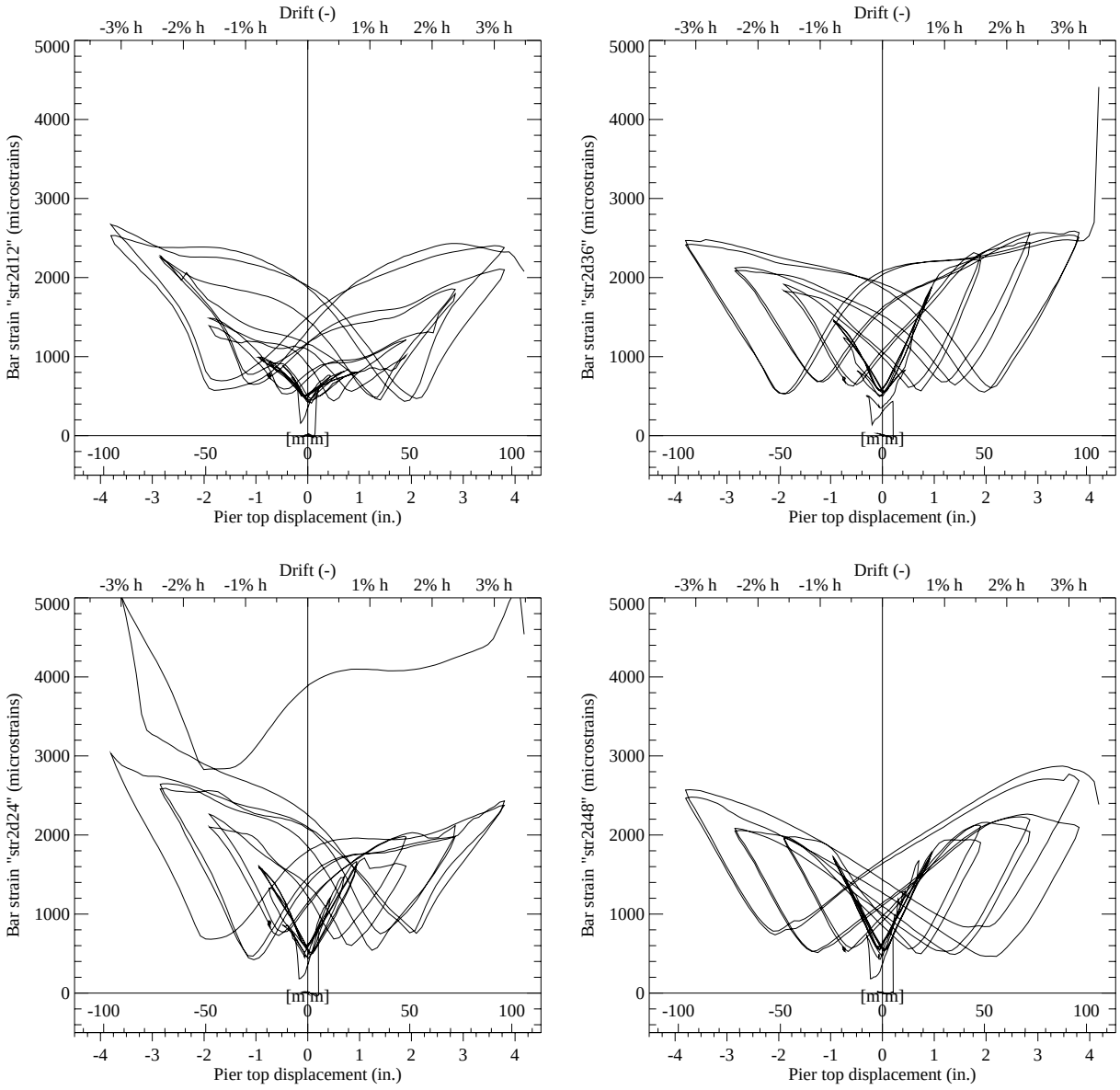

Figure C.4: Test Unit 3A, transverse bar strain hysteresis for gages STR2D12, STR2D24, STR2D36, STR2D48.

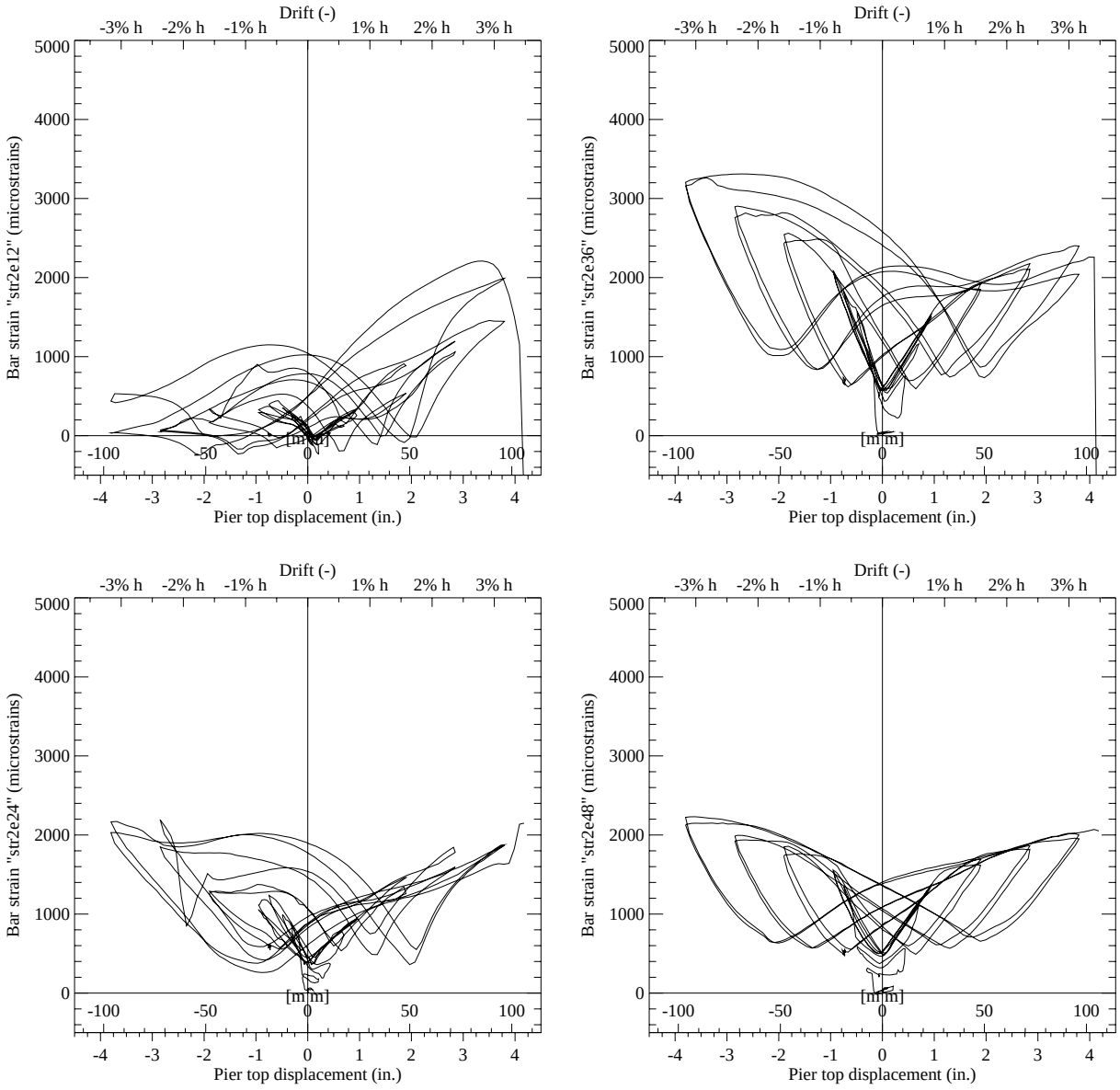

Figure C.5: Test Unit 3A, transverse bar strain hysteresis for gages STR2E12, STR2E24, STR2E36, STR2E48.

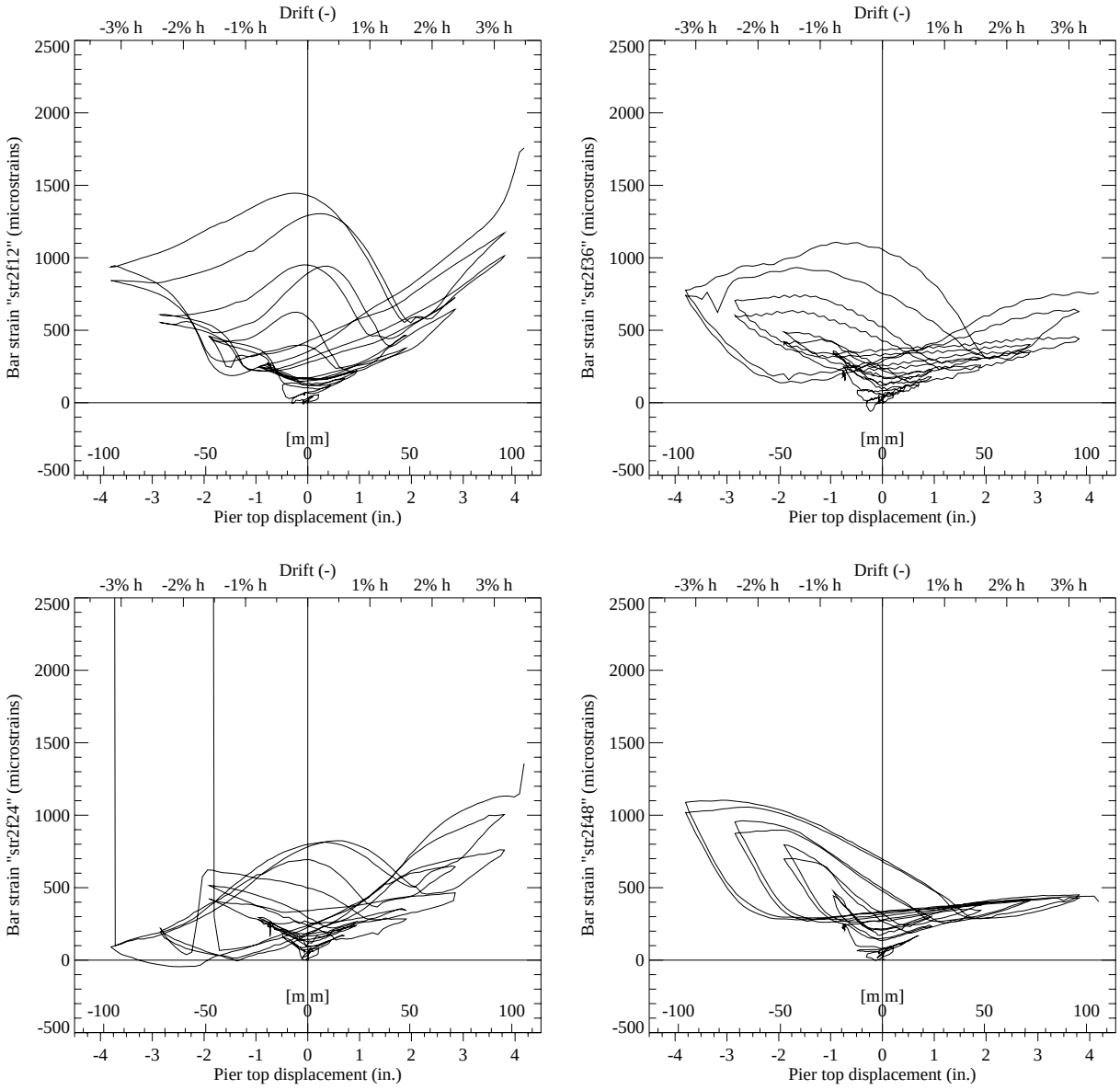

Figure C.6: Test Unit 3A, transverse bar strain hysteresis for gages STR2F12, STR2F24, STR2F36, STR2F48.

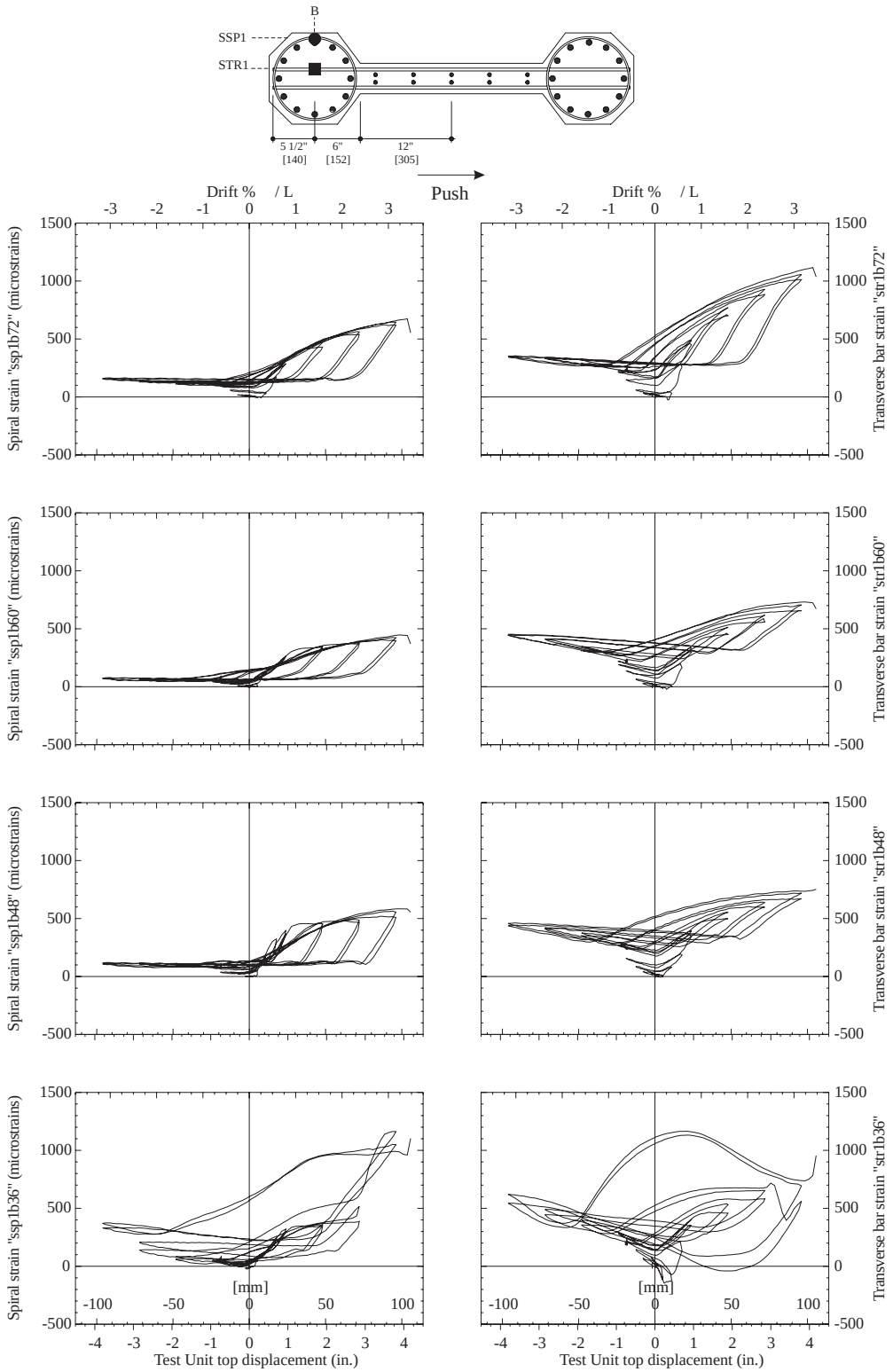

Figure C.7: Test Unit 3A, spiral strains and transverse bar strains at Position 1B, for heights 36 in. [914], 48 in. [1219], 60 in. [1524] and 72 in. [1829] above the footing.

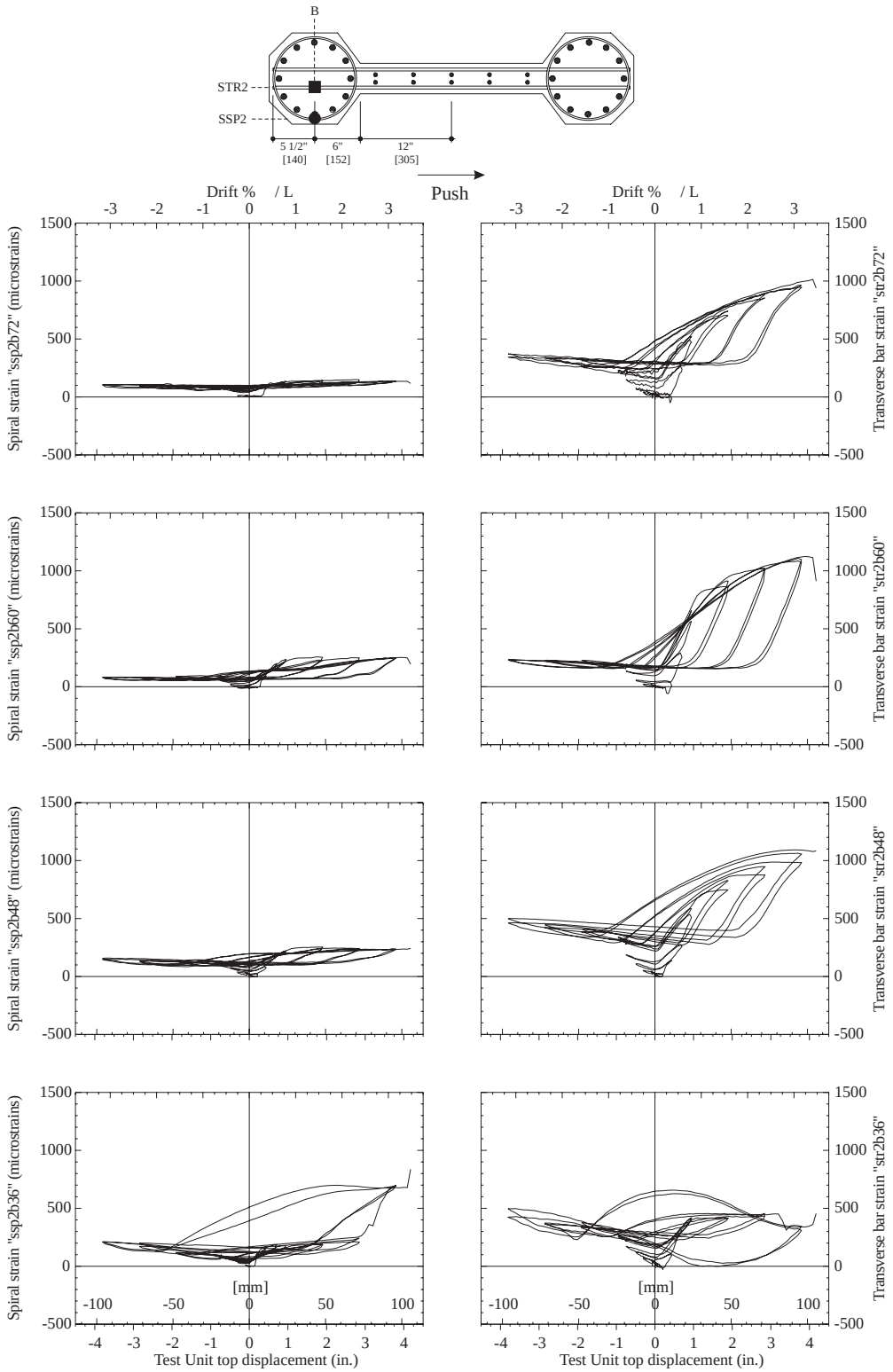

Figure C.8: Test Unit 3A, spiral strains and transverse bar strains at Position 2B, for heights 36 in. [914], 48 in. [1219], 60 in. [1524] and 72 in. [1829] above the footing.

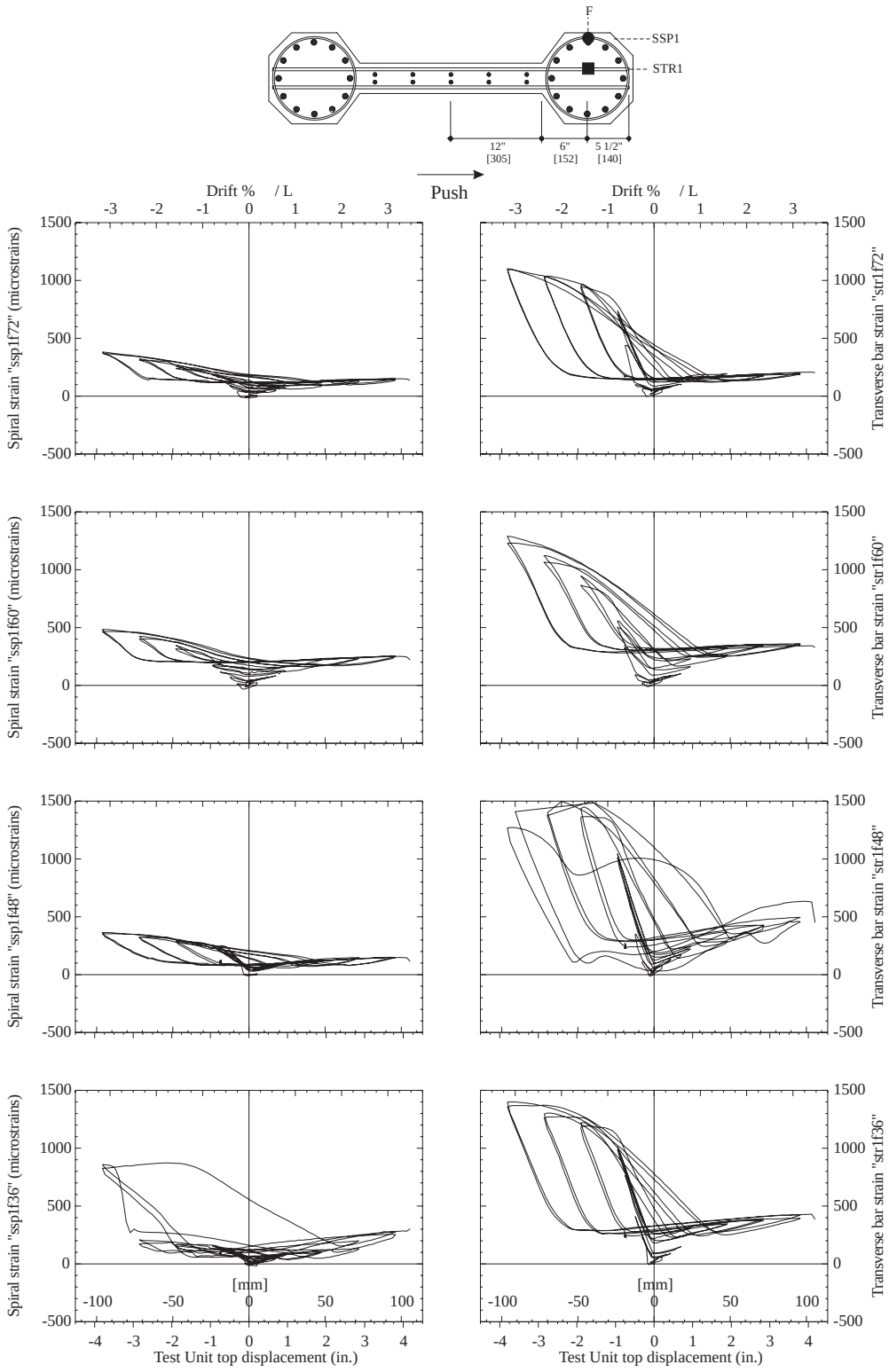

Figure C.9: Test Unit 3A, spiral strains and transverse bar strains at Position 1F, for heights 36 in. [914], 48 in. [1219], 60 in. [1524] and 72 in. [1829] above the footing.

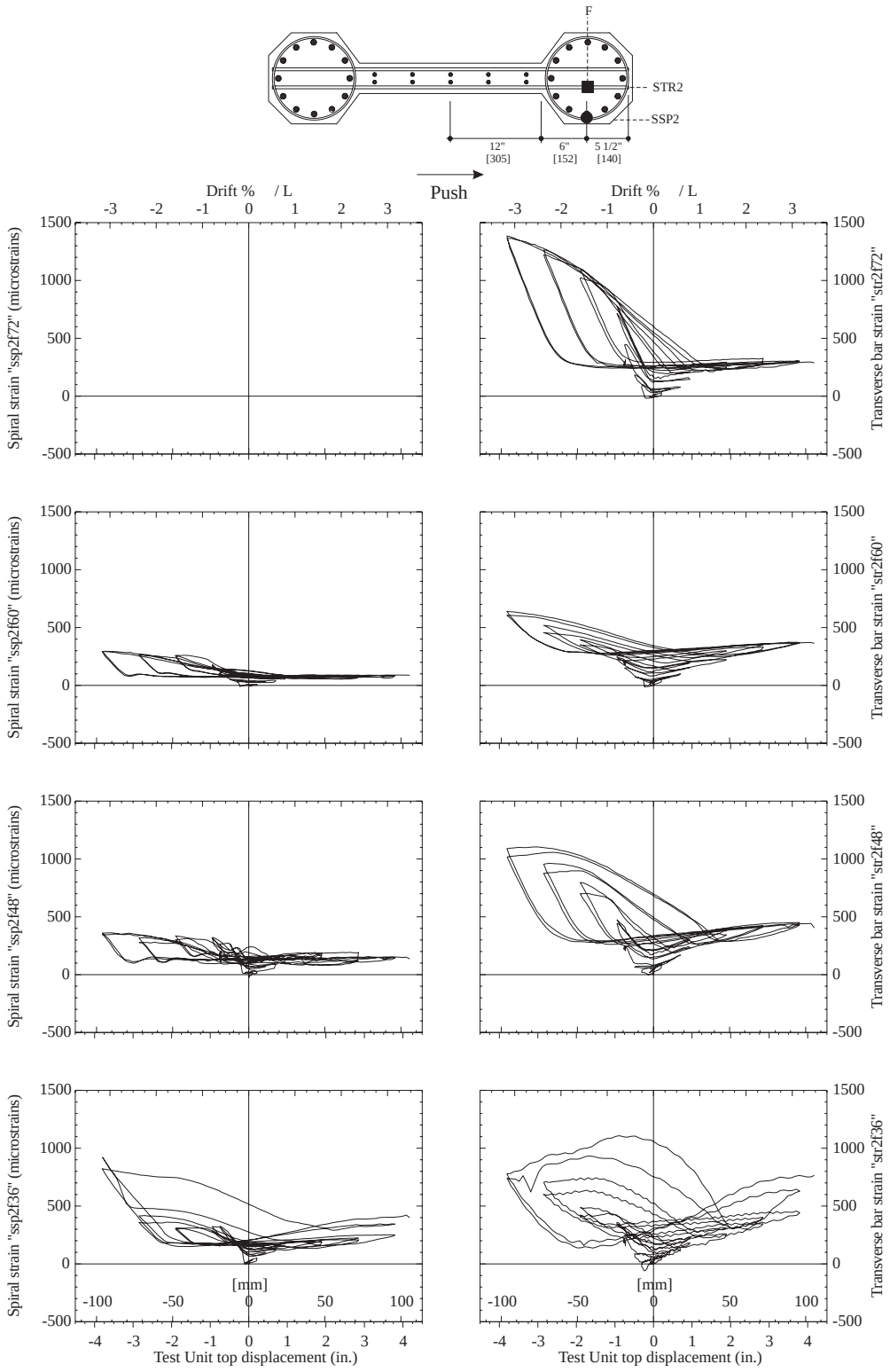

Figure C.10: Test Unit 3A, spiral strains and transverse bar strains at Position 2F, for heights 36 in. [914], 48 in. [1219], 60 in. [1524] and 72 in. [1829] above the footing.

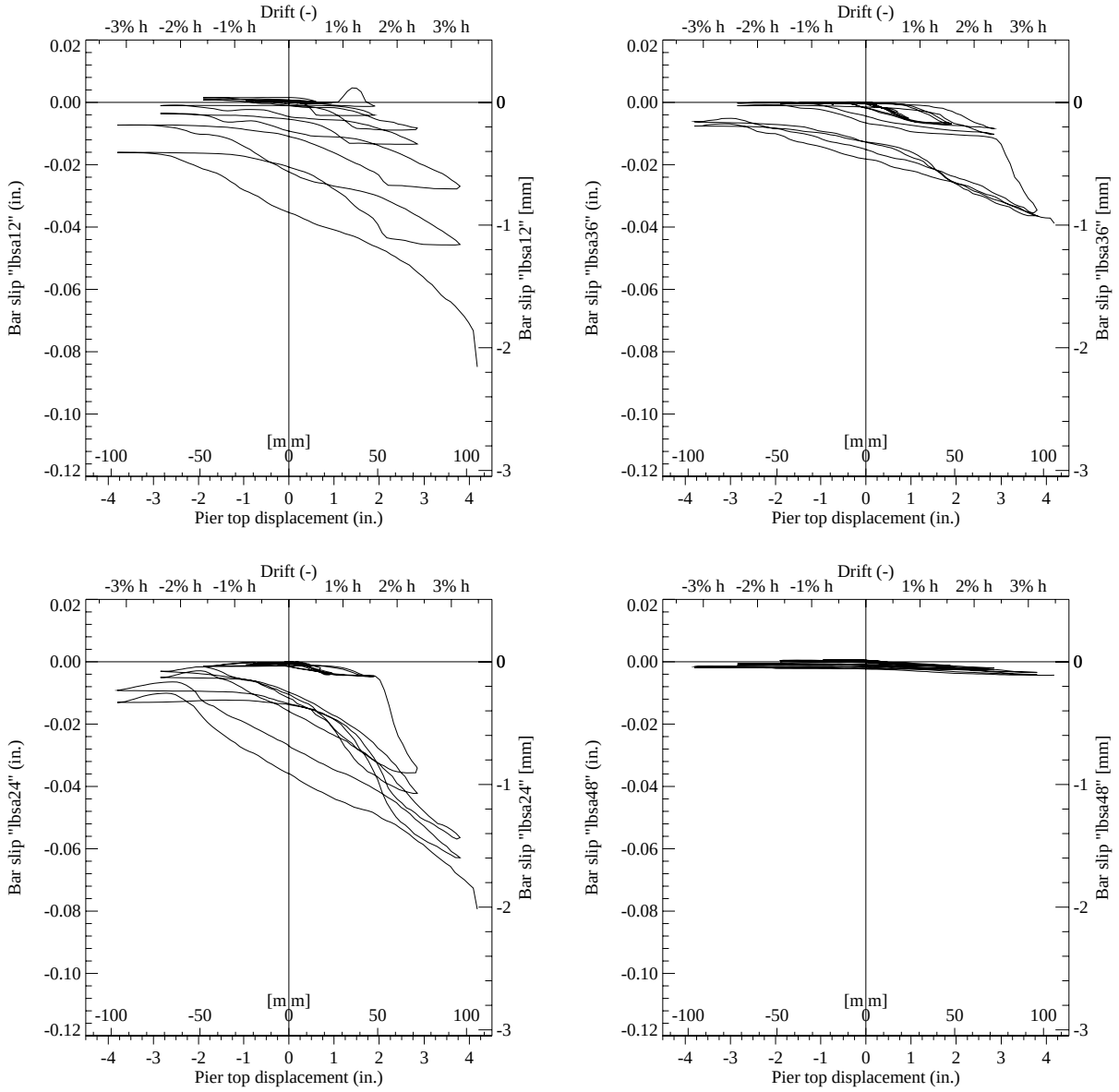

Figure C.11: Test Unit 3A, transverse bar slippage hysteresis at position A for potentiometers LBSA12, LBSA24, LBSA36, LBSA48.

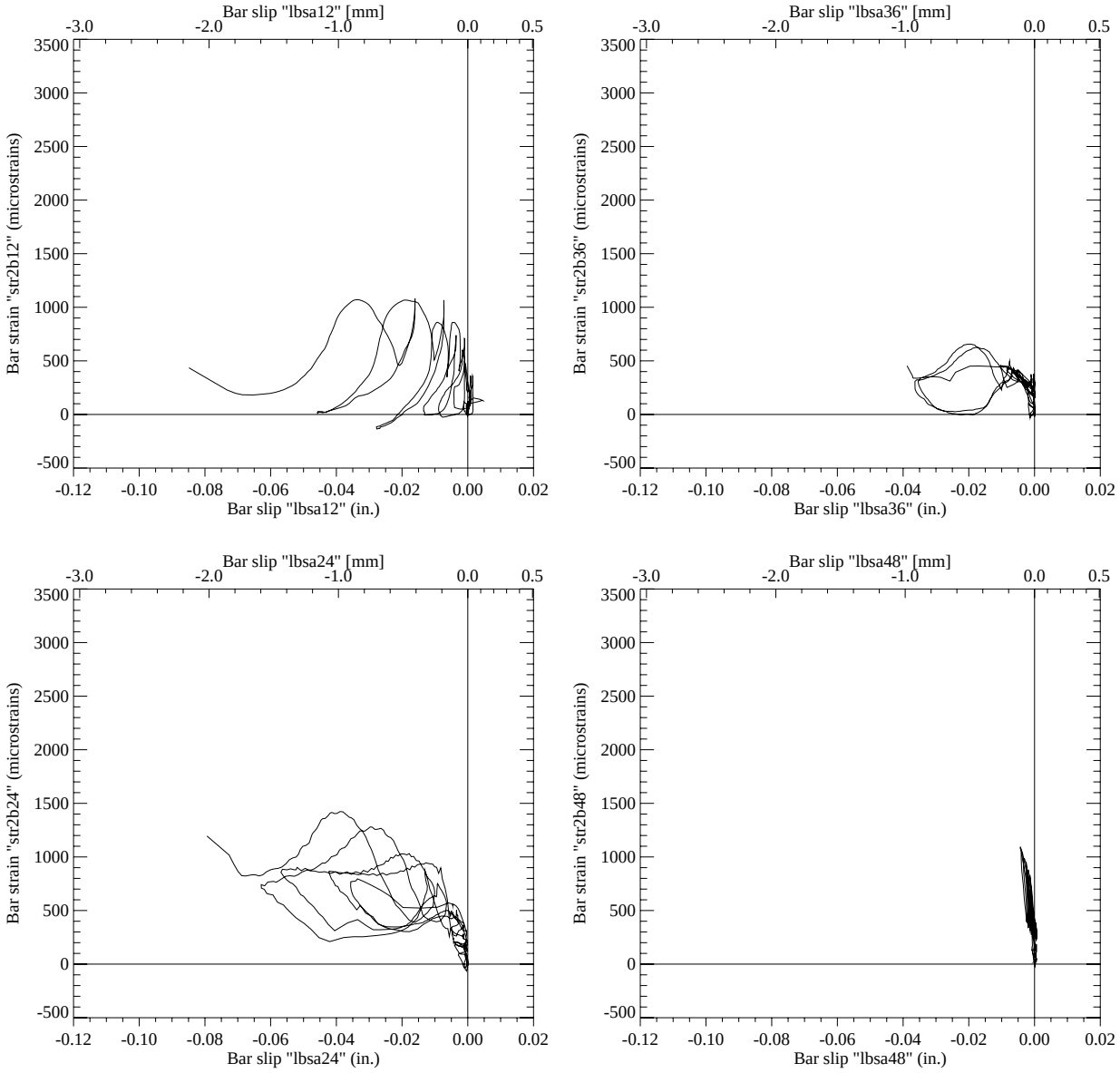

Figure C.12: Test Unit 3A, transverse bar strain as at position B as a function of transverse bar slippage at position A.

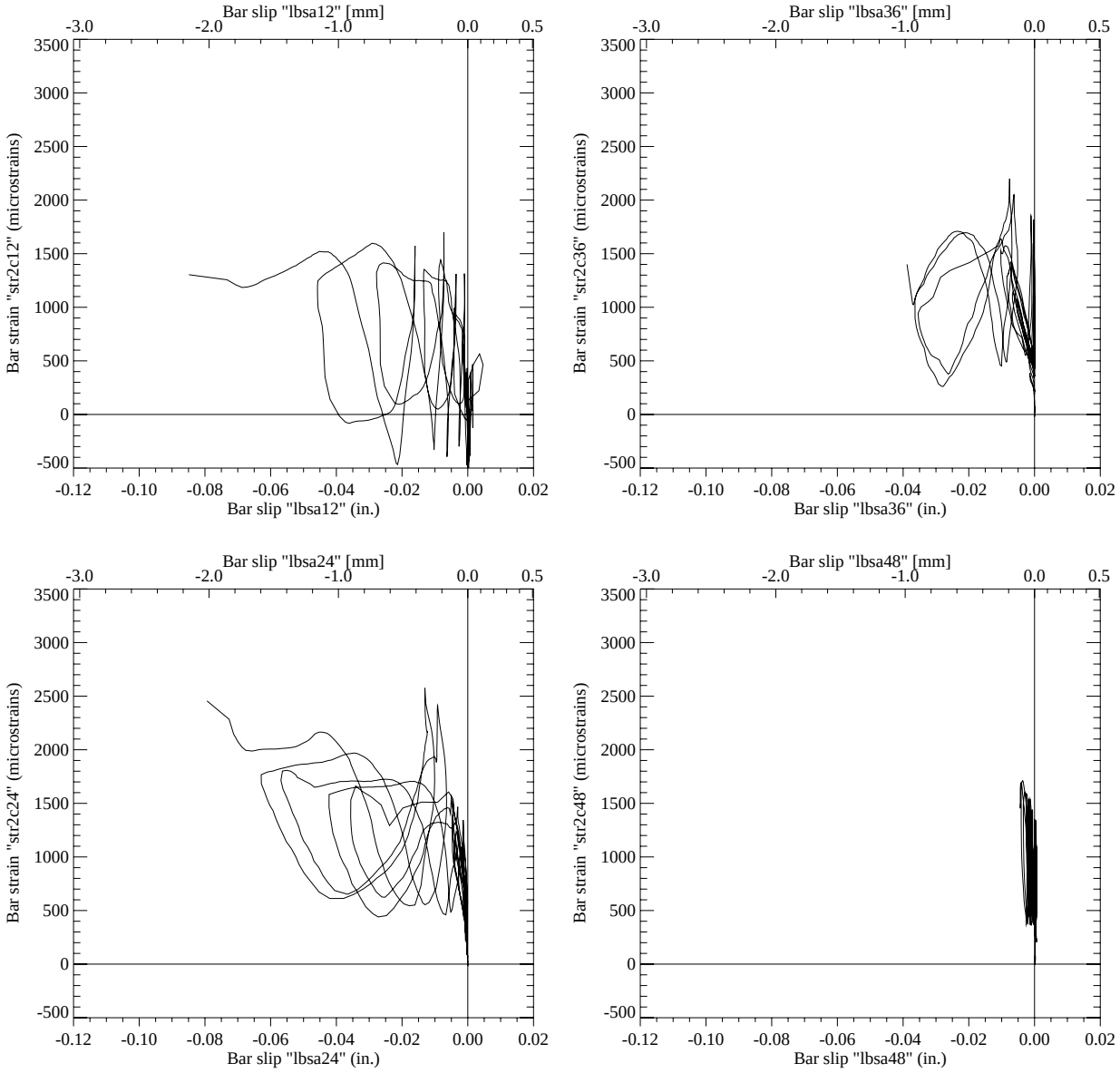

Figure C.13: Test Unit 3A, transverse bar strain as at position C as a function of transverse bar slippage at position A.

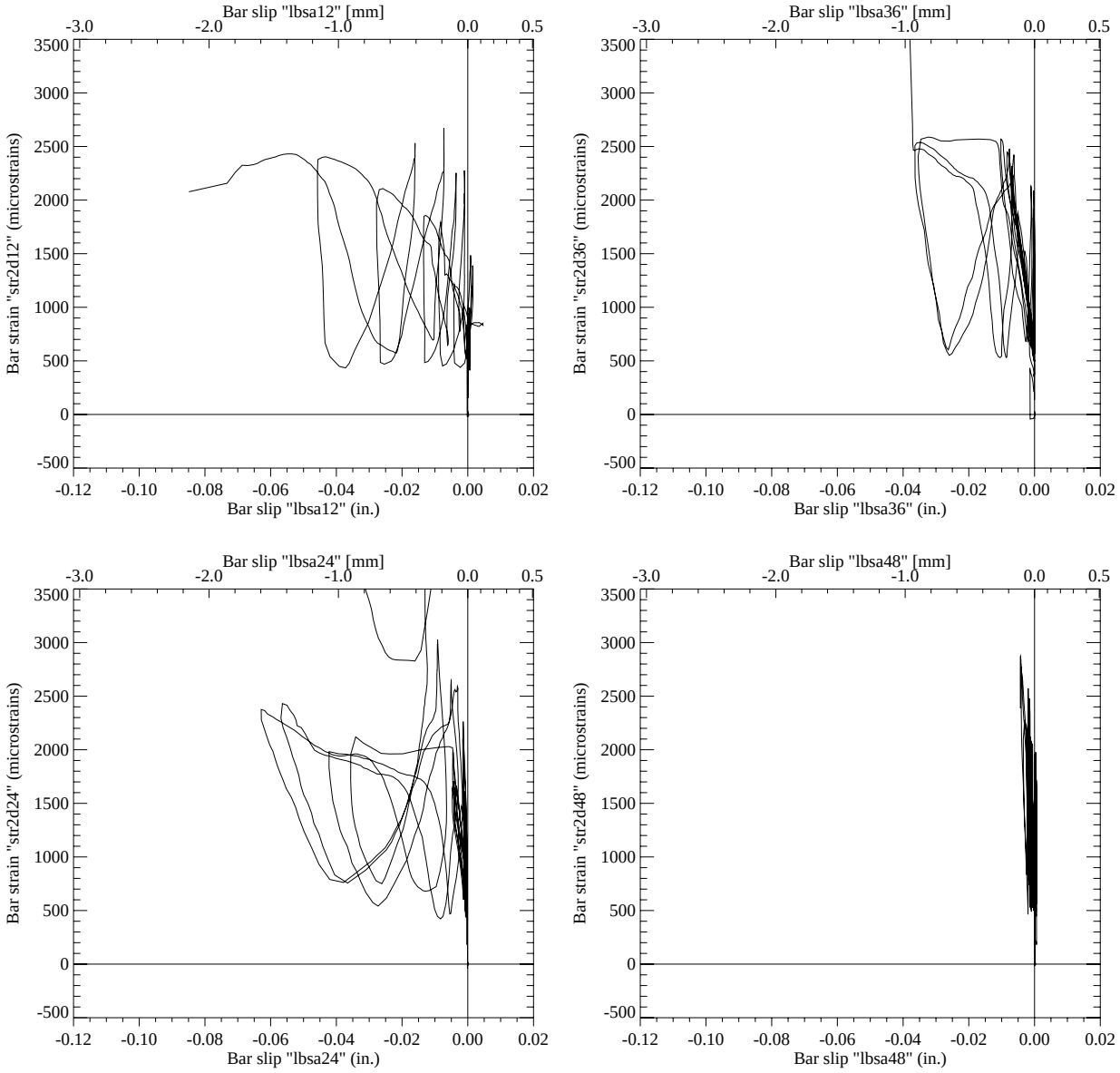

Figure C.14: Test Unit 3A, transverse bar strain as at position D as a function of transverse bar slippage at position A.

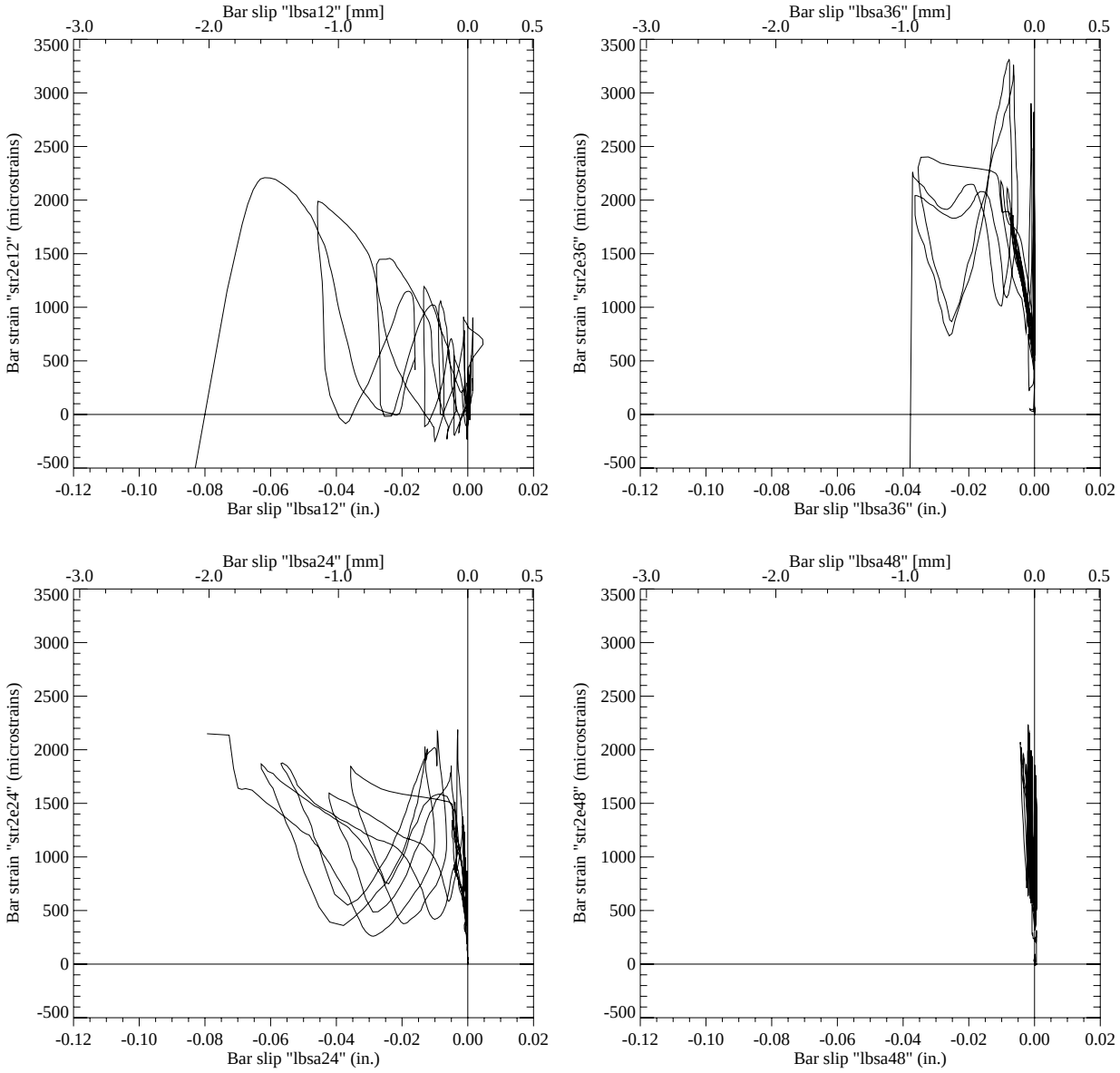

Figure C.15: Test Unit 3A, transverse bar strain as at position E as a function of transverse bar slippage at position A.

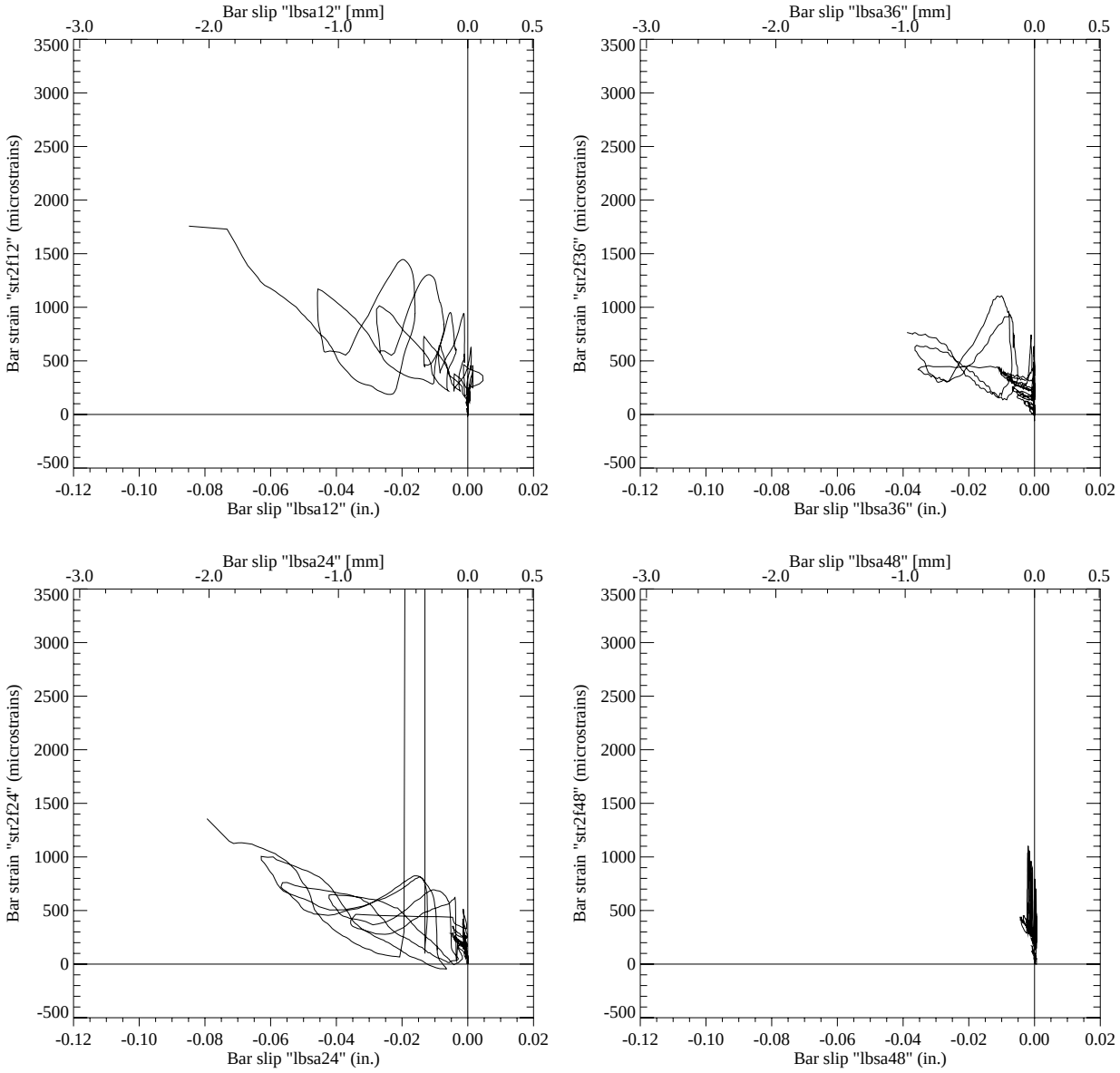

Figure C.16: Test Unit 3A, transverse bar strain as at position F as a function of transverse bar slippage at position A.

C.2 Test Unit 3B

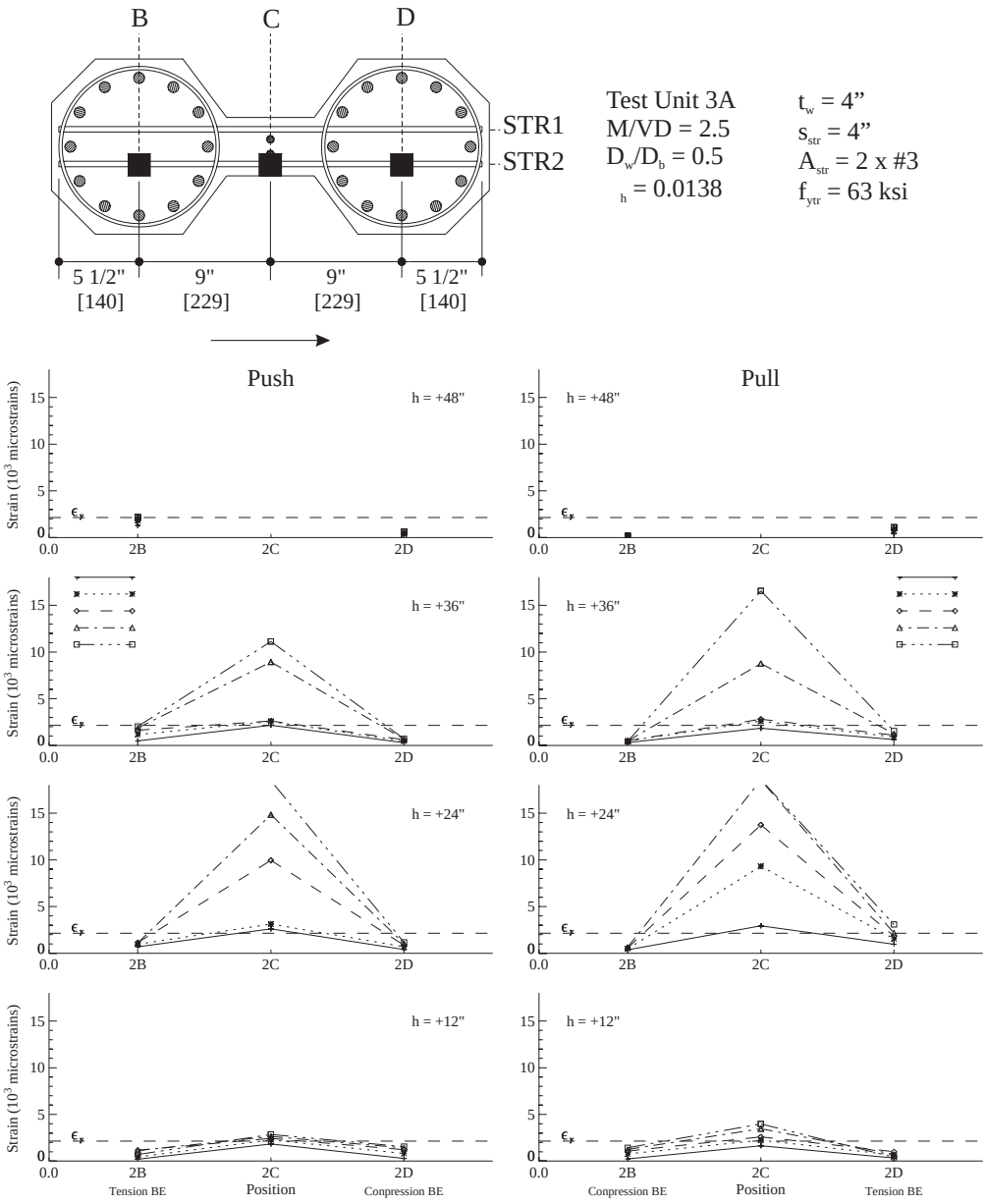

Figure C.17: Test Unit 3B, transverse bar strain profiles for bar STR2.

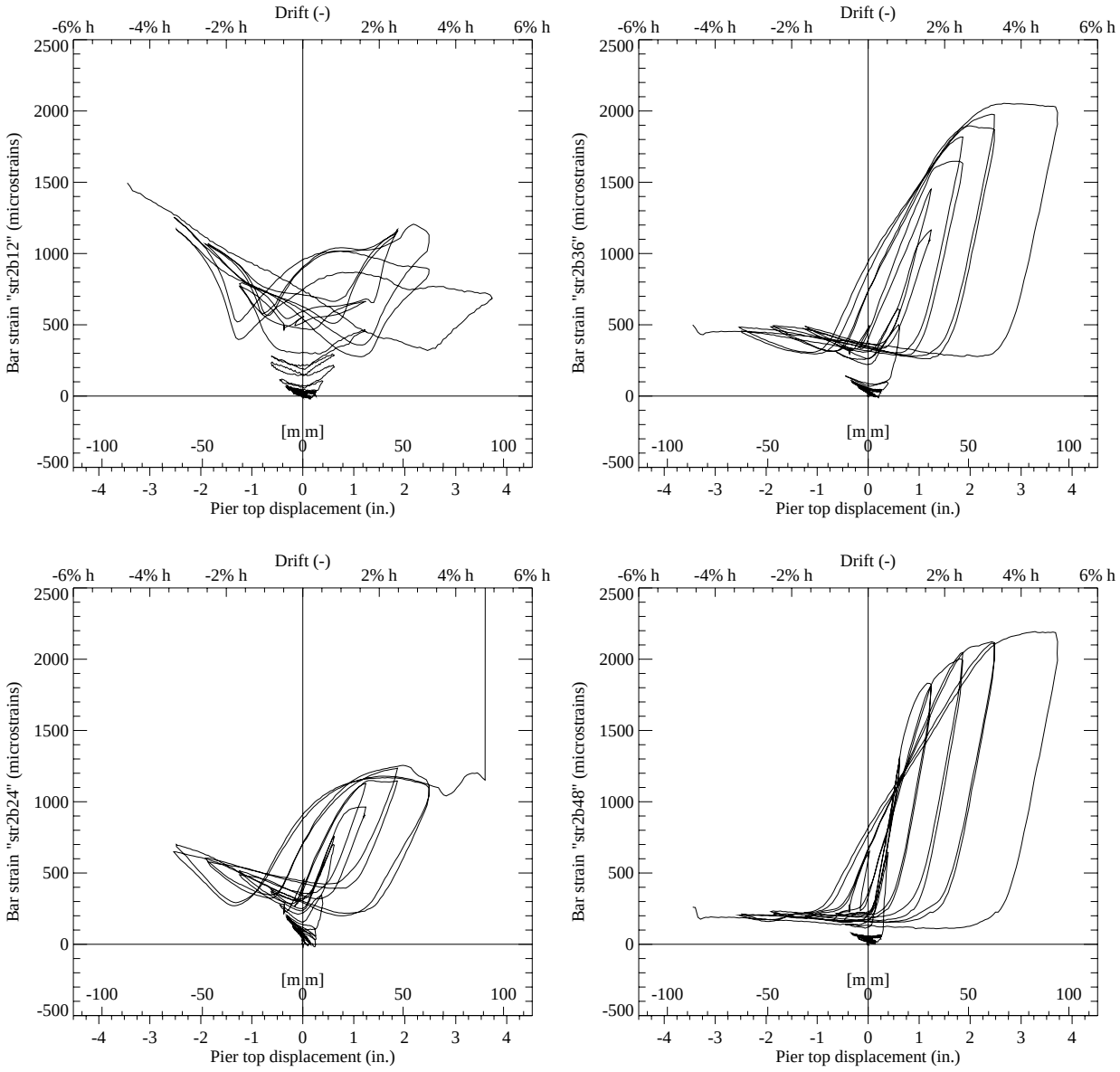

Figure C.18: Test Unit 3B, transverse bar strain hysteresis for gages STR2B12, STR2B24, STR2B36, STR2B48.

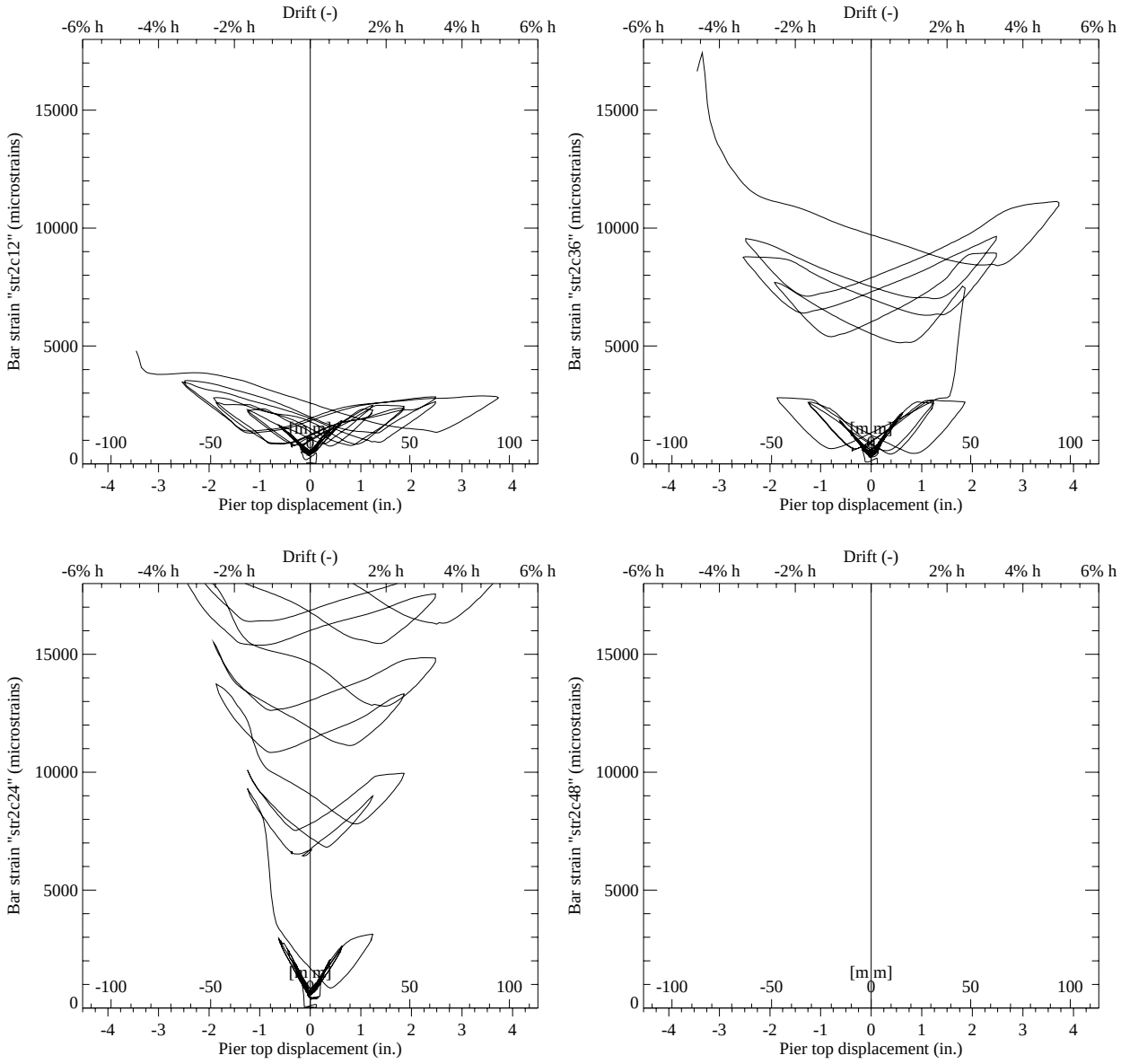

Figure C.19: Test Unit 3B, transverse bar strain hysteresis for gages STR2C12, STR2C24, STR2C36, STR2C48.

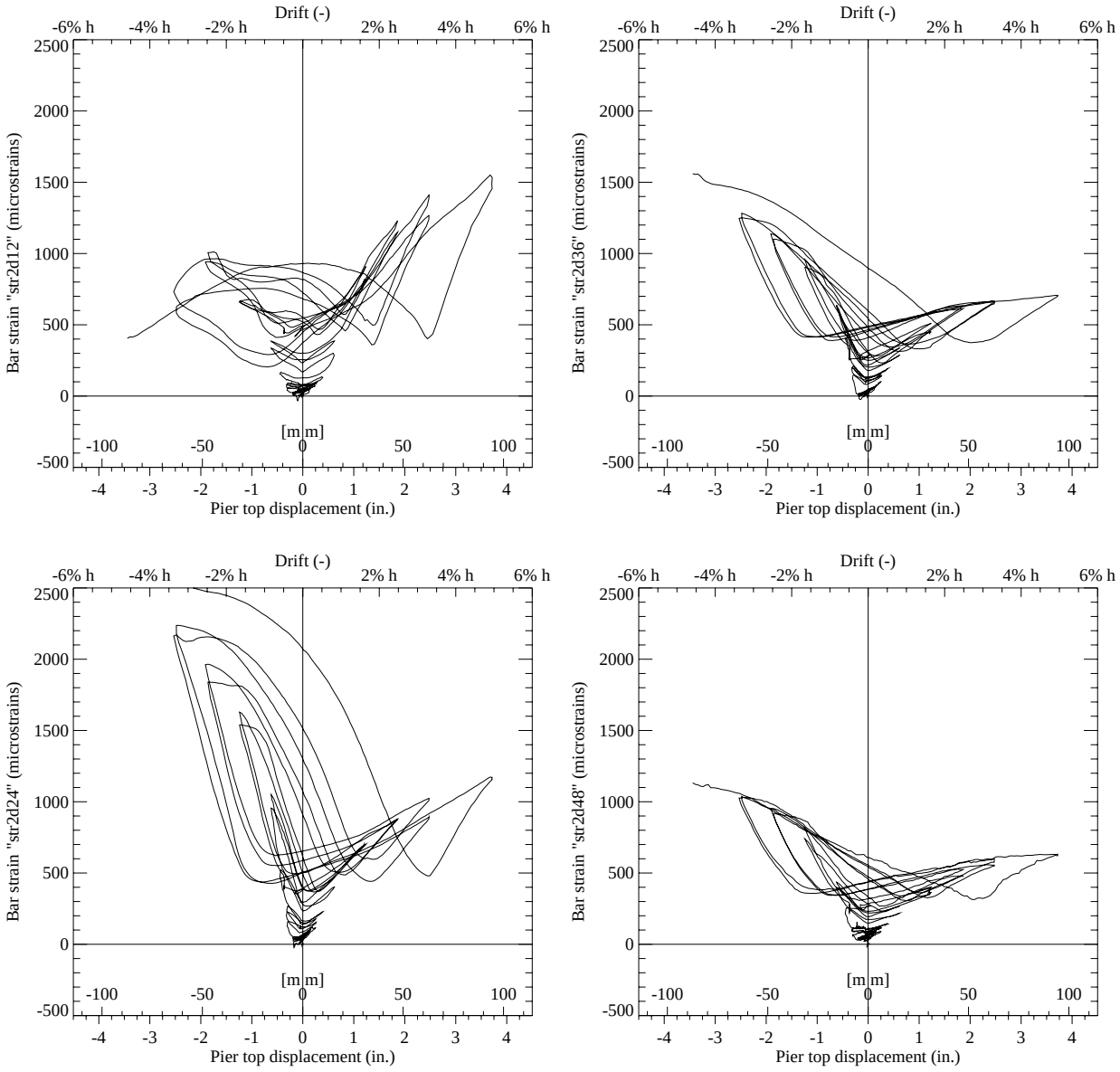

Figure C.20: Test Unit 3B, transverse bar strain hysteresis for gages STR2D12, STR2D24, STR2D36, STR2D48.

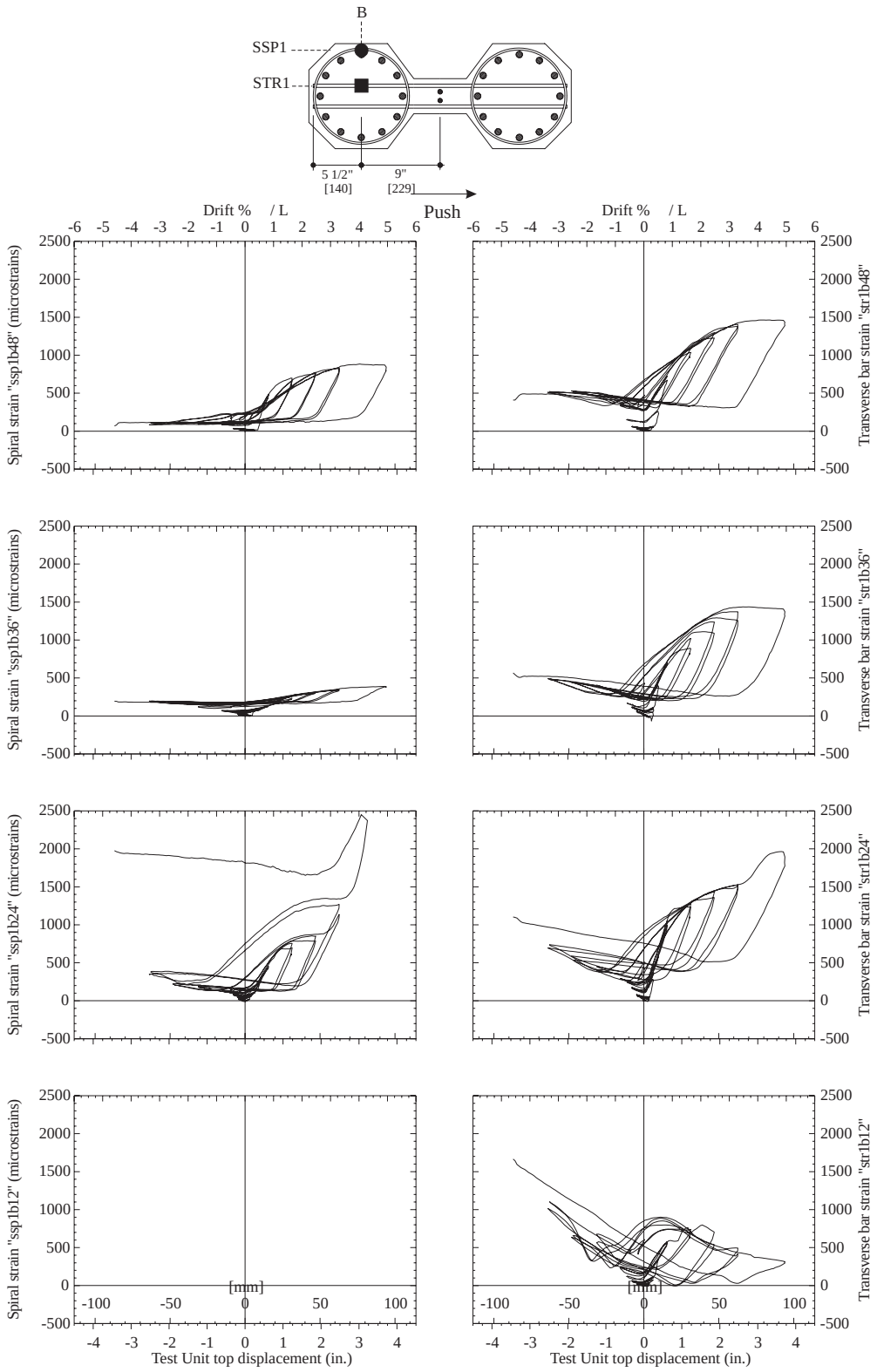

Figure C.21: Test Unit 3B, spiral strains and transverse bar strains at Position 1B, for heights 12 in. [305], 24 in. [610], 36 in. [914] and 48 in. [1219] above the footing.

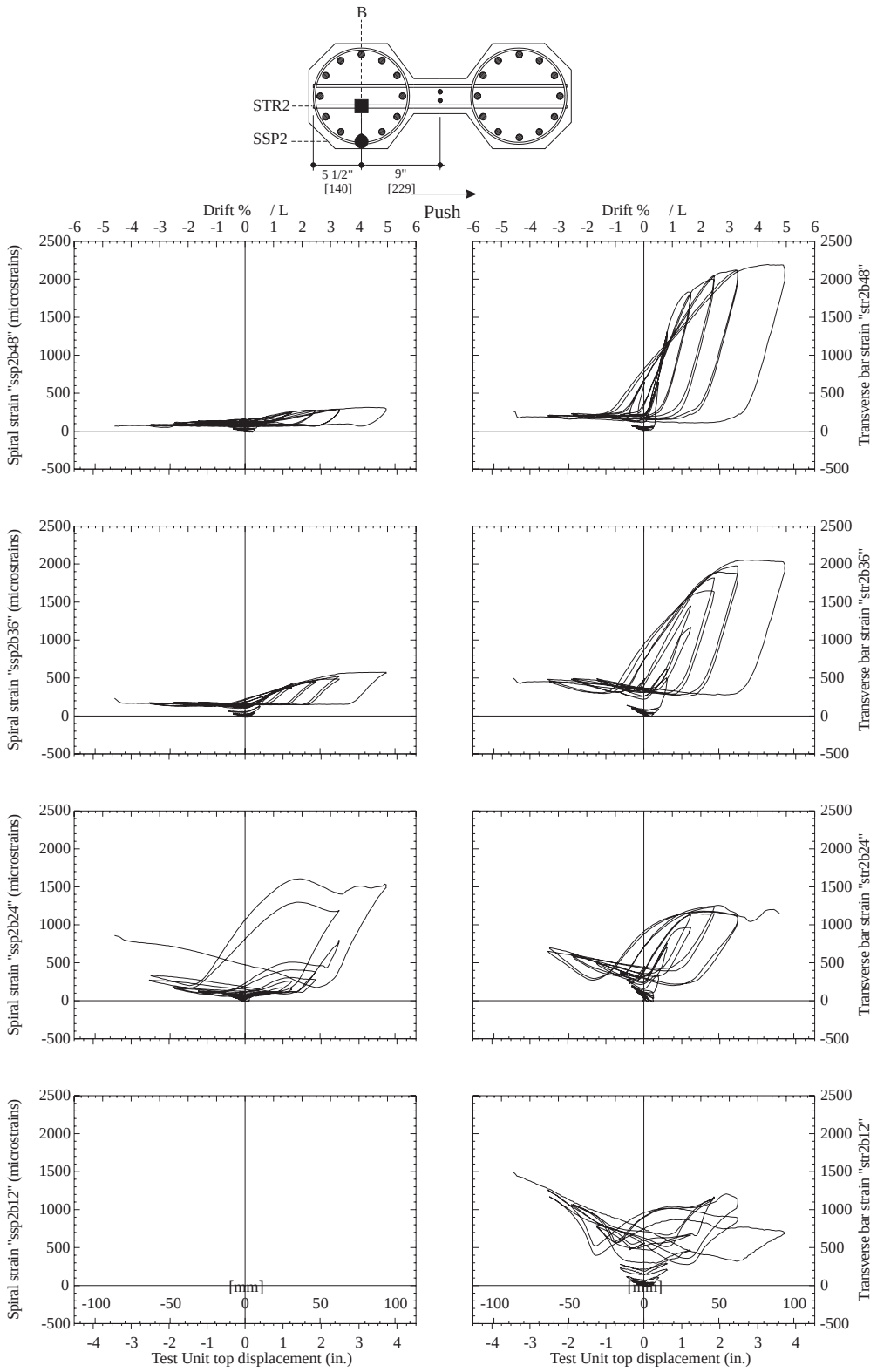

Figure C.22: Test Unit 3B, spiral strains and transverse bar strains at Position 2B, for heights 12 in. [305], 24 in. [610], 36 in. [914] and 48 in. [1219] above the footing.

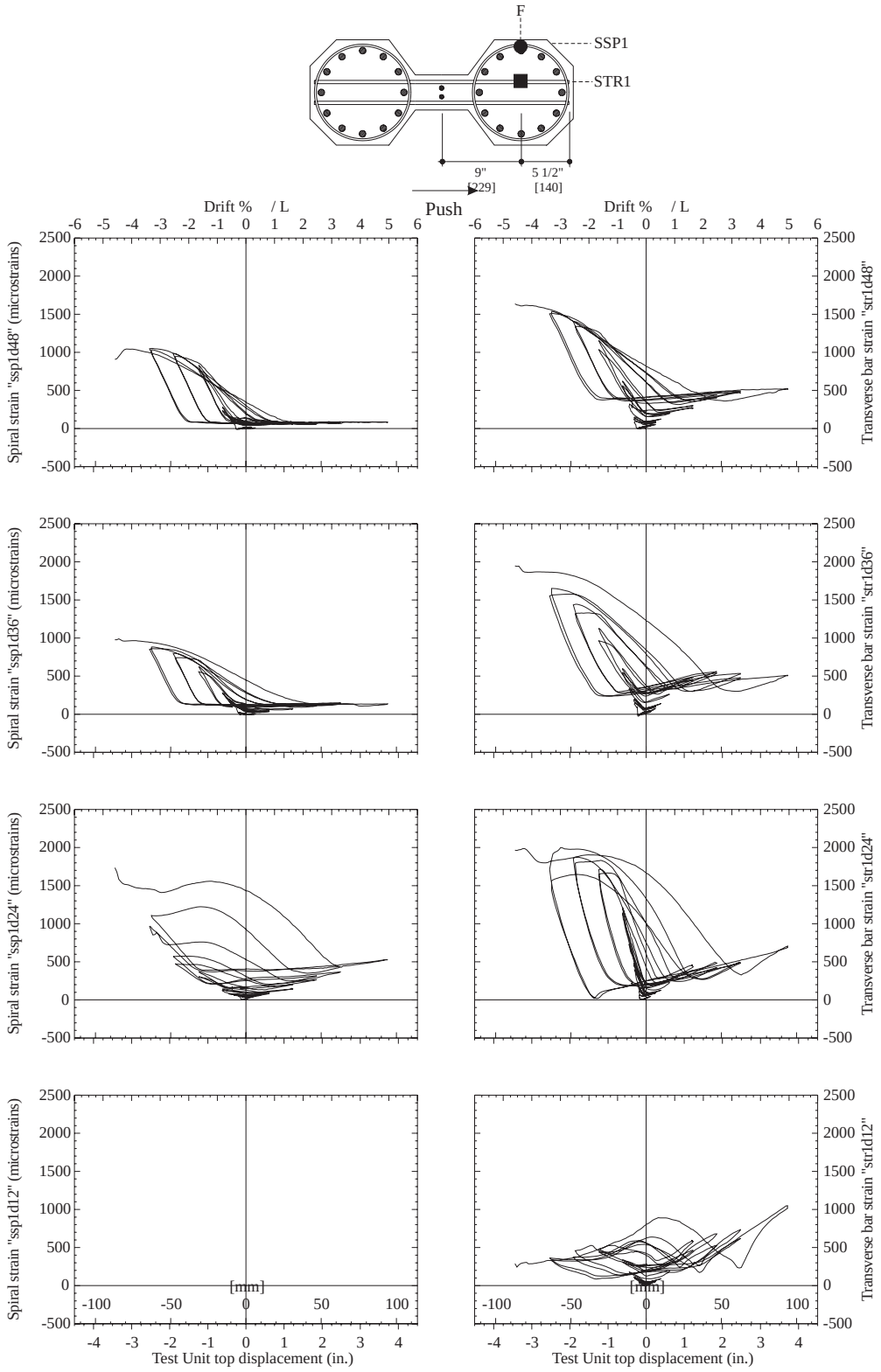

Figure C.23: Test Unit 3B, spiral strains and transverse bar strains at Position 1D, for heights 12 in. [305], 24 in. [610], 36 in. [914] and 48 in. [1219] above the footing.

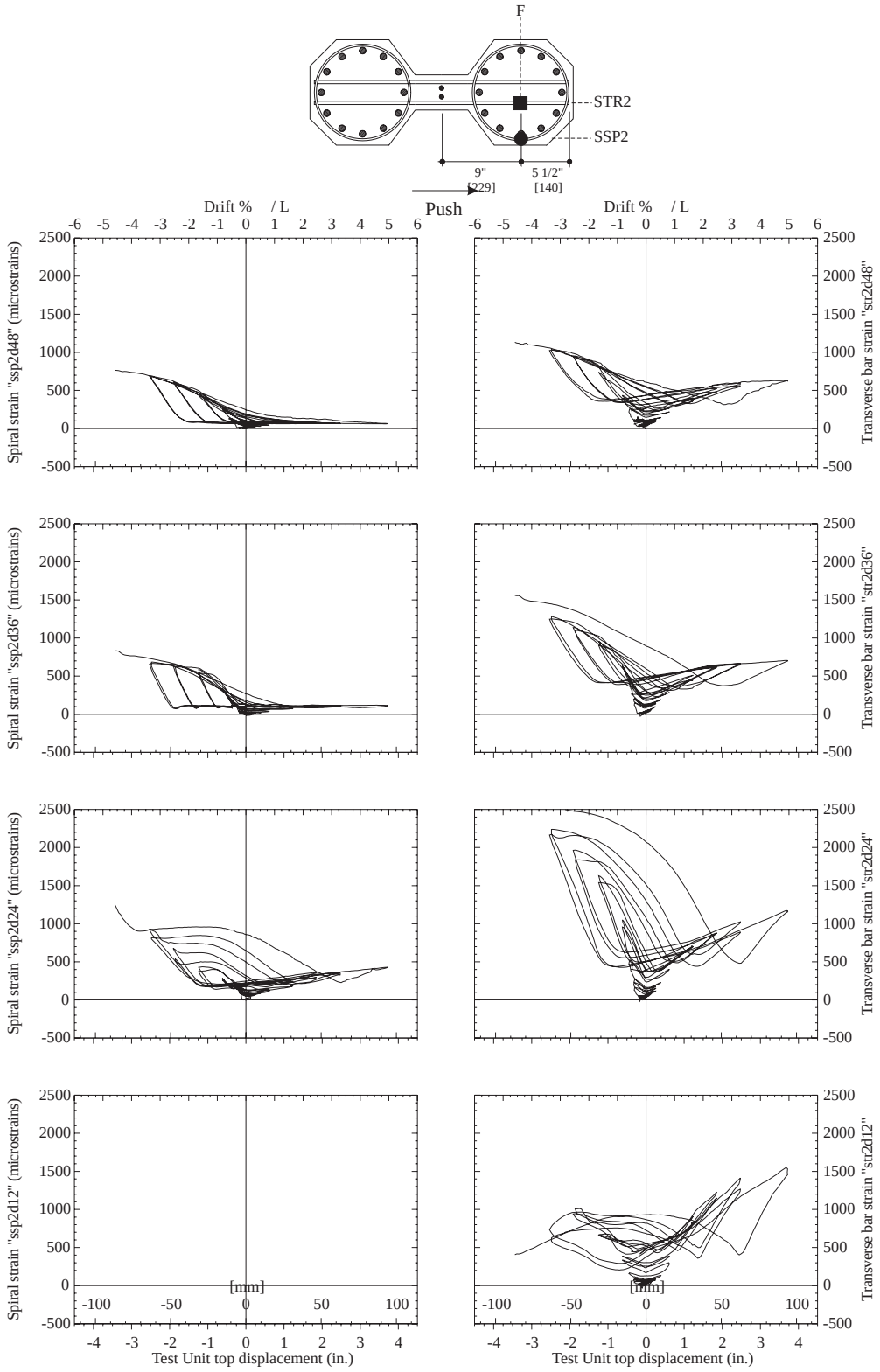

Figure C.24: Test Unit 3B, spiral strains and transverse bar strains at Position 2D, for heights 12 in. [305], 24 in. [610], 36 in. [914] and 48 in. [1219] above the footing.

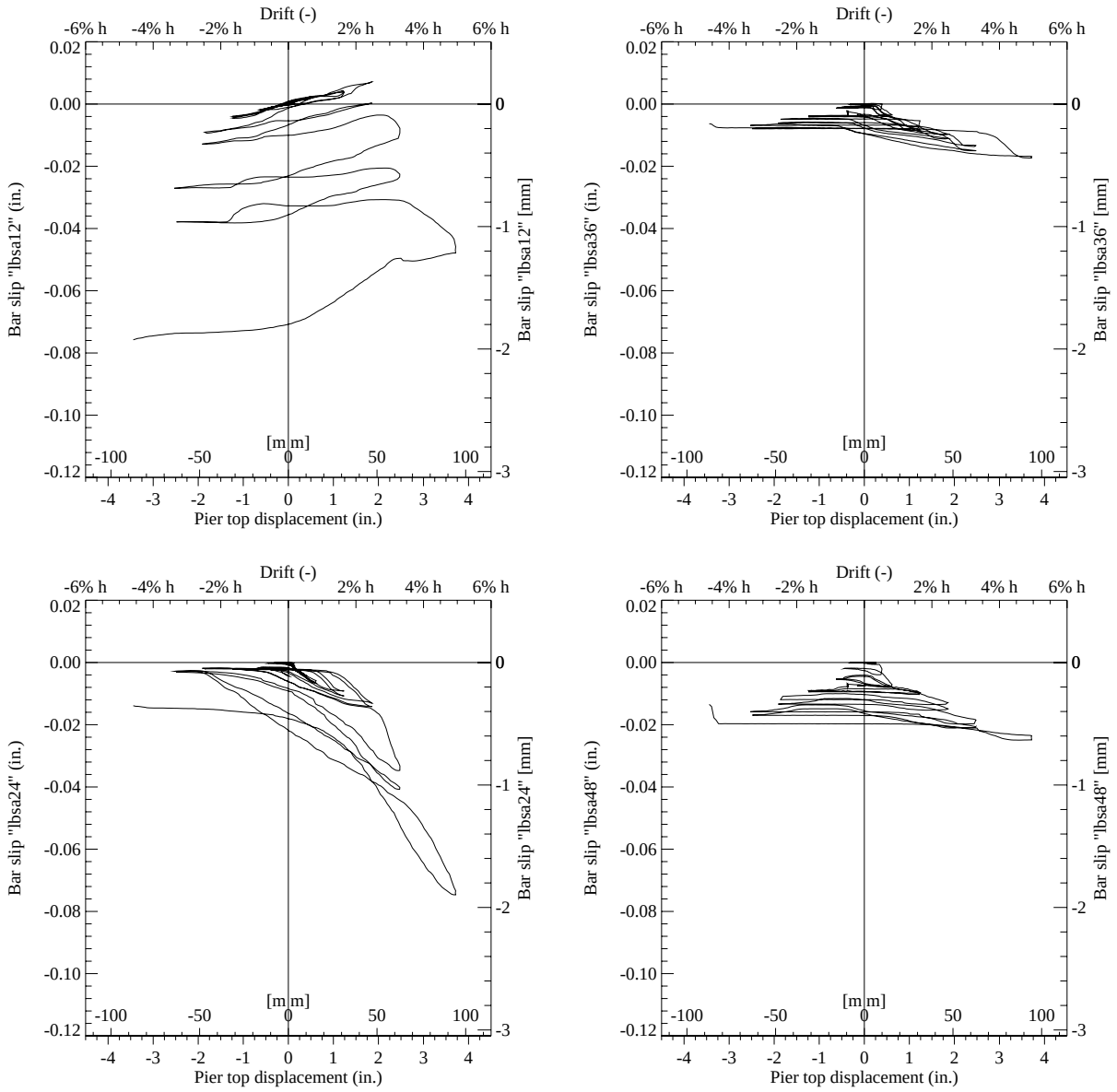

Figure C.25: Test Unit 3B, transverse bar slippage hysteresis at position A for potentiometers LBSA12, LBSA24, LBSA36, LBSA48.

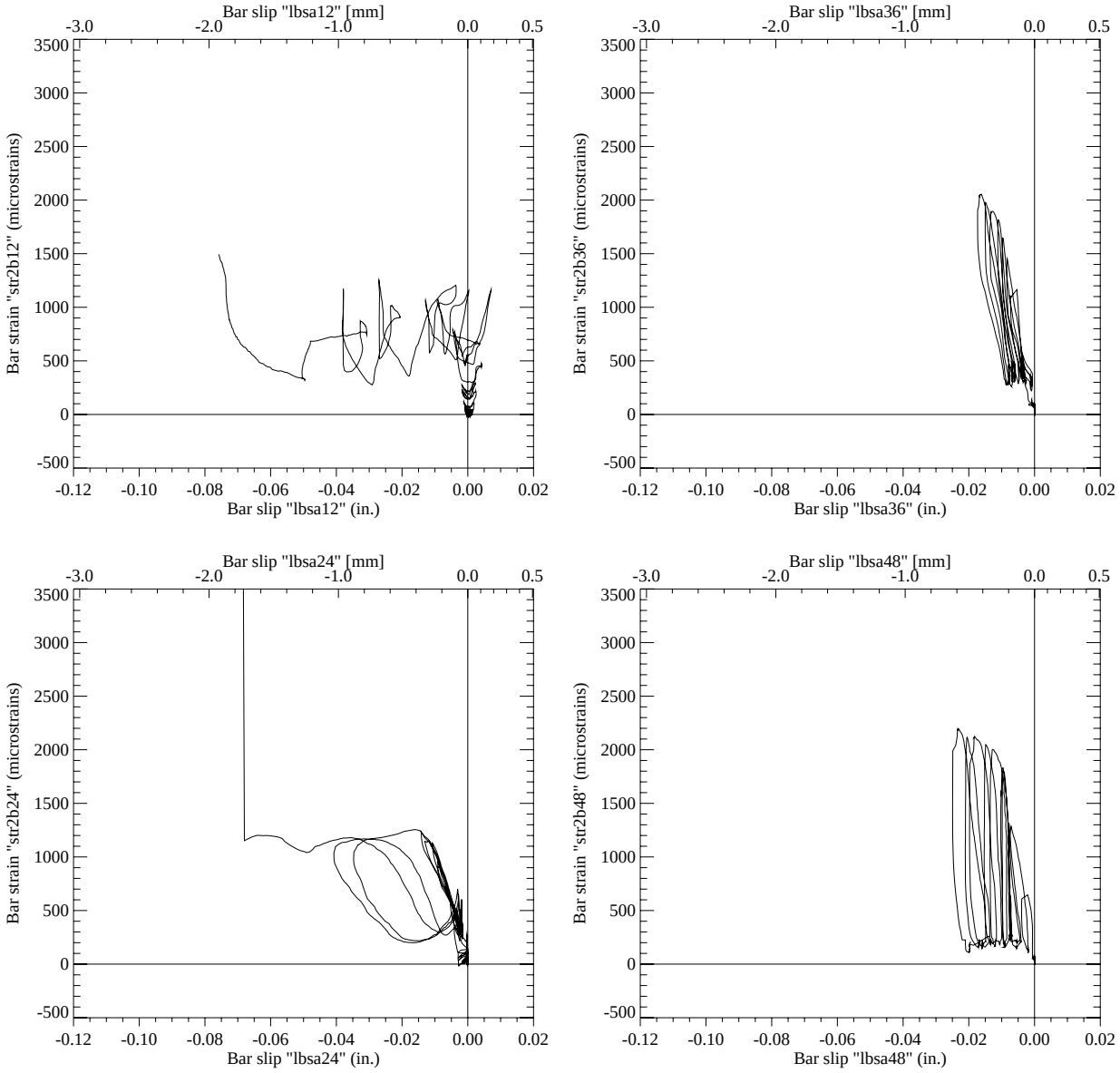

Figure C.26: Test Unit 3B, transverse bar strain as at position B as a function of transverse bar slippage at position A.

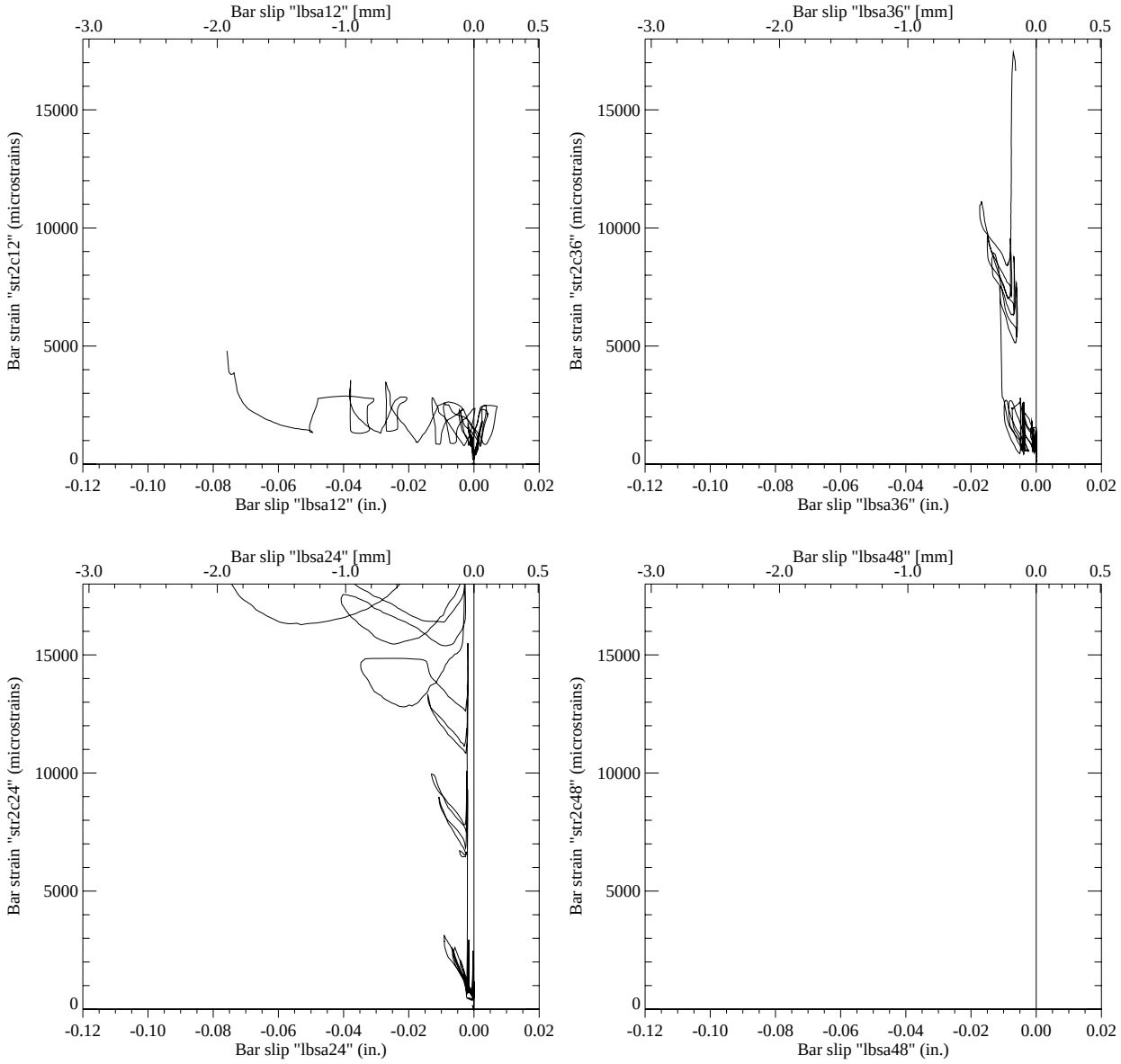

Figure C.27: Test Unit 3B, transverse bar strain as at position C as a function of transverse bar slippage at position A.

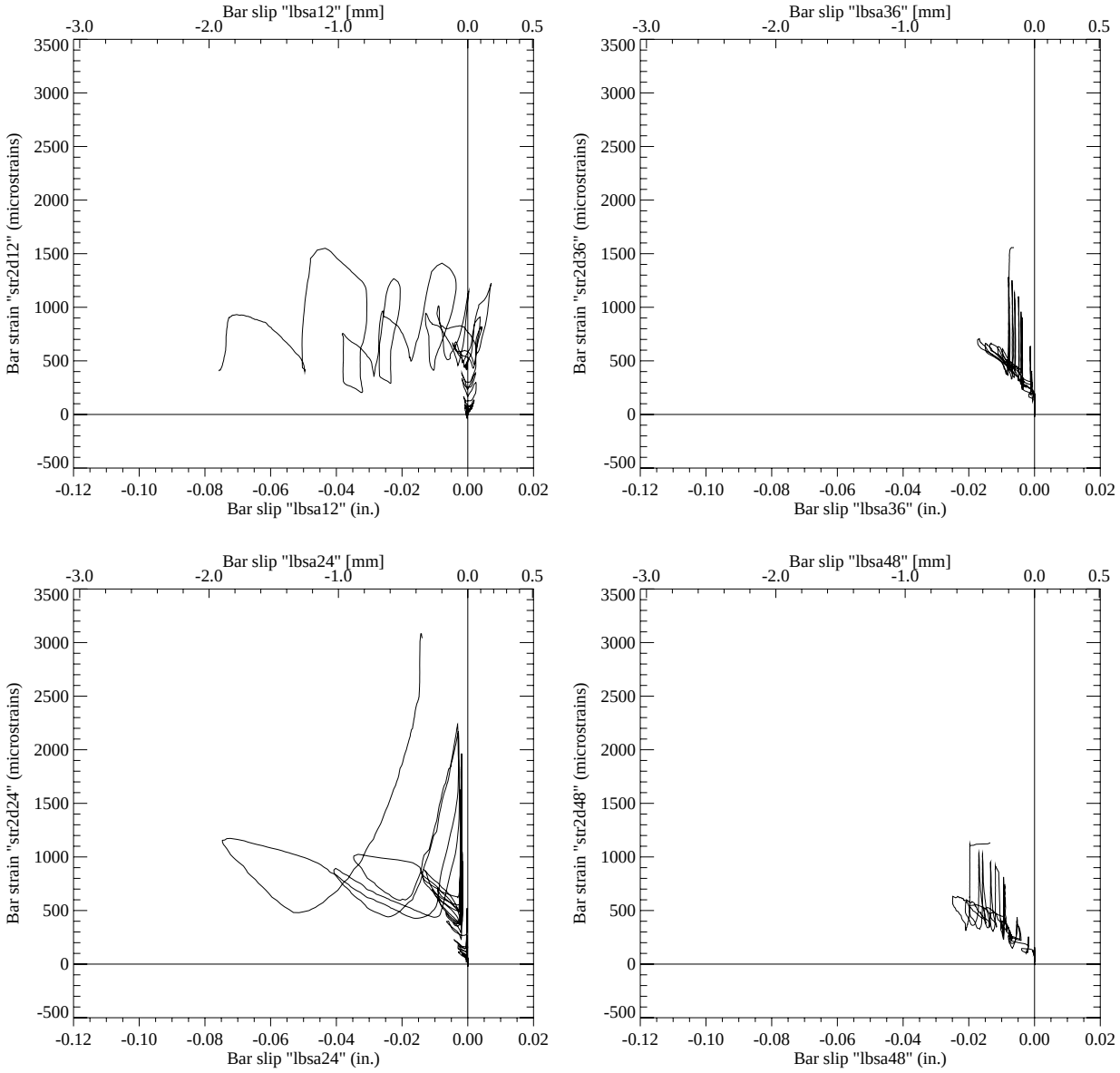

Figure C.28: Test Unit 3B, transverse bar strain as at position D as a function of transverse bar slippage at position A.

C.3 Test Unit 3C

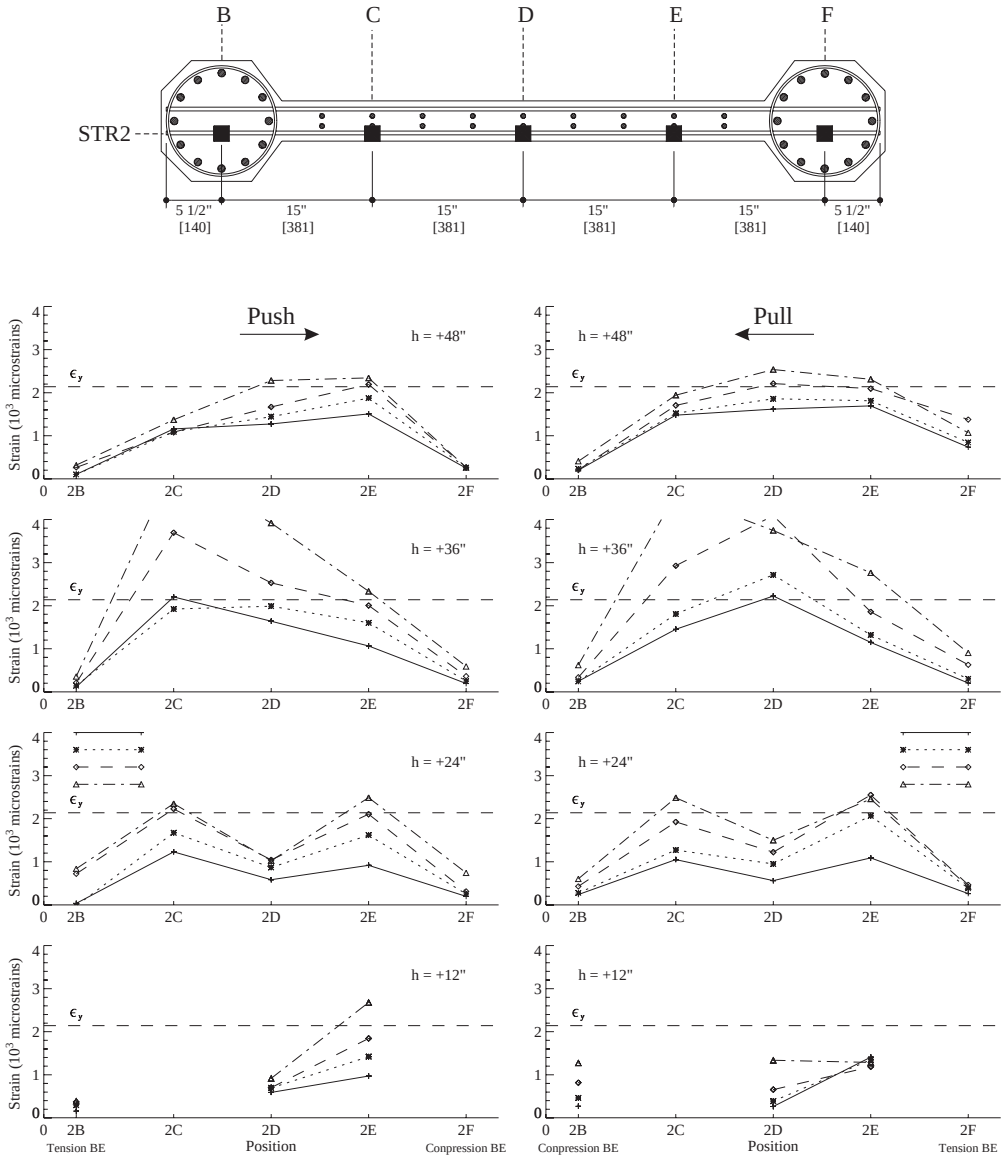

Figure C.29: Test Unit 3C, lower transverse bar strain profiles for bar STR2.

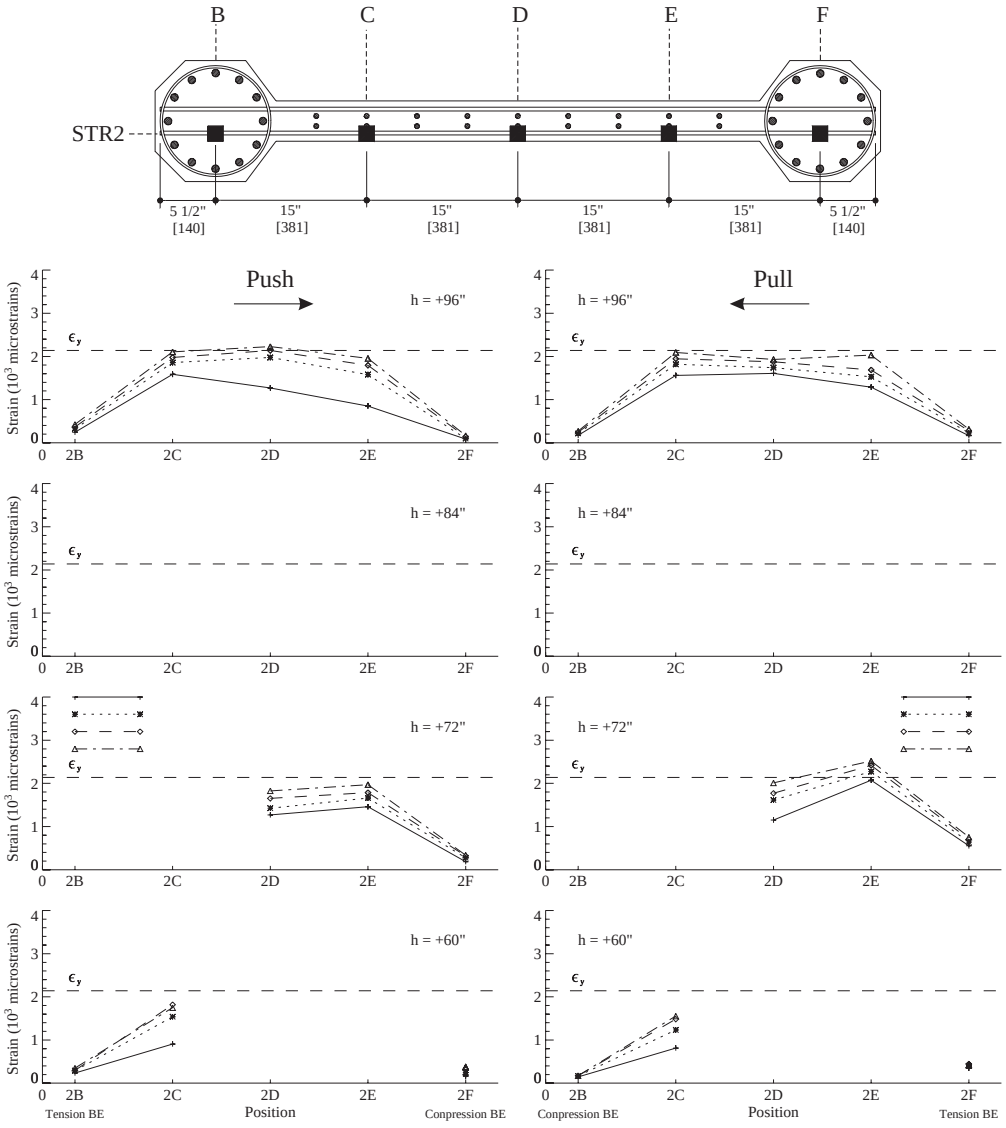

Figure C.30: Test Unit 3C, upper transverse bar strain profiles for bar STR2.

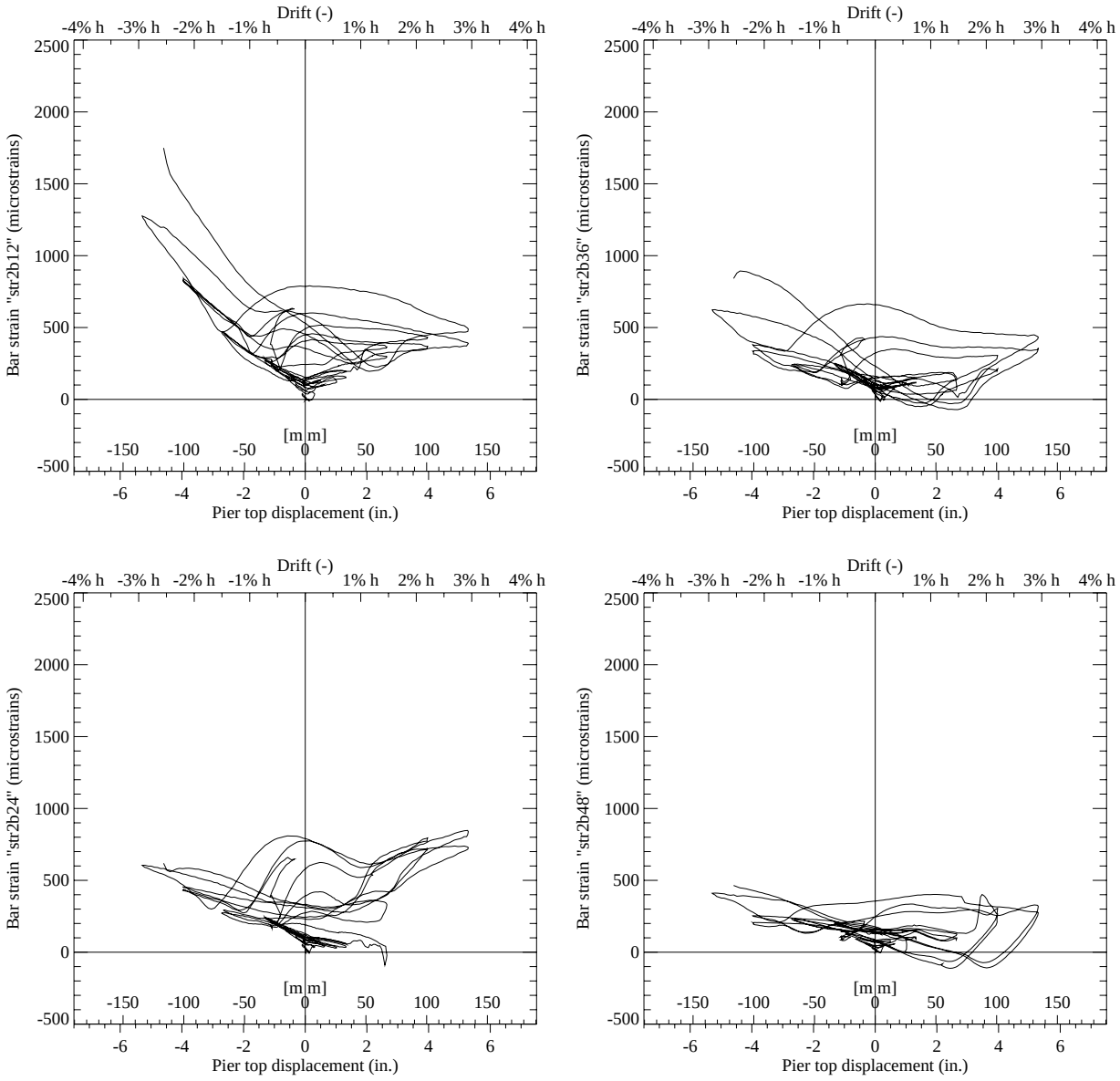

Figure C.31: Test Unit 3C, transverse bar strain hysteresis for gages STR2B12, STR2B24, STR2B36, STR2B48.

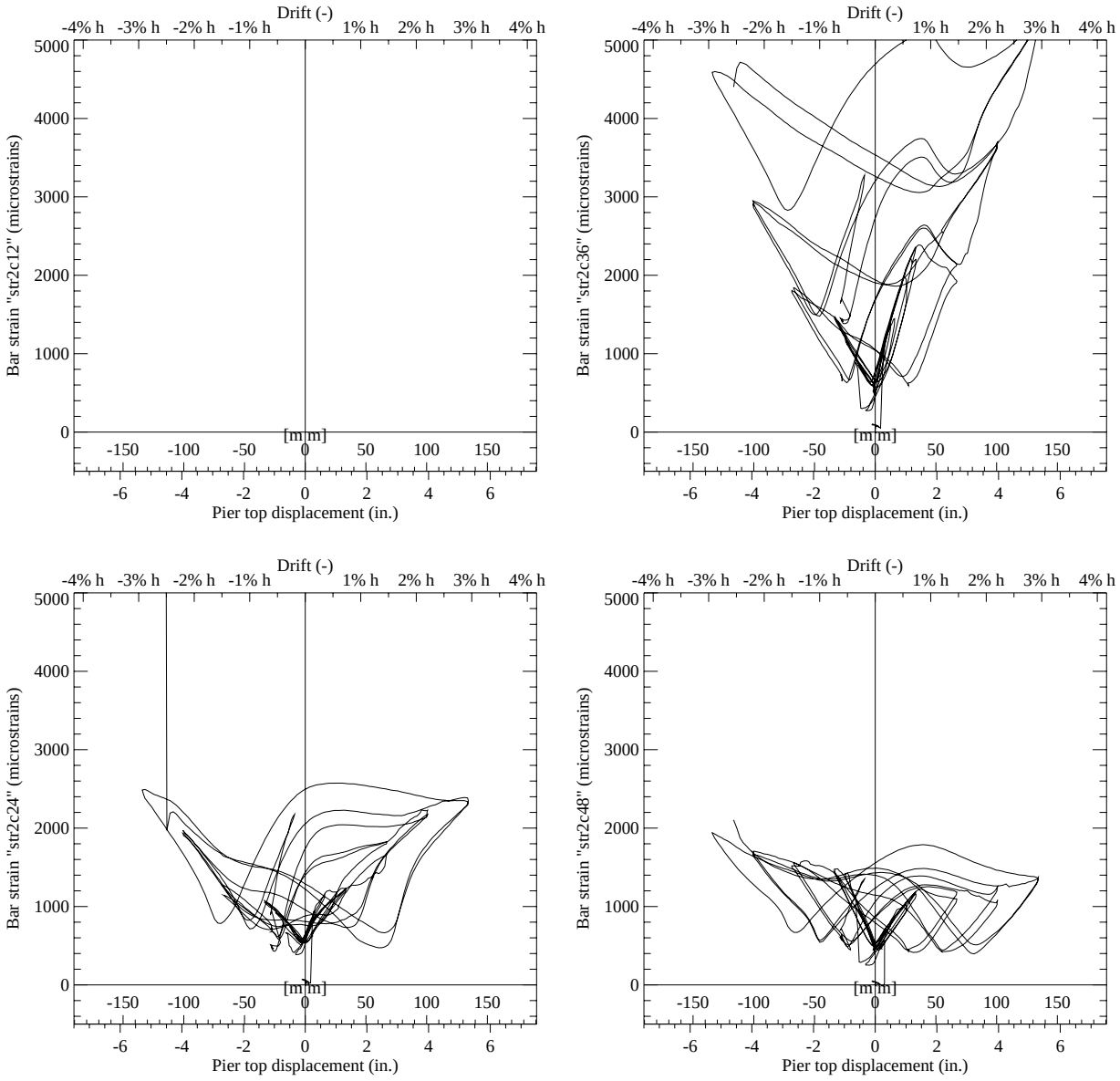

Figure C.32: Test Unit 3C, transverse bar strain hysteresis for gages STR2C12, STR2C24, STR2C36, STR2C48.

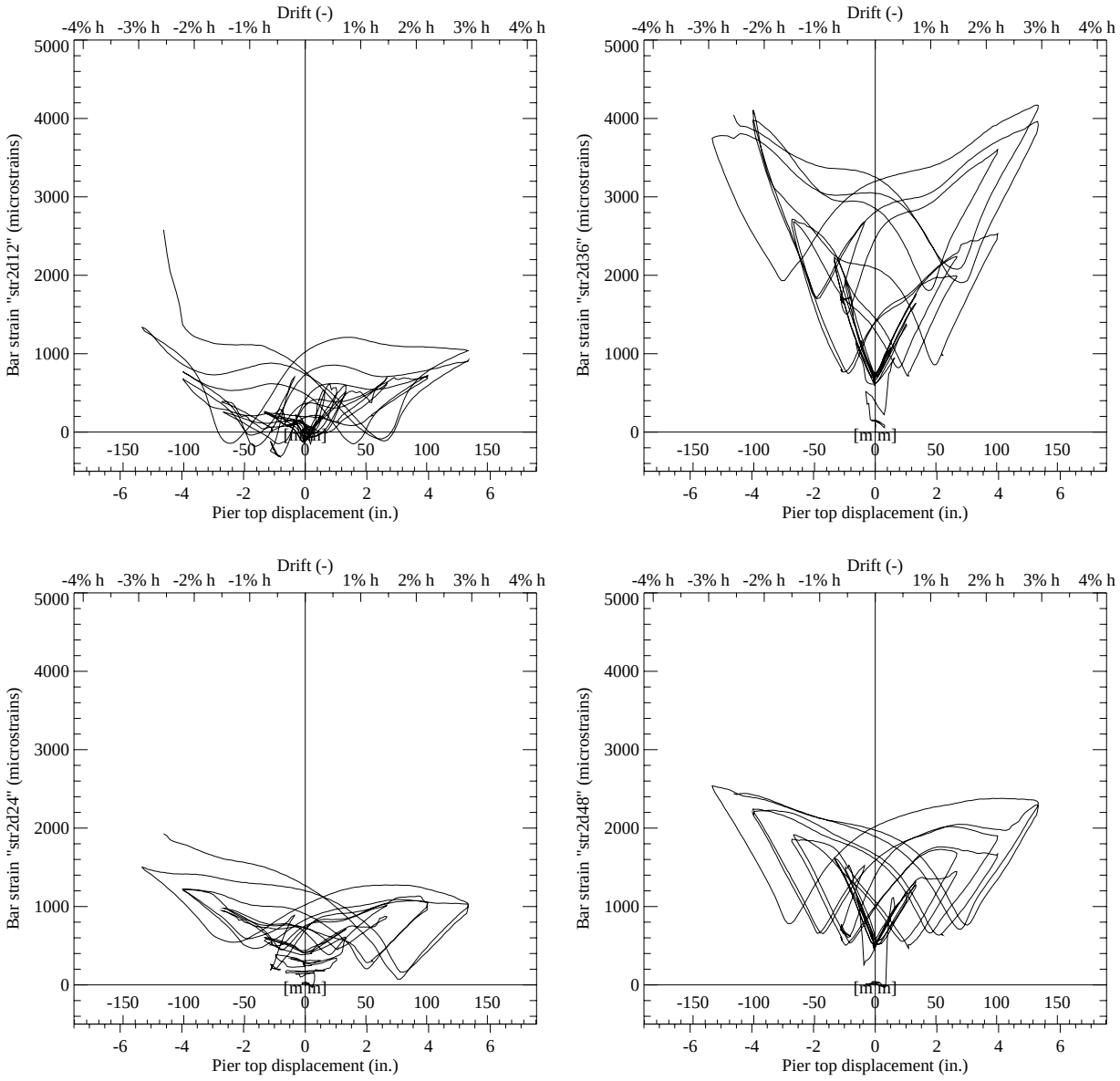

Figure C.33: Test Unit 3C, transverse bar strain hysteresis for gages STR2D12, STR2D24, STR2D36, STR2D48.

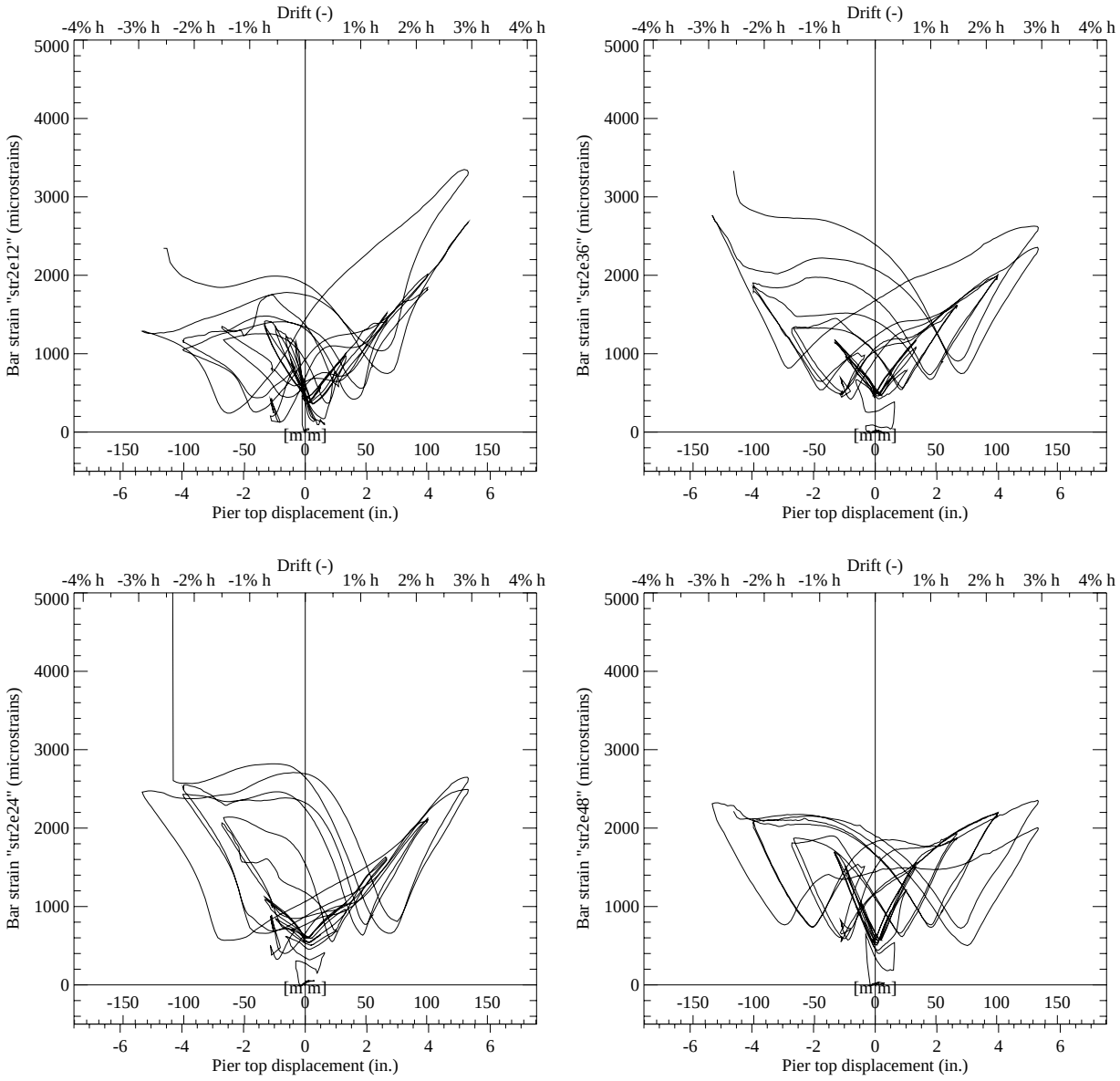

Figure C.34: Test Unit 3C, transverse bar strain hysteresis for gages STR2E12, STR2E24, STR2E36, STR2E48.

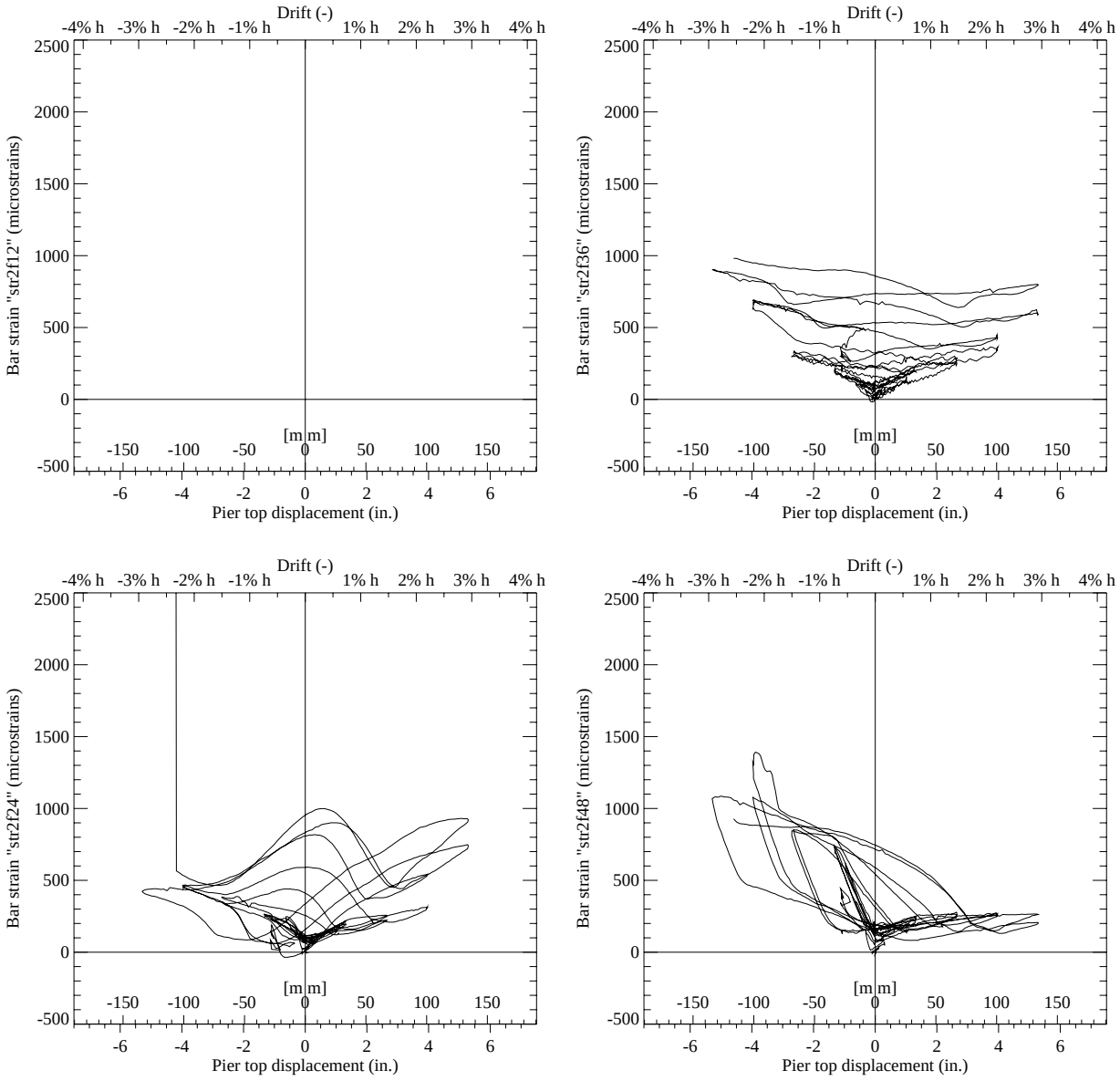

Figure C.35: Test Unit 3C, transverse bar strain hysteresis for gages STR2F12, STR2F24, STR2F36, STR2F48.

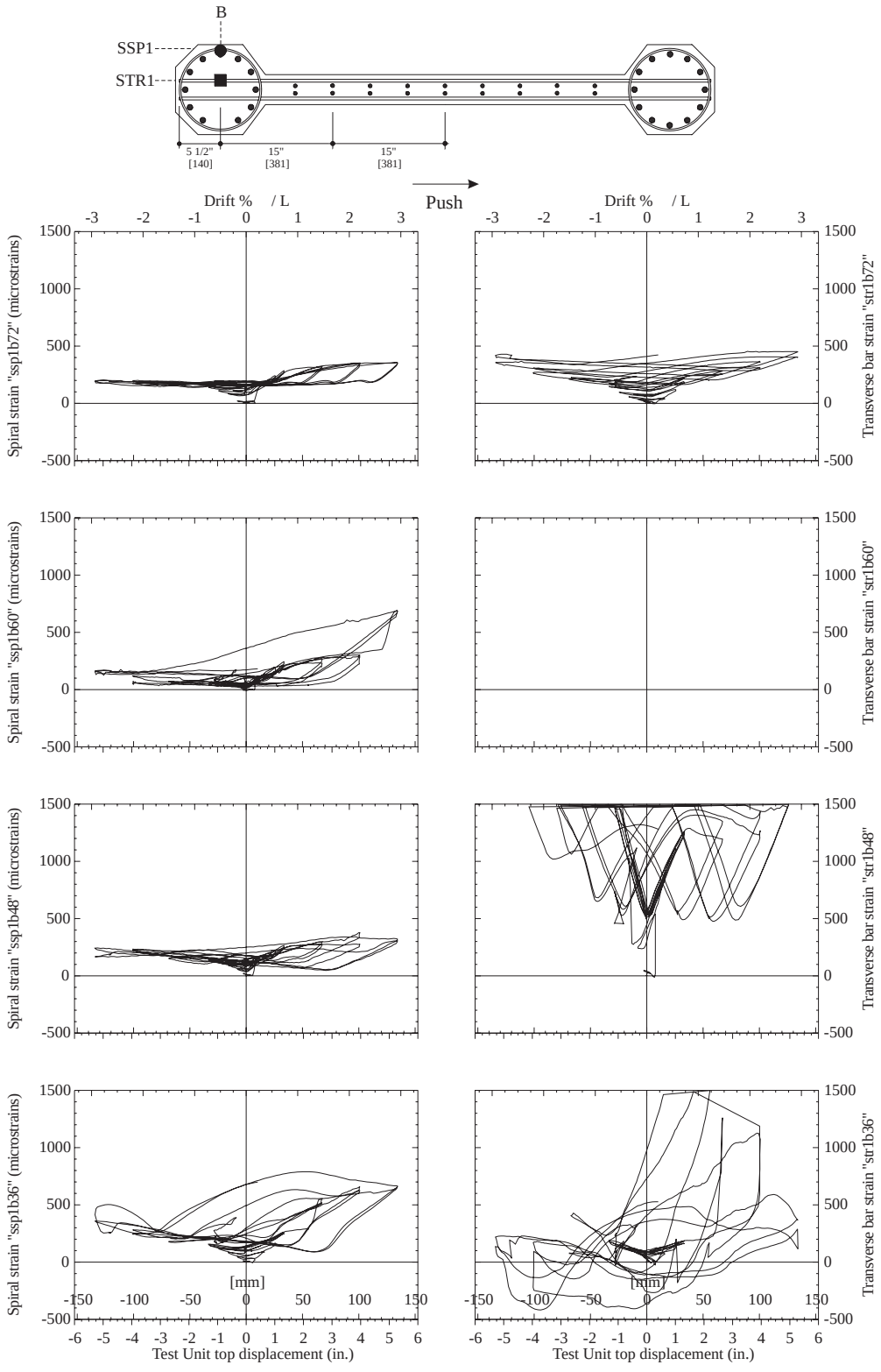

Figure C.36: Test Unit 3C, spiral strains and transverse bar strains at Position 1B, for heights 36 in. [914], 48 in. [1219], 60 in. [1524] and 72 in. [1829] above the footing.

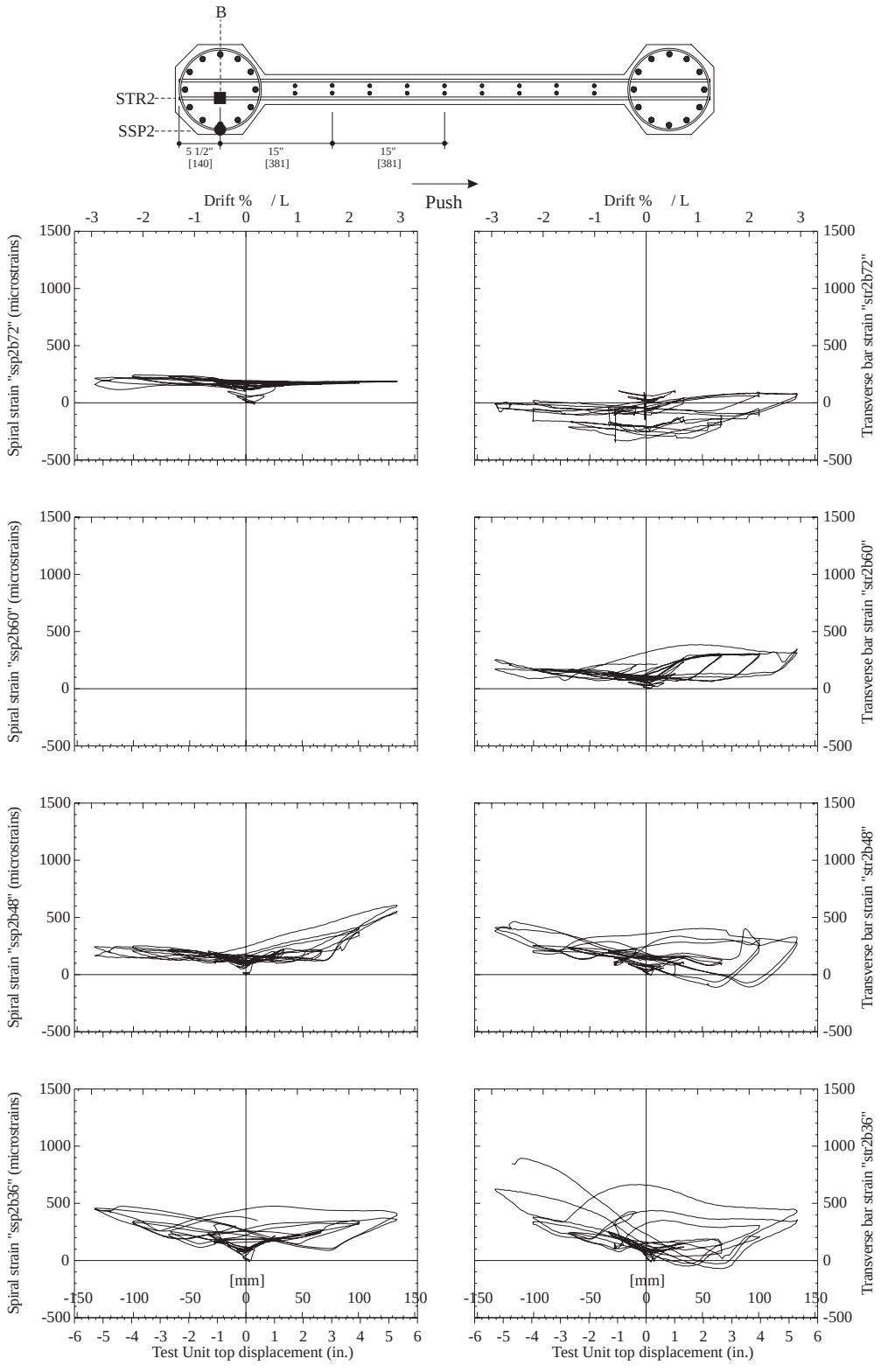

Figure C.37: Test Unit 3C, spiral strains and transverse bar strains at Position 2B, for heights 36 in. [914], 48 in. [1219], 60 in. [1524] and 72 in. [1829] above the footing.

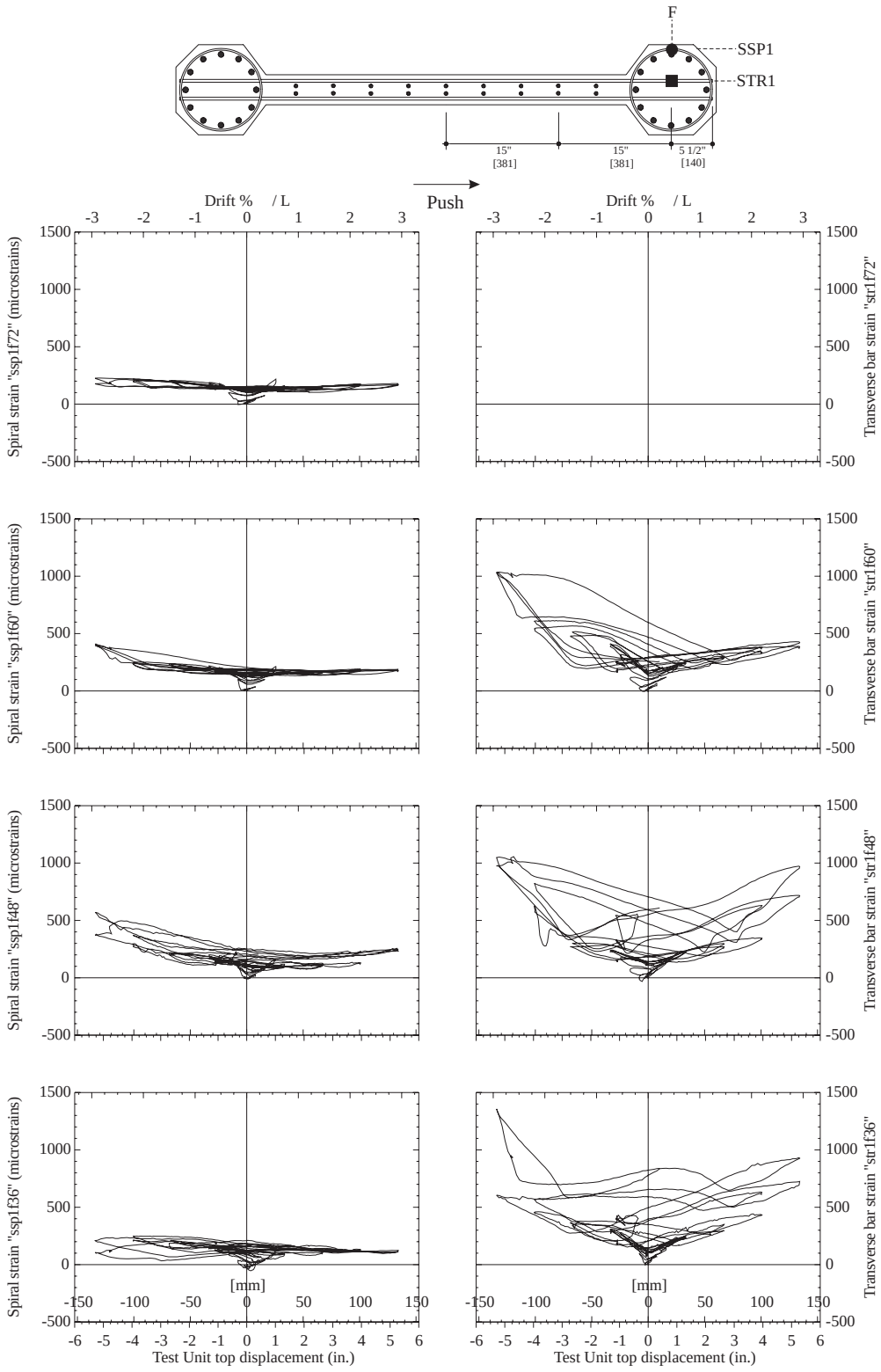

Figure C.38: Test Unit 3C, spiral strains and transverse bar strains at Position 1F, for heights 36 in. [914], 48 in. [1219], 60 in. [1524] and 72 in. [1829] above the footing.

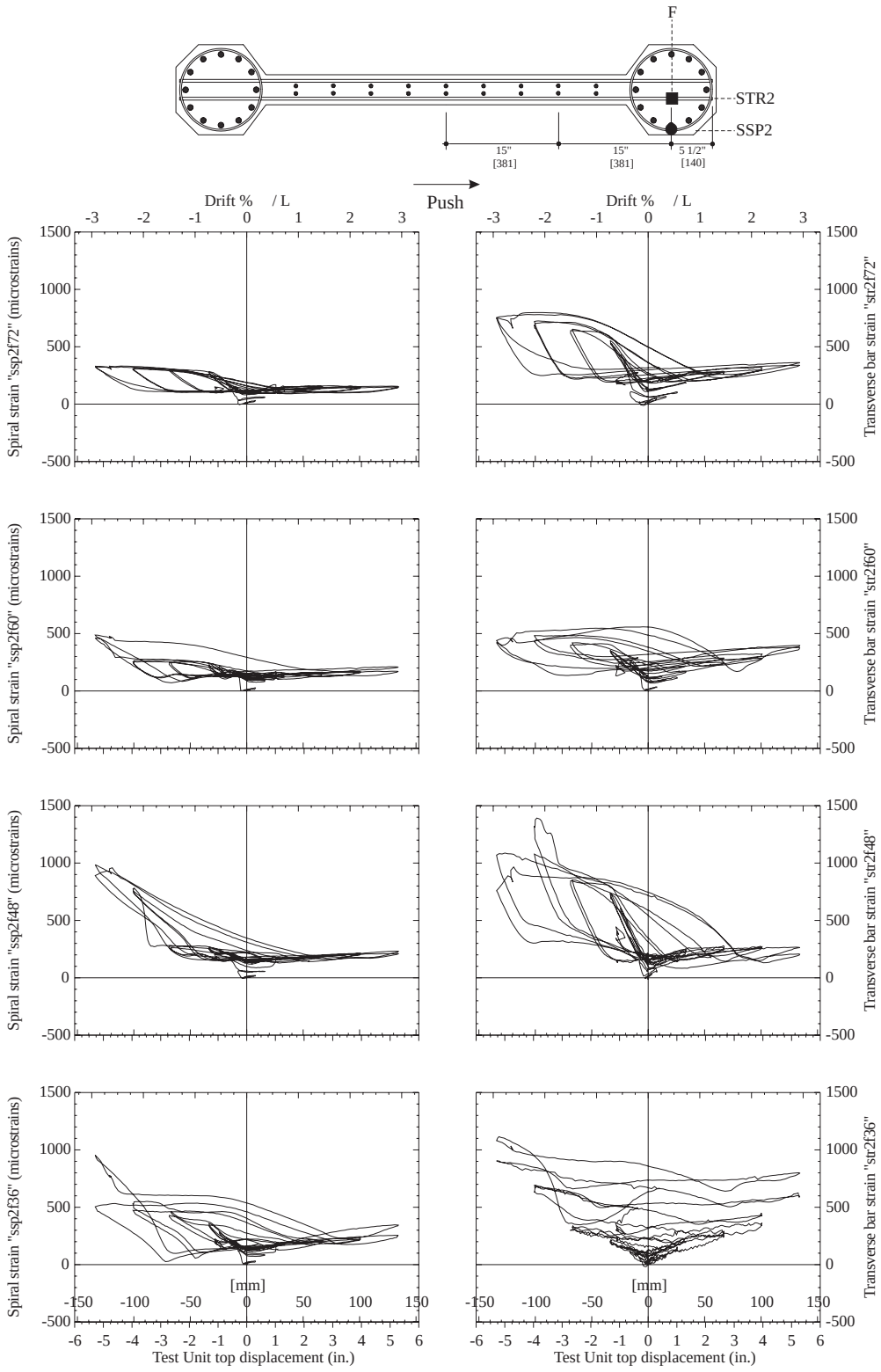

Figure C.39: Test Unit 3C, spiral strains and transverse bar strains at Position 2F, for heights 36 in. [914], 48 in. [1219], 60 in. [1524] and 72 in. [1829] above the footing.

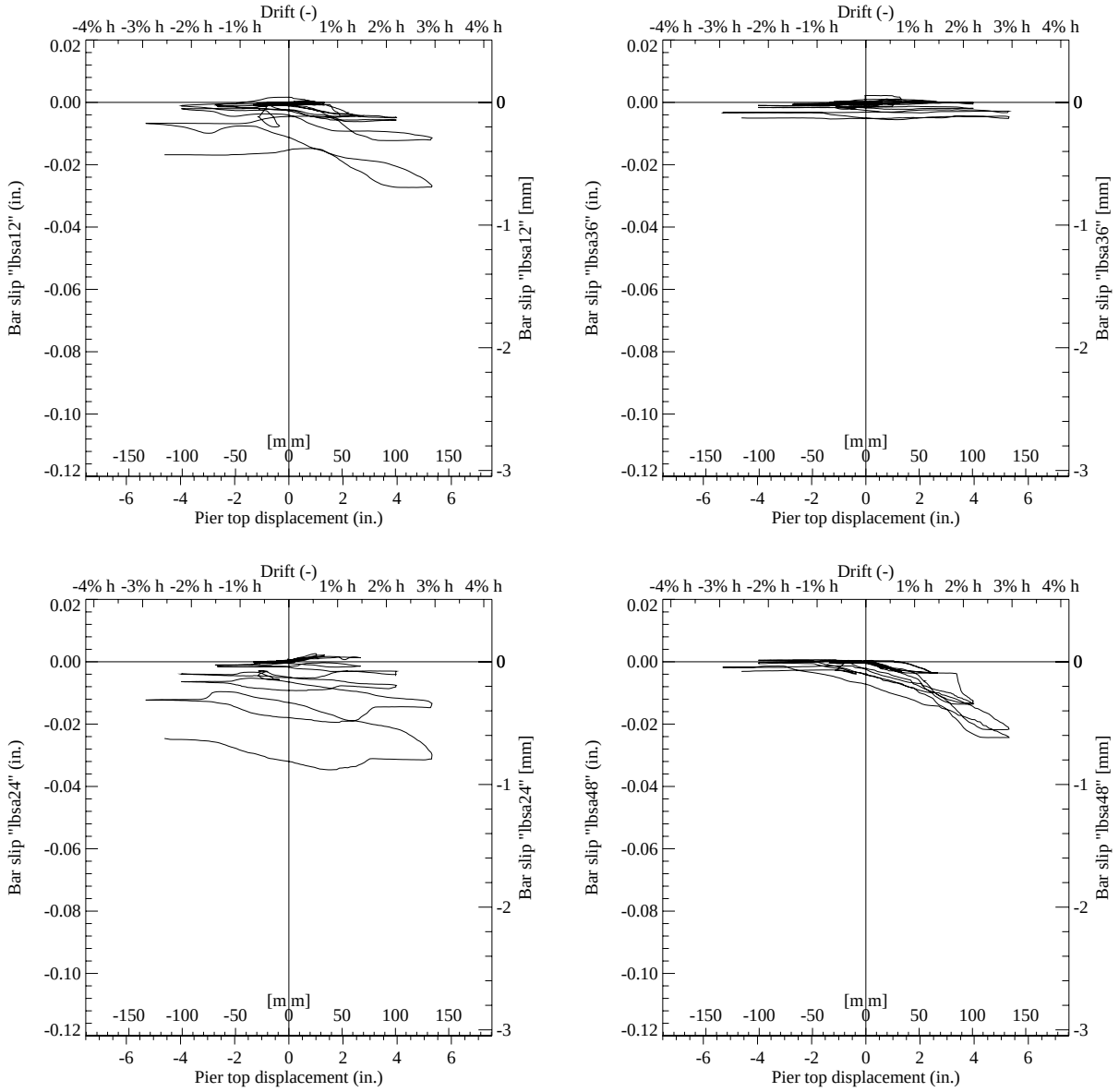

Figure C.40: Test Unit 3C, transverse bar slippage hysteresis at position A for potentiometers LBSA12, LBSA24, LBSA36, LBSA48.

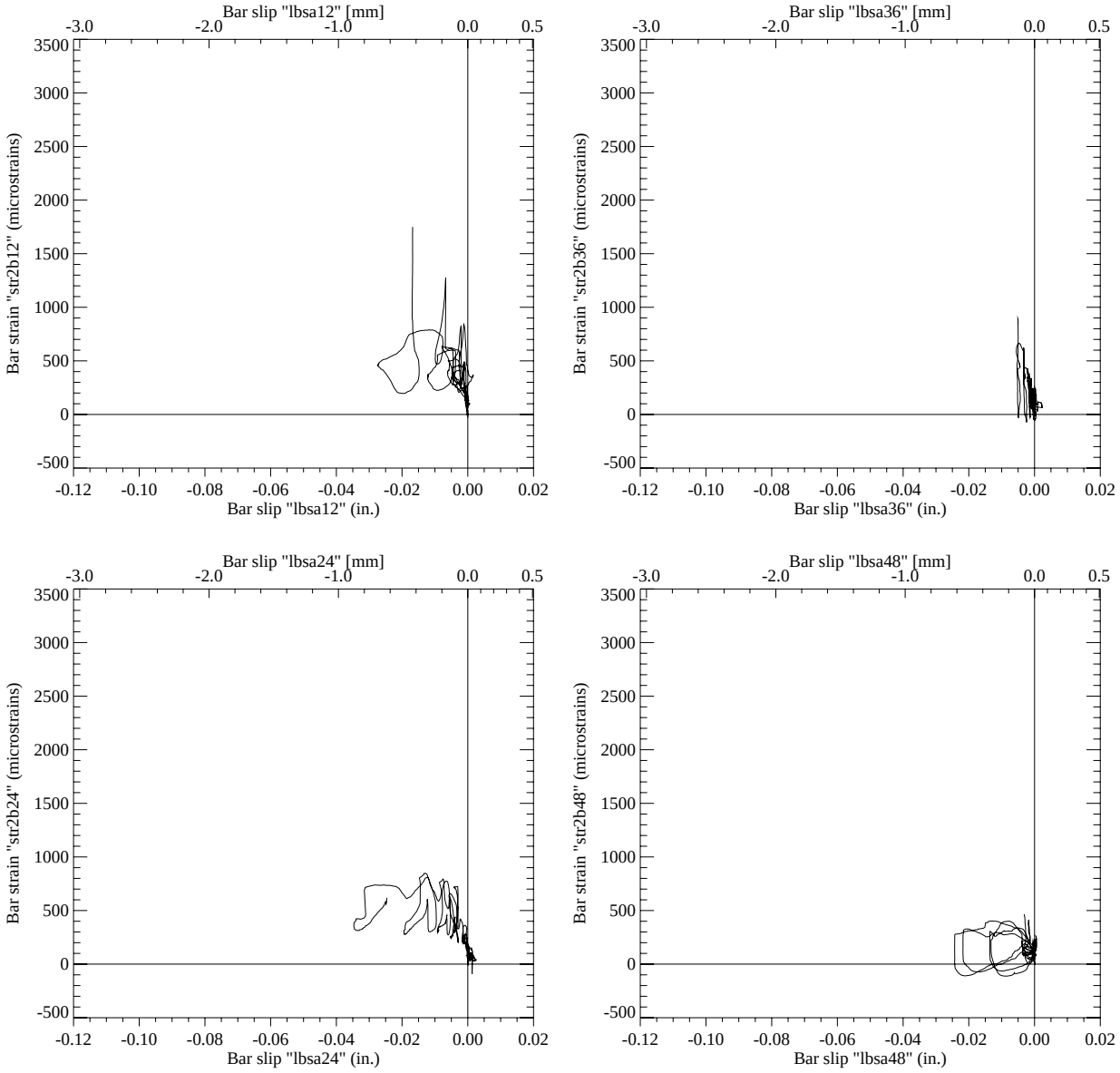

Figure C.41: Test Unit 3C, transverse bar strain as at position B as a function of transverse bar slippage at position A.

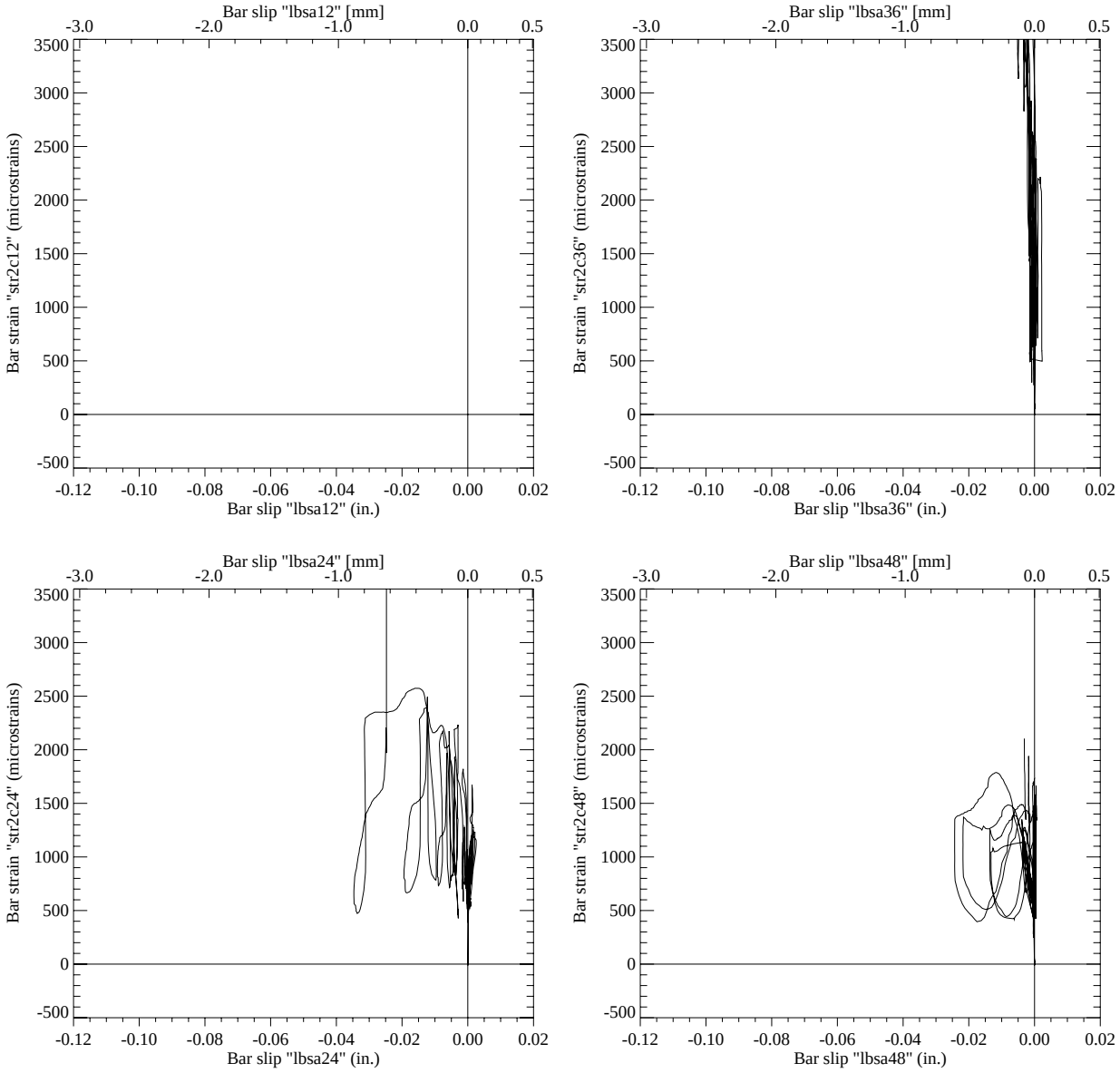

Figure C.42: Test Unit 3C, transverse bar strain as at position C as a function of transverse bar slippage at position A.

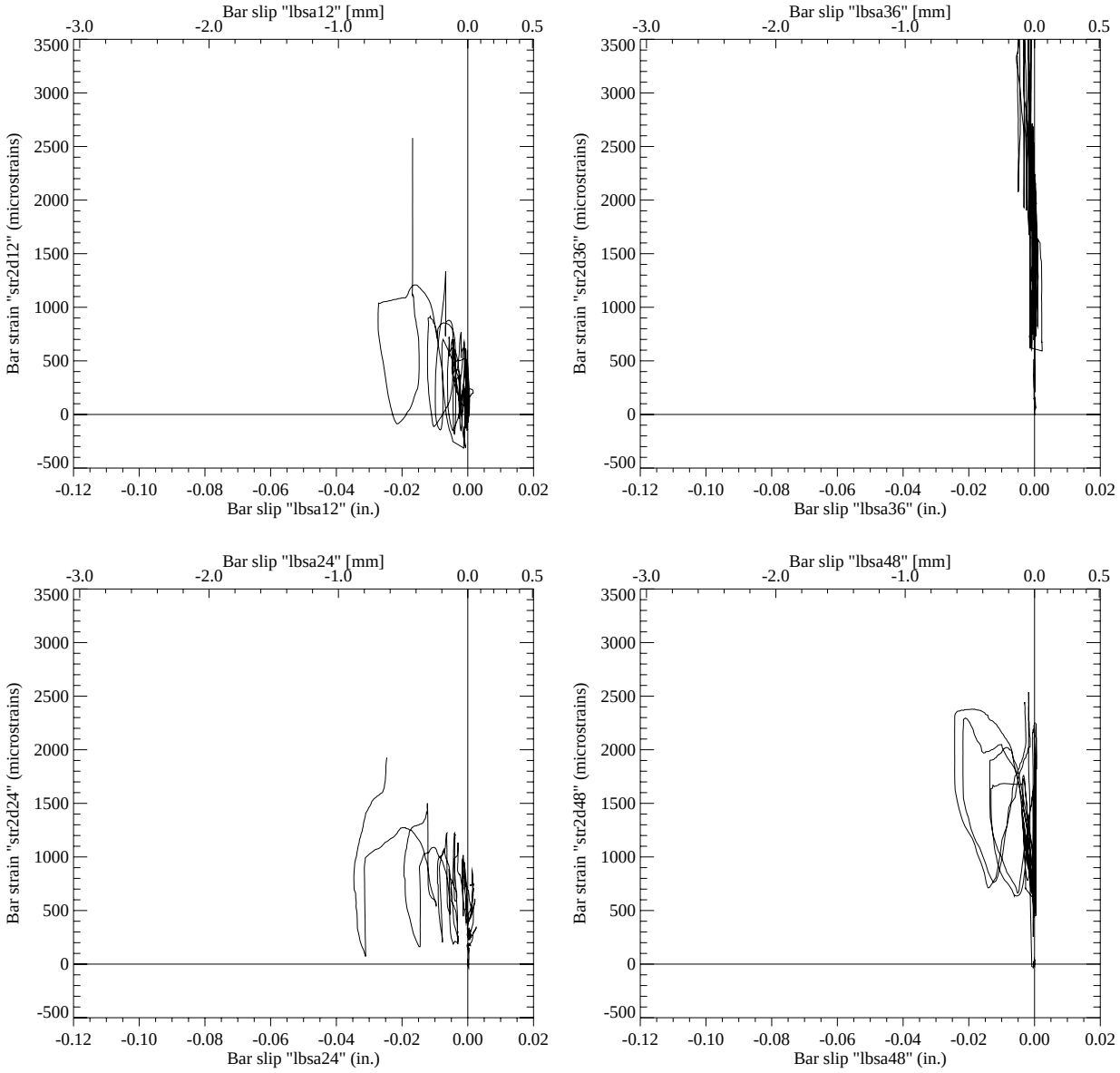

Figure C.43: Test Unit 3C, transverse bar strain as at position D as a function of transverse bar slippage at position A.

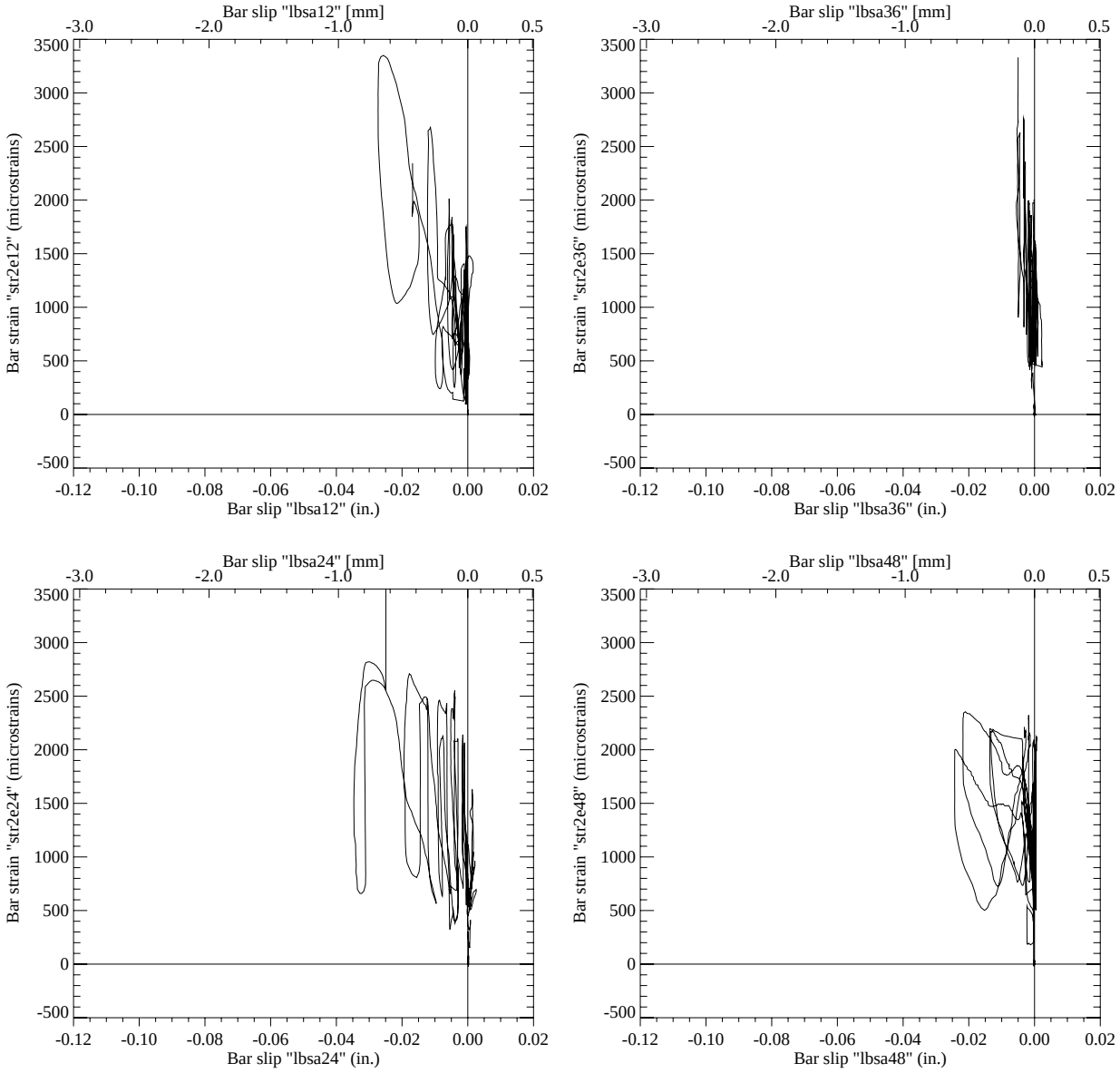

Figure C.44: Test Unit 3C, transverse bar strain as at position E as a function of transverse bar slippage at position A.

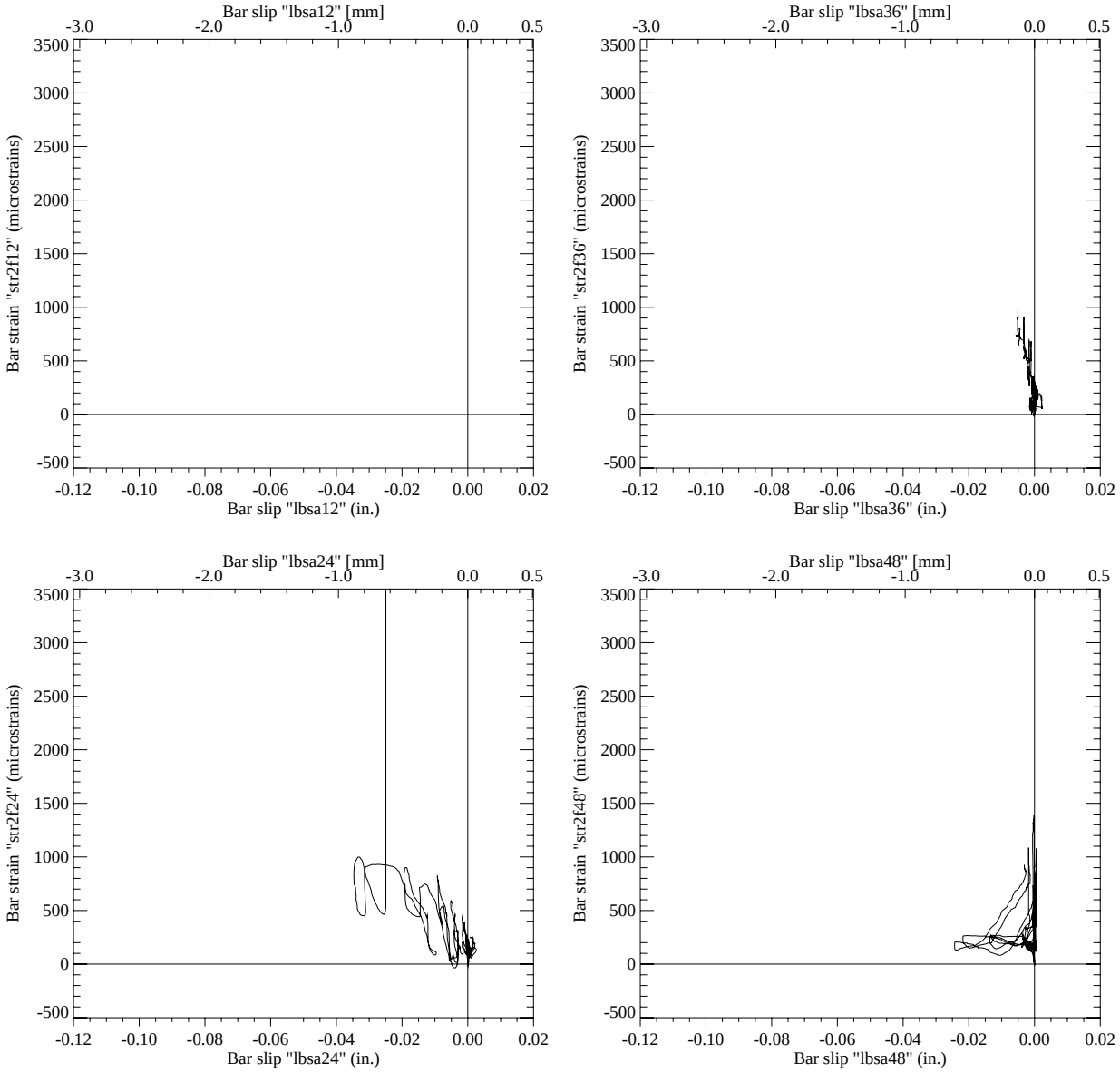

Figure C.45: Test Unit 3C, transverse bar strain as at position F as a function of transverse bar slippage at position A.

References

[1] E.M. Hines, F. Seible, and M.J.N. Priestley. Cyclic tests of structural walls with highly-confined boundary elements. Structural Systems Research Project SSRP 99-15, University of California, San Diego, La Jolla, CA, 1999.

[2] ACI. *Building Code Requirements for Reinforced Concrete*. American Concrete Institute, Detroit, MI, 1995.

[3] T. Paulay and M.J.N. Priestley. *Seismic Design of Reinforced Concrete and Masonry Buildings*. Wiley, New York, 1992.

[4] R.G. Oesterle, A.E. Fiorato, and W.G. Corley. Web crushing of reinforced concrete structural walls. *ACI Journal*, 81(3):231–241, May-June 1984.

[5] R.G. Oesterle, A.E. Fiorato, L.S. Johal, J.E. Carpenter, H.G. Russell, and W.G. Corley. Earthquake resistant structural walls–tests of isolated walls. NSF Report GI-43880, Portland Cement Association, Skokie, IL, November 1976.

[6] R.G. Oesterle, J.D. Ariztizabal-Ochoa, A.E. Fiorato, H.G. Russell, and W.G. Corley. Earthquake resistant structural walls–tests of isolated walls–phase ii. NSF Report ENV77-15333, Portland Cement Association, Skokie, IL, October 1979.

[7] M.J.N. Priestley, F. Seible, and Calvi G.M. *Seismic Design and Retrofit of Bridges*. Wiley, New York, 1996.

[8] M.P. Collins. Towards a rational theory for rc members in shear. *ASCE Journal of the Structural Division*, 104(ST4):649–666, April 1978.

[9] F.J. Vecchio and M.P. Collins. The modified compression-field theory for reinforced concrete elements subjected to shear. *ACI Journal*, 83(22):219–231, March–April 1986.

[10] M.J. Kowalsky and M.J.N. Priestley. "An improved analytical model for shear strength of circular RC columns in seismic regions". ACI Journal, 97(3):388–396, May-June 2000.

[11] E.M. Hines, F. Seible, R.K. Dowell, and A. Dazio. Structural testing of the san francisco-oakland bay bridge east span skyway structures: Longitudinal pier test. Test Report TR 2000-21, University of California, San Diego, La Jolla, CA, 2000.

[12] J.B. Mander, M.J.N. Priestley, and R. Park. Theoretical stress-strain model for confined concrete. *ASCE Journal of Structural Engineering*, 114(8):1804–1826, August 1988.

[13] J.B. Mander. *Seismic Design of Bridge Piers*. PhD thesis, University of Canterbury, Christchurch, New Zealand, 1984.

[14] L.L. Dodd. The dynamic behavior of reinforced concrete bridge piers subjected to new zealand seismicity. Research Report 92-04, University of Canterbury, Christchurch, New Zealand, Christchurch, NZ, 1992.

[15] S. Popovics. A numerical approach to the complete stress-strain curve of concrete. *Cement and Concrete Research*, 3(-):583–599, 1973.

[16] M.J.N. Priestley, M.J. Kowalsky, N. Vu, and C. McDaniel. Comparison of recent shear strength provisions for circular bridge columns. In *5th Caltrans Seismic Research Workshop*, pages :session 9, paper 3, Sacramento, CA, June 1998.

[17] A. Dazio. *Entwurf und Bemessung von Tragwandgebaeuden unter Erdbebeneinwirkung*. PhD thesis, ETH, Zuerich, CH, 2000.

[18] E.C. Bentz and M.P. Collins. *Response-2000, Reinforced Concrete Sectional Analysis using the Modified Compression Field Theory*. University of Toronto, Toronto, Canada, 0.7.5 (beta) edition, 1998.

[19] Inc. Hibbitt, Karlsson & Sorensen. *Abaqus*. HKS Inc., Pawtucket, RI, 5.8 edition, 1998.

[20] Y.R. et al. Rashid. *Constitutive Modeling of Reinforced Concrete and Steel*. ANATECH Corp., San Diego, CA, 1996.

[21] Anatech Corporation. *ANACAP-U User's Manual, Version 2.5*. ANATECH Corp., San Diego, CA, 1997.

[22] J.I. Restrepo-Posada. Seismic behavior of connections between precast concrete elements. Research Report 93-03, University of Canterbury, Christchurch, New Zealand, Christchurch, NZ, 1993.

[23] Y.D. Hose, D. Brestel, F. Seible, and R.K. Dowell. Assessment of hoop strains in the flexural plastic hinge region of typical bridge columns. Structural Systems Research Project SSRP - 2000/11, University of California, San Diego, La Jolla, CA, 2000.

[24] A.V. Sanchez, F. Seible, and M.J.N. Preistley. Seismic performance of flared bridge columns. Structural Systems Research Project SSRP - 97/06, University of California, San Diego, La Jolla, CA, 1997.

[25] A.V. Sanchez. *Seismic Performance of Flared Bridge Columns*. PhD thesis, University of California, San Diego, 1998.